Department of Physics and Astronomy

University of Heidelberg

Master thesis

in Physics

submitted by

Lars Henkelmann

born in Darmstadt

2018

Search for Dark Matter Using the $h(b\bar{b}) + E_T^{\text{miss}}$ Signature of the New "Two-Higgs-Doublet Model with Pseudoscalar Mediator" Benchmark Model with the ATLAS Detector

This Master thesis has been carried out by

Lars Henkelmann

at the

Kirchhoff Institut für Physik

under the supervision of

Priv. Doz. Dr. Oleg Brandt

Search for Dark Matter Using the $h(b\bar{b}) + E_T^{\text{miss}}$ Signature of the New "Two-Higgs-Doublet Model with Pseudoscalar Mediator" Benchmark Model with the ATLAS Detector:

The nature of Dark Matter is an open question, despite plentiful astrophysical evidence for its existence. Dark Matter searches at colliders complement other search strategies by providing a controlled laboratory environment and sensitivity to low-mass Dark Matter. The $h(b\bar{b}) + E_T^{\text{miss}}$ collider signature directly probes potential hard interactions of Dark Matter and the Higgs boson. However, such interactions are missing in conventional signal models, inhibiting comparisons to other signatures. The Two-Higgs-Doublet Model with Pseudoscalar Mediator (2HDM+a) [1] solves this problem by predicting a large variety of Dark Matter signatures with detectable production cross sections at the LHC.
This thesis identifies 2HDM+a parameter regions relevant to the $h(b\bar{b}) + E_T^{\text{miss}}$ signature. A 2HDM+a benchmark tuned to the ATLAS $h(b\bar{b}) + E_T^{\text{miss}}$ search [2] is constructed, using a simplified sensitivity estimate. This estimate is compared to the detailed simulation of the ATLAS sensitivity, and found to be consistent. The ATLAS $h(b\bar{b}) + E_T^{\text{miss}}$ search using $36.1\,\text{fb}^{-1}$ of pp collision data at $\sqrt{s} = 13\,\text{TeV}$ is interpreted in the 2HDM+a. No deviation from the Standard Model is observed. Limits are set on the 2HDM+a parameters, excluding masses up to 0.35 TeV of the light mediator and between 0.4 TeV and 1.3 TeV of the heavy mediator.

Suche nach Dunkler Materie mit der $h(b\bar{b}) + E_T^{\text{miss}}$ Signatur des neuen „Zwei-Higgs-Doublett Modell mit Pseudoskalarem Mediator" Referenz-Modells mit dem ATLAS Detektor:

Die Natur Dunkler Materie ist eine offene Frage, trotz vielfältiger Astrophysikalischer Hinweise auf ihre Existenz. Beschleunigersuchen nach Dunkler Materie ergänzen andere Suchstrategien durch eine kontrollierte Laborumgebung und Sensitivität auf leichte Dunkle Materie. Die $h(b\bar{b}) + E_T^{\text{miss}}$ Beschleunigersignatur ermöglicht die Untersuchung potentieller harter Wechselwirkungen Dunkler Materie mit dem Higgs Boson. Derartige Wechselwirkungen fehlen jedoch in den gebräuchlichen Signalmodellen, was Vergleiche mit anderen Beschleunigersignaturen behindert. Das Zwei-Higgs-Doublett Modell mit Pseudoskalarem Mediator (2HDM+a) [1] löst dieses Problem, da es eine große Vielfalt von an Hochenergie-Teilchenbeschleunigern beobachtbaren Signaturen Dunkler Materie voraussagt.
Diese Arbeit identifiziert 2HDM+a Parameterregionen, welche für die $h(b\bar{b}) + E_T^{\text{miss}}$ Signatur relevant sind. Ein 2HDM+a Referenz-Parameterscan wird anhand der Sensitivität der ATLAS Suche nach $h(b\bar{b}) + E_T^{\text{miss}}$ [2] konstruiert, mittels einer vereinfachten Sensitivitätsabschätzung. Diese Sensitivitätsschätzung wird mit der detailliert simulierten ATLAS-Sensitivität verglichen, und ist konsistent mit dieser. Die ATLAS $h(b\bar{b}) + E_T^{\text{miss}}$-Suche mit $36.1\,\text{fb}^{-1}$ von pp Kollisionsdaten bei $\sqrt{s} = 13\,\text{TeV}$ wird im 2HDM+a interpretiert, und keine signifikante Abweichung vom Standardmodell wird beobachtet. Es werden Auschlussgrenzen auf den Parameterraum des 2HDM+a gesetzt, welche Massen des leichten Mediators von bis zu 0.35 TeV und des schweren Mediators zwischen 0.4 TeV und 1.3 TeV auschliessen.

Contents

Chapter 1

Introduction

Then proudly smiled that old man
To see the eager lad
Rush madly for his pen and ink
And for his blotting-pad –
But, when he thought of publishing*,*
His face grew stern and sad.

— Lewis Carroll*, Poeta Fit, Non Nascitur (1883)*

1.1 Motivation

The nature of Dark Matter is a longstanding open question of physics and cosmology [3, 4, 5, 6, 7]. Cosmological and astrophysical evidence for the existence of the large class of phenomena explained by the Dark Matter hypothesis is plentiful [3, 8, 5]. Yet consistent and reproducible evidence for the existence of a new type of matter that can be interpreted as Dark Matter has not been found, despite decades of experimental effort [3, 9, 10].

Attempts to produce Dark Matter at high energy particle colliders are one category of the efforts to understand the nature of Dark Matter. They complement other search channels, such as direct and indirect detection searches, by providing an extremely well controlled laboratory environment. Moreover they are sensitive to Dark Matter particles of very low masses, unlike direct detection searches The Large Hadron Collider (LHC) at CERN has been a particular focus of these searches, due to the very high center of mass energies of the colliding beams. Dark Matter searches at the LHC do however face a unique theoretical peculiarity: the effective contact interaction operators used to describe and interpret other Dark Matter searches can not be used to describe LHC collisions [7, 11]. Such contact operators would predict scattering amplitudes that do not conserve probability, due to the high momenta involved in the proton collisions.

One widely used solution are simplified models, which specify the generic contact operators into diagrams where mediating particles are explicitly exchanged [7, 11]. Some simplified models involve interactions where Standard Model bosons are produced in hard decays of Dark Matter mediators, coupling them directly to the Dark Matter particle production. Such interactions are in contrast to the standard simplified models used to date, wherein Dark Matter particles are produced in Initial State Radiation (ISR), against which the Dark Matter producing mediator recoils. The $h + E_T^{\text{miss}}$ signature is particularly interesting in this regard, as the ISR production of a Higgs boson is strongly Yukawa-suppressed. Thus $h + E_T^{\text{miss}}$ signatures

provide direct probes of potential new interactions involving Dark Matter [2]. The $h(b\bar{b})+E_T^{\text{miss}}$ signature is furthermore very sensitive, as the $h \to b\bar{b}$ decay is expected to be the most frequent decay of the Higgs boson [2]. However, direct comparisons of the $h(b\bar{b}) + E_T^{\text{miss}}$ signature to other signatures have been difficult, due to a lack of signal models predicting both $h(b\bar{b})+E_T^{\text{miss}}$ and other signatures such as jet $+ E_T^{\text{miss}}$ within one framework.

The Two-Higgs-Doublet Model with Pseudoscalar Mediator (2HDM+a) solves this problem. It predicts a large variety of Dark Matter signatures, with cross sections that can be probed at the LHC [1]. To make use of this feature and perform the comparison of these signatures, a concrete set of benchmark parameters in the 2HDM+a is required. The first aim of the work presented in this Thesis is to find a set of benchmark parameters that allows testing the edges of the the $h(b\bar{b}) + E_T^{\text{miss}}$ sensitivity. This is of particular interest because the $h(b\bar{b}) + E_T^{\text{miss}}$ signature is not considered in the paper [1] that first demonstrated the large variety of signatures predicted by the 2HDM+a. It also represents one of the first application of the generic limits with reduced model dependence for the $h(b\bar{b}) + E_T^{\text{miss}}$ signature provided in Ref. [2].

The second aim of the work in this Thesis is to use that benchmark to interpret a search for the $h(b\bar{b}) + E_T^{\text{miss}}$ signature in ATLAS data. The resulting limits, the first $h(b\bar{b}) + E_T^{\text{miss}}$ limits on the 2HDM+a, contribute to an eventual comparison of the full variety of Dark Matter signatures in the 2HDM+a, giving a more complete overview of the extent and complementarity of Dark Matter searches performed at the LHC.

This Thesis is organized as follows: Section 1.2 gives a short summary of the Standard Model of Particle Physics. This summary is focused on the SM Higgs sector to prepare the later discussion of the 2HDM+a, which couples Dark Matter and ordinary matter by extending the SM Higgs sector. The concept of Dark Matter is next introduced in Section 1.3, placing LHC-based Dark Matter searches like the one discussed in this Thesis in the wider contexts of Dark Matter searches in general and the Dark Matter hypothesis as such. The experimental machinery used to obtain the data used is briefly described in Chapter 2 on the ATLAS detector and the LHC. Chapter 3 then describes how these data are analyzed with respect to the extraneous production of events with E_T^{miss} and a jet pair that is consistent with a $h \to b\bar{b}$ decay, which may be indicative of the production of Dark Matter candidate particles. The 2HDM+a is reviewed in Chapter 4 with a focus on its predictions of $h(b\bar{b}) + E_T^{\text{miss}}$ signals at the LHC. On the basis of the features of the $h(b\bar{b}) + E_T^{\text{miss}}$ search and 2HDM+a model described in the preceding chapters, Chapter 5 details the strategy used to construct the $h(b\bar{b}) + E_T^{\text{miss}}$- tailored 2HDM+$a$ benchmark. Focusing on the two main steps of that strategy, Chapters 6 and 7 then detail the construction of the 2HDM+a benchmark. The application of this benchmark for interpreting the $h(b\bar{b}) + E_T^{\text{miss}}$ search and its results are presented in Chapter 8, where they are also compared to the expectation of Chapter 7. Finally Chapter 9 presents some conclusions drawn from the work presented in the Thesis, and discusses some potential lines of further investigation.

Authors Contributions

The Author's work presented in this Thesis was done in the context of wider research projects pursued in collaboration with various members of the ATLAS collaboration and the LHC Dark Matter Working Group. To avoid uncertainty over the extent of the Authors contributions, they are detailed in this section.

The $h(b\bar{b})+E_T^{\text{miss}}$ search discussed in Chapter 3, and the dataset used in it, are the result of years of work and studies of many members of the ATLAS collaboration, to which the Author did not contribute. The resulting analysis strategy, data, background estimates, analysis tools etc. were used by the Author to obtain the 2HDM+a interpretation of the $h(b\bar{b}) + E_T^{\text{miss}}$ search presented in Chapter 8. This interpretation used simulated samples of $h(b\bar{b}) + E_T^{\text{miss}}$ events predicted by variants of the 2HDM+a. These simulated samples were generated using ATLAS tools and infrastructure. The generation used inputs designed, implemented, and validated by the Author. The interpretation in Chapter 8 of the $h(b\bar{b}) + E_T^{\text{miss}}$ search using these signal samples was done by the Author, using and adapting ATLAS tools. The design of the 2HDM+a benchmark in Chapters 6 and 7 is the Authors work. The simulated samples used in these studies were generated by the Author, and analyzed using tools developed by the Author for this purpose, using publicly available tools (MadGraph 5 (c.f. Section 5.2) and PyROOT). The vacuum stability constraints shown in Figure 4.2 are the result of the Author work, motivated by discussions of the relevance of such constraints in the LHC Dark Matter Working Group.

1.2 Standard Model of Particle Physics

This section gives a short overview of the Standard Model of Particle Physics, adapted from the descriptions in Refs. [12, 13]. Given the subject of this thesis, the overview is focused on the SM Higgs sector, to prepare the discussion of the extended Higgs sector in Chapter 4.

Particle physics is concerned with the study of the fundamental particles and forces[1] of nature. The current understanding of those particles and forces is summarized in one theory, called the Standard Model of particle physics (SM). Section 1.2.1 summarizes the fundamental particles described by the SM. The SM describes the dynamics of these fundamental particles using Quantum Field Theory (QFT). Therefore the SM describes the kinematics and spins of spin 1/2 and spin 1 or spin 0 particles using the Dirac and Klein-Gordon equations, respectively, as described in Section 1.2.2. The SM describes the interactions of these particles as arising from a local gauge principle, as discussed in Section 1.2.3. The masses of the particles in the SM are interpreted as effective masses that arise from interactions of all[2] massive particles with a constant background field permeating space, as described in Section 1.2.4.

While the SM is a theory describing the fundamental particles and interactions of nature, it itself is not fundamental, but rather an ad-hoc construction built to match the set of all observations. This means that it features 26 free parameters[3] that need to be determined using data, instead of naturally emerging from the fundamental equations as a prediction of the theory. Hence the SM is not just a summary of theoretical insights that are good predictions of the measurements, but it is furthermore an explicit summary of the measurement results that are used to determine the values of its 26 free parameters.

1.2.1 Particle Content

The SM contains 15 different species of particles, shown in Figure 1.1. This includes 12 fermions with spin 1/2, 4 vector bosons with spin 1, and one scalar boson with spin 0, called the Higgs boson.

The 4 vector bosons are the massless uncharged photon γ, the massive electroweak vector bosons W^+, Z^0, of which the W^+ carries electric charge, and the massless and color-charged gluon g. The photon is the particle mediating the electromagnetic interaction as described by Quantum Electrodynamics (QED). The $W^+$and Z^0 mediate the weak interaction, and g is the mediator of the strong interaction, as described in Quantum Chromodynamics (QCD).

The 12 fermions consist of 3 generations of 4 fermions. The only difference between the fermion generations are the masses of the fermions. Each generation of fermions consists of two types of quarks, which are color charged and thus couple to gluons, and leptons, which do not.

One quark in a fermion generation has an electric charge of 2/3. These are called up-type quarks after the first generation quark with charge 2/3, the up quark u. The up-type quarks of the second and third generation are called the charm quark c and top quark t, respectively. The other quark in any generation, with charge $-1/3$, is correspondingly called a down-type quark after the down quark d in the first generation. The down-type quarks of the second and third generation are called the strange quark s and bottom quark b.

Of the two leptons in a fermion generation, one carries an electric charge, and the other is electrically neutral. The neutral leptons, called neutrinos, have masses that are orders of

[1] except gravity

[2] except for neutrinos masses, the origin of which is not known

[3] counting 3 neutrino mass parameters

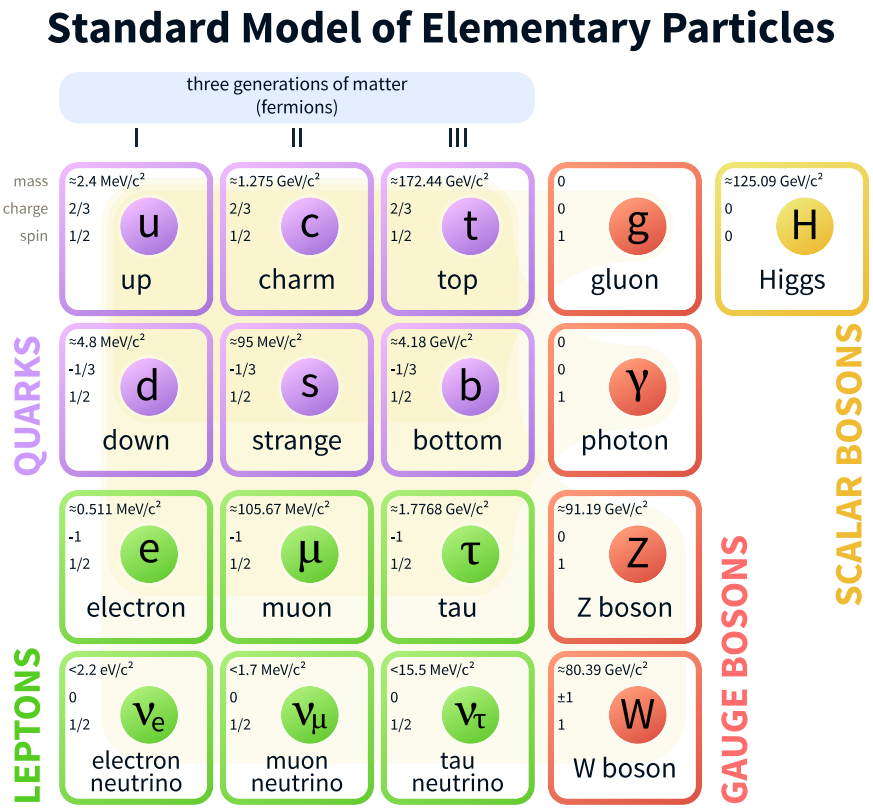

Figure 1.1: The particles of the Standard Model of elementary particles. Taken from Ref. [14]

magnitude smaller than the masses of the charged leptons. The charged leptons, in order of generation, are called electron e, muon μ, and τ-lepton τ. Neutrinos are either referred to by the charged lepton that they couple to in charged current interactions, as electron-, muon- or $\tau-$ neutrinos: ν_e, ν_μ, ν_τ. These charged current interaction neutrino eigenstates are very misaligned from the mass eigenstates of the neutrinos, which can e.g. be called ν_1, ν_2, ν_3.

All the electrically or color-charged particles in the SM have corresponding anti-particles, i.e. negative-energy solutions to the Klein-Gordon or Dirac Equation propagating backwards in time, interpreted as particles with opposite charges propagating forwards in time (Feynman-Stückelberg interpretation). The Z^0, y, g and h are not charged, thus they have no discernible anti particles. In other words, their negative energy solutions propagating backwards in time cannot be distinguished from the corresponding positive energy solution, propagating forwards in time.

1.2.2 Kinematics

The kinematics of the 12 spin-1/2 fermions in the SM are described by the Dirac equation, with a free-field Lagrangian density

$$\mathcal{L} = \bar{\psi}(i\partial\!\!\!/ - m)\psi\,, \tag{1.1}$$

where ψ is a fermion field operator, m is the mass of the fermion, and $\partial\!\!\!/ \equiv \gamma^\mu \partial_\mu . \gamma^\mu$ are the four elements of the Dirac Algebra, which can be defined by

$$\{\gamma^\nu, \gamma^\nu\} = \gamma^\nu\gamma^\mu + \gamma^\mu\gamma^\nu = 2\eta^{\mu\nu}\,, (\gamma^\mu)^\dagger = \eta^{\mu\nu}\gamma_\nu\,,$$

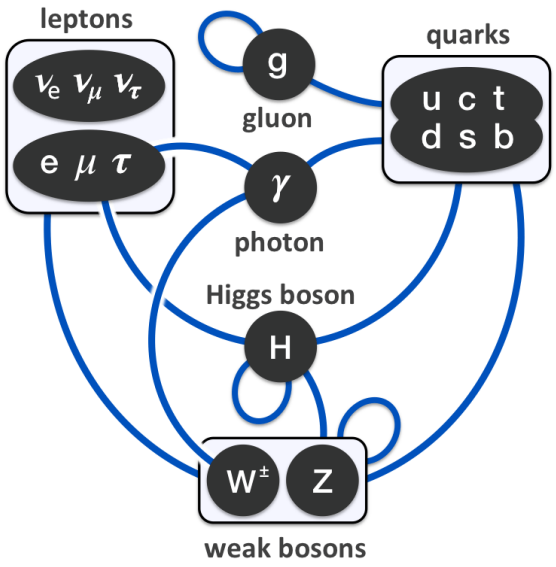

Figure 1.2: Interactions of the elementary particles in the Standard Model. Black ovals represent particles, blue lines connect particles that interact. Taken from Ref. [15]

where $\eta^{\mu\nu} = \text{diag}(1, -1, -1, -1)$ is the Minkowski metric and where $(\dots)^\dagger = ((\dots)^\star)^T$ denotes the hermitian conjugate. Equation (1.1) fixes the kinematics of the fermion to a momentum four vector with the energy $E = \pm\sqrt{\vec{p}^2 + m^2}$, and gives rise to an intrinsic angular momentum, i.e spin, of 1/2.

The kinematics of particles with spin 0 or 1 are expressed by the Klein-Gordon equation, with a Lagrangian density

$$\mathcal{L} = \frac{1}{2}\left[(\partial_\mu\phi)(\partial^\mu\phi) - m^2\phi^2\right] , \tag{1.2}$$

with a scalar (vector) field operator ϕ and m the mass of the scalar (vector) particle. While Equation (1.2) too specifies the energy-momentum relation of ϕ to $E^2 = m^2 + \vec{p}^2$, it does not require a specific representation of the Lorentz group. This is unlike Equation (1.1), which is solved only by Dirac spinors.

1.2.3 Local Gauge Symmetries

The SM Lagrangian is constructed as the sum of all Lorentz-invariant terms of mass dimension 4 or lower that are invariant under local field transformations in the gauge symmetry group $\text{SU}(3)_S \otimes \text{SU}(2)_L \otimes \text{U}(1)_Y$. The requirement of a mass dimension 4 or lower ensures that the theory is renormalizable, that is, the same set of operators with different prefactors is a valid description at any energy scale, ensuring the theory is self consistent up to arbitrarily large energies [16]. Requiring all terms to be Lorentz invariant ensures that the theory is consistent with special relativity. Specifically, it prescribes that kinetic terms of the field operators take forms corresponding to either the general Klein-Gordon equation, or the Dirac equation in the case of spinor fields. Thereby it guarantees that the four momenta of the particles obey the relation $E^2 = \vec{p}^2 + m^2$.

The structure of the interactions between the SM particles is given by the local gauge symmetry group $\text{SU}(3)_S \otimes \text{SU}(2)_L \otimes \text{U}(1)_Y$. Which particles couple to which other particles, and how, is given by the representation of the corresponding field operators with respect to

the gauge group $\mathrm{SU}(3)_S \otimes \mathrm{SU}(2)_L \otimes \mathrm{U}(1)_Y$. A qualitative overview of this interaction structure is given in Figure 1.2.

1.2.3.1 Quantum Chromodynamics

The strong interaction is described by QCD, which is included in the SM gauge group $\mathrm{SU}(3)_S \otimes \mathrm{SU}(2)_L \otimes \mathrm{U}(1)_Y$ via the $\mathrm{SU}(3)_S$ subgroup of rotations in three complex dimensions. All quarks transform like elements of a triplet under $\mathrm{SU}(3)_S$ transformations:

$$q(x) \to e^{ig_S \alpha^a(x) T^a} q(x)\,,$$

where T^a are the eight 3×3 dimensional generators of $\mathrm{SU}(3)_S$. Under such a transformation, Equation (1.1) is not invariant. Introducing gluons, which couple to quarks in a modified kinetic term

$$\mathcal{L}_{QCD} \supset \bar{q}(i\not{\partial} + ig_S \not{G}^a_\mu T^a - m)q \equiv \bar{q}(i\not{D}_S - m)q\,, \tag{1.3}$$

and transform as part of an octet under $\mathrm{SU}(3)_S$

$$G^c_\mu(x) \to G^c_\mu(x) - \partial_\mu \alpha^c(x) - g_S f_{abc} \alpha^a(x) G^b_\mu(x)\,,$$

with f_{abc} the $\mathrm{SU}(3)_S$ structure constants, defined by $[T^a, T^b] = i f_{abc} T^c$. By defining the covariant derivative D_S of $\mathrm{SU}(3)_S$ in Equation (1.3), the form of Equation (1.1) is recovered, reflecting the fact that in an interacting theory, fermion four momenta may be modified in interactions with the mediator. Defining the gluon field strength tensor [17]

$$\mathcal{G}^a_{\mu\nu} \equiv \partial_\mu G^a_\nu - \partial_\nu G^a_\mu - g_S f_{abc} G^b_\mu G^c_\nu\,, \tag{1.4}$$

one can then write the full QCD Lagrangian density by adding the kinetic and self-interaction terms of the gluons to Equation (1.3) and summing over all the quark flavors [17]:

$$\mathcal{L}_{QCD} = \sum_q \bar{q}(\not{D}_S)q - \frac{1}{2}\mathrm{tr}(\mathcal{G}_{\mu\nu}\mathcal{G}^{\mu\nu})\,, \tag{1.5}$$

where the trace gives rise to the $m = 0$ Klein-Gordon term of the gluons and gluon self-interaction terms.

By Noether's theorem, the $\mathrm{SU}(3)_S$ symmetry exhibited by Equation (1.5) yields an associated conserved charge, called color charge. Since quarks and gluons are triplets and octets under $\mathrm{SU}(3)_S$, they carry color charge. All other SM particles transform as singlets under $\mathrm{SU}(3)_S$, i.e. they are unchanged. Thus the other SM particles are color-neutral.

No free particles carrying color charge have been observed [17], but only color neutral systems of bound quarks, i.e. hadrons. This non-existence of free colored states is called color confinement. It is hypothesized to be due to the gluon self-interaction giving rise to an attractive force of qluon field lines between two quarks. Thus the field lines would not spread out as a function of the distance of the quarks, as they would for an electromagnetic field. Hence the energy stored in the field between two separated color charges increases with the distance, until it is large enough to pair-produce new quarks, shielding the quark fields in bound states.

1.2.3.2 The Electroweak Interaction

The electroweak local gauge symmetry group $\mathrm{SU}(2)_L \otimes \mathrm{U}(1)_Y$ is the non-QCD part of the SM gauge group $\mathrm{SU}(3)_S \otimes \mathrm{SU}(2)_L \otimes \mathrm{U}(1)_Y$. $\mathrm{SU}(2)_L$ corresponds to rotations in two complex dimensions. $\mathrm{U}(1)_Y$ corresponds to a free complex phase.

The left-handed components of all SM fermion fields transform as doublets under $\mathrm{SU}(2)_L$:

$$L_\ell = (\nu_{\ell,L}, \ell_L^-)^T, \quad \ell \in \{e, \mu, \tau\}\,, \tag{1.6}$$

$$Q = (\mathcal{U}_L, \mathcal{D}'_L)^T, \tag{1.7}$$

$$(\mathcal{U}, \mathcal{D}') \in \left\{ \left(u, d' = \sum_{\mathcal{D}\in\{d,s,b\}} V_{u\mathcal{D}}\mathcal{D} \right), \left(c, s' = \sum_{\mathcal{D}\in\{d,s,b\}} V_{c\mathcal{D}}\mathcal{D} \right), \left(t, b' = \sum_{\mathcal{D}\in\{d,s,b\}} V_{t\mathcal{D}}\mathcal{D} \right) \right\},$$

where V_{ij} are the elements of the Cabibbo-Kobayashi-Maskawa (CKM) quark mixing matrix, nontrivial as a result of the misalignment of the quark mass eigenstates with the states forming the $\mathrm{SU}(2)_L$ doublets. The right-handed components are $\mathrm{SU}(2)_L$ singlets. Here "handedness" refers to the chiral projections $\psi_{L,R} = P_{L,R}\psi$ with $P_{L,R} \equiv \frac{1}{2}(1 \mp \gamma^5), \gamma^5 \equiv i\gamma^0\gamma^1\gamma^2\gamma^3$. Since the chirally projected fermion fields change when applying the parity operator $P = \gamma^0$, the interaction described by the $\mathrm{SU}(2)_L$ symmetry group does not conserve parity. Furthermore, the combination of charge and parity CP is not conserved either, due to a complex phase in the CKM matrix.

Similarly to the $\mathrm{SU}(3)_S$ gluon octet of QCD, to allow local gauge transformations of the fermion doublets as

$$L_\ell(x) \to e^{ig_W \alpha^a(x) t^a} L_\ell(x)\,,$$
$$Q(x) \to e^{ig_W \alpha^a(x) t^a} Q(x)\,,$$

with t^a as the three generators t^1, t^2, t^3 of $\mathrm{SU}(2)_L$, the coordinate derivative is replaced by a covariant derivative

$$D_{\mu,L} = \partial_\mu - it^a W^a_\mu(x)\,,$$

in the Dirac Equation (1.1), thus introducing a $\mathrm{SU}(2)_L$ triplet of gauge bosons $(W^1, W^2, W^3)^T$. The transformation of the W^a under $\mathrm{SU}(2)_L$ is exactly analogous to that of the gluons under $\mathrm{SU}(3)_S$ in Equation (1.4), with 3 W^a fields instead of 8 gluon fields G^a and the generators and structure constants of $\mathrm{SU}(2)_L$ instead of the $\mathrm{SU}(3)_S$ ones. Like color in QCD, the $\mathrm{SU}(2)_L$ symmetry gives rise to a conserved charge by Noether's theorem, which is called weak isospin. The name is due to the fact that the inherent symmetry of a spin-1/2 system can also be described as an SU(2) symmetry. Unlike in the case of color, particles carrying different isospin can occur in isolation, e.g. as isolated electrons or neutrinos. Consequently specific weak isospin projections are assigned to the components of the $\mathrm{SU}(2)_L$ lefthanded fermion doublets in Equations (1.6) and (1.7). The t_3 eigenvalue I_3 for charged lefthanded leptons and lefthanded up-type quarks is $+\frac{1}{2}$. For lefthanded neutrinos and lefthanded down-type quarks I_3 is $-\frac{1}{2}$. All righthanded fermions are $\mathrm{SU}(2)_L$ singlets, and thus have $I_3 = 0 = I$.

Both left- and right-handed fermions have a nontrivial transformation under the remaining $\mathrm{U}(1)_Y$ symmetry group. Its only generator is the identity map, thus the gauge transformation for fermions is to apply a complex phase factor

$$\psi(x) \to e^{iY g_Y \alpha(x)} \psi(x)\,,$$

where the weak hypercharge Y is the conserved charge associated to the $\mathrm{U}(1)_Y$ symmetry. Because there is only one generator, all transformations commute and there are no structure constants. Consequently the $\mathrm{U}(1)_Y$ gauge boson B transforms as

$$B_\mu(x) \to B_\mu(x) - \partial_\mu \alpha(x)\,,$$

which restores gauge invariance in the dirac term after replacing the coordinate- with the covariant derivative

$$D_{\mu,Y} = \partial_\mu - iY g_Y B_\mu\,.$$

Left-handed leptons have weak hypercharge $Y = -1$, right-handed leptons have weak hypercharge $Y = -2$, left-handed quarks have $Y = \frac{1}{3}$, right-handed up type quarks have $Y = \frac{4}{3}$, and right-handed down type quarks have $Y = -\frac{2}{3}$. In extensions of the SM that include neutrino masses by the presence of right-handed neutrinos, there are right-handed neutrinos. These right handed neutrinos would then have $Y = 0$, i.e. they would be sterile.

Collecting the above constructions, and defining field strength tensors $\mathcal{B}, \mathcal{W}$ for the B, W fields in the way of Equation (1.4), the SM Lagrangian thus far reads:

$$\begin{aligned}\mathcal{L}_{\text{massless}} = &-\frac{1}{2}\mathrm{tr}(\mathcal{G}_{\mu\nu}\mathcal{G}^{\mu\nu}) - \frac{1}{2}\mathrm{tr}(\mathcal{W}_{\mu\nu}\mathcal{W}^{\mu\nu}) - \frac{1}{4}\mathcal{B}_{\mu\nu}\mathcal{B}^{\mu\nu} \\ &+ \sum_Q \bar{Q} i \not{D}_Q Q + \sum_{\mathcal{U}_R} \bar{\mathcal{U}}_R i \not{D}_{\mathcal{U}_R} \mathcal{U}_R + \sum_{\mathcal{D}_R} \bar{\mathcal{D}}_R i \not{D}_{\mathcal{D}_R} \mathcal{D}_R \\ &+ \sum_\ell \bar{L}_\ell i \not{D}_\ell L_\ell\end{aligned} \tag{1.8}$$

with the covariant derivative for the three left handed quark doublets Q

$$D_Q \equiv \partial - i\frac{1}{3} g_Y B - i g_S T^b G^b - i g_W t^a W^a\,,$$

and the covariant derivative for the three left handed lepton doublets L_ℓ

$$D_{L_\ell} \equiv \partial + i g_Y B - i g_W t^a W^a\,,$$

and the covariant derivative for the three right handed down-type quark singlets $\mathcal{D}_R$

$$D_{\mathcal{D}_R} \equiv \partial + i\frac{2}{3} g_Y B - i g_S T^a G^a\,,$$

and the covariant derivative for the three right handed up-type quark singlets $\mathcal{U}_R$

$$D_{\mathcal{U}_R} \equiv \partial - i\frac{4}{3} g_Y B - i g_S T^a G^a\,,$$

and the covariant derivative for the three right handed charged lepton singlets ℓ_R

$$D_{\ell_R} \equiv \partial + i 2 g_Y B\,.$$

1.2.4 Higgs Mechanism

The part of the SM Lagrangian written out in Equation (1.8) contains descriptions of all the SM fermions and vector bosons. For the Lagrangian density written in Equation (1.8), all

particles are massless. Mass terms of the forms given in Equations (1.1) and (1.2) would break the $\mathrm{SU}(2)_L \otimes \mathrm{U}(1)_Y$ gauge symmetry of the SM. Adding a Klein-Gordon mass term as in Equation (1.2) for e.g. the B boson breaks the underlying $\mathrm{U}(1)_Y$ symmetry: $\frac{m_B^2}{2} B^\mu B_\mu \rightarrow \frac{m_B^2}{2}(B^\mu - \partial^\mu\alpha)(B_\mu - \partial_\mu\alpha) \neq \frac{m_B^2}{2} B^\mu B_\mu$. Similarly, since the left-handed fermion fields are $\mathrm{SU}(2)_L \otimes \mathrm{U}(1)_Y$ doublets, but the right-handed fermion fields are $\mathrm{SU}(2)_L \otimes \mathrm{U}(1)_Y$ singlets, a mass term like $m\bar{\psi}_L\psi_R$ breaks $\mathrm{SU}(2)_L$.

To keep the local gauge symmetry principle intact, the SM interprets the observed masses of the charged fermions and weak gauge bosons as effective masses. These effective masses originate from couplings to a scalar field, which is present everywhere in space in its vacuum state. This mass generation mechanism is called the Higgs mechanism. Section 1.2.4.1 describes the construction of this scalar field. Section 1.2.4.2 discusses how the couplings to the scalar vacuum give rise to effective mass terms.

1.2.4.1 Scalar Sector Lagrangian

Calling the scalar field ϕ and ignoring all couplings to other fields, its associated Lagrangian density is

$$\begin{aligned} \mathcal{L}''_\phi &= \frac{1}{2}(\partial_\nu\phi)(\partial^\nu\phi) - V(\phi) \\ &= \frac{1}{2}\left[(\partial_\nu\phi)(\partial^\nu\phi) - \mu^2\phi^2 - \frac{\lambda}{2}\phi^4\right], \end{aligned} \tag{1.9}$$

where $V(\phi)$ is called the scalar potential. In order to balance the left-handed fermion doublet appearing in fermion mass terms, the scalar field needs to transform as a $\mathrm{SU}(2)_L$ doublet. This also generates mass terms for the W^a bosons. Furthermore, mass terms for the B boson are needed to obtain the correct chiral coupling structure for the Z^0 boson. Thus the scalar field is a complex doublet under $\mathrm{SU}(2)_L$, and has a weak hypercharge, $Y = -1$. Introducing the coupling to the $\mathrm{SU}(2)_L \otimes \mathrm{U}(1)_Y$ gauge bosons, Equation (1.9) becomes

$$\mathcal{L}'_\phi = (D_{\phi,\nu}\phi)^\dagger(D^\nu_\phi\phi) - \mu^2\phi^\dagger\phi - \lambda(\phi^\dagger\phi)^2\,, \tag{1.10}$$

with the covariant derivative

$$D_\phi \equiv \partial + ig_Y B - ig_W t^a W^a\,.$$

The scalar field of Equation (1.10) has the right quantum numbers and couplings to bosons, but no couplings to fermions. These are included as Yukawa couplings [17]:

$$\begin{aligned} \mathcal{L}_\phi = \mathcal{L}'_\phi &+ \sum_\ell y_\ell \left(\bar{L}_\ell\phi\ell_R + \bar{\ell}_R\phi^\dagger L_\ell\right) \\ &+ \sum_Q \left[\sum_\mathcal{U}\left(\bar{Q}\phi_c Y_{Q\mathcal{U}}\mathcal{U}_R + \bar{\mathcal{U}}_R Y^\dagger_{Q\mathcal{U}}\phi^\dagger_c Q\right) + \sum_\mathcal{D}\left(\bar{Q}\phi Y_{Q\mathcal{D}}\mathcal{D}_R + \bar{\mathcal{D}}_R Y^\dagger_{Q\mathcal{D}}\phi^\dagger Q\right)\right], \end{aligned} \tag{1.11}$$

with y_ℓ the strength of the Yukawa coupling to lepton $\ell = e, \mu, \tau$, and $Y_{Q\mathcal{D}}$ and $Y_{Q\mathcal{U}}$ two 3×3 matrices inscribing the Yukawa coupling strengths to down-type quarks $\mathcal{D} = d, s, b$ and up-type quarks $\mathcal{U} = u, c, t$, and Q the doublets of left-handed quarks from Equation (1.7). The conjugate Higgs doublet $\phi_c \equiv \epsilon_2\phi^\star$ in Equation (1.11) transforms just like ϕ under $\mathrm{SU}(2)_L \otimes \mathrm{U}(1)_Y$, with ϵ_2 the fully anti symmetric tensor in 2 dimensions. The quark Yukawa couplings $Y_{Q\mathcal{U}}$ and $Y_{Q\mathcal{D}}$ define the CKM matrix V_{CKM}: $V_{\mathrm{CKM}} \equiv V^L_\mathcal{U}(V^L_\mathcal{D})^\dagger$, with $V^L_{\mathcal{U},\mathcal{D}}$ the matrices that diagonalize the quark Yukawa couplings by $V^L_{\mathcal{U},\mathcal{D}} Y_{Q\mathcal{U},Q\mathcal{D}} V^R_{\mathcal{U},\mathcal{D}}$ [17].

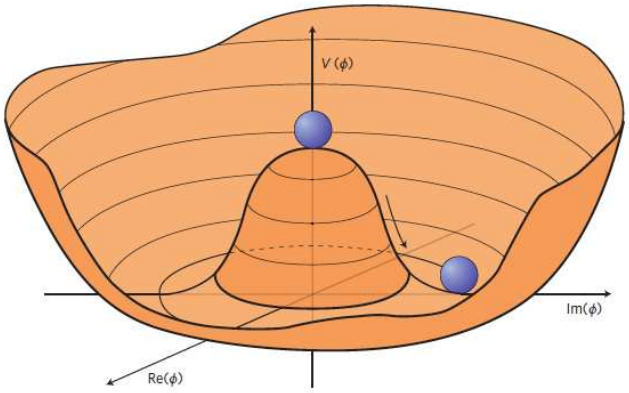

Figure 1.3: Illustration of the shape the SM Higgs potential using the potential $V = \mu^2\phi^\star\phi + \lambda(\phi^\star\phi)^2$ of a complex scalar ϕ for the case $\lambda > 0, \mu^2 < 0$. The SM Higgs potential has a similar dependence, but since it is a complex doublet, the SM potential is a function of four real parameters, not two. Taken from Ref. [18].

1.2.4.2 Spontaneous Electroweak Symmetry Breaking

The potential of the Higgs doublet ϕ in Equation (1.10), with $\mu^2 < 0, \lambda > 0$, is minimal on a sphere in ϕ-space satisfying

$$\phi^\dagger\phi = -\frac{\mu^2}{2\lambda} \equiv \frac{v^2}{2}\,, \tag{1.12}$$

where the last step defines the (norm of the) vacuum expectation value v. If the Higgs field is not excited by interactions with other fields, it will be in a vacuum state of minimal potential, i.e. a state fulfilling Equation (1.12). While the set of all these possible vacuum states retains the full $\mathrm{SU}(2)_L \otimes \mathrm{U}(1)_Y$ symmetry, any concrete vacuum state breaks the symmetry, as illustrated in Figure 1.3. In this way, the non-zero vacuum expectation value of the Higgs doublet is said to "spontaneously break" the $\mathrm{SU}(2)_L \otimes \mathrm{U}(1)_Y$ symmetry. Despite this nomenclature, the full symmetry is still present, if one takes into account the now non-trivial gauge transformations of the Higgs vacuum.

Specifying the vacuum expectation value of ϕ such that only the neutral real component is non- vanishing

$$\langle 0|\,\phi\,|0\rangle = \frac{1}{\sqrt{2}}\begin{pmatrix}0\\ v\end{pmatrix}\,,$$

ensures that the photon is massless in the broken phase. Writing ϕ as relative to the vacuum expectation value one obtains

$$\phi(x) = \frac{1}{\sqrt{2}}\begin{pmatrix}\phi_1(x) + i\phi_2(x)\\ v + H(x) + i\phi_4(x)\end{pmatrix}\,,$$

which can be simplified by picking a gauge in $\mathrm{SU}(2)_L \otimes \mathrm{U}(1)_Y$ such that only the real neutral component is non- vanishing

$$\phi(x) = \frac{1}{\sqrt{2}}\begin{pmatrix}0\\ v + H(x)\end{pmatrix}\,,$$

which is called the unitary gauge. The degrees of freedom $\phi_{1,2,4}$ reappear via gauge terms of the $\mathrm{SU}(2)_L \otimes \mathrm{U}(1)_Y$ gauge bosons W^a, B. They can be absorbed as longitudinal degrees of

freedom into the vector bosons. In the unitary gauge, the kinetic term from Equation (1.10) can be written as

$$\begin{aligned}(D_{\phi,\nu}\phi)^\dagger(D^\nu_\phi\phi) =& \frac{1}{2}(\partial_\mu H)(\partial_\mu H) + \frac{g_W^2}{8}(v+H)^2(W^1+iW^2)_\mu(W^1-iW^2)^\mu \\ &+ \frac{1}{8}(v+H)^2(g_W W^3 - g_Y B)_\mu(g_W W^3 - g_Y B)^\mu\,,\end{aligned} \tag{1.13}$$

where by defining $W^\pm \equiv \frac{W^1 \mp iW^2}{\sqrt{2}}$ and considering the term

$$(D_{\phi,\nu}\phi)^\dagger(D^\nu_\phi\phi) \supset \frac{1}{2}\left(\frac{g_w v}{2}\right)^2 W^-_\mu W^{+\mu}\,,$$

one can identify the mass

$$M_W = \frac{g_W v}{2}\,.$$

Writing the term with W^3, B in Equation (1.13) as a matrix multiplication

$$(D_{\phi,\nu}\phi)^\dagger(D^\nu_\phi\phi) \supset \frac{v^2}{8}\begin{pmatrix}W^3 & B\end{pmatrix}\begin{pmatrix}g_W^2 & -g_W g_Y \\ -g_W g_Y & g_Y^2\end{pmatrix}\begin{pmatrix}W^3 \\ B\end{pmatrix}\,,$$

and rotating $(W^3, B)^T$ into the eigenbasis $(A_\gamma, Z)^T$, thus diagonalising the matrix

$$(D_{\phi,\nu}\phi)^\dagger(D^\nu_\phi\phi) \supset \frac{1}{2}\begin{pmatrix}A_\gamma & Z\end{pmatrix}\begin{pmatrix}0 & 0 \\ 0 & (\frac{v}{2})^2(g_Y^2+g_W^2)\end{pmatrix}\begin{pmatrix}A_\gamma \\ Z\end{pmatrix}\,,$$

one can identify the masses

$$\begin{aligned}M_\gamma &= 0\,, \\ M_Z &= \frac{v\sqrt{g_W^2+g_Y^2}}{2}\,,\end{aligned} \tag{1.14}$$

where A_γ is the photon field. Thus the photon is the gauge boson of the remaining $\mathrm{U}(1)_{\mathrm{e.m.}}$ unbroken gauge symmetry of complex rotations around the axis defined by the direction of $\langle\phi\rangle$. The angle of the rotation into the mass eigenstates A_γ, Z is the Weinberg angle

$$\theta_W = \arctan\left(\frac{g_Y}{g_W}\right)\,,$$

which happens to be related to the ratio of the masses of the weak gauge bosons by

$$\cos\theta_W = \frac{M_W}{M_Z}\,.$$

The remaining neutral scalar degrees of freedom H is called the Higgs boson. Its couplings to the massive vector bosons $W^\pm, Z$ can also be read off from Equation (1.13). Thus e.g. the triple couplings are given by:

$$\begin{aligned}(D_{\phi,\nu}\phi)^\dagger(D^\nu_\phi\phi) &\supset \frac{g_W^2 v}{2}W^+_\mu W^{-\mu}hH + \frac{g_W^2 v}{2}Z_\mu Z^\mu H \\ &= \frac{2M_W^2}{v}W^+_\mu W^{-\mu}H + \frac{M_Z^2}{v}Z_\mu Z^\mu H\,.\end{aligned}$$

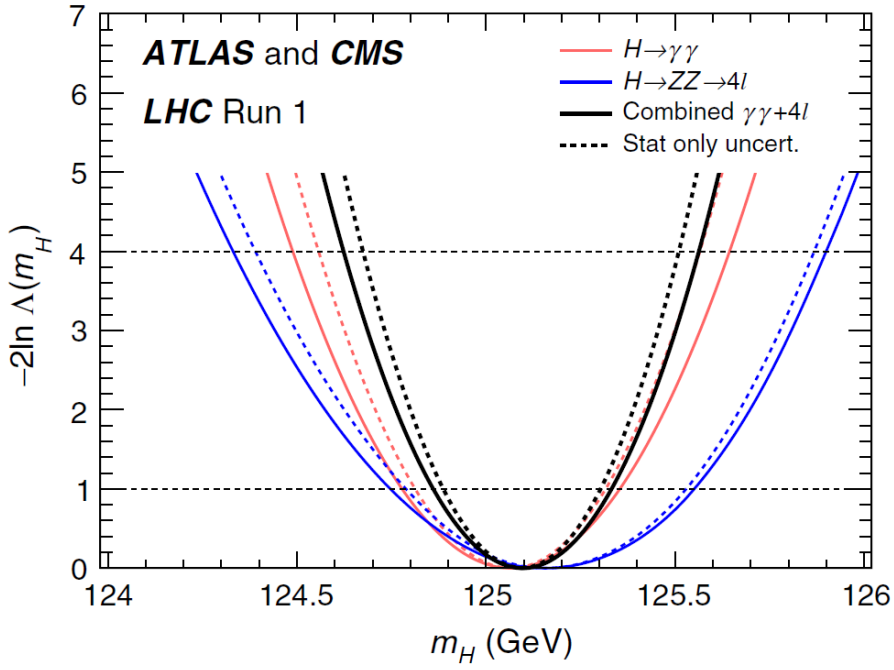

Figure 1.4: Scans of twice the logarithmic likelihood ratio $-2\ln\Lambda(M_H)$ as functions of the Higgs Boson mass M_H for the ATLAS and CMS combination of the $H \to \gamma\gamma$ (red), $H \to ZZto4\ell$ (blue), and combined (black) channels. The dashed curves show the results accounting for statistical uncertainties only, with all nuisance parameters associated with systematic uncertainties fixed to their best-fit values. The 1 and 2 standard deviation limits are indicated by the intersections of the horizontal lines at 1 and 4, respectively, with the log-likelihood scan curves. Figure and caption taken from Ref. [19].

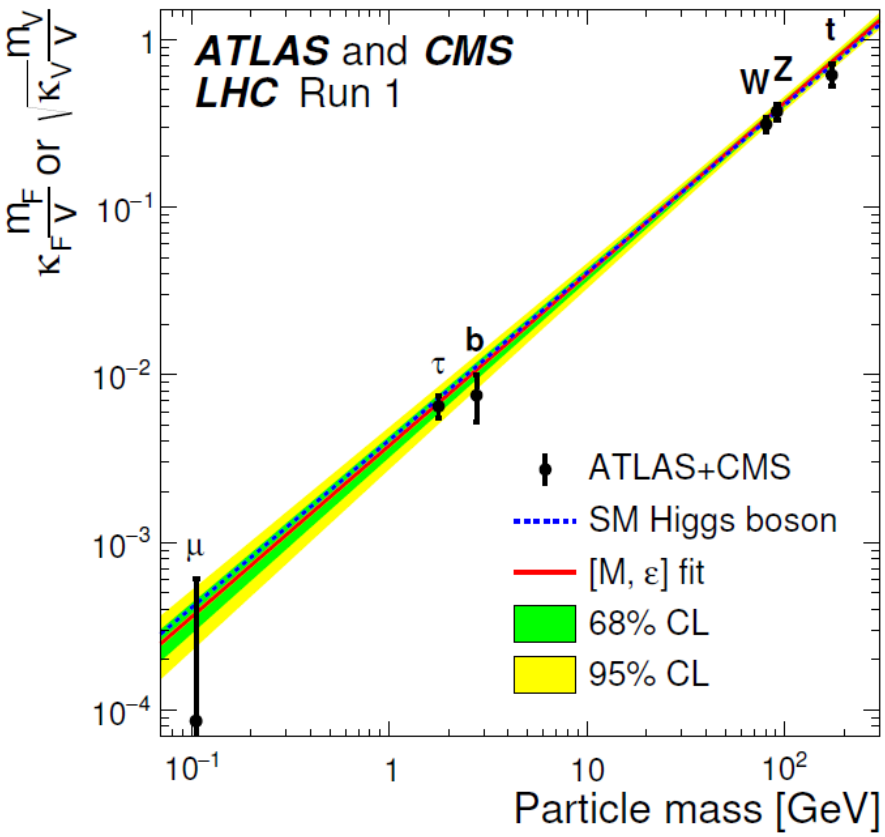

Figure 1.5: The ATLAS and CMS combined best fit results of coupling parameters κ_i, which express the ratio of observed Higgs couplings to particle species i. The κ_i are constructed relative to the SM prediction, i.e. the SM predicts $\kappa_i = 1$. For fermions, the κ_i are then scaled to $\kappa_f \frac{m_f}{v}$, for the vector bosons $W^\pm, Z$, they are scaled $\sqrt{\kappa_V}\frac{m_V}{v}$, where $v = 246\,\text{GeV}$ is Higgs vacuum expectation value from Equation (1.12) and m_i is the mass of i. Taken from Ref. [21].

The potential term in Equation (1.10), in the unitary gauge, has a term $V \supset v^2\lambda H^2$ and thus the Higgs boson H has a mass

$$M_H = \sqrt{2\lambda}v\,.$$

While v can be determined precisely from measurements of the Fermi coupling constant $G_F = \frac{v^2}{\sqrt{2}} = 1.1663788(7) \times 10^{-5}\,\text{GeV}^{-2}$, e.g. from measurements of the muon lifetime [20, 17], λ is a free parameter of the theory that affects only M_H. Thus M_H is not predicted and must be measured. The most precise determination of M_H to date is the combination of the ATLAS and CMS measurements of M_H in the $H \to \gamma\gamma$ and $H \to ZZ^* \to 4\ell$ with $\ell = e, \mu$ channels in Ref. [19], shown in Figure 1.4. The maximum-likelihood estimate of the Higgs mass is $125.09 \pm 0.24\,\text{GeV}$ [19].

Finally, the Yukawa couplings in Equation (1.11) give rise to effective fermion masses. For the example of the electron, one gets

$$\mathcal{L}_\phi \supset -\frac{vy_e}{\sqrt{2}}(\bar{e}_L e_R + \bar{e}_R e_L)\,,$$

and thus the fermion masses are

$$M_f = \frac{y_f v}{\sqrt{2}}\,,$$

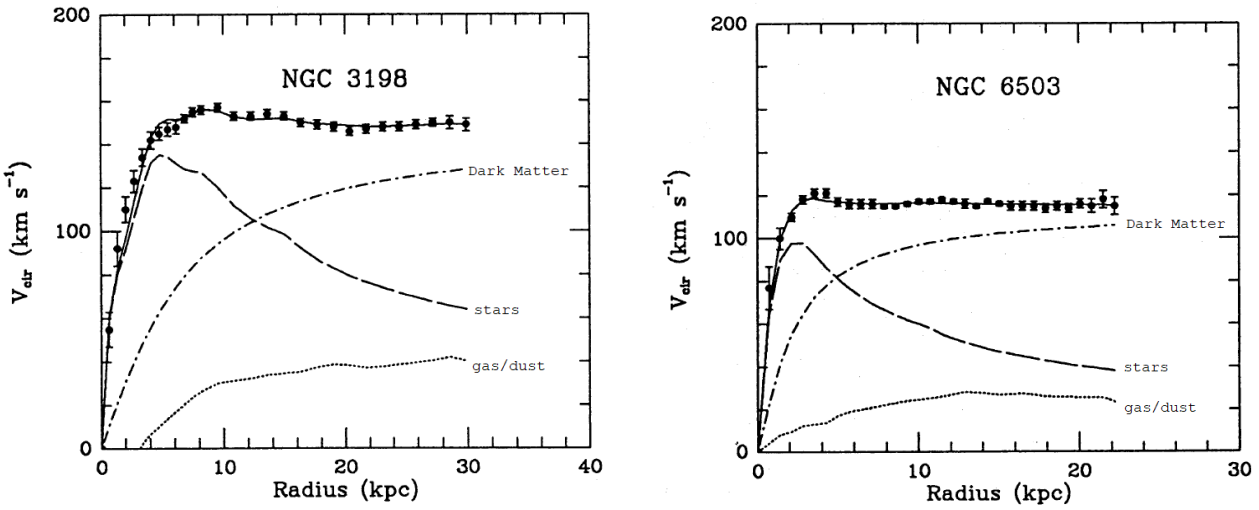

(a) (b)

Figure 1.6: Observed galactic rotation curves of two spiral galaxies, NGC3918 in (a) and NGC6503 in (b), the expectations based on only the visible stars and interstellar medium, and the best fit Dark Matter halo. Taken from Ref. [22]

and a similar way the fermion couplings to the Higgs boson are read off

$$\begin{aligned}\mathcal{L}_\phi \supset & -\frac{y_e}{\sqrt{2}}(\bar{e}_L e_R + \bar{e}_R e_L)H \\ & = -\frac{M_e}{v}(\bar{e}_L e_R + \bar{e}_R e_L)H\,.\end{aligned}$$

Thus the tree-level couplings of the Higgs boson to both fermions and vector bosons are proportional to the mass of the fermion or boson under consideration. This is illustrated in Figure 1.5. Note that while the fit results shown in Figure 1.5 indirectly confirm this linearity, as they are in agreement with the SM, they do not represent a direct probe of the mass-coupling linearity.

1.3 Dark Matter

A large body of astrophysical and cosmological evidence [3, 8, 5] indicates the existence of significantly more matter than what is bound in luminous stars or radiating gas clouds. This additional non-luminous matter is called "Dark Matter". This section discusses some of the evidence for Dark Matter in Section 1.3.1 and goes on to examine a selection of hypothetical descriptions of the nature of Dark Matter in Section 1.3.2. The focus of this Thesis is the class Dark Matter particles that interact with SM particles in some non- gravitational way, but are not part of the SM. Hence, several experimental strategies for searching for interacting Dark Matter particles are discussed in Section 1.3.3.

1.3.1 Astrophysical Evidence

The evidence for Dark Matter comes from astrophysics and cosmology [3, 8, 5, 23]. The physical systems that provide evidence for Dark Matter range in size from hundreds of light years, a typical radial size of a galaxy [23], to 40 Ly, the scale of the observable universe at the time of recombination [3, 23]. The observable phenomena occurring in these systems influenced

by Dark Matter are diverse, and this diversity of phenomena is reflected in the varied areas of physics involved; the thermodynamics of the hot gas bound in galaxy clusters [24], the classical Newtonian mechanics of the orbits of stars bound in galaxies, the fluid dynamics and atomic physics of the primordial plasma [25], the strong lensing of photons by heavy galaxy clusters [23], and many more. However diverse though, all existing evidence for Dark Matter relies ultimately only on its defining feature: that it has mass, and thus couples gravitationally [23]. This is illustrated by the following three examples of evidence for Dark Matter, adapted from Refs. [3, 4]:

Galactic Rotation Curves

The dependence of the average circular velocity of the matter in a spiral galaxy on the radial distance from the galactic center is called a galactic rotation curve. Two examples of galactic rotation curves are shown in Figure 1.6. The circular velocity $v(r)$can be calculated from Newtonian dynamics,

$$v(r) = \sqrt{\frac{G_N M(r)}{r}}\,,$$

where G_N is the Gravitational constant, r is the radial distance from the center of mass of the galaxy, and $M(r) \equiv 4\pi \int \rho(r) r^2\,\mathrm{d}r$, with $\rho(r)$ the mass density profile. Based on just the visible matter, the expectation is that most of the mass of a galaxy resides in the luminous stars, the majority of which are located in the central spherical bulk. Thus, beyond a few kpc from the center, the expected rotation curve falls steeply $v \propto \frac{1}{\sqrt{r}}$. However, the observed rotation curves are flat to very large radii. The observed flatness of the rotation curves can be explained by invisible halos of dark matter, with a mass density profile $\rho \propto \frac{1}{r^2}$.

X-ray Emissions and Gravitational Lensing by Galaxy Clusters

Galaxy clusters can trap gas in their deep gravitational potential wells. In the simplified case of a spherically symmetric system, and an ideal gas, requiring that the gas cloud is in hydrostatic equilibrium, i.e. that the gas pressure is balanced by the gravitational of the gas towards the cluster, yields a gas temperature

$$T \approx (1.3 - 1.8)\,\mathrm{keV} \left(\frac{M(r)}{10^{14} M_{\mathrm{sun}}}\right) \left(\frac{1\,\mathrm{Mpc}}{r}\right)\,, \tag{1.15}$$

with M_{sun} the mass of the sun, and $M(r)$ the total mass within a radial distance r from the center of the cluster. As the thermal radiation emitted by the gas cloud is in equilibrium with the gas, the gas cloud can be traced and its size and mass measured with X-ray astronomy. The mass estimate thus obtained can be compared to the mass estimated based on the amount of intergalactic gas and bright galaxies observed directly. While the visible mass is dominated by the mass of the hot gas, the mass according to Equation (1.15) is typically many times larger. This indicates the presence of significant amounts of Dark Matter gravitationally confining the gas in the cloud.

According to Einsteins theory of general relativity, the space-time curvature of large amounts of mass- energy, by curving the geodesics of passing photons, can bend photon trajectories [23]. The phenomenon is called lensing, since the effect on the photons appears similar to the effect of a glass lens. The strength of the gravitational lensing is thus a measure of the total curvature, i.e. mass, near the line of sight [23]. Hence, if there is a sufficiently bright and

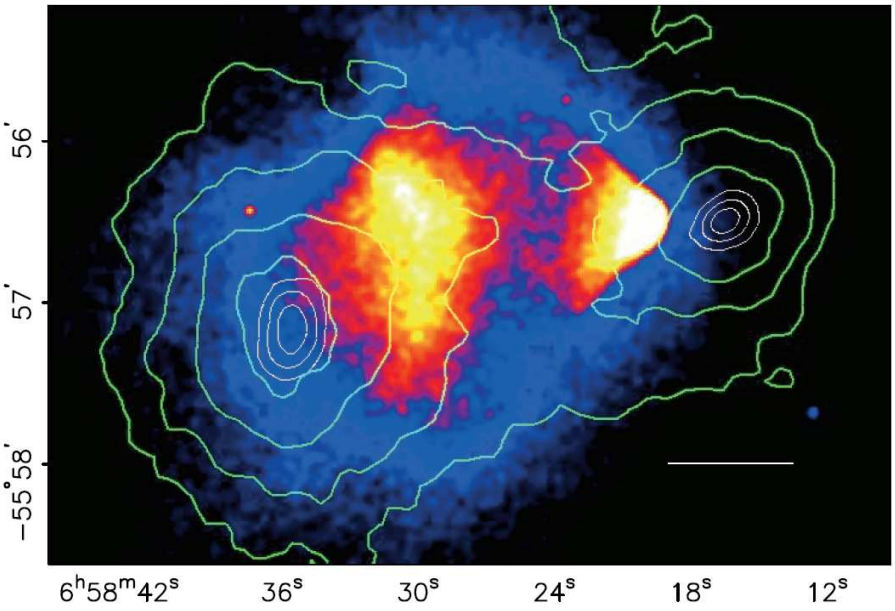

Figure 1.7: The bullet cluster 1E 0657-558. The white bar indicates 200 kpc at the redshift of the cluster. The green lines are contours of constant convergence. The convergence is the shape-independent increase in the apparent size of a galaxy due to gravitational lensing, which is proportional to the mass density. The white contours delimit the regions covering the locations of the mass peaks at 68.3%, 95.5%, and 99.7% confidence level. The underlying heatmap shows the observed X-ray image of the cluster. Taken from Ref. [8].

sufficiently far away light source located behind the cluster along the line of sight from earth, i.e. an ancient galaxy, gravitational lensing can provide and independent estimate of the mass of the galaxy cluster. In aggregate, the lensing results are in agreement with the observed gas temperatures [3].

Finally, systems of colliding galaxy clusters provide examples of Dark Matter spatially separated from the hot gas that constitutes most of the baryonic matter in a cluster [4]. The so-called "Bullet Cluster" 1E 0657-558 is a striking example [8, 26]. It is illustrated in Figure 1.7. The Bullet Cluster is a system of two clusters that recently[4] collided. The galaxies of the clusters, observable in the optical spectrum, are very sparsely distributed, very dense, and locally neutral. Thus they mostly pass by each other, getting slowed down slightly by gravitational interaction. The X-ray emitting hot gas clouds, however, are more uniformly distributed and interact electromagnetically, thus they produce a shock front, visible in the gamma ray image, and get caught in one another. This hot gas is about 9 times as massive as the luminous matter in the galaxies of the cluster [26]. Thus, if there was only baryonic matter, one would expect gravitational lensing to indicate most of the mass residing with the gas clouds. However, the lensing data suggest that roughly 80% of the mass resides in two clusters around the visible galaxies, strongly indicating that Dark Matter is distinct from the baryonic mass distribution [8].

Baryon Acoustic Oscillations in the Cosmic Microwave Background

Under the standard paradigm of cosmology, the very early universe contains a primordial plasma of matter and radiation [23]. As time goes on, the universe expands, cooling the

[4] within the last 10^8 years [8]

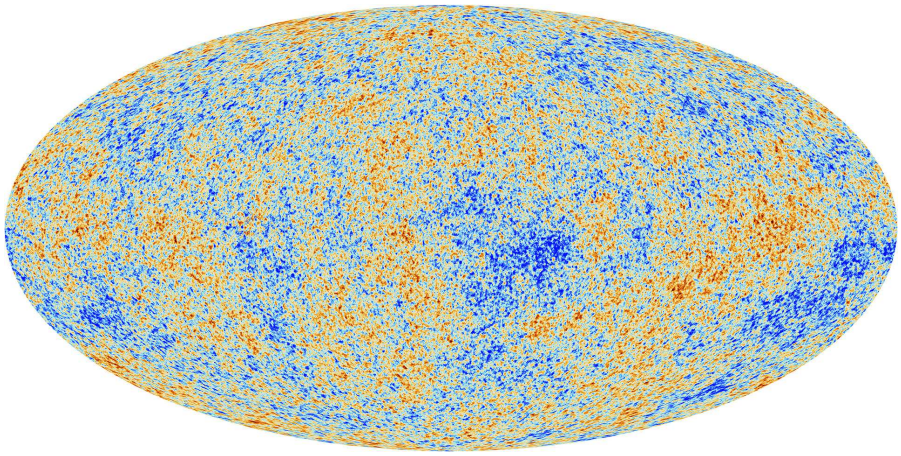

Figure 1.8: The anisotropies of the cosmic microwave background as observed by the Planck [27] mission. Taken from Ref. [28]

plasma. As the plasma temperature drops, particle species drop out of the thermal equilibrium when they, on average, interact more slowly than the universe expands, or are to heavy to be produced at the current temperature and thus either decay or persist. The last particles to decouple are photons, protons and electrons. After that, the electrons and protons are bound in neutral hydrogen atoms, while the photons start to stream freely through the universe. Thus these relic photons carry the image of the plasma just before it formed the first atoms.

The relic photons permeate space to this day. However, gravitational redshift due to the expansion of the universe reduces the relic photon energy. Thus the relic photon temperature has dropped from the initial ≈ 3000 K to ≈ 2.7 K today [23]. This temperature corresponds to typical wavelengths 1 mm, and thus these photons are collectively called the Cosmic Microwave Background (CMB). The observed CMB is isotropic at the level of $10^{-}5$ [3], below which anisotropies start appearing. A map of these anisotropies is shown in Figure 1.8. The observed anisotropies are conventionally expanded as a series of spherical harmonics. The expansion coefficients as a function of the multipole order in the series of spherical harmonics are shown in Figure 1.9, also called the CMB power spectrum.

The CMB power spectrum in Figure 1.9 is formed of a succession of peaks and troughs. This means that at certain powers l, i.e. certain typical distance scales, anisotropies are more common than at others. This observation is explained by oscillations in the primordial baryonic plasma, called baryon acoustic oscillations [30, 31]. In the remainder of this section, a very basic overview based on the descriptions in [30, 31, 25] is presented.

Assuming random quantum fluctuations initiated some over-and underdensities in the early universe, then both Dark Matter and the baryonic plasma are gravitationally attracted to the overdensities. Thus matter starts to clump around the random initial fluctuations. As the plasma density grows, the mean path between two interactions of the electrons or protons is reduced. This increases the rate at which photons are radiated in these interactions, and thus the radiation pressure exerted by the photons on the electrons and protons of the plasma grows. At high enough radiation pressure, the plasma is pushed away from the overdense spot. This reduces the radiation pressure, such that the baryons can fall in again, and so on. The result of these elecromagnetic interactions of the protons, electrons and photons are density oscillations, called baryon acoustic oscillations. Since Dark Matter does not feel the radiation pressure of the photons, it continuously falls into the overdense locations, giving rise to an ever increasing gravitational driving force on the baryon acoustic oscillations.

The baryon acoustic oscillations go on until the plasma combines into hydrogen atoms, and

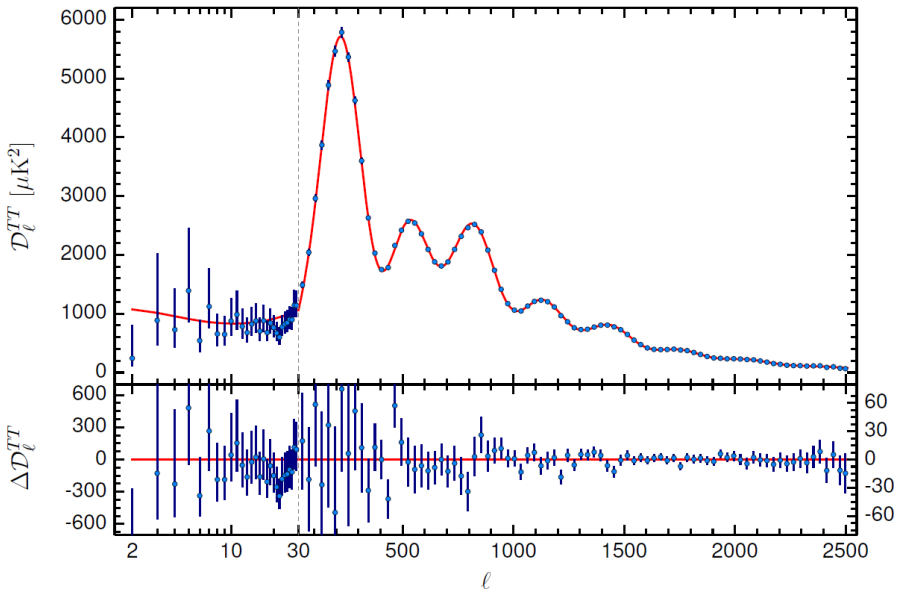

Figure 1.9: Planck 2015 temperature power spectrum [29]. Data are shown in blue, the best-fit model in red.

the photons decouple. At this moment the oscillations stop. The photons start propagating freely, with energies corresponding to the local temperature distribution caused by the density oscillations. As they propagate, some of the photons lose some energy as they leave their local gravitational potential well. The two effects together thus imprint upon the CMB photon energies the anisotropy structure of the early universe, as hot and cold spots, as shown in Figure 1.8. The peaks in Figure 1.9 are the result of oscillations that were frozen by the last scattering while they happened to be at an extremum of their oscillation. Since the speed of light is limited, there is a horizon limiting how far the baryon oscillation "sound" can have traveled prior to recombination, while still being observed in the CMB today. This sets a length scale, giving a minimum wavenumber, or minimum harmonic power ℓ, which determines the location of the acoustic peaks in Figure 1.9. Odd numbered peaks correspond to maximal temperatures, even numbered peaks to minimal temperatures. Since the oscillations are driven by the Dark Matter density, fits to the CMB power spectrum allow to extract, among others, the Dark Matter density in the Universe from the amplitude and locations of the peaks. In particular, the best-fit result $\rho_{\mathrm{DM}} = 0.258(11)\frac{3H(0)^2}{8\pi G_N}$ [29] is significantly away from 0. Thus the CMB power spectrum provides evidence for Dark Matter at cosmological scales.

1.3.2 Nature of Dark Matter

There is a large variety of evidence for Dark Matter, three examples of which were briefly introduced in Section 1.3.1. However, all of the evidence for Dark Matter comes from the studies of galaxies or even larger systems [3]. Beyond that, the evidence for Dark Matter relies on the interaction of Dark Matter via gravity, and that any potential other interactions are coupled far weaker than typical electromagnetic interactions. Thus, all that the evidence requires of Dark Matter is a mass and a small interaction cross section. This unknown nature of Dark Matter is the subject of this section.

The above conditions of some mass and small cross sections are in fact properties of at least two of the three species of neutrino. One expects that a large number of neutrinos was produced thermally in the early universe [23]. However, this explanation has several

insufficiencies. Firstly, if the neutrinos are produced thermally in the early Universe, then given the observed upper limits on their masses, the neutrino relic density may at most be ≈ 0.0062 [17], which is too low to explain the CMB anisotropies [3]. Secondly, the neutrinos would be produced at very high temperatures, and thus have velocities close to the speed of light around the time of structure formation [4]. This is inconsistent with the current understanding of structure formation, which indicates that Dark Matter started clumping into small structures, from which larger structures were formed, which attracted baryonic matter, thus forming galaxies and galaxy clusters [4]. Neutrinos, moving at close to the speed of light, cannot have initiated structure formation in this manner, since they are too fast to be caught in the gravitational potential of low mass structures [3]. Thus neutrinos, while likely being a small component of hot Dark Matter, are no the predominantly cold Dark Matter used to describe explains the cosmology of structure formation and the CMB.

Another way to construct a Dark Matter candidate to explain galactic rotation curves is to consider systems of bound SM particles,in non-luminous configurations, called Massive Compact Halo Objects (MACHOs). Examples include small stars that are too low in mass to initiate fusion under the pressure of their own weight, small black holes etc. Limits on the mass of such objects have been placed by monitoring the luminosities of nearby stars over several years, which would be expected to fluctuate due to gravitational lensing by the MACHOs [17], finding that no more than 8% of the mass of the halo of our galaxy can be due to MACHOs [32].

Asides from Dark Matter candidates based on known SM particles, Dark Matter could be composed of new particles that are not part of the SM. Two classes of Dark Matter candidate that have recieved particluar attention are Weakly Interacting Massive Particle (WIMPs) and Axion-Like Particles (ALPs) [5, 3].

ALPs are CP-odd scalar particles with very small interaction cross sections and masses typically in the sub-eV range [5, 3]. Due to the extremely low interaction rates, ALPs are challenging to study at a particle collider, and thus they are not discussed further in this Thesis. A WIMP is a new particle species with a mass approximately close to the electroweak (symmetry breaking -) scale, i.e. several GeV to TeV, and a thermally averaged annihilation cross section of a size typical for electroweak processes i.e. $\langle \sigma_{\text{ann.}} v \rangle \approx 1 \times 10^{-27} \frac{\text{cm}^3}{s}$ [5, 3, 4].

WIMPs, if produced thermally in the early universe, would be produced in an amount consistent with the Dark Matter abundance as fitted to the CMB. Furthermore, such WIMP particles would decouple from the primordial plasma at a time when the plasma temperature is far smaller than the particle mass [3, 4]. Hence these particles would have non-relativistic velocities after their decoupling, i.e. they would be cold Dark Matter, and thus consistent with a bottom-up structure formation mechanism [5]. Thus, WIMPs naturally match the cosmological constraints of Dark Matter [5], i.e. assuming only thermal production, as assumed also for other relics of the early universe, such as the CMB photons, or relic neutrinos.

There are several independently motivated theories of physics beyond the SM that can accommodate WIMP Dark Matter [3]. An example are $R-$parity conserving supersymmetric extensions of the SM [3, 5]. These feature a lightest supersymmetric particle, which, if it is a neutralino with appropriate mass and couplings, would constitute WIMP Dark Matter [3, 5].

Because they naturally provide the correct relic abundance of cold Dark Matter, and because they can be motivated in larger hypothetical theories such as supersymmetry, WIMPs have been the focus of many Dark Matter searches. These searches, aiming to either find evidence of or exclude the existence of WIMP Dark Matter, are discussed in Section 1.3.3 below.

A potential hint at the existence of Dark Matter– baryon interactions from cosmology is

the recently reported 21 cm hydrogen absorption feature, redshifted to a range centered on 78 MHz, in CMB photons [33, 34]. The absorption is about twice as strong as expected [33]. This absorption line is interpreted as originating from the hydrogen clouds in the early universe absorbing CMB photons with a wavelength of 21 cm, corresponding to the energy difference between the two possible hyperfine spin states of the hydrogen atom [33]. This absorption begins at the redshift when the first stars formed, which started emitting UV photons. When hitting a hydrogen atom, these high energy photons can excite the hydrogen atom. After relaxing back into the ground state, the hydrogen atom has an about equal chance of being in either hyperfine state. In this way, the first stars effectively increase the population of atoms in the higher-energy hyperfine state. This increased population in turn can then transition to the lower hyperfine state by absorbing a 21 cm CMB photon. The colder the gas clouds, the larger increase increase in the higher hyperfine population relative to the previous population, which is coupled to the gas temperature, and thus the stronger the absorption [33]. In this way the strength of the absorption feature indicates the temperature of the gas clouds [33]. Since the absorption appears to be twice as strong as expected, this indicates that the gas clouds are unexpectedly cold [33].

There are systematic effects that could fake such a 21 cm absorption signal, and the observation has yet to be tested by other, similar experiments [33]. If it is true, however, then one proposed explanation for the reduced gas temperature is that the gas was cooled in interactions with lower-temperature Dark Matter [34, 35]. Thus the observation of the 21 cm absorption feature could be the first indication of Dark Matter–baryon interactions. This would strengthen the case for Dark Matter searches, which all assume such an interaction to exist. However, to match the observed redshift and absorption strength, the Dark Matter would need a mass of a few GeV or below [34, 35], uncharacteristically low for WIMP Dark Matter, and a total scattering cross section on baryons larger than $10^{-21}\,\mathrm{cm}^2$, significantly larger than the typical weak scattering cross section assumed for a WIMP. Finally, as pointed out above, due to the large and difficult to estimate uncertainties affecting the observation, without independent confirmation, and the theoretical challenges of interpretating the observed feature as resulting from WIMP Dark Matter, it would be premature to treat it as evidence for DM - baryon interactions [33].

1.3.3 Dark Matter Searches

This section provides a brief overview of the three main approaches of searching for WIMP Dark Matter. These are direct detection experiments, indirect detection experiments, and Dark Matter searches at particle colliders [3, 4]. Direct detection experiments, which look for evidence of Dark Matter particles scattering the baryonic matter of a detector, and measuring the scattered baryonic matter [3], are described in Section 1.3.3.1. Indirect detection searches, looking for cosmic radiation produced when Dark Matter particles pair-annihilate into ordinary matter, are discussed in Section 1.3.3.2. Collider searches, looking for the signature of Dark Matter production in high-energy collisions of SM particles [3], are discussed in Section 1.3.3.3. To be able to compare the results of these three different approaches, a theoretical description of the Dark Matter- SM interactions is useful. As illustrated in Figure 1.10, the same effective Dark Matter- SM interaction term, interpreted with different time orderings, can be used to connect the interpretation of the results of different types of Dark Matter searches.

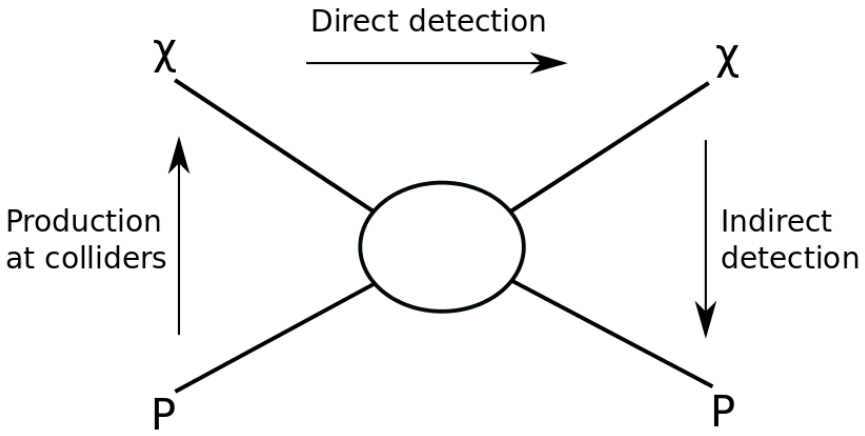

Figure 1.10: The three major avenues of Dark Matter searches, direct detection, indirect detection, and collider production experiments, probe the hypothetical interaction between WIMPs and SM particles in different time orderings. Taken from [9]

1.3.3.1 Direct Detection

Direct detection experiments search for evidence of Dark Matter particles scattering the baryonic matter of a detector [3, 9]. If the observed flatness of the rotation curves of the Milky Way and other galaxies is caused by a dark matter halo enveloping these galaxies, and if the dark matter halo is composed of WIMPs, then one would expect these WIMPs to permeate the galaxy. In particular, the Milky Way galaxy should be filled with WIMPs, and the Earth should pass through this sea of WIMPs as it rotates around the sun [3]. If there is some (albeit potentially weak) interaction of the WIMPs and baryonic matter, the WIMPs should occasionally scatter of the nuclei on earth.

The idea of direct detection WIMP searches is to try and observe such WIMP - nucleus scattering events. The recoil energy of the scattered nucleus can be measured via the generation of a photon, a phonon/heat, or ionization charges [9]. In principle one of these methods is sufficient, but many searches use a coincidence of two such signal types [3]. This makes background suppression easier, as one can then define refined two-dimensional signal regions, where the background rate is low [9].

The main backgrounds for a typical current direct detection experiment are cosmic radiation, e.g. neutrons produced in the interactions of cosmic muons, and gamma rays and neutrons from the decays of unstable isotopes occurring naturally on earth [9]. To reduce the background of cosmic radiation scattering of the detector material, the detectors are installed in old mines or other locations shielded from the cosmic radiation. To reduce the background due to natural radioactivity, much care is taken to reduce the fraction of unstable isotopes in the active detector material while it is produced, and its activation from cosmic radiation during its transport [9]. Furthermore the detector is shielded by successive layers of increasingly low-activity materials with large absorption cross sections, such as lead [9]. The effects of natural radioactivity can be suppressed further by placing separate detectors around the active volume, and vetoing events coincident with a signal in any of these edge detectors [9]. The current generytion of experiments is not yet sensitive enough to observe the scattering of solar or cosmic neutrinos on the detector nuclei [9]. However, as the sensitivity of the detectors is increased, this neutrino- nucleon scattering is expected to eventually become a large background. Experimentally, such events would furthermore be challenging to distinguish from a

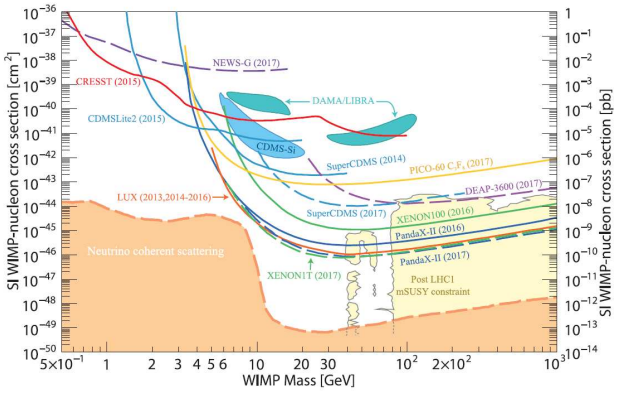

(a) spin-independent scattering

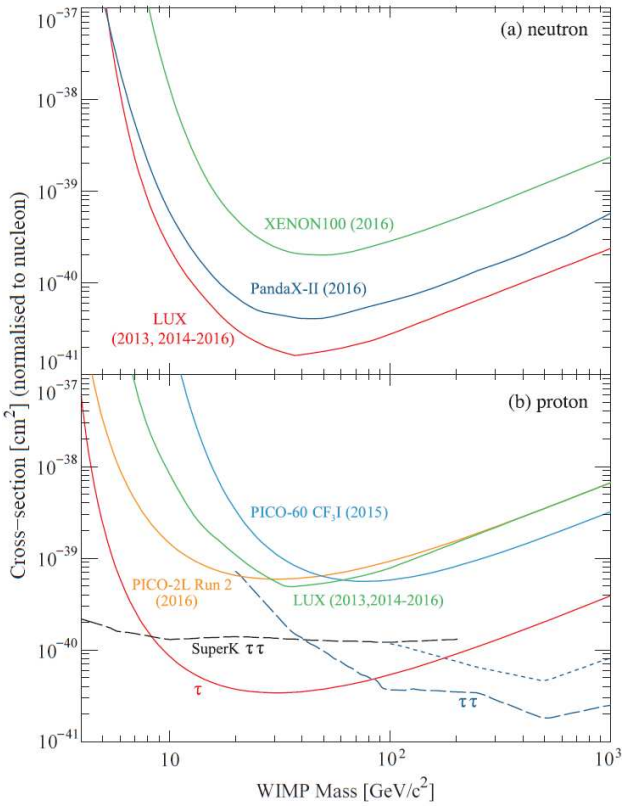

(b) spin-dependent scattering

Figure 1.11: Direct detection limits on the Dark Matter- nucleon scattering cross section (solid lines). Dashed lines correspond to constraints from indirect detection, discussed in Section 1.3.3.2. (a) shows the limits on the spin-independent scattering cross section. The spin-dependent cross section is shown in (b), with the top plot collating limits on the Dark Matter-neutron cross section, and the bottom plot collating limits on the Dark Matter-neutron cross section. Taken from Ref. [17]

WIMP signal, severely limiting the direct detection sensitivity to very low cross section Dark Matter models [9, 17].

The expected rate of signal events can be calculated according to the WIMP-nucleon scattering cross-section $\sigma_{i\chi}$ and local number density n_χ [3]:

$$\dot{N} = \sum_{i \in \text{ nuclei species}} n_i n_\chi \langle \sigma_{i\chi} \rangle \tag{1.16}$$

where n_i is the number of nuclei of species i in a detector and the brackets $\langle \ldots \rangle$ indicate the average with respect to the relative velocity distribution of the WIMPs and the target.

Because the Dark Matter is assumed to be cold, i.e. non-relativistic, the energies exchanged between WIMP and incident nucleus are typically small compared to the WIMP or nucleon masses. Thus effective contact operators are used to calculate the WIMP-Nucleon scattering cross section in Equation (1.16) [9], as illustrated in Figure 1.10. This Effective Field Theory description has integrated out any potentially more complicated underlying parametrization in just two degreess of freedom: the WIMP mass m_χ and the effective mass scale of the contact interaction [3, 9]. Correspondingly, the results of direct detection experiments are limits in a two dimensional parameter space, which is conventionally chosen as the plane of $m_D M$ and $\sigma_{i\chi}$. A summary of several such limits from different experiments is shown in Figure 1.11.

Depending on the spin structure of the Dark Matter-baryon interaction, two kinds of scattering can be distinguished: spin-independent and spin-dependent scattering [3, 9]. Spin dependent scattering is the result of Dark Matter coupling to the spin content of the nucleus, e.g. with a axial vector or pseudosscalar symmetry of the interaction term. Thus the contributions of nucleons with opposing spins cancel, and hence the cross section scales as $J(J+1)$ relative to the nuclear spin J [9]. For spin-independent scattering, e.g. for a scalar symmetry of the interaction, there is no such cancellation, and the cross section increases with the number of nucleons, i.e the mass of the nucleus. Since there are many stable elements with heavy nuclei, but only a few with even moderate nuclear spins, the direct detection sensitivity to spin independent scattering is orders of magnitude weaker than that to spin dependent scattering. Correspondingly, the direct detection limits on the spin independent scattering cross section, shown in Figure 1.11(a), are stronger than those on the spin dependent cross section, shown in Figure 1.11(b) [9, 17].

The sensitivity of direct detection experiments as a function of the WIMP mass is limited by two effects. Toward low WIMP masses, the mass of the nuclei used for the active detector volume is so much higher than the WIMP mass that the momentum the nucleus incurs from the recoil of the WIMP is too small to be observed [9]. Towards high WIMP masses, the number density of WIMPs, given the known Dark Matter mass density, is so low that the rate of signal events decreases linearly, according to Equation (1.16) [9].

To date, no significant direct detection signal has been observed that is not in contradiction with the limits of competing direct detection experiments [9, 17], as illustrated in Figure 1.11.

1.3.3.2 Indirect Detection

Indirect detection searches look for cosmic radiation produced in Dark Matter annihilation into SM particles [3, 4, 10]. Since the average number density of Dark Matter in the halo is assumed to be low, the annihilation rate in most of the halo is expected to be too low to be observable. Thus the Dark Matter annihilation signal is expected to originate from regions of space where the Dark Matter density is significantly higher than the average of the Dark Matter halo [10]. One such region would be the galactic center of the milky way [10], where the large amount of ordinary matter may bind Dark Matter particles gravitationally (or equivalently, be bound gravitationally by the Dark Matter).

An increased flux of photons with energies of about several GeV have been observed as originating from the galactic center [36], shown in Figure 1.12. The flux and energy range of this excess at the galactic center are consistent with interpretations of WIMPs decaying into e.g. $\bar{b}b$ or $\bar{\tau}\tau$. However, the interpretations of the observed excess are affected by large systematic uncertainties in the modelling of the propagation of the photons through the gas and dust clouds of the interstellar medium, and the models of known gamma ray sources. Finally, the observed excess could also be explained by a population of point sources that Fermi can not resolve as points sources, a hypothesis that better fits the observed photon statistics than uncorrelated Dark Matter annihilations [37]. Such point sources could e.g. be rapidly spinning neutron stars, called millisecond pulsars [38]. Therefore, it is not clear that the observed gamma ray excess is due to Dark Matter annihilation into SM particles [36, 37, 38].

Another avenue for indirect Dark Matter searches is charged cosmic radiation, such as positrons and anti-protons [3]. The trajectories of these charged particles are bent and distorted by the magnetic fields in the galaxy. Therefore they do not point in the direction of their source. But the flux and energy of these particles nevertheless carry important information about the abundance and nature of their sources. An excess of high-energy positrons has been reported

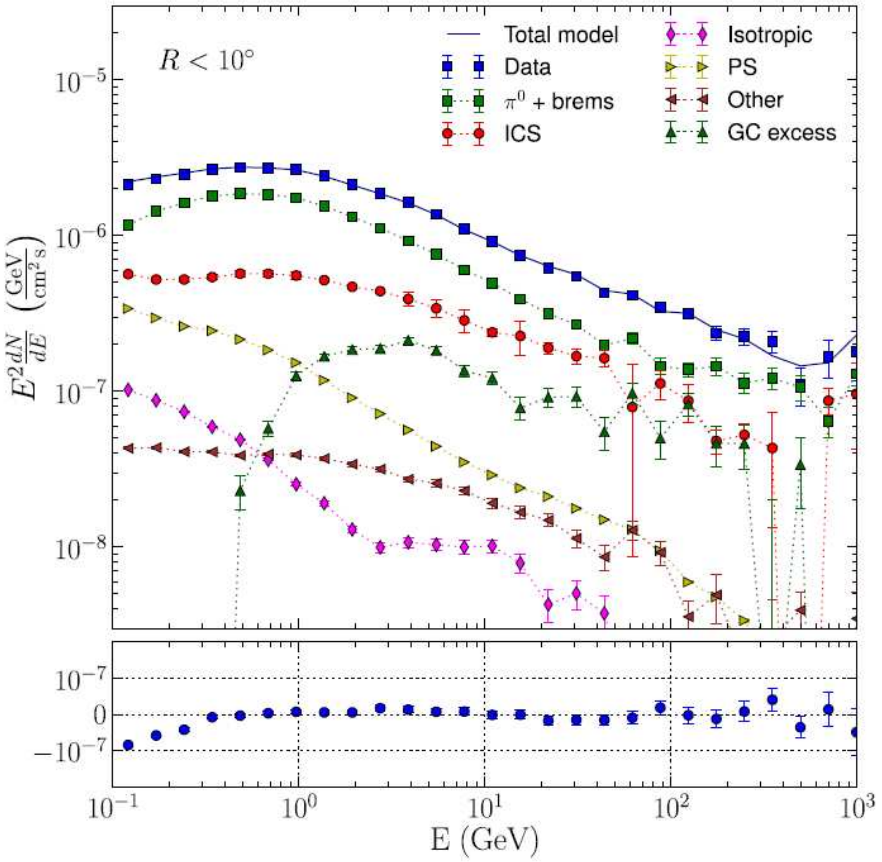

Figure 1.12: Integrated gamma ray flux within a 10° radius from the galactic center reported by the Fermi-LAT collaboration. The results of a fit of various component sources to the observed spectrum and spatial distribution are also shown. There are several background sources: bremsstrahlung and neutral pion decays from hadronic collisions ("π_0 + brems"), inverse compton scattering of photons from starlight, the CMB, or IR radiation of cold dust, to higher energies ("IC"), various diffuse and isotropic emission sources ("isotropic"), and known point sources ("PS"). The fitted excess is marked "GC excess". Taken from [36].

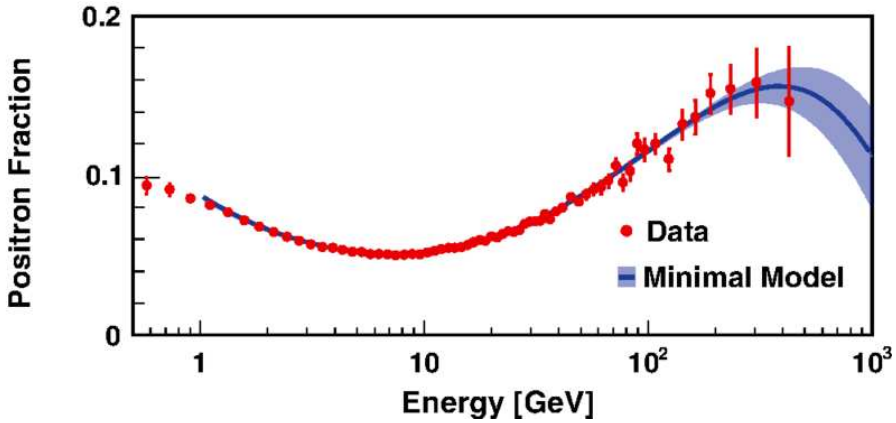

Figure 1.13: Energy spectrum of the positron fraction, defined as the ration of fluxes $\frac{\phi_{e^+}}{\phi_{e^+}+\phi_{e^-}}$, measured with the AMS-02 detector. A fit to the data with a model assuming that the positron and electron flux spectra are described by two independent distributions, both of which are a sum of a diffuse power term and point source term of a power law with an exponential cutoff at high energies. Adapted from Ref. [39]

Figure 1.14: Illustration of Dark Matter signals at colliders. An additional final state particle is required to allow triggering the event. Due to the very high momentum transfers achievable at the LHC, the generic contact interaction description shown in (a) needs to be specified into simplified models with explicit mediators, as illustrated in (b). Taken from Ref. [11].

by e.g. the AMS collaboration using the AMS-02 detector on the international space station [39]. The observed positron fraction, shown in Figure 1.13 can be interpreted as resulting from Dark Matter annihilations [40, 41], but there are also consistent explanations of the observed spectrum that do not require Dark Matter annihilations, such as rotating neutron stars (pulsars) [42] or secondary positron production[43].

There is a large variety of indirect Dark Matter searches, beyond the two examples sketched above [3, 4, 10]. Gamma ray searches can be extended to regions of the galaxy other than the galactic center, or the centers of other galaxies than the milky way. One can use neutrino detectors to search for excessive neutrino production in e.g. the Sun. Charged cosmic radiation fluxes further extend the number of possible search avenues. As searches extend their sensitive phase space, the existing descriptions of non - Dark Matter sources of cosmic radiation are extended. Thus not every observed excess is necessarily indicative of Dark Matter, as historically such excesses have often been indicative of the limited understanding of more conventional potential sources. This makes the interpretation of indirect searches more challenging than that of direct or collider based searches. However, indirect searches provide additional constraints on the results of the other two search channels, and thus they are useful to distinguish otherwise indistinguishable Dark Matter scenarios [41, 4].

1.3.3.3 Collider Searches

Collider searches for Dark Matter are looking for events where Dark Matter particle are produced in high energy particle collisions [3, 4, 7]. Although searches at other colliders can be done [44], this thesis will only consider proton-proton collisions at the LHC. Because the Dark Matter particles are thought to be long-lived or stable, as well as very weakly interacting, they can leave any detector placed around the collision point undetected. Hence collider searches consider events where invisible particles have been produced simultaneously with at least one observed particle X, which enables triggering the recording of the event. Example Feynman graphs for such events are shown in Figure 1.14. The Dark Matter particles can carry significant momenta, which, because the initial state partons have negligible momentum components transverse to the colliding beams, can be identified as missing transverse momentum (E_T^{miss}), i.e. the difference to 0 of the vector sum of all transverse momenta in the event. Such searches are called "mono-X" or $X + E_T^{\text{miss}}$ searches. The X in $X + E_T^{\text{miss}}$ can for example be a jet [45], a photon [46], an electroweak vector boson [47], a higgs boson [2], a top quark [48] or a pair of top quarks [49].

The description of the Dark Matter-SM interaction as a pure contact interaction, such as in Figure 1.14(a) is sufficient for direct detection, and many cases of indirect detection signals, because the relative momenta of the interacting particles are far below the suppression scale

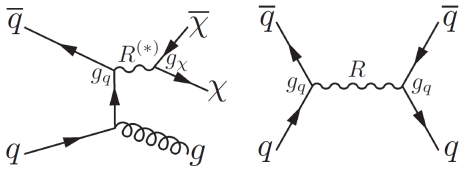

Figure 1.15: Relation between jet + E_T^{miss} and dijet searches. The mediator R of a simplified model can, if it exists, not only decay into Dark Matter, but also into SM final particles. This motivates collider searches for resonant Dark Matter mediator decays into two jets or two leptons. Taken from Ref. [7].

of the effective field theory (EFT) in question [7]. This is not necessarily true for Dark Matter searches at the LHC, where the relative momenta of the initial state partons can be large enough to resolve mediators with masses on the order of several TeV. Trying to describe such interactions as EFTs can yield wrong kinematics and unitarity violating scattering amplitudes [7, 11]. To obtain correct predictions, simplified models are used instead, which explicitly include one or several mediator states. An example of a Feynman graph for a $X + E_T^{\text{miss}}$ event in such a simplified model is shown in Figure 1.14(b). Simplified models can be connected with the corresponding effective contact operator by integrating out higher-energy degrees of freedom. For example, for an s-channel vector mediator Z' one gets [11]:

$$\frac{g_q g_\chi}{Q^2 - m_{Z'}^2} \approx -\frac{g_q g_\chi}{m_{Z'}^2} + \mathcal{O}\left(\frac{Q^2}{m_{Z'}^2}\right)$$

with g_q the coupling of the mediator to quarks, g_χ the coupling to Dark Matter, and Q^2 the momentum transfer in the $s-$channel. The suppression scale Λ of the corresponding effective contact operator $\frac{\bar{\chi}\gamma^\mu\chi\bar{q}\gamma_\mu q}{\Lambda^2}$ can then be read off to be $\Lambda = \frac{\sqrt{g_q g_\chi}}{m_{Z'}}$.

Simplified models feature explicit mediators of the SM-Dark Matter interaction. Thus one can further constrain such models by looking for the decay of the mediator back into SM particles, e.g. a pair of quarks [7]. This concept is illustrated in Figure 1.15. The resulting dijet resonance searches can not provide direct evidence of the existence of a Dark Matter candidate, but they can provide strong constraints on the viable parameter space of simplified models.

Figure 1.16 shows an overview of different $X + E_T^{\text{miss}}$ and dijet searches with the ATLAS detector at the LHC. The search results are interpreted in the vector mediator simplified model [59], with a single massive vector mediator coupling to Dark Matter and to quarks, but not leptons.

In Figure 1.16(a), different search signatures are compared in the mediator mass - Dark Matter mass plane. $X + E_T^{\text{miss}}$ signatures are sensitive in a triangle shaped region in this plane. The reason is that the model predicts large $X + E_T^{\text{miss}}$ production cross sections while the mediator is on-shell, i.e. $M_{\text{med.}} > 2M_\chi$, but strongly suppressed cross sections in the off-shell regime with $M_{\text{med.}} < 2M_\chi$ [7]. The production cross section falls with increasing mediator mass, because the parton distribution functions of the proton fall with increasing momentum fraction. Thus at some mediator mass, the predicted signal rate is too small to be distinguishable from backgrounds, giving the upper end of the sensitivity in terms of the mediator mass.

In the vector mediator simplified model, there is a clear sensitivity hierarchy of the $X + E_T^{\text{miss}}$ searches. This can be seen in the mass reach of the respective exclusion contours in Figure 1.16(a): the jet + E_T^{miss} search is more sensitive than the $\gamma + E_T^{\text{miss}}$ search, and both are more sensitive than the $Z(ll) + E_T^{\text{miss}}$ search. This hierachy reflects the fact that,in the

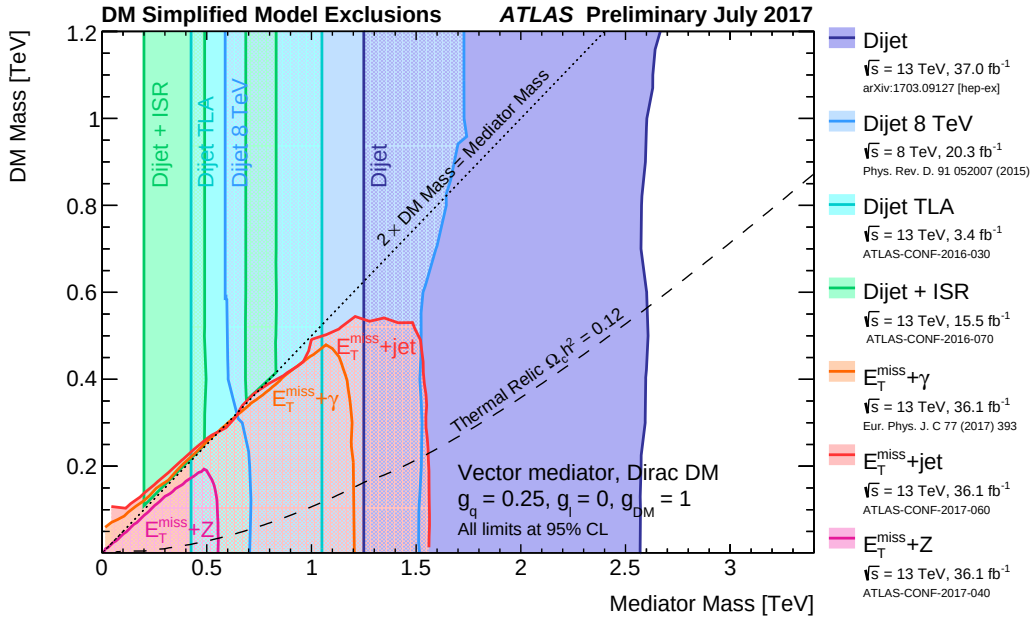

(a) ATLAS dijet and $X + E_T^{\text{miss}}$ exclusion limits from Refs. [50, 51, 52, 53, 46, 45, 47].

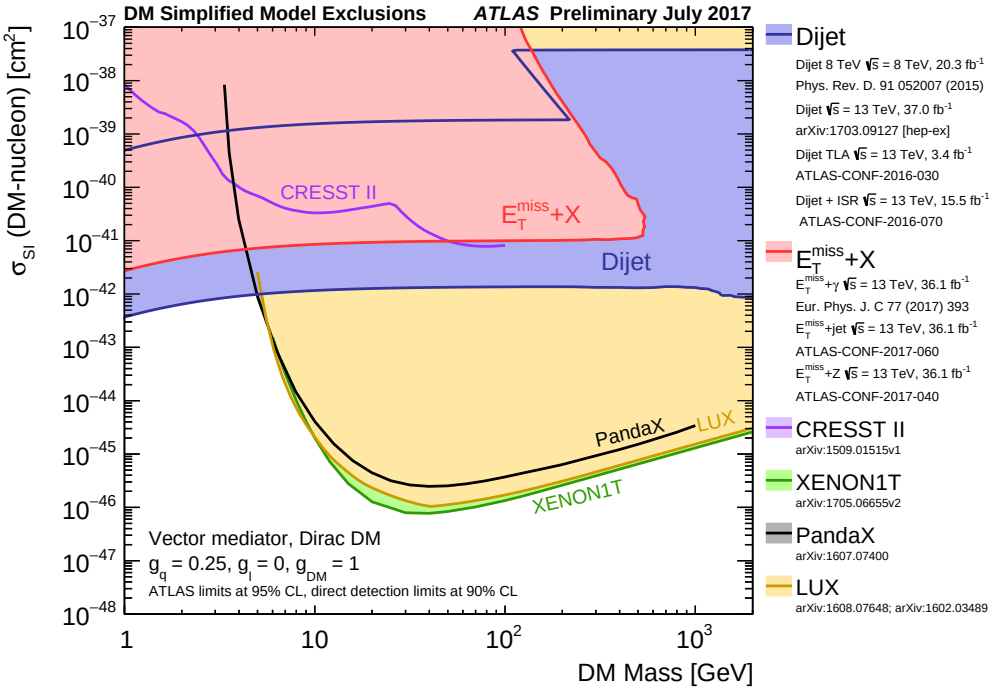

(b) Comparison of the ATLAS limits from (a) to direct detection results from [54, 55, 56, 57, 58]

Figure 1.16: Summary of selected ATLAS searches for Dark Matter. The results of different searches in a variety of final states in the plane of mediator and Dark Matter masses are shown in (a). The combined exclusion is compared to direct detection results in the plane of spin-independent Dark Matter-Nucleon scattering cross section and Dark Matter mass in (b). The exclusions are computed the vector-mediator simplified model in Ref. [59] with a dark matter coupling $g_{DM} = 1.0$, a quark coupling $g_q = 0.25$ universal to all flavors, and a lepton coupling g_l set to zero. The plots are taken from Ref. [60].

vector mediator simplified model, the X of $X + E_T^{\text{miss}}$ is Initial State Radiation (ISR), as indicated in Figures 1.14 and 1.15. Consequently, the sensitivity of the respective searches is determined by the respective expected rate of ISR production for the different X. Thus the sensitivity hierarchy reflects the hierarchy of couplings of the strong, electromagnetic, and weak interactions to quarks.

The various searches for dijet resonances in Figure 1.16(a) are to first order independent of the Dark Matter mass. The low mass end of the dijet sensitivity arises due to the trigger thresholds [50]. The lower the mass of the resonance, the lower the maximum transverse momentum of the resulting jets. Below a certain threshold of transverse momentum, a potential signal event is not triggered, in order to keep the data readout rate of the detector within the technical limitations of the data acquisition and readout systems. Thus signal events below a certain mediator mass would not be recorded, and the search is not sensitive to such a model. To extend the sensitivity to lower masses, different approaches are used:

- Collider runs with lower center-of-mass energy [51], where the trigger thresholds can be lowered, corresponding to the "Dijet 8 TeV" line in Figure 1.16(a).
- A Trigger Level Analysis (TLA) dijet search using jets reconstructed at trigger level [53]. Trigger level jets can be constructed very fast and take up little bandwidth even at high event rates, thus they help evade usual bandwidth constraint, allowing the use of reduced trigger thresholds. The result of this approach is shown as "Dijet TLA" in Figure 1.16(a)
- A search for events with ISR in addition to the dijet system [52]. The ISR is momentum balanced with the dijet system, which is therefore boosted with respect to the detector rest frame. Thus the jets in the event can have large transverse momenta, above the trigger threshold, even when the mass of the mediator is low. This is shown as "Dijet + ISR" in Figure 1.16(a).

At high masses, similarly to the $X+E_T^{\text{miss}}$ searches, the parton distribution functions, which fall towards larger momentum fractions, reduce the expected rate of producing massive resonances, and eventually limiting the upper mass reach of the dijet search sensitivity. There is a slight residual dependence of the sensitivity on the Dark Matter mass [50]. It arises from the Dark Matter mass affecting the partial decay width of the mediator into Dark Matter, thus changing its total decay width. The total width of the mediator affects the signal acceptance, because the searches are optimised for narrow resonances, and thus the sensitivity changes with the Dark Matter mass.

Figure 1.16(b) presents the comparison of the ATLAS Dark Matter search results to the results of direct detection experiments. Higher mediator masses correspond to lower DM-nucleon scattering cross sections. While direct detection searches are sensitive to lower scattering cross sections than the collider searches, the collider searches are sensitive to far lower Dark Matter masses. Furthermore, collider searches are insensitive to the difference between CP-even and CP-odd mediators, whereas direct detection experiments are much less sensitive to spin-dependent DM-nucleus couplings. These observations illustrate that direct detection and collider based WIMP searches are complementary.

The notable absence of more exotic Dark Matter signatures such as $h(b\bar{b}) + E_T^{\text{miss}}$, $h(\gamma\gamma) + E_T^{\text{miss}}$, $\mathrm{t} + E_T^{\text{miss}}$, $b\bar{b} + E_T^{\text{miss}}$, $t\bar{t} + E_T^{\text{miss}}$, and $t\bar{t}$-resonance from the summary plot in Figure 1.16 reflects the limitation of the vector mediator simplified model [59] used for the interpretation, as mentioned in Section 1.1. The parameter benchmarks in the 2HDM+a constructed in Chapters 6 and 7 and used in Chapter 8 attempt to overcome this limitation.

Chapter 2

The ATLAS Detector at the LHC

This Chapter describes the experimental machinery used for the $h(b\bar{b}) + E_T^{\text{miss}}$ search described in Chapter 3 and its interpretation in Chapter 8, providing context for the studies presented in Chapters 6 and 7. The Large Hadron Collider (LHC) at CERN near Geneva in Switzerland is the most powerful particle collider in operation at the time of writing. The ATLAS detector is one of several detectors recording the LHC hadron collisions. Section 2.1 briefly describes the LHC, following Ref. [61, 62]. Section 2.2 gives a short overview of the ATLAS Detector, following Ref. [63]. The concept of luminosity and its measurement with the ATLAS detector are introduced in Section 2.3.

2.1 The Large Hadron Collider

The LHC consists of two counter-rotating storage rings. The storage rings are located in a single circular underground tunnel with a circumference of 26.7 km located near Geneva, Switzerland, at a depth between 45 m and 175 m below the surface. The storage rings can be filled with either protons or lead ions, but since only the operation with protons is relevant in this thesis, only it is discussed in the following.

The protons for the LHC are produced by ionising hydrogen gas with an electric field. Once the electrons are stripped away by the electric field, the remaining protons are accelerated in a sequence of pre- accelerators, displayed in Figure 2.1. These include, in sequence, the linear accelerator LINAC2, followed by the synchrotron accelerators BOOSTER, proton Synchrotron (PS), and Super Proton Synchrotron (SPS). Because the pre-accelerating synchrotons use radio frequency (RF) cavities to accelerate the protons, the protons travel as *bunches* of $\approx 10^{11}$ protons. The proton bunches from the SPS are injected into the two LHC rings at two injection points, from where they are accelerated to the final beam energy. Accelerating a proton beam to the final LHC beam energy takes around two hours in total, of which the proton beam spends roughly half an hour being accelerated in the LHC. The proton bunch is then stored in the LHC for dozens of hours. During this time it is collided with other bunches repeatedly. One LHC beam can consist of up to 2808 bunches spaced 25 ns apart.

The LHC rings consist of a sequence of 8 straight segments and 8 curved segments. The straight segments host RF cavities that accelerate protons in a certain phase of an electromagnetic field which oscillates at 400 MHz and has an effective field strength of 2 MV/m. The straight sections are interspersed with curved sections. The curved sections contain a total of 1232 superconducting NbTi magnet coils. These coils produce dipole fields up to 8.33 T in strength that force the protons on a circular trajectory. Thus, despite gaining only 2 MeV of energy per RF cavity, the protons can revolve many times, and reach kinetic energies up to

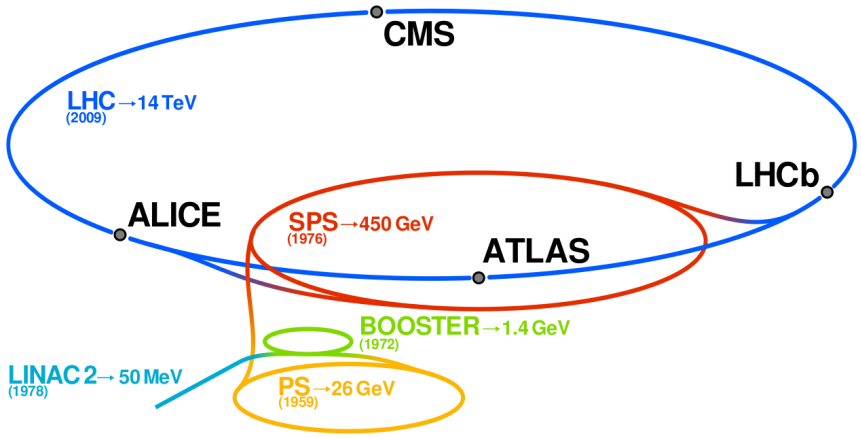

Figure 2.1: Schematic illustrating the LHC and the associated chain of lower energy accelerators. The names, final beam energy and year of first operation are given for the injectors. For the LHC, the maximum design collision energy is given instead. The position of the four main LHC detectors is indicated by grey dots. Taken from Ref. [64].

the nominal design energy of 7 TeV. The maximum energy is limited by the strength of the dipole magnets, given the curvature radius of the tunnel. The maximum energy reached in stable operation is 6.5 TeV Furthermore, 858 quadrupole magnets are used to squeeze the beam, counteracting beam dispersion and focusing the beam to a radius of 16 μm prior to reaching an interaction point. The LHC magnets are cooled down to 1.9 K, using superfluid and therefore highly heat-conducting helium as coolant. The two beam pipes, the magnets, their iron return yokes, the cooling system, and all the corresponding mechanical supports share the same tunnel. The two counter-rotating beams are brought to collision at four interaction points. Around these interaction points, detectors are installed to record the particles produced in the collisions. These locations are indicated in Figure 2.1. The four main detectors installed at the LHC are:

- ALICE [65], specialized towards the study of heavy ion collisions and Quantum Chromo Dynamics (QCD);
- ATLAS [63], a general purpose detector constructed to allow reconstructing the results of particle collisions as close to completely as possible, to facilitate precise measurements of SM properties and searches for physics not predicted by the SM;
- CMS [66], a general purpose detector like ATLAS and sharing the same physics goals, but using a different technological implementation;
- LHCb [67], a single-arm forward spectrometer specialised towards the study of CP violation in hadron collisons and rare processes involving the decays of hadrons containing b quarks.

2.2 The ATLAS Detector

The ATLAS detector, illustrated in Figure 2.2 is a multi-purpose detector, surrounding interaction point 1 of the LHC. Its three main components are the Inner Detector (ID), the calorimeters, and the muon spectrometers. These components successively and concentrically

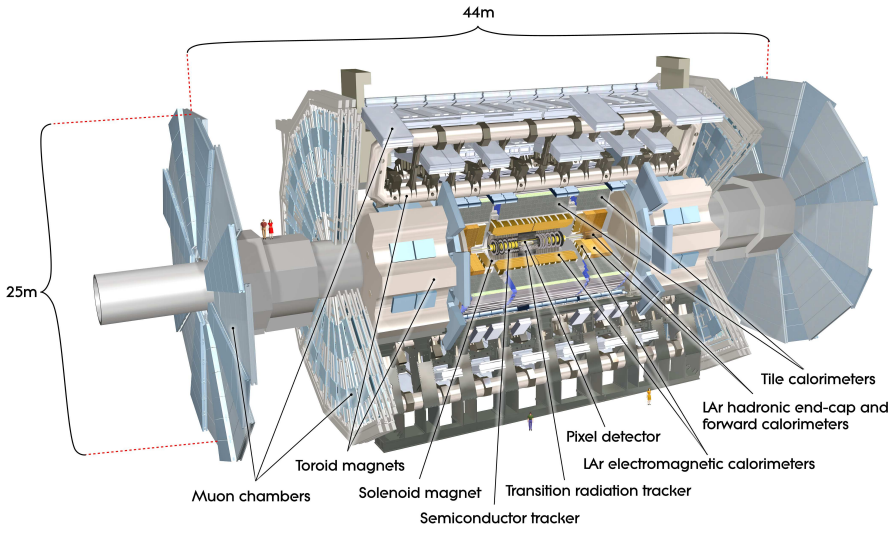

Figure 2.2: The components of the ATLAS Detector. Taken from Ref. [68].

surround the beam axis, in a forward-backwards symmetric way. A system of several magnets is installed to force charged particles into curved trajectories, allowing track based momentum measurements in the ID and muon spectrometer. The magnet system consists of one solenoid magnet surrounding the ID, and a toroid magnet system in the barrel and end-cap regions close to the muon spectrometers. The ATLAS detector is 44 m long in the beam direction, 25 m high, and weighs a total of 7000 tons.

When describing the geometry of the ATLAS detector and events recorded with it, a reference coordinate system is used. The reference coordinate system is a right handed and orthogonal coordinate system. The coordinate origin is the nominal interaction point, and the direction of the z axis is given by the beam axis. Thus the $x-y$ plane is transverse to the beam direction. In the transverse plane, the x axis points towards the center of the idealized LHC ring, and the y-axis points upwards.

An alternative description, often used for describing the momenta of final state particles, uses (ϕ, η, p_T) instead of (x, y, z). ϕ is the azimuthal angle in the transverse plane, $\vec{p}_T$, $\vec{E}_T^{\text{miss}}$, and similar transverse quantities are defined as projections into the transverse plane, and p_T, E_T^{miss} are the corresponding two-dimensional norms of the projection in the transverse plane. The polar angle θ is defined relative to the z axis, which is the beam axis. The rapidity is defined as $y \equiv \frac{1}{2}\ln\frac{E+p_z}{E-p_z}$, and the pseudorapidity is $\eta \equiv -\ln\tan\frac{\theta}{2}$. A measure of the distance between two objects in η, ϕ is defined as $\Delta R \equiv \sqrt{(\Delta\eta)^2 + (\Delta\phi)^2}$, which is covariant with respect to Lorentz boosts along the beam axis.

2.2.1 Magnets

A superconducting solenoid around the ID and a set of superconducting toroids in the outer detector comprise the ATLAS magnet system. Their geometric arrangement is shown in Figure 2.3. The magnets give rise to magnetic fields that curve the trajectories of charged particles traveling through them, enabling track based momentum measurements and charge discrimination. Because the momenta of these particles can be quite high, the magnets are cooled to 4.5 K. At this temperature, the magnets material is superconducting, and thus the field strength is high.

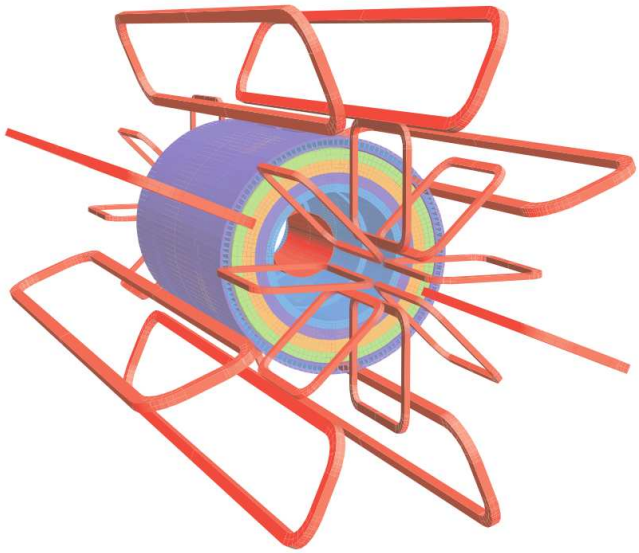

Figure 2.3: The ATLAS magnet system [63]. The magnets are shown in red. The inner solenoid is located inside the tile calorimeter, the outermost layer of which plays the role of a return yoke. The other return yokes and the end-cap shielding are not pictured.

The superconducting solenoid is shaped as a cylinder aligned with the beam axis. Its length is 5.8 m, with a diameter of 2.56 m. It is made from a NbTi alloy stabilised with aluminium, to achieve high field strengths while avoiding putting a lot of material between the ID and the calorimeters, which would reduce the resolution of the energy measurements in the calorimeters. The thickness of the solenoid corresponds to 0.66 electron radiation lengths, which is the distance an electron an electron will on average travel until interactions with the material have reduced its energy to $1/e$ of the energy it had before entering the material [17]. The single layer of solenoid coil generates a 2 T axial magnetic field, which deflects the trajectories of charged particles in the ID in the transverse plane. Instead of a dedicated return yoke, the surrounding calorimeters return the flux of the solenoid field.

There are three superconducting toroid magnets: eight coils envelop the barrel, and interleaved with them are two sets of eight coils near the forward and backward end-caps. Multiple scattering in the toroids, which would reduce the track reconstruction precision, is reduced by the toroid coils being filled with air. All toroid coils are composed of an aluminium-stabilized NbTiCu alloy. The resulting field bends the trajectories of charged particles traversing the muon spectrometer in R and z. The central barrel toroid has an outer diameter of 20.1 m with a length of 25.2 m along the beam direction, providing a 0.5 T magnetic field within $|\eta| < 1.4$. The end-cap toroids have outer diameters of 10.7 m and are 5 m long. They yield magnetic fields with a strength of 1 T in the $1.6 < |\eta|2.7$ region. The overlap region between $1.4 < |\eta| < 1.6$ the fields of the barrel and end-cap toroids are superposed.

2.2.2 Inner Detector

The Inner Detector (ID) is designed to allow precisely reconstructing charged particle tracks with $p_T > 0.5\,\text{GeV}$, which can be used for momentum measurements, particle identification, and vertex reconstruction. It is 6.2 m long and has a diameter of 2.1 m, thus covering the region of $|\eta| < 2.5$. Charged particle trajectories are reconstructed by combining the locations where ionisation charges in the active ID material, indicating a the passage of a charged particle, into

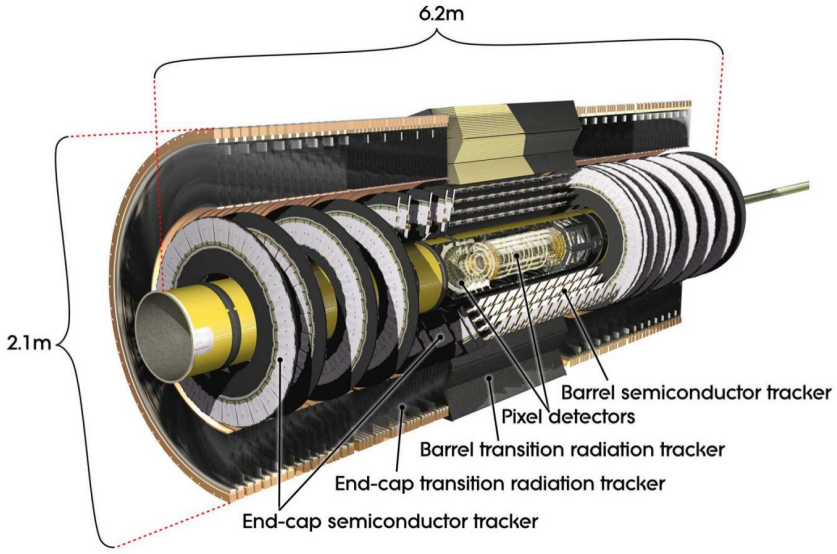

Figure 2.4: The ATLAS inner detector. Taken from Ref. [69].

tracks. Because the ID is entirely contained in the $2T$ magnetic field of the solenoid magnet, the tracks are curved. The radius of curvature is connected to the track momentum via the Lorentz force, which deflects the charged particle and gives rise to the curved trajectory.

The ID is composed out of three independent tracking subsystems. From inner- to outermost, these are the silicon pixel detectors, the silicon microstrip layers, and the transition radiation tracker. The design of the ID is illustrated in Figure 2.4. The individual tracking subsytems are each separated into a central barrel region, consisting of concentric cylinders, and an end-cap region, consisting of arrays of wheels positioned transversal to the beam line. This is done to optimise the angle of incidence of charged particles originating from the interaction points. This improves the resolution by reducing the material a passing charged particle is exposed to, reducing the effects of multiple scattering and energy loss in the ID.

The silicon pixel and silicon microstrip detectors are constructed from layers of semiconducting silicon. Externally applied voltages generate depletion zones, which are ionized when a charge particle passes through them. The ionization charges are collected and measured as electronic signal, which is converted into a space point based on the location of the microstrip or pixel. The dimension of the strip or pixel determine the resolution with which the space-point is determined. The pixel and microstrip detectors are cooled to -5 to $-10\,^{\circ}\mathrm{C}$ in order to reduce thermal noise, which is increased by the radiation damage the pixel and microstrip detectors sustain due to their close proximity to the beam pipe.

The silicon pixel detector is located closest to the beryllium beam pipe, to utilize the fact that it has the best resolution of all ID subsystems. It is comprised of 3 barrel layers, the innermost of which has a distance to the nominal interaction point of 5 cm, and 3 wheels at each end. In $R-\phi\times z$, the smallest pixel size is $50\times 400\,\mu\mathrm{m}^2$, corresponding to spatial resolutions of $10\,\mu$m in $R-\phi$ and $115\,\mu$m in z, for the barrel region, or R, for the end-cap region.

The silicon microstrip detector consists of 4 barrel layers and 18 wheels. The microstrip layers are divided into strips $6.4\,\mathrm{cm}\times 80\,\mu$m large. Half of the barrel strip layers are longitudinally aligned to the beam axis, the other half are at an angle of $40\,\mu$rad w.r.t. the beam axis, and are alternated with the aligned strips. In the end-cap wheels, the microstrips are radially aligned with the beam axis, and half have a $40\,\mu$rad angle, as well. This design increases the

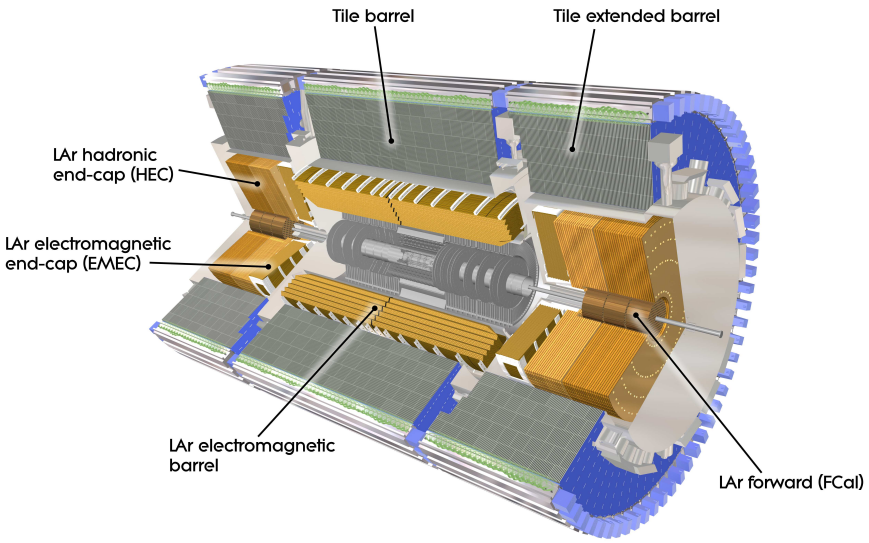

Figure 2.5: The ATLAS calorimeters. Taken from Ref. [70].

resolution of the silicon microstrip tracker to 17 μm in $R-\phi$ and a z resolution in the barrel or a R resolution in the end-caps of 580 μm.

The Transition Radiation Tracker (TRT) consists of straw tubes filled with a gas mixture of xenon, carbon dioxide, and oxygen. The straw tubes are interleaved with polypropylene, and cover the region $|\eta| < 2$. The diameter of the straw tubes is 4 mm, and a gold plated tungsten wire runs centrally through each straw tube. When a charged particle traverses the TRT, it locally ionizes the gas mixture in the tubes it passes through. The wires, acting as anodes, collect the ionization charges, generating an electronic signal. In the barrel region, the tubes are 144 mm long, with anodes segmented in two halves, and are aligned with the z-axis. In the end-cap, the tubes have a length of 37 cm. The TRT provides no measurement in z, but can greatly enhance the momentum resolution by typically yielding 36 hits per track in the transverse $R-\phi$ plane, in which the tracks are bent. The $R-\phi$ accuracy of a single straw signal is 130 μm.

The TRT furthermore provides electron identification information in addition to that provided by the calorimeters. The polypropylene filling the space between the straw tubes gives rise to transition radiation in the form of a y ray when a charged particle passes the boundary of the tube material and the polypropylene. Electrons can be distinguished from hadrons because the lower electron mass causes the signal from transiting electrons to be higher. The low energetic transition radiation signal is discriminated from the signal due to minimum ionising particles using hte much larger signal amplitude of transition radiation. The TRT is operated at room temperature.

The resolution of the combined charged track momentum measurement with the ID was measured to be $\sigma_{p_T}/p_T = (4.83 \pm 0.16) \times 10^{-4}\,\text{GeV}^{-1} \times p_T$, using data of cosmic rays traversing the ID [69].

2.2.3 Calorimeters

The ATLAS calorimeter is designed to completely stop incoming particles, such that they deposit all of their energy in the calorimeters. This allows measuring the energy of the incident particle by measuring the energy deposited when it was stopped. The calorimeter is constructed

as a sampling calorimeter, meaning it consists of alternating layers of absorber material and active material. The absorber material is dense and has a high atomic number Z, causing particles passing through to generate showers of secondary particles in their interactions with the absorber. These secondary particles then shower further themselves, and generate a signal in the active material by ionization or scintillation light.

The design of the ATLAS calorimeter is shown in Figure 2.5. The ATLAS calorimeter is 12 m long, has an outer diameter of 8.5 m, and covers the pseudorapidity range $|\eta| < 4.9$. It consists of three subsystems. The electromagnetic calorimeter, designed to absorb and measure the energy of photons and electrons, is the innermost part of the calorimeter, and described in Section 2.2.3.1. The hadronic calorimeter, designed to absorb and measure the energy of hadrons in the event, surrounds the electromagnetic calorimeter and is described in Section 2.2.3.2.

2.2.3.1 Electromagnetic Calorimeter

The electromagnetic calorimeter (ECAL) is optimized for the absorption of electrons and photons. Other particles will in general also deposit energy there, but will not lose all of it. It uses liquid argon as the active material, in which $1.113 - 1.54$ mm thick lead plates are immersed, acting as absorbers. The lead plates are interleaved with copper electrodes. Two electrodes are used to apply a high voltage, and the third electrode provides readout capabilities. The lead plates are shaped like an accordion, avoiding acceptance losses across the ϕ direction due to gaps.

High energy particles entering the ECAL start losing energy via pair production and bremsstrahlung, primarily in the lead absorber, generating a cascade of increasing numbers of particles with reduced energy. When the particles have sufficiently low energies, typically several MeV, they start losing most of their energy via the photoeffect and ionization. The ionisation charges in the liguid argon are made to drift by the $2000V$ voltage applied between the first second copper electrode. Capacitative coupling via the third copper electrode then generates an electronic signal.

The ECAL is segmented into a central barrel wrapped concentrically around the beam the solenoid magnet, and a forward and a backward end-cap. The barrel covers $|\eta| < 1.475$, the end-caps cover $1.375 < |\eta| < 3.2$. The ECAL barrel consist of 3 separately sampled segments at different radii, where the innermost segment has the highest cell granularity in η, ϕ and the outermost segment has the lowest. The ECAL encaps are similarly axially segmented into two separately sampled segments.

The energy resolution of the ECAL has been determined experimentally at test-beams, using electrons of known energy. The energy resolution in the ECAL end-caps has thus been found to be $12.1\%/\sqrt{E} \bigoplus 0.4\%$ [71], while the energy resolution of the ECAL barrel was found to be $10.1\%/\sqrt{E} \bigoplus 0.17\%$ [72].

2.2.3.2 Hadronic Calorimeter

The hadronic calorimeter (HCAL) is optimized for the apsorption of hadrons. These will typically lose only a fraction of their energy in the ECAL, because even if they are charged, their energy loss due to Bremsstrahlung is suppressed by their mass, which is much larger than the electron mass. Consequently the HCAL is optimized to induce hadrons such as protons, neutrons, pions and kaons to lose energy via inelastic nuclear interactions with the detector material.

The hadrons lose energy in spallation processes, which at high energies yields a cascade of nuclear fragments and secondary particles, forming a hadronic shower. As the hadron energies decrease and the multiplicity increases, the spallation processes tend to more frequently result hadrons traversing the nuclei, radiating more hadrons. The traversing hadron can also activate the nucleus into an excited state, that later relaxes via fission or evaporation. Since the average rate of nuclear interactions in a material is much lower than that of electromagnetic interactions, hadronic showers are deeper than electromagnetic ones. Finally, decays $\pi^0 \to \gamma\gamma$, causing electromagnetic showers, direct ionization or scintillation by charged hadrons, and indirect ionization by charged nuclei scattered by slow neutrons, allow measuring part of the deposited energy. However, the kinetic energy of escaping neutrinos and muons, as well as the activation energy of nuclei excited into long-lived higher energy states, are not detected.

The HCAL wraps around the ECAL. It comprises the central barrel covering and the extended barrel, together covering $|\eta| < 1.7$, two end-caps covering $1.5 < |\eta| < 3.2$ and two forward calorimeters, extend the coverage by $3.1 < |\eta| < 4.9$.

The central barrel and extended barrel are located far away from the beam pipe. Thus they are built from less radiation hard but cost effective material. They use iron plates as absorbers, alternating with scintillating paraterphenyl-doped polysterene tiles used as the active material. The 1.97 m thick central and extended barrels are built from 64 modules witha size of $\Delta\Phi$ 0.1. Wavelength-shifting fibres transport the scintillation light to the outside of the calorimeter, where photomultilpliers measure the scintillation light.

The HCAL end-caps and the forward calorimeter are closer to the beam line, thus they use liquid argon as the active material, and tungsten and copper plates as absorber. The readout is done by capacitative coupling to drifting ionization charges, like in the ECAL.

The energy resolution of the HCAL components was measured at test beams using pions. The tile calorimeter was found to have a resolution of $52.7\%/\sqrt{E} \bigoplus 5.7\%$ [73]. The HCAL end-caps were found to have a resolution of $70.6\%/\sqrt{E} \bigoplus 5.8\%$ [74]. The energy resolution of the forward calorimeter is $94.2\%/\sqrt{E} \bigoplus 7.5\%$ [75].

2.2.4 Muon System

Muons, being much heavier than electrons, lose only very little energy by bremsstrahlung in the atomic fields of the matter in the calorimeters. Furthermore, they do not couple with the strong nuclear force, so their cross section for interactions with nuclei are strongly suppressed when compared to hadrons in a similar mass range. Thus muons typically leave the calorimeters keeping most of their kinetic energy.

To identify muons originating from the interaction point, or secondary muons produced in interactions in the detector material, the ATLAS detector features a dedicated muon system. It is the outermost active part of the ATLAS detector. It is depicted in Figure 2.6. It comprises the Thin Gap Chambers (TGCs), the Resistive Plate Chambers (RPCs), the Cathode Strip Chambers (CSCs), and the Monitored Drift Tubes (MDT). The MDTs and CSCs provide precise tracking information for $2.7 < |\eta|$. The TGCs and the RPCs are used for fast triggers on muons in the region with $2.4 < |\eta|$.

The MDTs are three to eight layers of aluminium drift tubes with a diameter of 30 mm per tube. The drift tubes are filled with a gas mixture consisting of argon and carbon dioxide, at a pressure of 3 bar. A central tungsten- rhenium wire with a diameter of $50\,\mu$m functions as the anode. Charged particles passing through the drift tubes ionize the gas that fills them, and the ionization charges are collected at the anode wire, generating an electronic signal that indicates a hit. The resulting resolution in the direction of the beam is $35\,\mu$m.

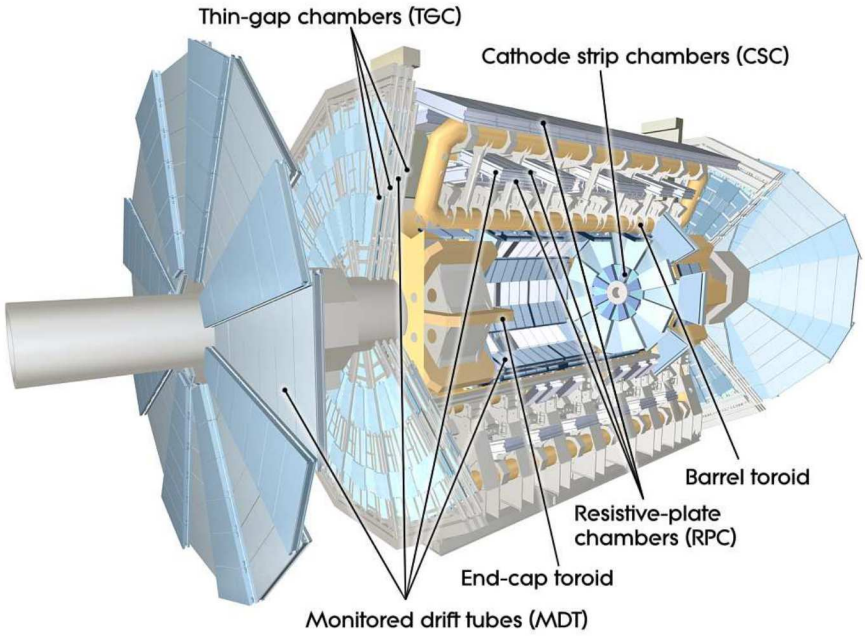

Figure 2.6: Cutaway view of the ATLAS muon system. Taken from Ref. [63]

The CSCs are multiwire proportional chambers. They are installed at $2.0 < |\eta| < 2.7$ in the innermost layer, where the rate and resolution requirements are highest, as dictated by the large expected rate of incident particles. The diameter of the segmented anode wires is $35\,\mu$m. The CSCs are filled with a gas mixture consisting of carbon dioxide and argon. The charges from gas that has been ionized by a passing charged particle are collected at the anodes and the timing and wire segment information are combined into localized hit information. The resulting resolution is $40\,\mu$m in the radial direction, and 5 mm in the direction transverse to the bending plane, i.e. the ϕ direction parallel to the toroid field.

The RPCs are parallel electrode plates spaced 2 mm apart, with a potential difference of 9.8 kV between them. They cover $|\eta| < 1.05$, in the barrel region. Muons passing through an RPC ionize the gas in the gap between the plates. The high field in the gap creates an avalanche of secondary ions and electrons that quickly create a large signal when they hit the electrode plates. The time resolution of these signals is 1.5 ns. Hit locations are measured with a resolution of 10 mm in the $z - \phi$ plane. The hit location information is used to supplement the tracking information of the MDTs and CSCs.

The TGCs are multiwire proportional chambers installed in the end-cap regions, covering the $1.05 < |\eta| < 2.7$ region. The distance between the electrodes is smaller than the distance from one anode wire to another, allowing quasi-saturated operation. The TGCs are filled with a highly quenching gas that is a mixture of carbon dioxide and n-pentane. The TGCs achieve a time resolution of 4 ns, and between $2 - 6$ mm in the $R - \phi$ plane.

The combined design resolution of the muon system is 10% at 1 TeV muon momentum. In practice, the muon momentum resolution is significantly improved by matching the tracks in the muon system to tracks in the ID [76].

2.2.5 Trigger

While running, the LHC delivers up to 4×10^7 bunch crossings per second, and tens of proton-proton interactions per bunch crossing are typical. However, only about a thousand full events per second can be written to the permanent data storage. Thus the event rate needs to be

reduced, which is the task of the trigger system. The trigger system reduces the event rate by selecting events that are deemed interesting, and rejecting events that are not. Several categories of interesting events are defined, such as events with a lepton candidate with a transverse momentum above a certain threshold, called a "single lepton p_T trigger" or a minimum amount of imbalance in the transverse momenta of the particles reconstructed in the event, called a "E_T^{miss} trigger". The ATLAS trigger system uses 2 consecutive stages, or levels. The stages operate at successively slower rates, allowing increasingly refined selections.

The first trigger stage is called the level 1 trigger. It reduces the rate of incoming events to the design rate of 100 kHz. The level 1 trigger is implemented in custom built hardware so that it can keep up with the incoming event rate. It uses partial information from the calorimeter and muon subsystems to coarsely reconstruct candidate muons, electrons, photons, jets, and hadronically decaying τ leptons, as well as total energy and missing transverse energy. If the transverse momenta of these objects or the energy sums exceed threshold values, the event is accepted. The decision to accept or reject events is taken within 2.5 μs. Accepted events are read out and then buffered, while being evaluated further in the second trigger stage.

The second trigger stage, called the high level trigger, evaluates events using the full granularity of the detector, but considers only certain regions of interest. Regions of interest are high occupancy regions, indicated by the level 1 trigger. Due to the reduced rate of incoming events, the level 2 trigger is implemented as software running on commercially available hardware. If an event is accepted by the high level trigger, it is written to permanent storage and is available to be used in later analyses. The design rate at which the high level trigger should accept events is 1 kHz.

There can be trigger items with low momentum or multiplicity thresholds that are physically interesting, but occur so frequently that accepting each such event would make the trigger system exceed the design acceptance rates. In such cases, the corresponding triggers are prescaled, meaning that only a fraction of the events passing the trigger requirement are accepted. A trigger that is prescaled with prescale S accepts only one out of S events that satisfy its conditions.

2.3 Luminosity

The instantaneous luminosity of a particle collider is a measure of the rate at which collisions occur. It can be calculated from the number of bunches n_B, the particles per bunch $N_{1,2}$ in the bunches of beams $1, 2$, the revolution frequency of the beams f and the cross sectional area of the beams A:

$$L = \frac{n_b N_1 N_2 f}{A} \,. \tag{2.1}$$

The corresponding integrated luminosity $L_{int} \int_{t_0}^{t_1} L\mathrm{d}t$ is a measure of the number of collisions that occured in the time interval $[t_0, t_1]$. The concept of luminosity is useful because it decouples the observed number of events with a certain final state n_{process}, which is specific to the collider and the running conditions, from the probability for a process to occur given that a collision happened:

$$\sigma_{\text{process}} = n_{\text{process}} / L_{int} \,, \tag{2.2}$$

which is called the production cross section of the process.

In order to determine production cross sections using Equation (2.2), the luminosity needs to be measured. This is done using several forward detectors providing relative and absolute

measurements of the bunch-wise instantaneous luminosity. The Beam Conditions Monitor (BCM) [77] and the LUCID detector are examples of detectors providing relative luminosity measurements, the ALFA detector is an example providing an absolute measurement.

The BCM is located 1.84 m up- and downstream of the interaction point [77]. At both points it consists of 4 diamond sensors with a cross sectional detector area of $1cm^2$, arranged in a cross pattern around the beam pipe at a radius of 5.5 cm. The relative luminosity is measured by the rate at which particles traversing the material induce ionisation.

The LUCID detector is located ± 17 m up and down from the interaction point. At each point a module c containing 16 gas-filled tubes with diameter of 15 mm and a length of 1.5 m, enclosing the beam axis. Particles passing through the tubes generate Cherenkov light. Photomultiplier tubes measure the Cherenkov light. Again, the rate at which particles are detected serves as an indicator of the relative luminosity.

The ALFA detector is placed ± 240 m from the interaction point. At both locations, scintillating fibre trackers are installed inside roman pots that can be moved uo to 1 mm close to the beam, inside the beam pipe. For the absolute luminosity measurements, special LHC runs are performed, during which the roman pots are deployed, allowing measurements of the rate of elastic proton scattering at angles smaller than he nominal beam divergence. This allows determining the total cross section from the measured elastic forward scattering cross section via applying the optical theorem. By then applying Equation (2.2), an absolute luminosity measurement can be performed, allowing the calibration of the relative measurements obtained by LUCID and the BCM during regular LHC runs.

It is not necessary to use ALFA to obtain an absolute luminosity measurement for calibration. Instead the other detectors can also calibrate their interaction rate measurements to the luminosity using displacement scans, in a technique initially developed by van der Meer [78] to determine the Luminosity at the Intersecting Storage Rings (ISR) at CERN. During a displacement scan the two beams are vertically (horizontally) displaced at different subsequent displacements. By monitoring the change in the observed interaction rates as a function of the displacement, one can extract the beam profile, either (as done at the LHC) by a simple fit of the beam profiles [79], or (as proposed by van-de-Meer for the ISR), by considering a suitable ratio of displacement-integrated observed rates [78, 80]. With the beam profile known, Equation (2.1) can be used to calculate the luminosity, as f and n_b are known operational parameters, and the N_i can be determined by measuring the beam currents using pickup electrodes placed in close proximity to the beam.

Chapter 3

ATLAS Search for Dark Matter in Association with a Higgs Boson Decaying to Two b Quarks

This chapter describes the ATLAS search for events where a Higgs boson is produced in association with Dark Matter, and the Higgs boson decays to a b quark pair, which is its most common decay channel in the SM [2, 17]. The Higgs boson is assumed to be and consistent with the 125 GeV scalar observed by the ATLAS and CMS collaborations at the LHC [19, 21]. The Dark Matter can not be observed directly in the ATLAS detector, but can be inferred from the presence of missing transverse momentum (E_T^{miss}). Thus the search for $h(\rightarrow \bar{b}b$ + Dark Matter production is a search for an excess of events in the $h(b\bar{b}) + E_T^{\text{miss}}$ signature.

A potential excess of $h(b\bar{b}) + E_T^{\text{miss}}$ events would be very unlikely to be due to Initial State Radiation (ISR) of Higgs bosons, in contrast to e.g. jets in the jet + E_T^{miss} signature. This is because the Yukawa coupling of the Higgs bosons to quarks is proportional to the mass of the quarks, and since the masses of the quark species present in protons at LHC energies are small, so are the couplings [17]. Since ISR contributions to $h(b\bar{b}) + E_T^{\text{miss}}$ are suppressed, potential signals are due to Higgs couplings not to initial state quarks or gluons, but to the BSM states that mediate the SM-Dark Matter interaction [2]. Thus the $h(b\bar{b}) + E_T^{\text{miss}}$ signature directly probes potential new physics couplings. This is especially interesting when considering WIMP interpretations of Dark Matter, as Dark Matter states coupled to EW states naturally have weak couplings.

3.1 Analysis Overview

The analysis uses 36 fb^{-1} of pp collisions at $\sqrt{s} = 13$ TeV recorded with the ATLAS detector during Run 2 of the LHC in 2015 and 2016 [2]. Signal candidate events are triggered by a E_T^{miss} trigger, and the leptons and jets observed in the event are reconstructed as described in Section 3.3. The background contributions, described in Section 3.2, are simulated with samples of Monte Carlo events [2, 81]. A set of selection requirements, described in Section 3.4, is applied to the reconstructed events to supress the SM backgrounds, and the effect of these requirements is studied using simulated samples. The cuts strongly reduce the multijet contribution, but the other backgrounds give rise to a large number of events after the cuts. To account for the remaining expected background events, control regions are defined by requiring additional leptons in the event, as detailed in Section 3.4. Samples of hypothetical signal events are simulated using a signal model called the Z'-2HDM [82, 2, 81]. A simultaneous

fit of signal and backgrounds to the invariant mass of the Higgs candidate across signal and control regions is performed. The fit uses the different Higgs candidate mass distributions to further discriminate signal and background, to transfer the background yield constraints from the control regions into the signal region, and to determine the yield of $h(\rightarrow b\bar{b})$+ Dark Matter events compatible with the observed events. The fit is described in Section 3.5. Finally, the fit results are interpreted as limits on the $h(b\bar{b}) + E_T^{\text{miss}}$ production cross section, as described in Section 3.5.

3.2 Background Processes

There are several SM background processes contributing to the $h(b\bar{b}) + E_T^{\text{miss}}$ signature at ATLAS. The three dominant backgrounds are [2]

- $Z(\rightarrow \nu\bar{\nu})$+jets production, where the invisible Z decay gives rise to real E_T^{miss} and the jets are falsely identified as the products of a $h \rightarrow b\bar{b}$ decay. Depending on the E_T^{miss} region, this background contributes $30\% - 60\%$ of the events expected in the signal region.
- $W(\rightarrow \ell\nu)$ + jets production, where there is real E_T^{miss} due to the invisible ν, the ℓ is misreconstructed or lost, and the jets are falsely identified as the products of a $h \rightarrow b\bar{b}$ decay. Depending on the E_T^{miss} region, this background contributes $10\% - 25\%$ of the events expected in the signal region.
- $t\bar{t}$ production, where $t\bar{t} \rightarrow WbWb$ can give rise to real E_T^{miss} from neutrinos from leptonic W decays, and there are actual B hadrons present due to the b quarks from the t decays, giving rise to falsely identified $h \rightarrow b\bar{b}$ candidates. Depending on the E_T^{miss} region, this background contributes $15\% - 50\%$ of the events expected in the signal region.

Besides these three dominant backgrounds, there are also sub-dominant backgrounds contributing [2]:

1. associated Vh production with $V = W, Z$, where e.g. the $Z(\rightarrow \nu\bar{\nu})h(\rightarrow b\bar{b})$ is an irreducible background.
2. associated VV production with $V = W, Z$ ("di-boson production"), where e.g. $Z(\rightarrow b\bar{b})Z(\rightarrow \bar{\nu}\nu)$, which can only distinguished from the signal using the invariant mass of the $b\bar{b}$ candidate.
3. production of single top quarks
4. QCD production of multiple jets, called "multijet" background [2], which can contribute due to jet mismeasurements giving rise to fake E_T^{miss}.

3.3 Object Reconstruction

This Section gives an outline of the reconstruction of the main event properties used in the search for $h(b\bar{b}) + E_T^{\text{miss}}$ in Ref. [2].

The Primary Vertex (PV) is the vertex which has the largest squared sum of associated transverse track momenta [2]. Here vertices are intersection of Inner Detector (ID) tracks extrapolated to the beam spot.

Jets are clustered from topologoical clusters of calorimeter cells, using the anti-k_t clustering algorithm [83, 84, 2]. *Large-R jets* are clustered using a radius parameter of $R = 1.0$ and trimmed [85] to reduce the effects of pileup and the underlying event [2]. *Small-R jets* are clustered using a radius parameter of $R = 0.4$ [2]. *Track-jets* are not clustered from calorimeter cells, but from tracks in the ID matched to the PV, using a radius parameter of $R = 0.2$ [2]. Jets are called "central" when the total momentum vector of the jet has a pseudorapidity of $|\eta| < 2.5$. A small-R or track-jet is said to be "b-tagged" [2] when the jet is identified as being likely to contain B-hadrons with multivariate algorithms detailed in Ref. [86].

Muon candidates are constructed from tracks or track segments in the muon spectrometer that match tracks in the ID. They are required to satisfy the "loose" identification criteria from Ref. [76], have $|\eta| < 2.7$ and be isolated in the sense that the sum of p_T for tracks within a cone of ΔR around the muon is limited, as described in Ref. [76].

Electron candidates are constructed from tracks in the ID matched to clusters of energy deposits in the calorimeter, required to fulfill "loose" identification criteria of Ref. [87], and need to be isolated in the sense that the sum of p_T for tracks within a cone of ΔR around the electron is limited, as described in Ref. [87].

The E_T^{miss} observable of an event is calculated as the negative vector sum of the transverse momenta of all electron, muon, and jet candidates and all tracks in the ID not associated to a candidate object [2]. Furthermore, the $p_T^{\text{miss,tracks}}$ observable is similarly defined as the negative vector sum of the p_T of all tracks in the ID that are associated to the PV and have $|p_T| > 0.5\,\text{GeV}$ and $|\eta| < 2.5$ [2].

3.3.1 The $h \to b\bar{b}$ Candidate and its Mass

In signal events, the $h \to b\bar{b}$ candidate is expected to recoil back-to-back to Dark Matter particles, i.e to the E_T^{miss}. Thus the E_T^{miss} and the p_T of the Higgs candidate should be balanced in signal-like events, and the E_T^{miss} is a measure of the Higgs p_T. Consequently, the $b\bar{b}$ daughters of the Higgs are seperated by about $\Delta R(b,\bar{b}) \approx \frac{2m_h}{E_T^{\text{miss}}}$. Thus, when the E_T^{miss} is small, the angular separation is large, and the two jets corresponding to the two b's of the $h \to b\bar{b}$ are reconstructed as two separated small-R jets [2], as described in Section 3.3.1.1. Conversely, if the E_T^{miss} is large, the angular separation is small, and the two jets from the $h \to b\bar{b}$ decay have significant overlap. In this case, the Higgs is reconstructed as a single large-R jet [2], as described in Section 3.3.1.2.

3.3.1.1 In the Resolved Regime

If the $E_T^{\text{miss}} < 500\,\text{GeV}$, the event is said to be in the "resolved regime" and the Higgs candidate is reconstructed as two small-R jets [2]. If there are two b-tagged small R jets originating from the PV, the Higgs candidate is reconstructed from these two. If there is only one central b tagged small R jet originating from the PV, the Higgs candidate is reconstructed from the b-tagged small-R jet and the highest p_T ("leading") non-b-tagged central small-R jet originating from the PV. In either case, the invariant mass of the dijet system is taken as the mass of the Higgs candidate.

Table 3.1: Summary of the main event selection criteria [2].

Region	SR	1μ-CR	2ℓ-CR
Trigger	$E_{\mathrm{T}}^{\mathrm{miss}}$	$E_{\mathrm{T}}^{\mathrm{miss}}$	Single lepton
Leptons	No e or μ	Exactly one μ	Exactly two e or μ 83 GeV $< m_{ee} <$ 99 GeV 71 GeV $< m_{\mu^{\pm}\mu^{\mp}} <$ 106 GeV
Resolved	$E_{\mathrm{T}}^{\mathrm{miss}} \in [150, 500)$ GeV $p_{\mathrm{T}}^{\mathrm{miss,trk}} > 30$ GeV (1 b-tag only) $\min\left[\Delta\phi\left(\vec{E}_{\mathrm{T}}^{\mathrm{miss}}, \vec{p}_{\mathrm{T}}^{j}\right)\right] > \pi/9$ $\Delta\phi\left(\vec{E}_{\mathrm{T}}^{\mathrm{miss}}, \vec{p}_{\mathrm{T}}^{\mathrm{miss,trk}}\right) < \pi/2$ –	$p_{\mathrm{T}}(\mu, E_{\mathrm{T}}^{\mathrm{miss}}) \in [150, 500)$ GeV $p_{\mathrm{T}}(\mu, \vec{p}_{\mathrm{T}}^{\mathrm{miss,trk}}) > 30$ GeV $\min\left[\Delta\phi\left(\vec{E}_{\mathrm{T}}^{\mathrm{miss}}, \vec{p}_{\mathrm{T}}^{j}\right)\right] > \pi/9$ $\Delta\phi\left(\vec{E}_{\mathrm{T}}^{\mathrm{miss}}, \vec{p}_{\mathrm{T}}^{\mathrm{miss,trk}}\right) < \pi/2$ –	$p_{\mathrm{T}}(\ell, \ell) \in [150, 500)$ GeV – – – $E_{\mathrm{T}}^{\mathrm{miss}} \times \left(\sum_{\mathrm{jets,leptons}} p_{\mathrm{T}}\right)^{-1/2} < 3.5\ \mathrm{GeV}^{1/2}$
	Number of central small-R jets ≥ 2 Leading Higgs candidate small-R jet $p_{\mathrm{T}} > 45$ GeV $H_{\mathrm{T},2j} > 120$ GeV for 2 jets, $H_{\mathrm{T},3j} > 150$ GeV for > 2 jets $\Delta\phi\left(\vec{E}_{\mathrm{T}}^{\mathrm{miss}}, \vec{p}_{\mathrm{T},h}\right) > 2\pi/3$ Veto on τ-leptons $\Delta R\left(\vec{p}_{h}^{\,j_1}, \vec{p}_{h}^{\,j_2}\right) < 1.8$ Veto on events with > 2 b-tags Sum of p_{T} of two Higgs candidate jets and leading extra jet $> 0.63 \times H_{\mathrm{T,all\,jets}}$ b-tagging : one or two small-R calorimeter jets **Final discriminant = Dijet mass**		
Merged	$E_{\mathrm{T}}^{\mathrm{miss}} \geq 500$ GeV $p_{\mathrm{T}}^{\mathrm{miss,trk}} > 30$ GeV $\min\left[\Delta\phi\left(\vec{E}_{\mathrm{T}}^{\mathrm{miss}}, \vec{p}_{\mathrm{T}}^{j}\right)\right] > \pi/9$ $\Delta\phi\left(\vec{E}_{\mathrm{T}}^{\mathrm{miss}}, \vec{p}_{\mathrm{T}}^{\mathrm{miss,trk}}\right) < \pi/2$	$p_{\mathrm{T}}(\mu, E_{\mathrm{T}}^{\mathrm{miss}}) \geq 500$ GeV $p_{\mathrm{T}}(\mu, \vec{p}_{\mathrm{T}}^{\mathrm{miss,trk}}) > 30$ GeV $\min\left[\Delta\phi\left(\vec{E}_{\mathrm{T}}^{\mathrm{miss}}, \vec{p}_{\mathrm{T}}^{j}\right)\right] > \pi/9$ $\Delta\phi\left(\vec{E}_{\mathrm{T}}^{\mathrm{miss}}, \vec{p}_{\mathrm{T}}^{\mathrm{miss,trk}}\right) < \pi/2$	$p_{\mathrm{T}}(\ell, \ell) \geq 500$ GeV – – –
	Number of large-R jets ≥ 1 Veto on τ-lepton not associated to large-R jet Veto on b-jets not associated to large-R jet H_{T}-ratio selection (<0.57) b-tagging : one or two ID track jets matched to large-R jet **Final discriminant = Large-R jet mass**		

3.3.1.2 In the Merged Regime

If the $E_T^{\mathrm{miss}} \geq 500\,\mathrm{GeV}$, the event is said to be in the "merged regime" and the Higgs candidate is reconstructed as the leading large-R jet originating from the PV [2]. The large-R jet is required to contain one or two b-tagged track jets. The mass of the Higgs candidate is the combined mass, i.e. the resolution-weighted mean of the mass of the large-R jet determined using only calorimeter information, and the track-assisted mass [88, 2]. The track-assisted mass is calculated by determining the jet mass using the associated ID tracks, which have a superior angular resolution compared to calorimeter clusters, and then scaling it by the ratio of the total associated calorimeter-measured p_T to the total associated ID-track based p_T, thus accounting for the neutral jet component that is not included in the track based mass measurement [88].

3.4 Event Selection

This Section discusses some of the main event selection criteria of Ref. [2]. An overview is provided in Table 3.1. The selections are applied to select events consistent with the $h(b\bar{b}) + E_T^{\mathrm{miss}}$ signature, and reject background events, defining the signal region. To constrain the backgrounds remaining in data after the cuts, control regions are defined. Signal and control

regions are defined by the number of isolated muons or electrons in the event. In the signal region, described in Section 3.4.1, there are no isolated muons or electrons. In the single muon control region, described in Section 3.4.2 ,there is exactly one isolated muon in the event. In the two lepton control region, described in Section 3.4.3, there is either a muon pair or an electron pair in the event.

The signal and control regions are further subdivided by the number of b-tagged jets in the event. This is done because the backgrounds contribute differently to the selection with one b-tagged jet compared to that with two b-tagged jets, as a result of different expected numbers of true B- hadrons. Finally, the signal and control regions with either one or two b-tagged jet are further subdivided into four bins of E_T^{miss}. The three lowest E_T^{miss} bins $[150\,\text{GeV}, 200\,\text{GeV}), [200\,\text{GeV}, 350\,\text{GeV}), [350\,\text{GeV}, 500\,\text{GeV})$ correspond to the resolved regime, and the final E_T^{miss} bin $E_T^{\text{miss}} > 500\,\text{GeV}$ corresponds to the merged regime. Thus, depending on lepton multiplicity, b-tag multiplicity, and E_T^{miss} bin, an event can be selected into one of 8 orthogonal signal regions.

3.4.1 Signal Region

Events are selected by a E_T^{miss} trigger [89], operating at a threshold of 110 GeV or less. Events with $E_T^{\text{miss}} < 150\,\text{GeV}$ are not accepted in the offline analysis. Events with isolated electrons or muons as defined in Section 3.3 are vetoed.

Contributions due to the multijet background can bypass the E_T^{miss} cuts and enter the selection only when one or more jets are mismeasured. This contribution is effectively suppressed [2] by

- rejecting events where $\Delta\Phi(E_T^{\text{miss}}, p_T^j) < \frac{\pi}{9}$ for any of the three leading small-R jets, i.e. mismeasurements of the p_T of the leading jets ,
- rejecting events where $\Delta\Phi(E_T^{\text{miss}}, p_T^{\text{miss,tracks}}) \geq \frac{\pi}{2}$, i.e. events where the E_T^{miss} direction has been mismeasured, and
- rejecting events with only one central b-tagged small-R jet if $p_T^{\text{miss,tracks}} < 30\,\text{GeV}$.

3.4.1.1 Requirements Unique to the Resolved Regime

In the resolved regime, where $E_T^{\text{miss}} < 500\,\text{GeV}$, the back-to-back topology expected in the signal process is enforced by requiring that the azimuthal angular distance $\Delta\Phi(E_T^{\text{miss}}, p_T^h)$ between the E_T^{miss} and theHiggs candidate dijet system is larger than $\frac{2\pi}{3}$. The $\bar{t}t$ background is reduced by requiring the following:

- Reject events containing τ lepton candidates. τ candidates are vetoed both if they fulfill the loose τ identification working point of a boosted decision tree trained to identify τ leptons [90], or if they are identified as small-R jets containing 1-4 tracks within the jet core and $\Delta\Phi(E_T^{\text{miss}}, p_T^j) < \frac{\pi}{8}$.
- Reject events with more than 2 central b-tagged small-R jets .
- Events need to have a scalar sum of the transverse momenta (H_T) of the Higgs candidate and a potential additional leading small-R jet that is larger than 0.63 times the scalar sum of the transverse momenta of all jets in the event. This selects topologies where the Higgs candidate is momentum-balanced by the E_T^{miss}, instead of other jets [91].

- The angular distance $\Delta R(p_h^{j_1}, p_h^{j_2})$ of the two small-R jets that constitute the Higgs candidate needs to be smaller than 1.8, enforcing that the Higgs candidate jets are not back to back to each other, which is indicative of $t\bar{t}$ decays.

3.4.1.2 Requirements Unique to the Merged Regime

In the merged regime where $E_T^{\text{miss}} \geq 500\,\text{GeV}$, a different set of requirements is implemented to reduce the impact of the $\bar{t}t$ background:

- Events with τ candidates are rejected unless the τ candidate lies within the Higgs candidate large R jet.
- Events with central b tagged small-R jets that are not associated to the large-R Higgs candidate are rejected.
- Events need to have a scalar sum of the small-R jets outside of the large-R Higgs candidate that is smaller than 0.57 times the that sum added to the p_T of the Higgs candidate, again rejecting $t\bar{t}$-like topologies [91].

3.4.2 Single Muon Control Region

The single muon control region is constructed to constrain the $W+\text{jets}$, $t\bar{t}$ and diboson backgrounds in the signal region. Events in the single muon control region are triggered and selected as in the signal region, except for the following differences:

- exactly one isolated μ candidate with $p_T^{\mu} > 27\,\text{GeV}$ in the event is required
- use the transverse momentum of the combined E_T^{miss} and p_T^{μ} system in place of E_T^{miss}

3.4.3 Lepton Pair Control Region

The two lepton control region is constructed to constrain the $Z+\text{jets}$ and diboson backgrounds. Its selections mirror those in the signal region, with the following differences:

- events are selected using single lepton p_T triggers [89]
- either exactly two isolated e candidates or one isolated $\mu^+\mu^-$ pair is required
- the mass of the lepton pair is required to be in the Z mass window: $83\,\text{GeV} < m_{ee} < 99\,\text{GeV}$ or $71\,\text{GeV} < m_{\mu^\pm\mu^\mp} < 106\,\text{GeV}$.
- in the resolved regime ($E_T^{\text{miss}} < 500\,\text{GeV}$), $\frac{E_T^{\text{miss}}/\,\text{GeV}}{\sqrt{\sum_{\text{small}-R\,\text{jets}} p_T^j/\,\text{GeV}}} < 3.5$, to ensure that $Z+\text{jets}$ and not $\bar{t}t$ events are selected.

3.5 Fit

To extract the cross section of a potential signal, the simulated signal and background Higgs candidate mass distributions are fit to the Higgs candidate mass distribution observed in data [2]. In the single muon control region the muon charge is used as the fit discriminant instead of the Higgs candidate mass, and in the two lepton control region, only the total event yield in

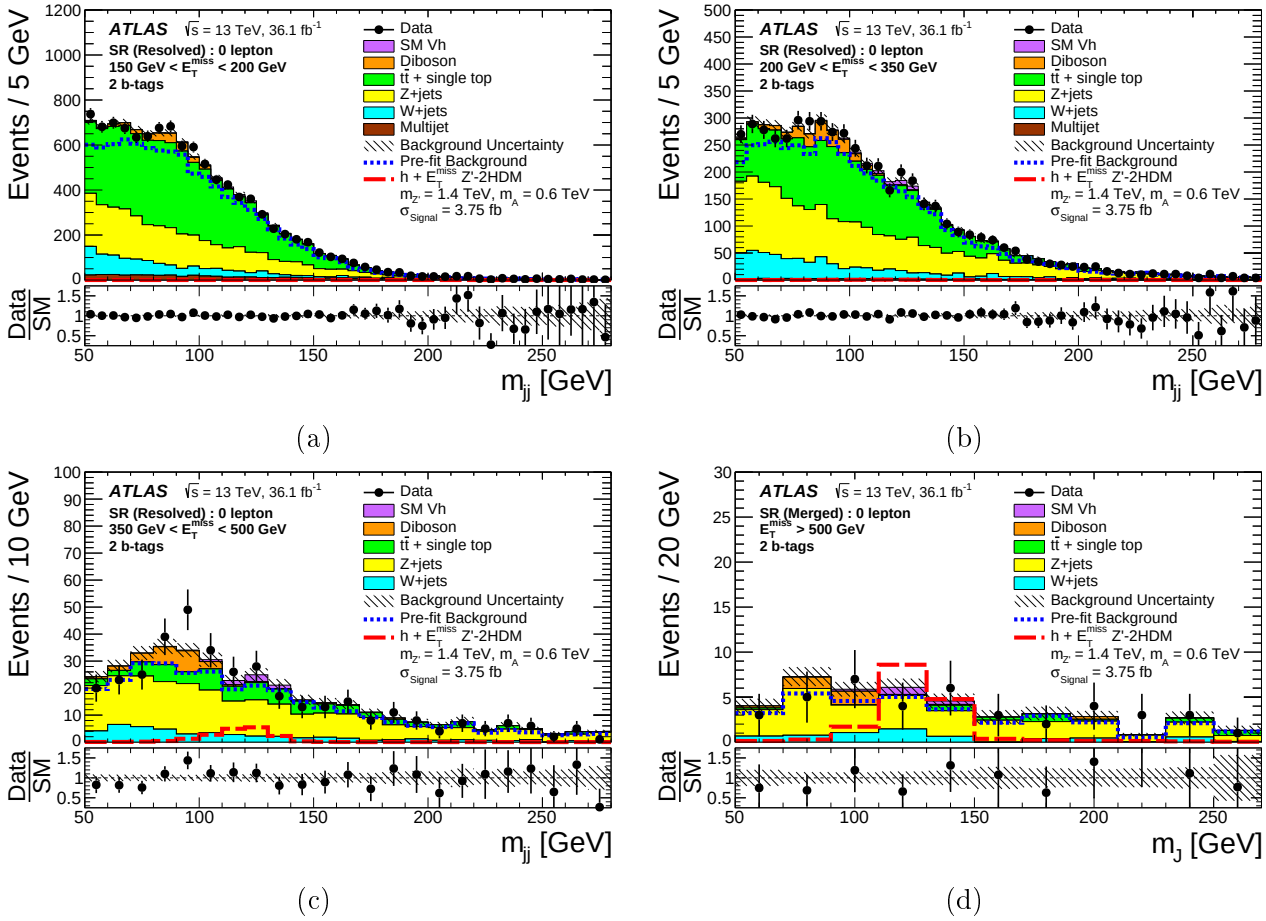

Figure 3.1: Distribution of the invariant mass of the Higgs candidate in the signal region, for two b-tags. The signal region is split according to the observed E_T^{miss} ($150\,\text{GeV} - 200\,\text{GeV}$ in (a), $200\,\text{GeV} - 350\,\text{GeV}$ in (b), $350\,\text{GeV} - 500\,\text{GeV}$ in (c), and $> 500\,\text{GeV}$ in (d)). The upper panels show a comparison of data to the SM expectation before (dashed lines) and after the fit (solid histograms) with no signal included. The lower panels display the ratio of data to SM expectations after the fit, with its systematic uncertainty considering correlations between individual contributions indicated by the hatched band. The expected signal from a representative Z'-2HDM model is also shown (long-dashed line). Taken from Ref. [2].

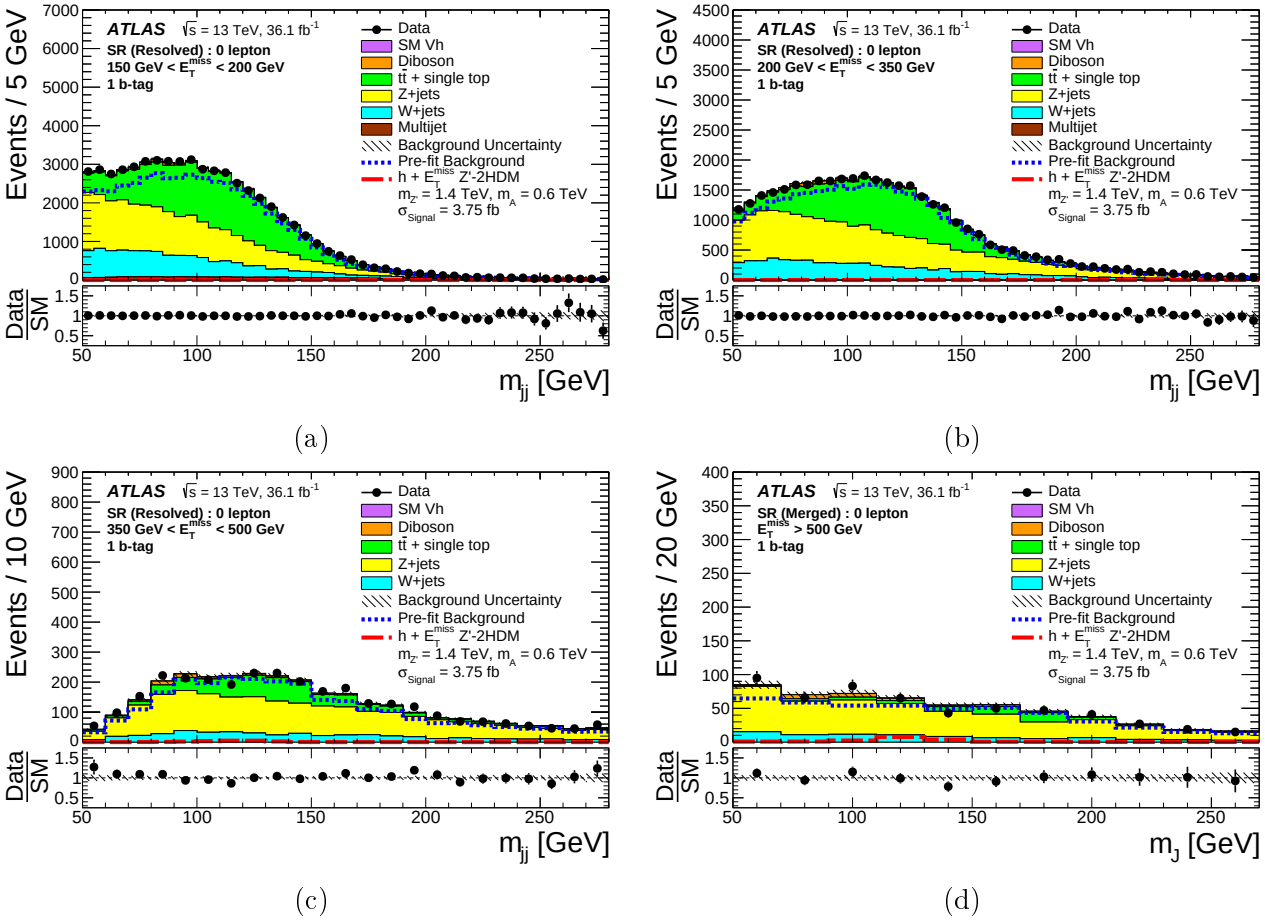

Figure 3.2: Distribution of the invariant mass of the Higgs candidate in the signal region, for one b-tag. The signal region is split according to the observed E_T^{miss} ($150\,\text{GeV} - 200\,\text{GeV}$ in (a), $200\,\text{GeV} - 350\,\text{GeV}$ in (b), $350\,\text{GeV} - 500\,\text{GeV}$ in (c), and $> 500\,\text{GeV}$ in (d)). The upper panels show a comparison of data to the SM expectation before (dashed lines) and after the fit (solid histograms) with no signal included. The lower panels display the ratio of data to SM expectations after the fit, with its systematic uncertainty considering correlations between individual contributions indicated by the hatched band. The expected signal from a representative Z'-2HDM model is also shown (long-dashed line). Taken from Ref. [2].

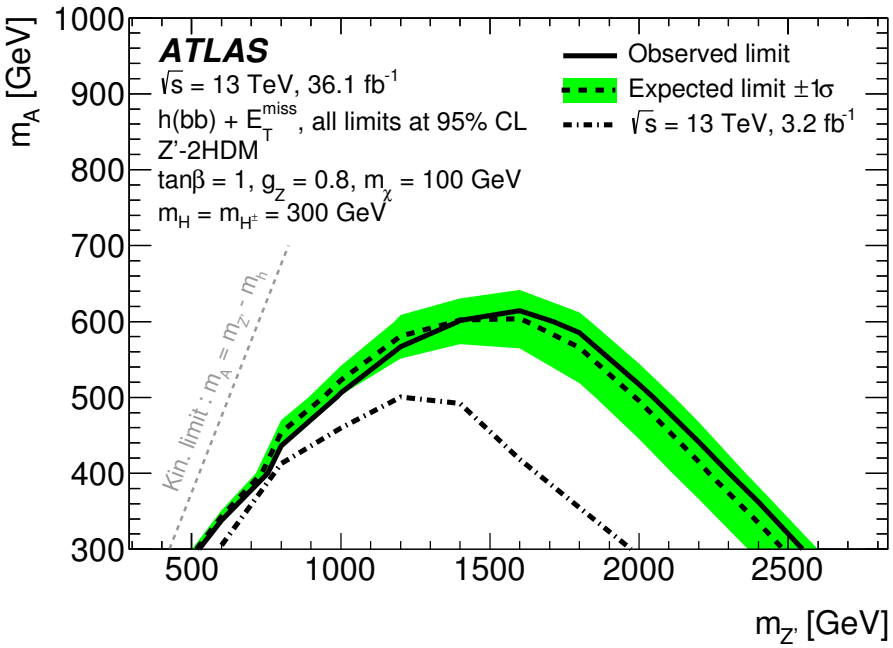

Figure 3.3: 95% C.L. CL_s exclusion contours for the $Z'-$2HDM simplified model in the plane of the $m_{Z'}, m_A$ parameters. Taken from Ref. [2].

the respective m_{ee} or $m_{\mu^\pm\mu^\mp}$ mass window is used because the number of data events in this region is too low for shape discrimination. The fit to the data is performed simultaneously across all signal and control regions in the analysis. The pre- and post- fit background, signal and data m_{bb} distributions in the signal region are shown in Figures 3.1 and 3.2.

The fit is a binned maximum likelihood fit [2], i.e. it adjusts the signal cross section to maximise the likelihood of the observed Higgs candidate mass distribution histograms given a signal cross section. The likelihood incorporates systematic uncertainties such as the yields of sub-dominant ackgrounds as nuisance parameters, i.e. by extending the likelihood by the prior probability distributions of the nuisance parameters. For the yields of the dominant Z+jets,W+jets, and $t\bar{t}$ backgrounds a flat prior is assumed, such that their yields are constrained using only data. The likelihood is then profiled [92, 2], meaning that the nuisance parameters are replaced by their maximum likelihood estimate given some signal cross section. The resulting profile likelihood is then only a function of the signal cross section. Upper limits on the signal cross section are then calculated based on the maximum likelihood estimates of signal yield and nuisance parameters using approximate likelihood ratio formulas. The approximate likelihood ratio formulas use a single simulated sample as the Asimov representative [93] of the wider ensemble it is a member of [92]. Figure 3.3 shows the resulting limits on the $m_{Z'}, m_A$ parameters of the $Z'-$2HDM used as a signal model.

3.5.1 Generic Limits with Reduced Model Dependence

An effort is made to provide limits corresponding to the generic signature of a Higgs boson being produced back to back with E_T^{miss} from Dark Matter with a minimal dependence on further model assumptions [2]. To this end a series of four individual fits to only one of the four different E_T^{miss} bins in the signal region is performed [2]. For each E_T^{miss} bin, several signal models are fitted. In each bin, the weakest individual limit $\sigma_{\text{fit}}(h + \text{DM})$ for any model fitted

Table 3.2: Generic limits on $h(bb)$+ Dark Matter production. Shown are the observed (obs) and expected (exp) 95% C.L. limits on the visible Dark Matter production cross section as defined in Equation (3.1), and the probability $\mathcal{A} \times \epsilon$ to reconstruct and select an event in the same E_T^{miss} bin as generated. Taken from Ref. [2].

Range in $E_{\text{T}}^{\text{miss}}$ [GeV]	$\sigma^{\text{obs}}_{\text{vis},h(b\bar{b})+\text{DM}}$ [fb]	$\sigma^{\text{exp}}_{\text{vis},h(b\bar{b})+\text{DM}}$ [fb]	$\mathcal{A} \times \varepsilon$ [%]
[150, 200)	19.1	$18.3^{+7.2}_{-5.1}$	15
[200, 350)	13.1	$10.5^{+4.1}_{-2.9}$	35
[350, 500)	2.4	$1.7^{+0.7}_{-0.5}$	40
[500, ∞)	1.7	$1.8^{+0.7}_{-0.5}$	55

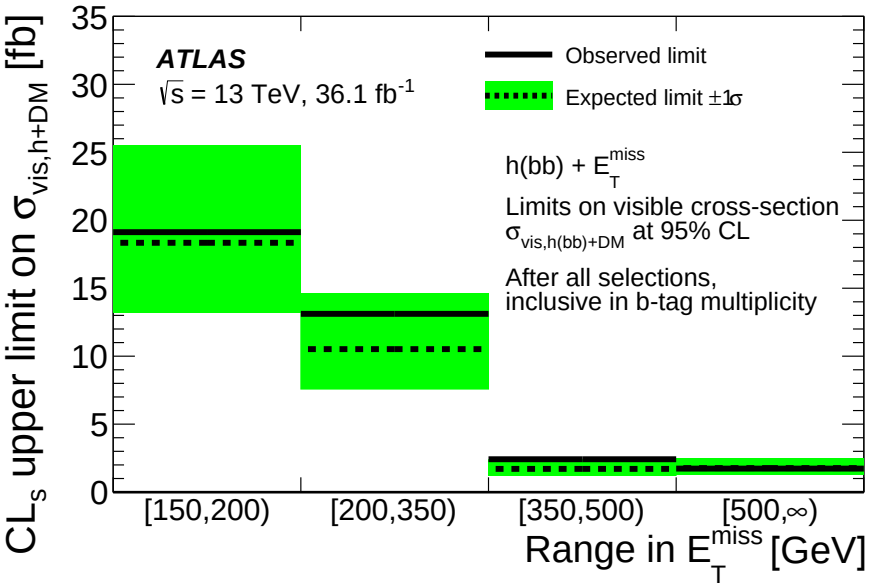

Figure 3.4: Graphical representation on the generic limit on the visible $h(bb)+$ Dark Matter production cross section in Table 3.2. Taken from Ref. [2].

to that bin is interpreted as a limit on the visible $h(bb) + \text{DM}$ production cross section,

$$\sigma_{\text{vis}}(h(bb) + \text{DM}) \equiv \sigma_{\text{fit}}(h + \text{DM}) \times \mathcal{BR}(h \to b\bar{b}) \times \mathcal{A} \times \epsilon\,, \tag{3.1}$$

where $\mathcal{BR}(h \to b\bar{b})$ is the SM $h \to b\bar{b}$ branching fraction, and the acceptance times efficiency $\mathcal{A} \times \epsilon$ is the probability that a signal event generated in a given E_T^{miss} bin is detected and reconstructed in that same E_T^{miss} bin [2]. In each E_T^{miss} bin, the weakest limit and the lowest $\mathcal{A} \times \epsilon$ among the results of all the fitted models are used. This choice reduces the dependence on the specific model kinematics, and makes the results somewhat conservative. The resulting limits with reduced model dependence are shown in Table 3.2 and Figure 3.4. These limits with reduced model dependence will be used in Chapter 7 to obtain simple estimates of the acceptance and sensitivity of the $h(b\bar{b}) + E_T^{\text{miss}}$ analysis from Ref. [2] to a new signal model, the 2HDM+a.

Chapter 4

The Two-Higgs-Doublet Model with a Pseudoscalar Dark Matter Mediator

This chapter provides an introduction to the Two-Higgs-Doublet Model with Pseudoscalar Mediator (2HDM+a). After giving a general overview of the model in Section 4.1, existing indirect constraints on the 2HDM+a parameter space are discussed in Section 4.2. Finally Section 4.3 introduces the basic features and terminology of the $h(b\bar{b}) + E_T^{\text{miss}}$ signature in the 2HDM+a which will be used and referred to repeatedly in Chapters 6 and 7.

4.1 Overview

The model studied here is the 2HDM+a in the form described in [1]. This simplified model for Dark Matter is a combination of three model ingredients:

- A Two-Higgs-Doublet model (2HDM) extension of the SM Higgs sector, described in Sections 4.1.1 and 4.1.2.
- A self-interacting dark sector with a massive Dirac fermion as a Dark Matter candidate and a pseudoscalar coupling to the Dark Matter candidate, described in Section 4.1.3.
- A set of portal terms giving rise to mixing between the pseudoscalar from the 2HDM and the pseudoscalar from the dark sector, described in Section 4.1.4.

A model of this kind is first constructed in Ref. [94] as a renormalizable interpretation for the galactic center GeV excess (see e.g. [36] and references therein) assuming it originates from Dark Matter annihilation. With a slightly simplified potential for the pseudoscalar mediating the Dark Matter self-interaction, the model is later studied in Ref. [95] with a focus on potential collider phenomenology, particularly the possibility of resonant $h + E_T^{\text{miss}}$ and $Z + E_T^{\text{miss}}$ signatures, which simpler (axial-) vector mediator + Dark Matter models do not predict. Soon after, Ref. [96] finds that a 2HDM+a can produce relic densities of Dark Matter consistent with the observed value. In the same year, Ref. [1] describes another variation, keeping the simpler pseudoscalar potential from Ref. [95, 96] but adding higher order portal terms. Crucially, Ref. [1] gives the first description of the wide range of collider signatures predicted by the 2HDM+a, which includes $h + E_T^{\text{miss}}$, $Z + E_T^{\text{miss}}$, jet + E_T^{miss}, $t\bar{t} + E_T^{\text{miss}}$, $t\bar{t}$-resonance, and $b\bar{b} + E_T^{\text{miss}}$. The precise 2HDM+$a$ variant studied in this thesis is the one described in Ref. [1].

The large variety of collider signatures predicted by the 2HDM+a [1] is a noteworthy feature, and it is the main motivation for studying the 2HDM+a. The 2HDM+a can thus

provide a common benchmark for non-standard collider signatures such as resonant $Z + E_T^{\text{miss}}$ and $h + E_T^{\text{miss}}$ production [95, 1]. In these signatures, h and Z are not produced as initial state radiation (ISR), but in a hard interaction outside of the SM, directly probing the Dark Matter coupling. This direct probe of the SM-Dark Matter interaction sets the $h + E_T^{\text{miss}}$ and $Z + E_T^{\text{miss}}$ signatures apart from conventional signatures such as jet $+ E_T^{\text{miss}}$, where the jet is ISR due to SM couplings. The standard jet $+ E_T^{\text{miss}}$ signature, as well as exotic signatures like $h(b\bar{b}) + E_T^{\text{miss}}$, $b\bar{b} + E_T^{\text{miss}}$, and $t\bar{t}$-resonance, are related in the 2HDM+a, and can furthermore be compared to the observed relic density, direct detection etc. Such comparisons of a large variety of signatures in one unified framework motivate the interpretation of the existing Dark Matter searches in the 2HDM+a, which for the ATLAS search for $h(b\bar{b}) + E_T^{\text{miss}}$ specifically is done in this Thesis.

The choice of using a mixing of mediators to couple Dark Matter to SM particles can seem overly involved. E.g. a direct gauge or Yukawa coupling of a fermionic Dark Matter candidate and SM fermions to some massive mediator can also describe SM -Dark Matter interactions, and involves fewer new particles and parameters. Being of mass dimension 4, such operators appear to be renormalisable. However, many models of this kind violate the local $\mathrm{SU}(3)_S \otimes \mathrm{SU}(2)_L \otimes \mathrm{U}(1)_Y$ gauge symmetry of the SM, and thus are nonrenormalizable and not UV-complete, despite the new operators being of mass dimension 4 [97, 1] and references therein. These theoretical inconsistencies can give rise to e.g. violations of perturbative unitarity in some parameter region of the simplified model [97], which reduces the applicability of the model. The UV-completion can introduce new mediators affecting the signal kinematucs. Such problems are avoided in the 2HDM+a by mixing the singlet pseudoscalar with the $\mathrm{SU}(2)_L \otimes \mathrm{U}(1)_Y$-doublets from the 2HDM, which is the simplest way to construct pseudoscalar boson coupled to the SM in a gauge invariant way [1]. Thus, from a theoretical perspective, the 2HDM+a is an improvement over previous simplified models, which are not UV-complete.

4.1.1 2HDM Potential

The 2HDM potential, adapted from Ref. [1], has the form:

$$\begin{aligned} V_H = {} & \mu_1 H_1^\dagger H_1 + \mu_2 H_2^\dagger H_2 + \mu_3 \left(H_1^\dagger H_2 + \text{h.c.} \right) + \lambda_1 \left(H_1^\dagger H_1 \right)^2 + \lambda_2 \left(H_2^\dagger H_2 \right)^2 \\ & + \lambda_3 \left(H_1^\dagger H_1 \right) \left(H_2^\dagger H_2 \right) + \lambda_4 \left(H_1^\dagger H_2 \right) \left(H_2^\dagger H_1 \right) + \left[\lambda_5 \left(H_1^\dagger H_2 \right)^2 + \text{h.c.} \right] \quad , \end{aligned} \tag{4.1}$$

corresponding to all Lorentz-invariant contractions of the two Higgs doublets H_1 and H_2 that are of mass dimension 4 or lower, are gauge invariant under $\mathrm{SU}(2)_L \otimes \mathrm{U}(1)_Y$, and are not kinetic terms (i.e. do not contain covariant derivatives of the Higgs doublets).

In addition to the above conditions, a $\mathbb{Z}_2$ symmetry is imposed, requiring invariance under the transformation $H_1 \to H_1, H_2 \to -H_2$ [1]. As discussed in more detail in Section 4.1.2, the symmetry is imposed to suppress Flavor Changing Neutral Currents (FCNCs) by prohibiting them at tree level. This FCNC-suppressing $\mathbb{Z}_2$ symmetry is softly broken by the the term $\mu_3 \left(H_1^\dagger H_2 + \text{h.c.} \right)$ [1], where "softly broken" refers to the fact that the mass dimension 2 parameter μ_3 assigns an explicit and ideally low energy scale to the effects of this term. The soft breaking does not interfere with the FCNC suppression [98].

After spontaneously breaking the $\mathrm{SU}(2)_L \otimes \mathrm{U}(1)_Y$ into $\mathrm{U}(1)_{e.m.}$ through the vacuum expectation values $\langle H_1 \rangle = \frac{1}{\sqrt{2}}(0, v_1)^T$ and $\langle H_2 \rangle = \frac{1}{\sqrt{2}}(0, v_2)^T$ of the Higgs doublets [99], the Higgs doublets, the $W^\pm$ and Z^0 bosons of the SM, and the $\mathrm{U}(1)_{e.m.}$ charged SM fermions obtain effective mass terms [99, 98]. Choosing a basis in which the mass matrix of the Higgs doublets

is diagonal except for the eventual mixing with the dark sector pseudoscalar, the 8 real degrees of freedom in the 2 complex Higgs doublets H_1 and H_2 can be written as 3 massless Goldstone bosons corresponding to the longitudinal degrees of freedom of the now massive $W^{\pm}, Z^0$ gauge bosons, and 5 massive scalars [1]:

- a light CP-even scalar h;
- a heavy CP-even scalar H;
- a $\mathrm{U}(1)_{e.m.}$ charged scalar H^+;
- its corresponding anti-particle H^-;
- a CP-odd scalar A_0.

Apart from the four masses $M_h, M_H, M_{H^{\pm}}, M_{A_0}$ of these Higgs bosons, there remain four further parameter degrees of freedom in the 2HDM potential given in Equation (4.1), which are convenient to express as [1]:

- the ratio of vacuum expectation values: $\tan\beta = \frac{v_1}{v_2}$;
- the norm of the vacuum expectation values: $v = \sqrt{v_1^2 + v_2^2}$;
- the mixing angle of the CP-even scalars h and H: α;
- the remaining quartic coupling: λ_3.

The norm of the vacuum expectation values v, like the vacuum expectation value of a single Higgs doublet in the SM, determines the electroweak scale, which is very well constrained by measurements of the Fermi Coupling Constant $G_F = v^2/\sqrt{2}$ [17, 99, 98]. Thus v is fixed to $v = 246\,\mathrm{GeV}$.

Because the scalar resonance observed by ATLAS and CMS at the LHC appears to be entirely consistent with the SM Higgs boson prediction concerning its couplings and production cross sections [21], M_h is fixed to $M_h = 125\,\mathrm{GeV}$ to be consistent with the observed mass [19], and α is fixed such that $\sin(\beta-\alpha) = 1$, a choice known as the alignment limit. In the alignment limit, the couplings of $W^{\pm}$ and Z^0 bosons to the CP-even scalars in the 2HDM, given by [1]

$$\mathcal{L} \supset (\sin(\beta-\alpha)h + \cos(\beta-\alpha)H)\left(\frac{2M_W^2}{v}W_\mu^+ W^{-\mu} + \frac{M_Z^2}{v}Z_\mu Z^\mu\right) \quad , \tag{4.2}$$

are purely the coupling to the lighter CP-even scalar h, with a coupling strength identical to the SM one. Thus with $M_h = 125\,\mathrm{GeV}$, $v = 246\,\mathrm{GeV}$, and $\sin(\beta-\alpha) = 1$, the light CP-even scalar is constructed to be consistent with the observed 125 GeV scalar and similar to the SM Higgs. As an additional benefit, three a priori free parameters of the model are fixed by this choice.

4.1.2 2HDM Yukawa Assignments

In a 2HDM, the masses of the charged SM fermions are interpreted as effective terms appearing in the broken phase of the Higgs vacuum and originating from corresponding Yukawa couplings of the Higgs doublets to the charged SM fermions.

In the most general case of both Higgs doublets coupling to any fermion, 2HDMs predict FCNCs at tree level [98]. As mentioned in Section 4.1.1, a $\mathbb{Z}_2$ symmetry of the form $H_1 \to H_1, H_2 \to -H_2$ [1] is imposed to avoid this. The Yukawa couplings have the general form $y^1_{i,j}\bar{\Psi}_i\Psi_j H_1 + y^2_{i,j}\bar{\Psi}_i\Psi_j H_2$, and the resulting mass matrix is $M_{ij} = \frac{1}{\sqrt{2}}y^1_{i,j} + \frac{1}{\sqrt{2}}y^2_{i,j}$. Hence, in general there is no fermion basis that diagonalises M_{ij}, $y^1_{i,j}$ and $y^2_{i,j}$ at once [98]. The $\mathbb{Z}_2$ symmetry resolves this by ensuring that only one of the two doublets can couple to fermions of given quantum numbers, i.e. up- or down-type quarks or charged leptons. Thus there is only one matrix of Yukawa couplings per fermion field operator, and this Yukawa matrix can always be diagonalized simultaneously with the quark and fermion mass matrices. When coupling fermions to H_2, the corresponding Yukawa coupling is taken to transform under the $\mathbb{Z}_2$ as $y_{i,j} \to -y_{i,j}$ [98]. When the masses and couplings are diagonal, the quark flavor, being the mass eigenstate of the quark, cannot be changed by an interaction with a neutral Higgs boson. Consequently there are no tree level FCNCs, as in the SM.

As stated above, the FCNC supressing $\mathbb{Z}_2$ requires that all fermions with identical quantum numbers coupling to a Higgs doublet, need to couple to the same Higgs doublets [98]. This yields three relevant categories of fermions: up-type quarks, down-type quarks, and charged leptons. The $\mathbb{Z}_2$ symmetry does not specify which of these fermion categories couples to which doublet. Depending on this assignment of Yukawa couplings, one can distinguish 4 different combinations of Yukawa assignments, which in Ref. [1] are called type I through IV.

For the $h(b\bar{b}) + E_T^{\text{miss}}$ signature at the LHC, the Yukawa assignment of charged leptons is irrelevant. Thus the only difference relevant here is that between models where up-type quarks and down type quarks have a different Yukawa assignment, called type II and IV in Ref. [1], and those models where all quarks share the same assignment of Yukawa couplings, called type I and III in Ref. [1].

The only parameter region where the particular Yukawa assignment is of interest for the $h(b\bar{b})+E_T^{\text{miss}}$ signature is the signal production mode if $\tan\beta$ is very large [1], as is also discussed in Section 4.3 below. In types II and IV, $h(b\bar{b}) + E_T^{\text{miss}}$ signal events can be produced via $b\bar{b}$ annihilation for very large $\tan\beta$, because the large effective Yukawa coupling ratio $m_t/m_b \approx 60$ can be compensated for in the fundamental Yukawa coupling by tuning $\tan\beta$ [1]. This effect is described in more detail in Section 6.5.1. In types I and III, this production mode is always suppressed, since both up type and down type quarks have Yukawa couplings with identical $\tan\beta$ dependence. Hence the standard gluon fusion is the only relevant $h(b\bar{b})+E_T^{\text{miss}}$ production process in the entire parameter space in such models [1].

The specific model implementation provided by the authors of [1] and used for the studies in Chapters 6 to 8 has Yukawa assignments of type II. The $h(b\bar{b}) + E_T^{\text{miss}}$ results presented in this thesis are however expected to apply identically to models with Yukawa assignment of type IV, since this only changes the couplings to leptons [1]. Most of the results in this thesis are furthermore transferable to Yukawa types I and III, with the exception of the $b\bar{b}$ initiated production mode [1].

4.1.3 Dark Sector

The dark sector potential is minimal [95, 1]:

$$V_{\text{dark}} = \frac{M_{a_0}^2}{2} a_0^2 + M_\chi \bar{\chi}\chi + y_\chi a_0 \bar{\chi} i\gamma_5 \chi \quad , \tag{4.3}$$

describing the Dirac fermion χ as the Dark Matter candidate, with a mass M_χ and no coupling apart from the Yukawa coupling y_χ to the pseudoscalar a_0 with mass M_{a_0}. Making χ a Dirac fermion is a mostly arbitrary choice, as replacing it by e.g. a Majorana fermion would not impact the collider phenomenology of the model. No higher dimensional potential operators are assumed for a_0, unlike in Ref. [94] where an additional term $\propto a_0^4$ is added, as theses terms are not expected to impact the collider phenomenology [1].

The spin of a_0 does not impact the phenomenology of a hadron collider search for $h(b\bar{b}) + E_T^{\text{miss}}$, which is mostly insensitive to the spin structure of the Dark Matter particles and mediator. However, the direct detection limits on the Dark Matter-nucleon scattering cross section are much stronger for spin-independent Dark Matter-nucleon interactions than for spin-dependent Dark Matter-nucleon interactions [9, 17]. Since interactions via pseudoscalar mediators contribute to the less constrained spin-dependent cross section, but scalar mediators contribute to the strongly constrained spin-independent cross-section [17], choosing a pseudoscalar mediator avoids the otherwise stringent direct detection constraints [94, 95].

Both a_0 and χ are singlets of the $\text{SU}(3)_S \otimes \text{SU}(2)_L \otimes \text{U}(1)_Y$ gauge group, and no non-singlet representation under any new gauge group is assumed for them. Furthermore, their masses are fundamental parameters of the simplified model, $\langle a_0 \rangle = 0$ in the vacuum, and a_0 has no Higgs mechanism. Thus, y_χ and M_χ are independent parameters.

4.1.4 Portal Terms

The portal terms [1]

$$V_{\text{portal}} = a_0 \left(i b_P H_1^\dagger H_2 + \text{h.c.} \right) + a_0^2 \left(\lambda_{P1} H_1^\dagger H_1 + \lambda_{P2} H_2^\dagger H_2 \right) \tag{4.4}$$

establish the connection between the dark sector described in Section 4.1.3 and the SM extended by the 2HDM as described in Sections 4.1.1 and 4.1.2. The portal terms in Equation (4.4) add 3 new model parameters: the mass-dimensional portal parameter b_P and the trilinear scalar portal couplings λ_{P1} and λ_{P2}. Additional gauge and Lorentz invariant couplings with terms such as $\bar{L} H_1 \chi_R + \text{h.c.}$, where L denotes a lefthanded $\text{SU}(2)_L \otimes \text{U}(1)_Y$ doublet of SM leptons, are forbidden by imposing an additional ad-hoc $\mathbb{Z}_2$ symmetry of the form $\chi \to -\chi$ [1].

The portal terms in Equation (4.4) open up the possibility of interpreting collider searches in this model, and make χ a viable candidate for thermal relic Dark Matter. The last two terms $\propto \lambda_{P1}, \lambda_{P2}$ in Equation (4.4) are not included in the portal terms described in Refs. [94, 95], but only in Ref. [1].

Due to the portal terms in Equation (4.4), a_0 and A_0 gain non-diagonal entries to their effective mass matrix; they are not mass eigenstates. To obtain mass eigenstates, a_0 and A_0 are diagonalised with a rotation by the mixing angle θ into the pseudoscalar mass eigenstates a and A [94, 95]:

$$\begin{aligned} a &= a_0 \cos\theta - A_0 \sin\theta \quad , \\ A &= a_0 \sin\theta + A_0 \cos\theta \quad . \end{aligned} \tag{4.5}$$

For $\theta \neq i\pi$ with $i \in \mathbb{Z}$, i.e. non-zero mixing, both a and A are Dark Matter mediators, and both have couplings to SM particles and the other scalars from the 2HDM. Thus, there are two Dark Matter mediators in the 2HDM+a, a and A.

After diagonalizing the mass matrix, there are two equivalent ways of distinguishing between a and A:

1. One can define A as the heavy pseudoscalar, and a as the light one, i.e. $M_A > M_a$.

2. One can define A as the pseudoscalar mass eigenstate which couples to Dark Matter $\propto \sin\theta$ and to Standard Model particles $\propto \cos\theta$, and vice versa for a.

The first definition is followed in Ref. [1]. For simplicity, a and A will be referred to as the light and heavy pseudoscalar, respectively, in this thesis. The second definition is used in Ref. [95] as well as in the numerical model implementation provided by the authors of Ref. [1]. For this reason, there are plots in Chapters 6 to 8 scanning $M_a > M_A$, which is nonsensical when adhering strictly to the first definition based on mass hierarchy.

The second definition does not, however, allow one to describe a larger set of physically distinct models than the first. A model with $M_a > M_A$ and some mixing angle θ_2 in definition 2 can be called a model with $M_a < M_A$ and mixing angle $\theta_1 = \cos^{-1}\left(\sqrt{1-\sin^2\theta_2}\right)$ in definition 1. This renaming makes use of the symmetry of the mixing definition in Equation (4.5), where by exchanging $a \to A$, $A \to a$, $\cos\theta \to (\pm)\sin\theta$, $(\mp)\sin\theta \to \cos\theta$, the original model description is recovered. In the limiting cases where $\sin\theta = 1/\sqrt{2} = \cos\theta$ or $M_A = M_a$, this freedom of definition is lost.

4.1.5 Model Parameters and Couplings after Mass Diagonalisation

In the full model, combining the dark sector and portal terms from Equations (4.4) and (4.5) with the 2HDM terms from Equation (4.1) and the relevant kinetic and Yukawa terms, all six massive scalar degrees of freedom have corresponding mass eigenstates [1]. In the diagonalised basis, it is convenient to parametrize the model using the 14 independent parameters given in Table 4.1.

After mass diagonalisation, most of the coupling parameters such as e.g. λ_1, λ_2, λ_4, and b_P in Equations (4.1) and (4.4) are absorbed into masses and mixing angles. Consequently, the effective trilinear scalar couplings of the mass eigenstates are functions of the masses and mixing angles. The coupling of the Aah vertex is [1]

$$\begin{aligned} g_{Aah} = \frac{1}{vM_A}\big[&M_h^2 - 2M_H^2 - M_A^2 + 4M_{H^\pm}^2 - M_a^2 - 2\lambda_3 v^2 \\ &+ 2\left(\lambda_{P1}\cos^2\beta + \lambda_{P2}\sin^2\beta\right)v^2\big]\sin\theta\cos\theta \quad , \end{aligned} \tag{4.6}$$

and the coupling of the aah vertex [1]

$$\begin{aligned} g_{aah} = \frac{1}{vM_h}\big[&\left(M_h^2 - 2M_H^2 + 4M_{H^\pm}^2 - 2M_a^2 - 2\lambda_3 v^2\right)\sin^2\theta \\ &- 2\left(\lambda_{P1}\cos^2\beta + \lambda_{P2}\sin^2\beta\right)v^2\cos^2\theta\big] \quad . \end{aligned} \tag{4.7}$$

will be useful when interpreting specific results presented in Chapters 6 and 7.

Table 4.1: The 14 independent 2HDM+a model parameters, as described in [1].

Parameter	Interpretation
M_A	mass of the heavy CP-odd scalar Dark Matter mediator A.
M_a	mass of the light CP-odd scalar Dark Matter mediator a.
M_H	mass of the heavy CP-even scalar H.
M_h	mass of the light CP-even scalar h. Fixed to 125 GeV [1] to allow h to be interpreted as the 125 GeV scalar observed at the LHC.
$M_{H^\pm}$	mass of the charged scalar $H^\pm$.
$\sin\theta$	sine of the mixing angle θ of the pseudoscalar mediators a and A.
α	mixing angle of the CP-even scalars h and H. Fixed such that $\sin(\beta-\alpha)=1$ to keep couplings of h aligned with the SM Higgs boson couplings.
$\tan\beta$	ratio of the vacuum expectation values of the two Higgs doublets.
v	norm of the vacuum expectation values of the two Higgs doublets. Fixed to 246 GeV [1] to give a value of G_F consistent with observations [17] and keep the couplings of h aligned to those of the SM Higgs boson.
λ_3	quartic coupling of the two Higgs doublets. Not constrained by mass diagonalisation.
λ_{P1}	a quartic portal coupling connecting the dark sector and the Higgs doublet H_1.
λ_{P2}	a quartic portal coupling connecting the dark sector and the Higgs doublet H_2.
M_χ	mass of the massive Dirac fermion singlet Dark Matter candidate χ.
y_χ	Yukawa coupling of the massive Dirac fermion singlet to the mediators a and A. The effective Yukawa coupling is furthermore a function of $\sin\theta$ [1].

4.2 Existing 2HDM+a Constraints

In this section, some existing constraints on the 2HDM+a parameter space, which are relevant to the studies specific to the $h(b\bar{b}) + E_T^{\text{miss}}$ signature at ATLAS presented in Chapters 6 to 8, are discussed. They are a combination of various constraints commonly applicable to 2HDMs, Dark Matter models, or both.

4.2.1 Perturbative Unitarity

An important constraint is the issue of the perturbativity and unitarity of scattering amplitudes. The perturbation series needs to converge reasonably fast, because otherwise the perturbation theory that LO simulations and fixed order formulas are predicated upon does not apply [17]. Non-unitarity of the scattering matrix implies non-conservation of probability, thus such a theory must be wrong [17]. Note that while a non-unitary scattering matrix implies that the theory predicting it is fundamentally wrong, a non-perturbative model is not unphysical; instead describing such a theory with the tools of perturbation theory produces wrong results. Following Ref. [1], the unitarity and perturbativity constraints are usually satisfied if $M_A, M_a, M_H \leq M_{H^\pm} = \mathcal{O}(1\,\text{TeV}), \lambda_3, \lambda_{P1}, \lambda_{P2} \approx \mathcal{O}(1)$ or below [1], $\tan\beta \geq 0.3$ [98], and $\Gamma_i \lesssim \frac{M_i}{3}$ for $i = A, H$. This is the case for most of the models studied in Chapters 4 and 6 to 8.

4.2.2 Electroweak Precision Measurements

In the SM with a single Higgs doublet, the Higgs sector Lagrangian possesses a symmetry SO(4) that is larger than just the electroweak gauge symmetry [17]. As a result, the relation $\rho \equiv \frac{M_W^2}{M_Z^2 \cos^2\theta_w} = 1$ of the W, Z masses M_W, M_Z, and the Weinberg angle θ_w, is protected from corrections arising at one-loop level [17]. This matches the experimentally observed smallness of deviations from $\rho = 1$ very well , which are $\mathcal{O}(10^{-3})$ or smaller [17].

In general, 2HDM potentials lack a custodial symmetry against such one loop contributions, and so they can predict quite large deviations from $\rho = 1$ [100]. In the 2HDM+a, the additional portal terms in Equation (4.4) modify the ρ prediction relative to the pure 2HDM case, and at one-loop level the result is [1]:

$$\Delta\rho = \frac{M_{H^\pm}^2}{(4\pi v)^2}\left[1 + f(M_H, M_a, M_{H^\pm}) + f(M_a, M_H, M_{H^\pm})\right]\sin^2\theta \quad , \tag{4.8}$$

with

$$f(a,b,c) = \frac{a^4(b^2-c^2)}{c^2(a^2-b^2)(a^2-c^2)}\log\left(\frac{a^2}{c^2}\right) \quad . \tag{4.9}$$

Thus, with $M_{H^\pm} = M_H$, $\Delta\rho = 0$ at one-loop level and one can avoid constraints on the other parameters [1]. In this respect, the 2HDM+a is similar to generic 2HDM models [100]. However, in the 2HDM case, $M_{H^\pm} = M_{A_0}$ is also sufficient for $\Delta\rho = 0$, and the analogue is not the case for the 2HDM+a, where for $M_A = M_{H^\pm}$ a strong $\Delta\rho$ dependence on the parameters in Equation (4.8) remains [1, 100]. Thus, the constraints from electroweak precision measurements of ρ are accounted for by fixing $M_{H^\pm} = M_H$ for the 2HDM+a studies in this thesis.

4.2.3 Limit on $h \to$ Invisible

In the 2HDM+a, there is a scalar vertex haa [1], with the corresponding coupling given by Equation (4.7). This vertex, depending on the masses of the h, a, and χ particles, can give rise

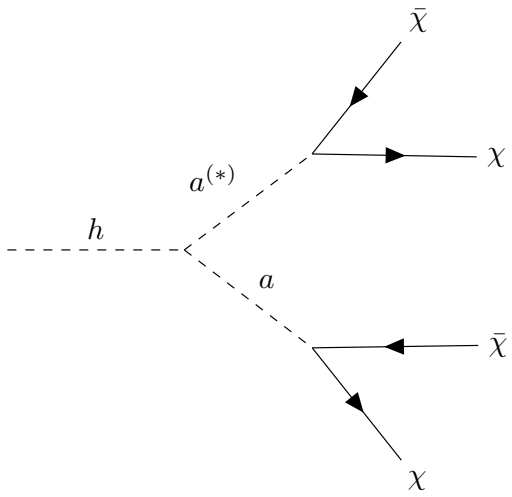

Figure 4.1: 2HDM+a Feynman diagram contributing to $\mathcal{BR}(h \to \text{inv.})$ [1].

to decays $h \to aa^{(*)} \to 2\chi 2\bar{\chi}$ [1], as depicted in Figure 4.1. These decays contribute to the invisible branching ratio $\mathcal{BR}(h \to \text{inv.})$ of the light CP-even scalar h [1].

Since h is interpreted as the 125 GeV scalar observed at the LHC, this gives rise to a constraint [1], as $\mathcal{BR}(h \to \text{inv.})$ needs to be consistent with the observed upper limit of 23% at 95% CL [101]. In general, this constraint can be avoided by $M_a > M_h$. Depending on the other model parameters, $M_a > M_h/2$ may not be sufficient, since even off-shell $h \to 2\chi 2\bar{\chi}$ processes can have partial widths far larger than any visible SM decay, leading to $\mathcal{BR}(h \to \text{inv.}) \approx 100\%$ [1]. Finally, this constraint exists even in the case of $\sin\theta = 0$, i.e. no a, A mixing, since the quartic portal terms in Equation (4.4) still contribute [1].

To incorporate the constraint from the limit on $h \to$ inv., the scans constructed in Chapter 7 are limited to $M_a \geq 100\,\text{GeV}$.

4.2.4 Vacuum Stability

When constructing a 2HDM, one of the implicit assumptions is that the scalars participate in what is called a Higgs mechanism [99, 102, 98, 103]. Higgs mechanism [17] refers to the idea that the scalars of the theory generate effective masses for all the fundamental massive interacting SM particles, as detailed for the SM case in Section 1.2.4. These particles obtain their effective masses by interacting with the non-vanishing vacuum states of the Higgs fields. This can only be consistent with the observed finite and constant masses [17, 104] of all observed SM particles if the vacuum expectation value is finite. This condition is the vacuum stability requirement.

Vacuum stability for a single Higgs doublet For a single Higgs doublet ϕ, the tree level potential is typically described as a polynomial of order 4 in ϕ [17], as seen in Equation (1.10) In this case, a finite vacuum expectation value at tree level is given when the prefactor λ of the $(\phi^\dagger\phi)^2$ term is positive: $\lambda > 0$. If $\lambda < 0$, the potential has no global minimum, and a false vacuum state sitting in any local minimum can, and eventually will, decay by tunneling to a lower energy state of arbitrarily large Higgs field expectation value. This decay of the false vacuum would radically change the masses of the SM fermions, and thus it is inconsistent with the experimental evidence [104, 17]. Based on the measured Higgs and top pole masses, a metastable SM vacuum when extrapolating to very high fields is most likely, but the current

measurements are not precise enough to rule out a stable vacuum either [105]. The vacuum stability condition $\lambda > 0$, also called the "bounded-from-below" condition, is thus a requirement of a realistic Higgs sector with one Higgs doublet.

Vacuum Stabilty in 2HDMs In a 2HDM, where there are two Higgs doublets, the same principle applies. The Higgs potential, i.e. Equation (4.1), is still a 4th order polynomial in the field operators. However, now there is not only one corresponding highest order term, but several. Even though the potential geometry is now more involved, a set of 4 conditions on the pre-factors λ_1, λ_2, ... can be found that correspond to the potential tending towards positive infinity in any field direction, thus ensuring a global minimum [99]:

$$\lambda_1 > 0, \quad \lambda_2 > 0, \quad \lambda_3 > -\sqrt{\lambda_1 \lambda_2}, \quad \lambda_3 + \lambda_4 - |\lambda_5| > -\sqrt{\lambda_1 \lambda_2} \quad . \tag{4.10}$$

In the special case of $M_H = M_{H^\pm}$ and $\sin(\beta - \alpha) = 1$, algebraic transformations of Inequality (4.10), explicitly performed in Appendix A, yield a set of stronger conditions where all λ_i except for λ_3 are replaced by more meaningful parameters:

$$M_H = M_{H^\pm}, \quad \sin(\beta - \alpha) = 1, \quad \lambda_3 \geq \frac{M_h^2}{v^2}, \quad v^2 \lambda_3 > M_H^2 - M_{A_0}^2 \quad . \tag{4.11}$$

Vacuum stability in the 2HDM+a The first question to raise when extending the vacuum stability conditions from the 2HDM to the 2HDM+a case is that of additional potential terms. If there were any additional quartic couplings introduced, this would mean that the conditions in Inequality (4.10) needed to be modified to apply in the 2HDM+a case. Fortunately, the only new quartic terms are those $\propto \lambda_{P1}, \lambda_{P2}$ in Equation (4.4). Since these terms are $\propto a_0^2$, and the vacuum expectation value of a_0 vanishes, these two terms do not affect the vacuum structure; all other terms are of order 3 or less in the fields. Thus, the conditions in Inequality (4.10) apply unmodified.

To use the conditions in Inequality (4.10), they need to be expressed in terms of the more meaningful parameters in Table 4.1. The steps leading to Equation (4.11) can be performed analogously for the 2HDM+a, with one difference: M_{A_0} is not a mass eigenvalue of any mass eigenstate in the 2HDM+a. Thus, it is replaced by the appropriate combination of the proper eigenvalues M_a and M_A, according to Equation (4.5), resulting in

$$M_H = M_{H^\pm}, \quad \sin(\beta - \alpha) = 1, \quad \lambda_3 \geq \frac{M_h^2}{v^2}, \quad v^2 \lambda_3 > M_H^2 - M_A^2 \cos^2\theta - M_a^2 \sin^2\theta \quad . \tag{4.12}$$

In the alignment limit, these conditions guarantee vacuum stability independently of $\tan\beta$.

Results As discussed in Sections 4.1.1 and 4.2.2 respectively, $\sin(\beta-\alpha) = 1, v = 246\,\text{GeV}, M_h = 125\,\text{GeV}$ correspond to SM-like h couplings, and $M_H = M_{H^\pm}$ is favored by electroweak precision constraints. With these parameter choices, two conditions from Equation (4.12) remain: a lower bound of ≈ 0.2581 for λ_3 and a quadratic equation in $M_H, M_A, M_a, \sin\theta$, again giving a lower bound to λ_3.

The resulting regions of parameter space allowed by vacuum stability are displayed in Figure 4.2. The vacuum stability dependence on M_a is small, as demonstrated in Figure 4.2(a). This is due to the choice of a small $\sin^2\theta$, which is a prefactor to the M_a^2 contribution in

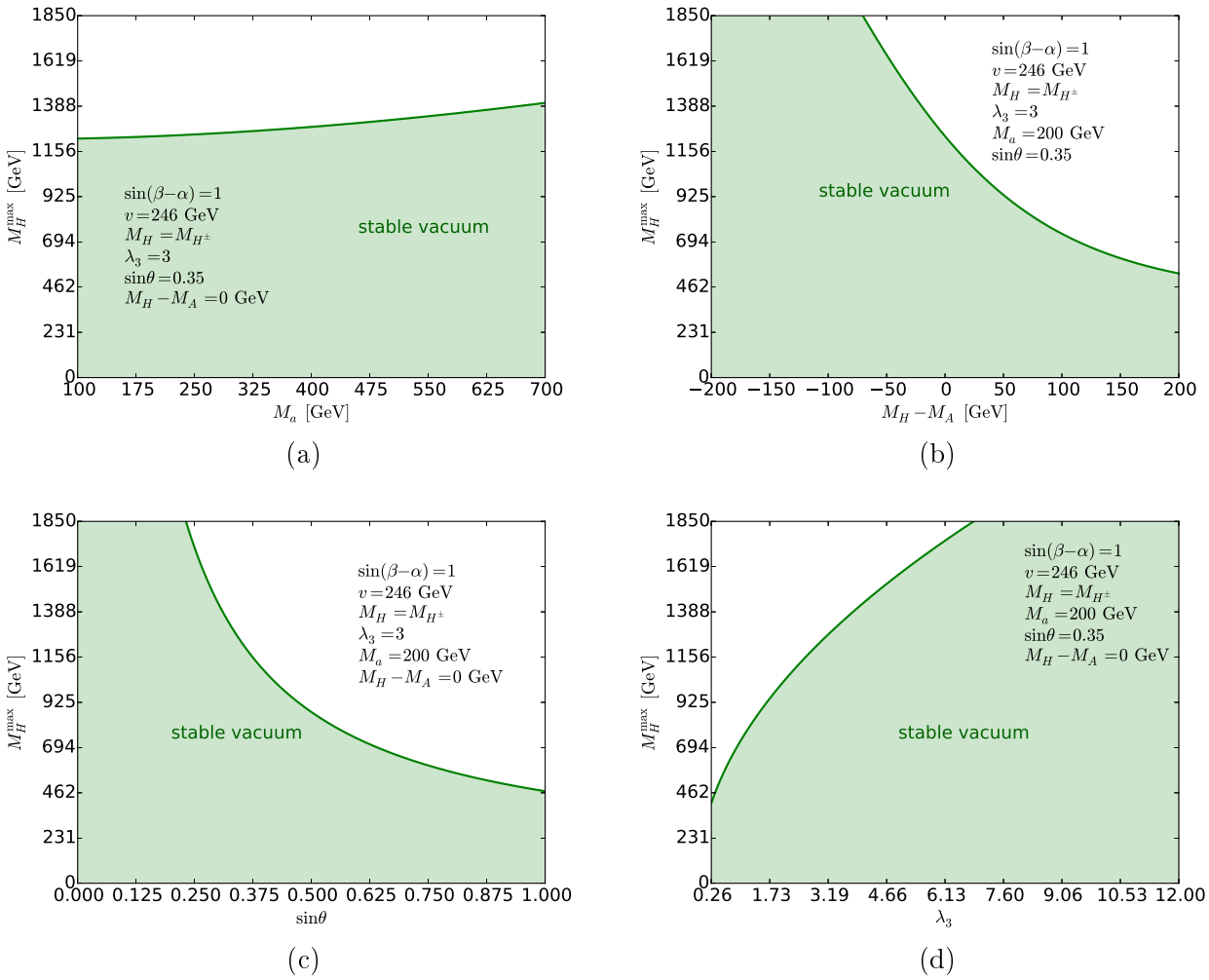

Figure 4.2: Tree level vacuum stability conditions in the 2HDM+a according to Equation (4.12). The inequality is displayed as the maximal $M_H = M_{H^\pm}$ allowed by tree level vacuum stability, as a function of the remaining 4 relevant parameters. The M_a dependence is shown in (a), the $M_H - M_A$ dependence is shown in (b), the $\sin\theta$ dependence is shown in (c), and the dependence on λ_3 is shown in (d). The respective other relevant parameters are fixed at $M_a = 200\,\text{GeV}, \sin\theta = 0.35, \lambda_3 = 3, \sin(\beta-\alpha) = 1, v = 246\,\text{GeV}, M_H = M_{H^\pm} = M_A$.

Equation (4.12). Correspondingly the effects of M_a and M_A on the vacuum stability are reversed for $\sin\theta > 1/\sqrt{2}$. The difference $M_H - M_A$ strongly affects the stability of the vacuum, disfavoring large positive differences, as shown in Figure 4.2(b). As a result, the weak constraint at low $\sin\theta$, shown in Figure 4.2(c), becomes strong at high $\sin\theta$. The reason is that the relevant mass difference at high $\sin\theta$ is not $M_H - M_A$, but $M_H - M_a$, which is larger for typical models. Finally, increasing λ_3 generally increases the parameter space with a stable vacuum, as one would expected and Figure 4.2(d) demonstrates.

Comparing the parameter space preferred by vacuum stability to the requirements of perturbative unitarity, described in Section 4.2.1, there is some trade-off. Tuning a parameter to minimize the occurrence of unstable vacua tends to drive that parameter towards the boundaries of the regions of unitarity and perturbativity. In the parameters chosen for Figure 4.2, these constraints are somewhat balanced, as there is a sizable region of overlap.

Limitations There are two major limitations of the above vacuum stability analysis as a tree-level bounded-from-below condition:

1. The potential at Next-to-Leading Order (NLO) can in general be different from the tree-level potential as given in Equation (4.1). Thus, parameter points that appear stable at tree level may turn out to be unstable in a one-loop corrected potential, and vice versa [106].

2. An unbounded vaccuum may in fact turn out to be bounded due to additional potential terms associated with high-energy degrees of freedom. However, even if such operators exist, they will then yield deeper potential minima at their respective energy scale. Hence high energy effects can only stabilize an unstable vacuum at the electroweak scale if the effects themselves occur at or close to the electroweak scale. Thus this is limitation is very dependent on the details of the high-energy embedding used to try and recover a stable vacuum.

4.2.5 Indirect Heavy Flavor Constraints

The mass of the charged Higgs boson $M_{H^\pm}$ is subject to a variety of indirect constraints arising from its Yukawa couplings to heavy-flavored quarks $H^+\bar{t}_L b_R + \text{h.c.}$ and $H^+\bar{t}_R b_L + \text{h.c.}$ [1], contributing to FCNC processes at one-loop order.

These FCNC contributions include rare decays of B mesons, $B \to X_s\gamma$ [1], shown in Figure 4.3(a), where the $H^\pm$ represent new particles that can appear in the loop in place of the SM $W^\pm$ [103]. A further relevant $H^\pm$ FCNC contribution is the one to the $B_s - \bar{B}_s$ oscillation amplitude [1], shown in Figure 4.3(b). Again similarly to the SM $W^\pm$, the $H^\pm$ contribute via box diagrams [103].

When ensuring that the 2HDM+a predictions of the above mentioned one-loop order FCNC processes are not in tension with measurements in the heavy flavor sector, the two most important parameters are $M_{H^\pm}$ and $\tan\beta$.

- Increasing $M_{H^\pm}$ reduces new FCNC amplitudes. This is because the loop amplitudes are functions of the mass ratios of the particles in the loops [103]. Thus, if $M_{H^\pm}$ is much larger than the mass of the heaviest quarks in the loops, the 2HDM+a FCNC amplitude is reduced.

- Increasing $\tan\beta$ also reduces new FCNC amplitudes. This is because the top quark Yukawa coupling y_t to the $H^\pm$ in the term $\propto H^+\bar{t}_R b_L + \text{h.c.}$ [1] is strongest for the top

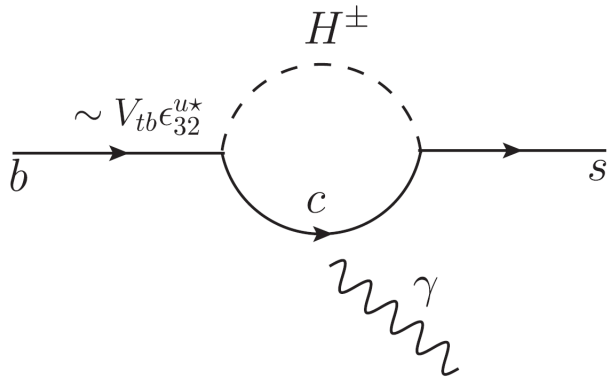

(a) Graph contributing to $B \to X_s\gamma$ decays [103]

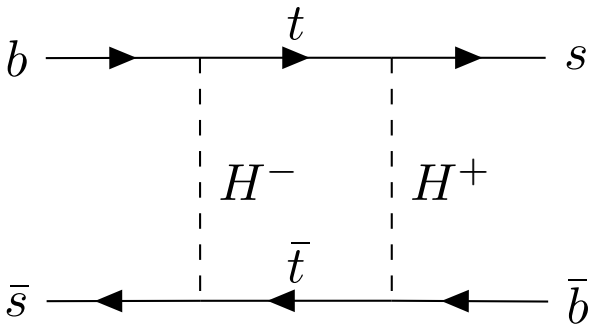

(b) Graph contributing to $B_s - \bar{B}_s$ oscillations

Figure 4.3: Examples of 2HDM diagrams giving rise to additional amplitudes for rare heavy flavor processes such as rare B decays, illustrated in (a), or B-meson flavor oscillation, shown in (b).

quark, since it is the heaviest quark. Thus, top quark couplings most strongly determine the size of the additional FCNC loop amplitudes. However, the top quark Yukawa coupling is $\propto \frac{1}{\tan\beta}$, irrespective of the other Yukawa assignments [1]. Consequently, increasing $\tan\beta$ reduces the 2HDM+a FCNC amplitudes.

Ref. [1] thus quote a lower limit of $\tan\beta \gtrsim 0.8$ for $M_{H^\pm} \gtrsim 750\,\text{GeV}$. However, these constraints may be weakened or avoided in more extended theories with additional Flavor Changing Charged Current (FCCC) mediators cancelling the $H^\pm$ loop contributions. Thus, heavy flavor constraints are indirect constraints in the sense discussed in Section 5.1. Consequently, care is taken that they do not rule out the entire parameter space studied in Chapters 6 to 8. But the usefulness of the parameter scan as a benchmark for models with a wide variety of signatures has a higher priority. As another model giving rise to a similar $h(b\bar{b}) + E_T^{\text{miss}}$ signal might avoid the indirect heavy flavor constraints, the 2HDM+a benchmark should be useful for providing a $h(b\bar{b}) + E_T^{\text{miss}}$-based constraint on such a model too. Hence, also some points that are inconsistent with these constraints are considered for the benchmark.

4.2.6 Relic Density

Since in the 2HDM+a the Dark Matter candidate χ couples to SM particles via the mediators a and A, it is expected to be a kind of thermal relic Dark Matter candidate. "Thermal relic" means that the Dark Matter is expected to be produced and pair-annihilated according to the thermodynamics of the hot plasma in the early universe [3, 4]. The pair production and annihilation are in thermal equilibrium, and thus the number and density of the χ are given by the temperature of the early universe. As time progresses, the early universe expands and cools [3, 4], until the temperature is so low that the annihilation-production processes drop out of thermal equilibrium, a process called "freeze-out" [4]. Another equivalent point of view is that the Dark Matter decouples at the time, or temperature, when the universe is expanding at a faster rate than the Dark Matter particles interact [3].

The thermal production of Dark Matter is thus embedded in the larger context of the ΛCDM cosmological model. The ΛCDM cosmological model is the standard working hypothesis of cosmology [23]. It assumes the existence of both Dark Energy in the form of a cosmological constant Λ appearing in the Einstein equations, and non-baryonic Dark Matter at

non-relativistic velocities, i.e. Cold Dark Matter (CDM), thus the name ΛCDM [23]. Its cosmological history starts from an initial extremely hot and dense plasma, colloquially called Big Bang, followed by a period of rapid spatial inflation, resulting in a universe that is spatially flat, isotropic and homogeneous [23]. The expansion rate of the universe is determined by the mass-energy content of the universe via the Einstein field equations of General Relativity [23]. Thus the ΛCDM universe evolves from a radiation dominated early era, through an intermediate phase dominated by (Dark) Matter, to the current and future Dark Energy driven phase of accelerated expansion [23].

Assuming the cosmology of the early universe until after the Dark Matter freeze-out is described by the standard ΛCDM cosmology, the resulting density of Dark Matter particles after the freeze-out can be calculated from just the Boltzmann Equation and the annihilation cross-section of the Dark Matter particles [107, 3, 4]. The Boltzmann Equation, in this case, has the form [3, 107]

$$\frac{dn_\chi}{dt} = -3H(t)n_\chi - \langle\sigma v_\chi\rangle\,(n_\chi^2 - n_{\chi,eq.}^2)$$

expressing that the number density of Dark Matter particles n_χ is reduced by two effects only: the expansion of the universe, parametrized by the Hubble parameter $H(t)$, and the annihilation of Dark Matter particles into SM particles, if the density is above the equilibrium density $n_{\chi,eq.}$. The rate of the annihilation to equilibrium is determined by the thermally averaged annihilation cross section $\langle\sigma v_\chi\rangle$, where v_χ is the velocity of a particular Dark Matter particle, and σ is the annihilation cross section for $\chi\bar{\chi} \to$ SM particles.

$\langle\sigma v_\chi\rangle$ needs to be calculated from the particle physics model, i.e. the 2HDM+a, which is usually done as a truncated series in powers of v_χ. Assuming that the Dark Matter is massive enough that v_χ is non-relativistic, v_χ is distributed according to a Maxwell-Boltzmann distribution. It turns out that $\langle\sigma v_\chi\rangle$ is dominated by the v_χ^0, v_χ^2 terms (uneven powers of v_χ drop due to symmetry), since for a non-relativistic particle $v_\chi \ll 1$ [4]. The result is a condition relating $n_{\chi,eq.}$ to M_χ and the temperature T [3, 107], which can be analytically solved for the cases of T much larger than the freeze-out temperature, and T much lower than the freeze-out temperature [3, 107]. The resulting relic density can then be found by numerically matching the two analytic solutions before and after freeze out [3, 107]. The result is conventionally expressed as the normalized relic abundance $\Omega_\chi = \rho_\chi/\rho_c$, i.e. the average mass density of Dark Matter in units of $\rho_c = \frac{3H(0)^2}{8\pi G_N}$, the average matter density required for a flat universe in the ΛCDM cosmology [3, 4].

The thermal relic abundance $\Omega_\chi = \rho_\chi/\rho_c$, however, can also be extracted from the power spectrum of the spatial anisotropies of the temperature of the photons in the Cosmic Microwave Background (CMB spectrum) [3] (c.f. Section 1.3.1). Fitting the CMB spectrum with the standard ΛCDM cosmological model, the Planck collaboration report a value equivalent to $\Omega_\chi = 0.258(11)$ [17]. This observation constrains the 2HDM+a parameter space to such parameter values that predict a compatible relic density.

The constraint provided by the relic density is indirect, since it depends on the twin assumptions of a ΛCDM cosmology, and a thermal production mechanism for Dark Matter as outlined above. These assumptions are not bad assumptions, but neither are they necessarily given, since there are nonstandard cosmological models that break them [3, 4].

The constraint of matching the observed relic density with a 2HDM+a is examined in Ref. [96], for a very similar model to the one considered here and first constructed in Ref. [1]. Ref. [96] reports that while strongly dependent on the model parameters, the models studied are capable of producing the observed relic abundance. However, these models lack the quartic

portal terms in Equation (4.4) [1], and thus their results do not necessarily apply to the class of models studied here. Preliminary studies [108] suggest that the parameter values chosen in Chapters 6 and 7 predict a too high relic density. However, this result depends sensitively on the Dark Matter fermion mass M_χ. Conversely the production cross section at the LHC is not affected by M_χ for a large region of the parameter space, as we will see in Section 6.8. Thus, one expects that excluding 2HDM+a models with low M_χ at the LHC can be translated into exclusion of Dark Matter models predicting relic densities consistent with the measured value from Ref. [29] by increasing M_χ, which does not affect the collider phenomenology[1]. The validity of this statement will be examined in greater detail in an upcoming whitepaper [109].

[1]The value of M_χ that correctly reproduces the Dark Matter relic density is a function of many model parameters affecting the collider phenomenology, such as the mediator masses [108, 109]. To keep the collider benchmarks simple, M_χ is thus fixed at a single low value, instead of being varied along with the paramezers scanned in the benchmarks.

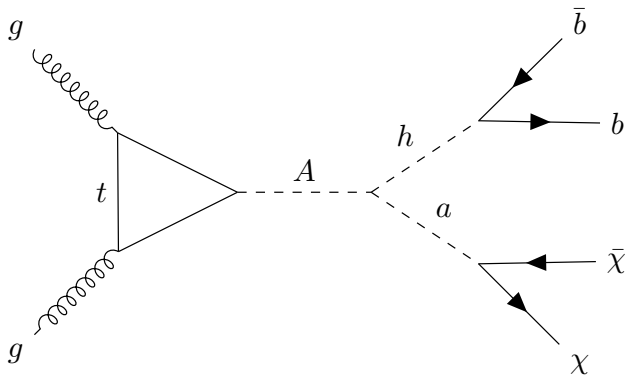

Figure 4.4: Resonant gluon fusion initiated diagram of the $h(b\bar{b}) + E_T^{\text{miss}}$ signature in the 2HDM+a [1]. The decay $h \to b\bar{b}$ is not part of the matrix element calculation, but instead simulated in the parton shower in the numerical simulation, which is described in Section 5.3.

4.3 The $h(b\bar{b}) + E_T^{\text{miss}}$ Signature in the 2HDM+a

The $h(b\bar{b}) + E_T^{\text{miss}}$ signature is an interesting potential DM signature at the LHC, as motivated in Chapter 3. High missing transverse momentum E_T^{miss} is rare for most SM processes, but is typically implied by the production of DM candidates in the 2HDM+a scenario. Furthermore, unlike for e.g. the jet $+ E_T^{\text{miss}}$ or $\gamma + E_T^{\text{miss}}$ signatures, ISR h production is heavily suppressed, due to the small masses of the sea and valence quarks. Thus the h needs to be produced as part of a BSM interaction, and the $h(b\bar{b}) + E_T^{\text{miss}}$ signature probes such interactions directly.

4.3.1 Resonant Signal and Jacobian Peak

The 2HDM+a predicts a resonant production of $h(b\bar{b}) + E_T^{\text{miss}}$ events [95, 1], via the Feynman graph shown in Figure 4.4. In this production mode a resonantly produced pseudoscalar A decays on shell in the $1 \to 2$ decay $A \to ah$, where the h proceeds to decay into the mostly visible final state $h \to b\bar{b} \to$ hadrons, and the a decays invisibly to $a \to \chi\bar{\chi}$. The kinematics of $1 \to 2$ processes are fixed by the masses of the involved particles. Hence the resonant $A \to ah$ process has a sharply peaked resonance in the invariant mass distribution of the final state system. This results in a peak in the momentum distribution of the Dark Matter system. Since the transverse component of the Dark Matter momentum can be reconstructed as the missing transverse momentum E_T^{miss}, there is a corresponding peak in the E_T^{miss} distribution. This peak in the E_T^{miss} distribution resulting from a resonant signal process is called the Jacobian peak.

Since it is fully determined by the masses of the particles involved in the signal process, the location of the maximum E_T^{miss} of the Jacobian peak can be calculated analytically [1, 95]:

$$E_T^{\text{miss,max}} \approx \frac{\sqrt{\left(M_A^2 - M_a^2 - M_h^2\right)^2 - 4M_a^2 M_h^2}}{2M_A} \quad . \tag{4.13}$$

Thus, increasing M_A is expected to lead to a Jacobian peak at harder E_T^{miss}, because higher M_A increases the relative momentum of the a to the h. Conversely, for models with higher M_a a Jacobian peak at softer E_T^{miss} is expected, because lower M_a means less of the energy freed by the A decay is converted into mass, and more into momentum.

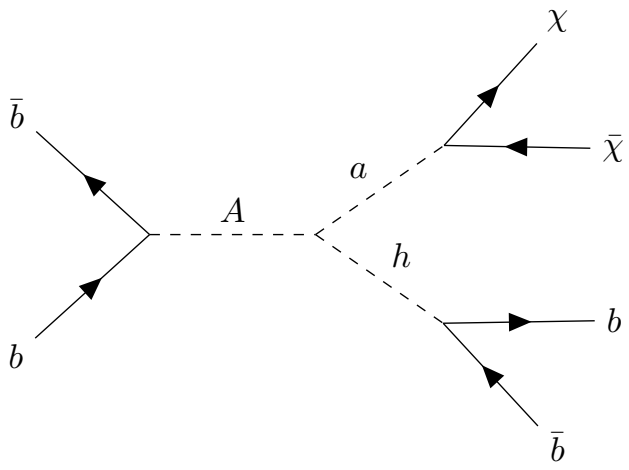

Figure 4.5: Resonant $b\bar{b}$ initiated diagram of the $h(b\bar{b}) + E_T^{\text{miss}}$ signature in the 2HDM+a [1]. The decay $h \to b\bar{b}$ is not part of the matrix element calculation, but instead simulated in the parton shower in the numerical simulation, which is described in Section 5.3.

4.3.2 Production Modes

There are two main $h(b\bar{b}) + E_T^{\text{miss}}$ production modes in the 2HDM+a, gluon fusion and $b\bar{b}$ annihilation. The resonant signal in Figure 4.4 is produced in a hard scattering of gluons, which fuse into a heavy pseudoscalar A via a top loop. This process, called gluon fusion, is the dominant production mode in most of the 2HDM+a parameter space [1], since the small Yukawa couplings of the light sea and valence quarks strongly suppress contributions from initial state quarks.

However, gluon fusion is not the only relevant production mode: in models with Yukawa assignments of types II or IV and for high values of $\tan\beta$, resonant production from pair annihilation of b quarks is also possible [1], via the diagram displayed in Figure 4.5. The reason is that in type II or IV models, the Higgs couplings to b quarks $y_b = \sqrt{2}\frac{m_b}{v}\tan\beta$ is enhanced for large $\tan\beta$, while the t quark coupling $y_t = -\sqrt{2}\frac{m_t}{v}\cot\beta$ is suppressed [1]. There is no interference between the two production modes, because the initial state particles are different [110].

4.3.3 Non-Resonant Signal

Beyond the resonant signal processes that are described in Section 4.3.1 and Figures 4.4 and 4.5, there also are non-resonant contributions from box graphs [1]. Some examples of such box graphs are shown in Figures 4.6(a) to 4.6(c).

One may expect that the resonant process in Figure 4.4 or Figure 4.5 will dominate the $h(b\bar{b}) + E_T^{\text{miss}}$ cross section whenever $M_A > M_a + M_h$ [1]. However, while this condition is necessary for the resonant process to happen, it turns out that it is not sufficient, as we will see in Chapter 6. The reason is that depending on the other model parameters, Γ_A can be large relative to its mass. This enhances further non-resonant processes, which are illustrated in Figures 4.6(d) and 4.6(e). The amplitudes associated to these diagrams can become larger than the resonant amplitude for moderately large Γ_A. Similarly, certain width-suppressed diagrams such as Figure 4.6(f) can be enhanced if the corresponding coupling, i.e. g_{aah} from Equation (4.7), is large enough. Moreover, the coupling g_{Aah} from Equation (4.6) can be small depending on the parameter configuration, actively *suppressing* the resonant contribution.

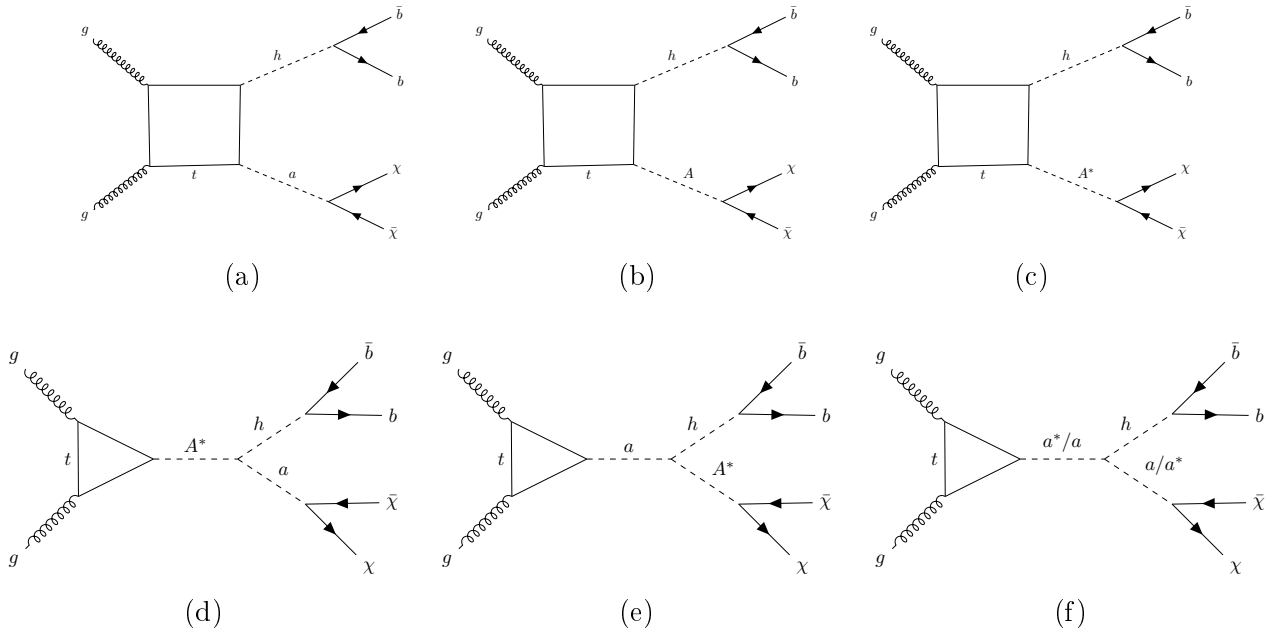

Figure 4.6: Non-resonant Feynman diagrams contributing to the $h(b\bar{b}) + E_T^{\text{miss}}$ signature with gluons in the initial state [1]. The decay $h \to b\bar{b}$ is not part of the matrix element calculation, but instead simulated in the parton shower in the numerical simulation, which is described in Section 5.3.

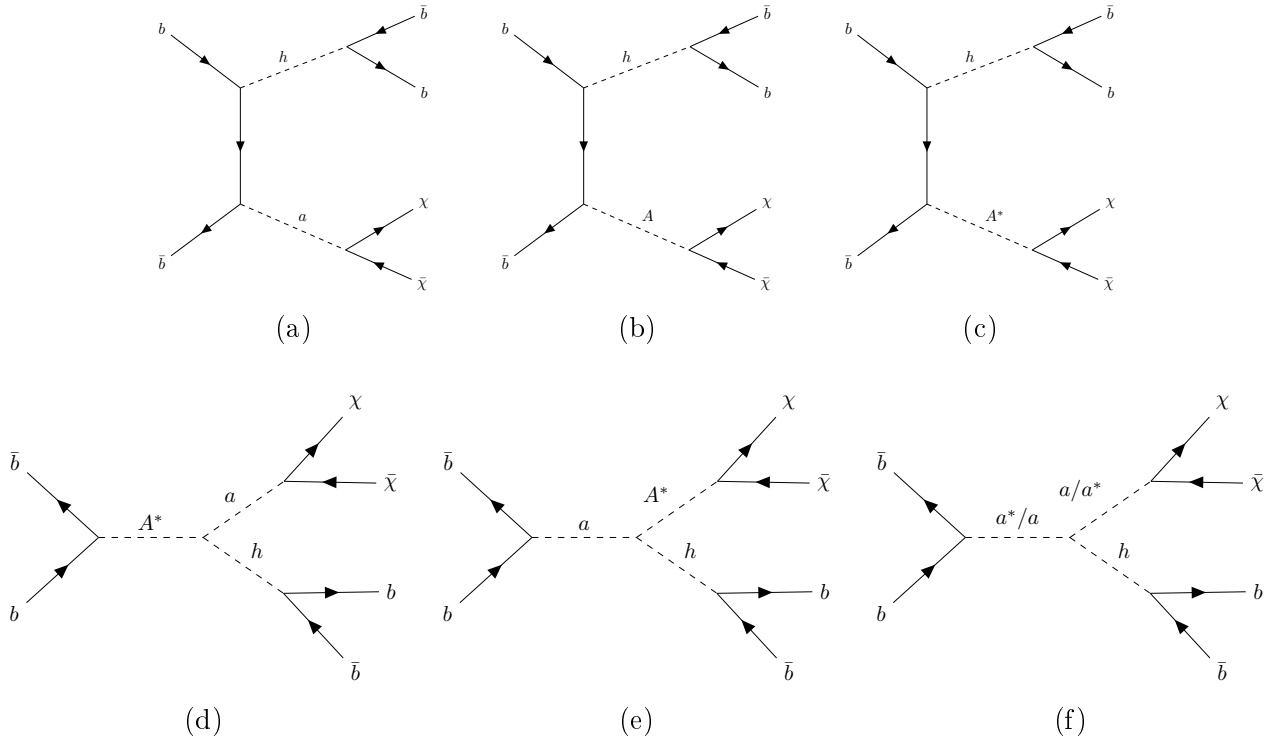

Figure 4.7: Non-resonant Feynman diagrams contributing to the $h(b\bar{b})+E_T^{\text{miss}}$ signature with $b\bar{b}$ in the initial state. The decay $h \to b\bar{b}$ is not part of the matrix element calculation, but instead simulated in the parton shower in the numerical simulation, which is described in Section 5.3.

The situation for $b\bar{b}$ initiated production is very similar. The analogous diagrams to the gluon fusion box diagrams in Figures 4.6(a) to 4.6(c) are diagrams with t-channel b quark exchange, displayed in Figures 4.7(a) to 4.7(c), which are suppressed relative to the resonant contribution in Figure 4.5. The resonant contribution exists whenever $M_A > M_a + M_h$. Depending on the other model parameters, it may not be the dominant contribution, since the diagrams in Figures 4.7(d) and 4.7(e) can dominate the cross section when Γ_A is large. Width suppressed diagrams like Figure 4.7(f) can be enhanced by extreme values of the corresponding coupling.

Resolving the ambiguity of where resonant processes do or do not contribute dominantly, and finding regions of parameter space where the resonant contribution is dominant, are the goals of the studies presented in Chapters 6 and 7, respectively.

Chapter 5

Strategy of the Parameter Scan Design

This Chapter discusses the overall strategy followed when designing, in Chapters 6 and 7, the benchmark parameter scans used in Chapter 8 to set limits on the parameters of the 2HDM+a introduced in Chapter 4. Section 5.1 describes the goals of the design of the 2HDM+a $h(b\bar{b}) + E_T^{\text{miss}}$ parameter scans. Then Section 5.2 briefly outlines the general strategy used to pursue those goals. Finally the numerical simulations used as the basis for these studies are described in Section 5.3.

5.1 Signal Grid Requirements

The aim of the study presented in this thesis is to find a set of 2HDM+a model parameters to be used in the interpretation of the ATLAS search for $h(b\bar{b}) + E_T^{\text{miss}}$ events. The ulterior motivation for a new interpretation of the search is to explore the sensitivity of this analysis to the 2HDM+a. This result can then be compared to the many other DM signatures in the 2HDM+a to expose the respective complementarity of the various Dark Matter signatures explored by the ATLAS and CMS collaborations. The first step towards this goal is to find a set of 2HDM+a model instances to study in the $h(b\bar{b}) + E_T^{\text{miss}}$ interpretation, that can be used as a general benchmark for other Dark Matter models and search channels. In other words, the goal is to find the regions of the 2HDM+a parameter space most relevant to $h(b\bar{b}) + E_T^{\text{miss}}$, without losing the capacity to meaningfully compare to other searches and models. This is challenging because of the large number of 14 model parameters. A resulting set of signal models, also called *signal grid*, should have the following properties:

- diverse signal kinematics
- sufficient sensitivity of existing searches, resulting from
  - sufficient signal cross sections
  - sufficient signal acceptance and efficiency
- exclusion potential beyond existing constraints, such that
  - directly excluded parameter space is avoided
  - indirect constraints are taken into account, but not when they limit the generality of the benchmark
- the diversity of complementary search channels is apparent

These goals are discussed in more detail in the following.

Diverse signal kinematics make the signal grid a representative benchmark demonstrating the full diversity of signals that may be constrained by the $h(b\bar{b}) + E_T^{\text{miss}}$ search. Exploring the full range of signal kinematics furthermore identifies corners of the phase space that have not been probed to date. Finally, it avoids erroneously optimizing the search for a small and very particular set of models going forward.

Sufficient sensitivity of the search to the signal grid, i.e. choosing signals that the search could discover if they were realized in nature, and could exclude otherwise. This requirement can be broken down by considering the requirements for high sensitivity:

Large enough signal cross-sections ensure that a measurably large number of signal events is predicted to be produced at the LHC. But the model is only used as a benchmark, and rescaling the predicted number of signal events to a higher value is straightforward to do by choosing model parameters. On the technical side this just increases the weights associated to each simulated event by a common factor. So this aspect of the sensitivity has a low priority.

Large enough signal acceptances and efficiencies ensure that there is a realistic probability for a signal event, once produced, to be measured and reconstructed in the detector, and then to pass the selection cuts of the analysis, as given in Section 3.4. Detector acceptance and selection efficiency are both determined by the kinematics of the signal event, i.e. the momenta of the final state particles. Event-by-event reweighting to obtain different kinematic distributions that yield higher acceptances and efficiencies is possible [111] but requires that all the phasespace one wants to reweight into is a subset of the phasespace covered by the (detector level) Monte Carlo sample on hand. Thus, unlike for the cross-section, it is crucial that the signal grid has sufficient acceptances and efficiencies, and as many phase space regions as possible are covered, since otherwise the signal samples are useless.

A parameter region not excluded already ensures that the search for this set of models has not been made redundant by existing studies. It is useful to distinguish existing constraints by how much their applicability to the $h(b\bar{b}) + E_T^{\text{miss}}$ search depends on model assumptions:

Direct constraints can be applied directly to the $h(b\bar{b}) + E_T^{\text{miss}}$ search, while introducing only a few or even no additional model assumptions. An extreme yet relevant example are existing searches for the same $h(b\bar{b}) + E_T^{\text{miss}}$ final state at ATLAS using another signal model. If the recasting of such a search unambiguously rules out a certain class of signal shape, a dedicated interpretation of the same data should not be expected to find deviations from the Standard Model. Thus the parameter space producing such clearly excluded signals is to be avoided in favor of parameter regions yielding signals that are close to, but not quite excluded, i.e. at the edge of the sensitivity. Other, less extreme examples include limits on the observed rate of $h \to inv.$ and measurements of the ρ parameter.

Indirect constraints rely on additional model assumptions to connect the constraining observation to the $h(b\bar{b}) + E_T^{\text{miss}}$ search.

One example would be the matching the observed relic density of Dark Matter, which assumes thermal Dark Matter production in the early universe, and identifying χ with all cold Dark Matter. Another example is requiring vacuum stability up to arbitrary field strengths, which assumes the theory remains a valid description of nature to arbitrary field strengths.

These constraints are strongly reliant on additional model assumptions beyond those inherently connected to the observable features of the $h(b\bar{b}) + E_T^{\text{miss}}$ signature.

The final set of signal samples is not just intended as a test of the 2HDM+a hypothesis specifically. Rather it should be a benchmark for the larger class of this and similar simplified models and their potential specifications into complete theories. Thus parameter regions that satisfy most or all of the indirect constraints are preferred regions in the parameter space. However, regions that break one or a few of these constraints can still be left as a part of the final set of benchmark models, since these constraints might not actually be broken by another model producing a similar signal at the LHC but with a different theoretical underpinning. This increases the generality of the result and reduces bias towards a particular kind of signal.

Diverse and complimentary search channels such as e.g. $h(b\bar{b}) + E_T^{\text{miss}}$, $h(\gamma\gamma) + E_T^{\text{miss}}$, $Z(ll) + E_T^{\text{miss}}$, jet $+ E_T^{\text{miss}}$, t $+ E_T^{\text{miss}}$ or $t\bar{t}$-resonance searches, allow thorough experimental tests of the 2HDM+a model. This is a key feature of the 2HDM+a simplified model, and should be apparent in the signal grid. Of course the main focus of the study is on the $h(b\bar{b}) + E_T^{\text{miss}}$ final state, but a parameter choice that predicts exclusively $h(b\bar{b}) + E_T^{\text{miss}}$ signals and no others would break this desired feature of the model.

5.2 Steps of the Study

The 2HDM+a simplified model is specified by 14 fundamental parameters [1], given in Table 4.1. The freedom of these 14 parameters is reduced by taking into consideration the constraints on the model discussed in Section 4.2. But considerable freedom remains, and it is necessary to understand the impact of the individual parameters on the signal to know which parameter values and variations result in interesting changes of signal kinematics, and how. This is the first step towards finding a grid with the properties outlined in Section 5.1. These studies of individual model parameters are described in Chapter 6.

Having understood how the different parameters affect the 2HDM+a signal, the signal grid is designed. Based on the previous study of individual parameters, a decision is made to fix some parameters and vary others. Parameters not affecting the signal, or only the signal cross section, can be kept fixed. Parameters that strongly impact the signal kinematics should be varied.

Next the sensitivity of the search for $h(b\bar{b}) + E_T^{\text{miss}}$ to these models is estimated. The sensitivity estimates are used to motivate specific choices of concrete values for the fixed and varied model parameters (parameter ranges). Furthermore, the necessary size of the signal samples to be produced at each parameter point is estimated. The studies of the signal grid design, and the phenomenological properties of the resulting signal grid are studied in Chapter 7.

Finally, in Chapter 8, limits on the 2HDM+a parameters are set using simulated detector level MC events generated according to the signal grid devised in Chapter 7 .

5.3 Event Generation

All studies of the properties of the $h(b\bar{b}) + E_T^{\text{miss}}$ signature in the 2HDM+a presented in Chapters 6 and 7 are performed at parton level. The event simulation and signal cross sections calculation for these chapters is performed using version 2.4.3 of the parton-level event generator MadGraph 5 (MG5_aMC@NLO) [112]. It includes automatic loop computation and

one-loop integral reduction tools [113, 114, 115], which are used to evaluate the gluon fusion top-loops occurring in the production mode that dominates most of the studied parameter space. The decay rates of the A, a, H, $H^{\pm}$, and h particles are computed using the corresponding tool distributed with MadGraph 5 [116]. The 2HDM+a is implemented using a Universal FeynRules Output [117] implementation provided by the authors of [1]. The leading order NNPDF30_lo_as_0130 set of parton distribution functions (PDFs) [118] is used in the matrix element calculation. It assumes a value of the strong coupling parameter of $\alpha_S(m_Z) = 0.130$ and massless b-quarks that occur in the proton as sea quarks. Thus the mass of the b quark is set as $m_b = 0$ in MadGraph 5 as well.

The generation of the simulated events used to set the limits on 2HDM+a parameters presented in Chapter 8 use identical settings to generate the matrix elements and cross sections. However, since these events are simulated up to and including the level of the ATLAS detector, more tools are used in addition to what is stated above. The parton shower and subsequent hadronization of the parton level events resulting from the matrix element calculation is done with Pythia8 [119], with several parameters tuned to obtain a better match of data and simulation when generating events with the NNPDF2.3 pdf sets. The interaction with the ATLAS detector is simulated with Geant4 [120, 81].

Chapter 6

Studies of Individual Model Parameters

This Chapter describes the results of detailed studies of the individual 2HDM+a model parameters with respect to their effect on the $h(b\bar{b}) + E_T^{\text{miss}}$ final state. Specifically, the studies focus on the E_T^{miss} observable since it is crucial to the $h(b\bar{b}) + E_T^{\text{miss}}$ search. The production cross section of signal events is considered as well. E_T^{miss} is the focus because the kinematics are not trivial to change by reweighting after the fact, and essential to the usefulness of the model as a benchmark, as discussed in more detail in Section 5.1. Having in this Chapter determined which parameters affect the signal kinematics, the cross section, neither, or both, the parameters with interesting effects on the kinematics are then scanned in the design of the set of benchmark models in Chapter 7. Parameters with no impact on the signal kinematic are instead fixed in the scans in Chapter 7.

6.1 Mass of the Heavy CP-odd Scalar Boson: M_A

6.1.1 Resonant Signals

The two crucial kinematic parameters are the masses of the pseudoscalars, M_A and M_a, if the mono-h signal process is in the resonant channel depicted in Figure 4.4, As discussed in Section 4.3.1, M_A and M_a determine the location of the Jacobian peak according to Equation (4.13), dominating the shape of the E_T^{miss} distribution.

The Jacobian peak in the E_T^{miss} distribution shifts to higher values with increasing M_A, as shown in Figure 6.1. This is a kinematic effect. At high M_A $\sqrt{s} = M_{h\chi\bar{\chi}}$ in the hard matrix element is large, since the $M_{h\chi\bar{\chi}}$ distribution is resonantly enhanced around the A pole at M_A. This is shown in Figure 6.2(a). $\sqrt{s} = M_{h\chi\bar{\chi}}$ is distributed among the products of the A decay, but the invariant mass of the Dark Matter system $M_{\chi\bar{\chi}}$ remains sharply peaked around M_a, as Figure 6.2(b) shows. As a result the momentum of the Dark Matter fermions $\chi\bar{\chi}$ relative to the light Higgs h, and thus the E_T^{miss}, is increased.

The $M_{h\chi\bar{\chi}}$ distributions shown in Figure 6.2(a) feature a smaller, secondary peak at $M_{h\chi\bar{\chi}} = M_a = 300\,\text{GeV}$ as well as a broad distribution stretching from $M_{h\chi\bar{\chi}} = M_a + M_h = 425\,\text{GeV}$ to the peak at $M_{h\chi\bar{\chi}} = M_A$. These features come from non-resonant contributions such as those shown in Figure 4.6(e) and Figure 4.6(a), respectively.

The structure of the correlations of $M_{\chi\bar{\chi}}$ and $M_{h\chi\bar{\chi}}$ shown in Figure 6.3(a) match the above interpretation. The majority of events cluster around the point $M_{h\chi\bar{\chi}} = M_A = 700\,\text{GeV}$, $M_{\chi\bar{\chi}} = M_a = 300\,\text{GeV}$, corresponding to resonant $A \to ha$ decays as shown in Figure 4.4. The non-resonant contributions from Figure 4.6(e) result in the cluster of events around $M_{h\chi\bar{\chi}} = M_a = 300\,\text{GeV}$ and have $M_{\chi\bar{\chi}}$ restricted to $\leq M_a - M_h = 175\,\text{GeV}$, since $M_{h\chi\bar{\chi}} \geq M_{\chi\bar{\chi}} + M_h$ by

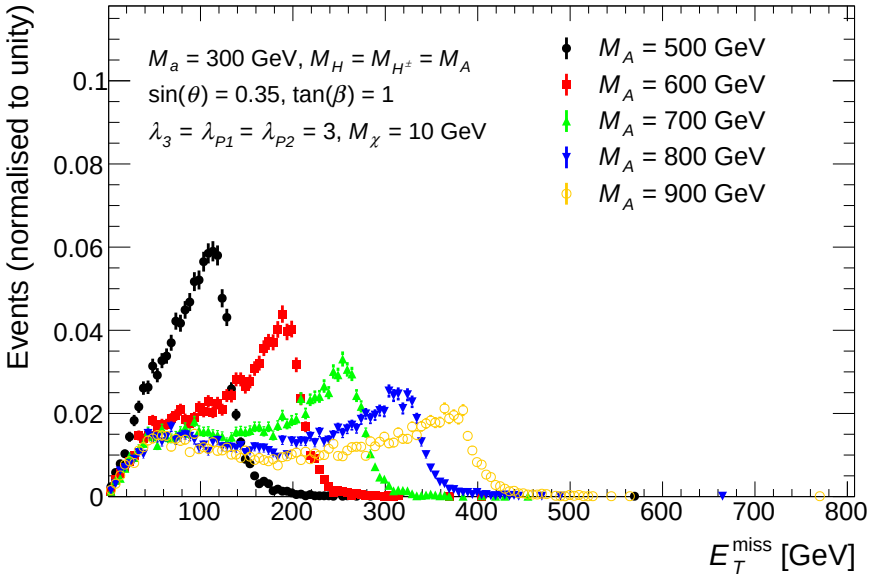

Figure 6.1: E_T^{miss} distribution at parton level of $h \to bb + E_T^{\text{miss}}$ signal events for five representative models with different $M_A (= M_H = M_{H^\pm})$ and fixed $M_a = 300$ GeV, $\sin\theta = 0.35, \tan\beta = 1, M_\chi = 10$ GeV, and $\lambda_{P1} = \lambda_{P2} = \lambda_3 = 3$.

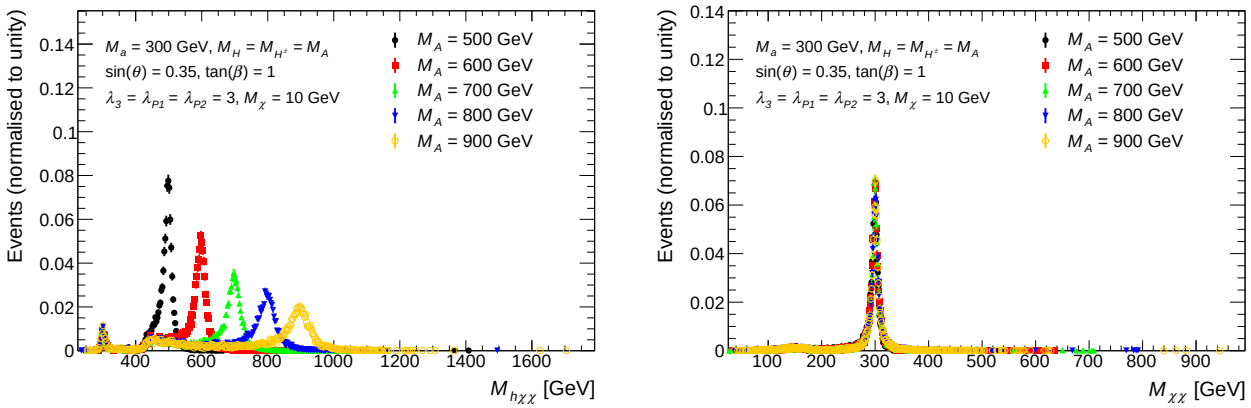

(a) $M_{h\chi\bar{\chi}}$ distributions for varied M_A

(b) $M_{\chi\bar{\chi}}$ distributions for varied M_A

Figure 6.2: Effect of M_A variations on the distributions of $M_{h\chi\bar{\chi}}$ (shown in (a)) and of $M_{\chi\bar{\chi}}$ (shown in (b)) for models with mostly resonant signals. The other parameters have the values $M_A (= M_H = M_{H^\pm})$,$M_a = 300$ GeV, $\sin\theta = 0.35, \tan\beta = 1, M_\chi = 10$ GeV, and $\lambda_{P1} = \lambda_{P2} = \lambda_3 = 3$

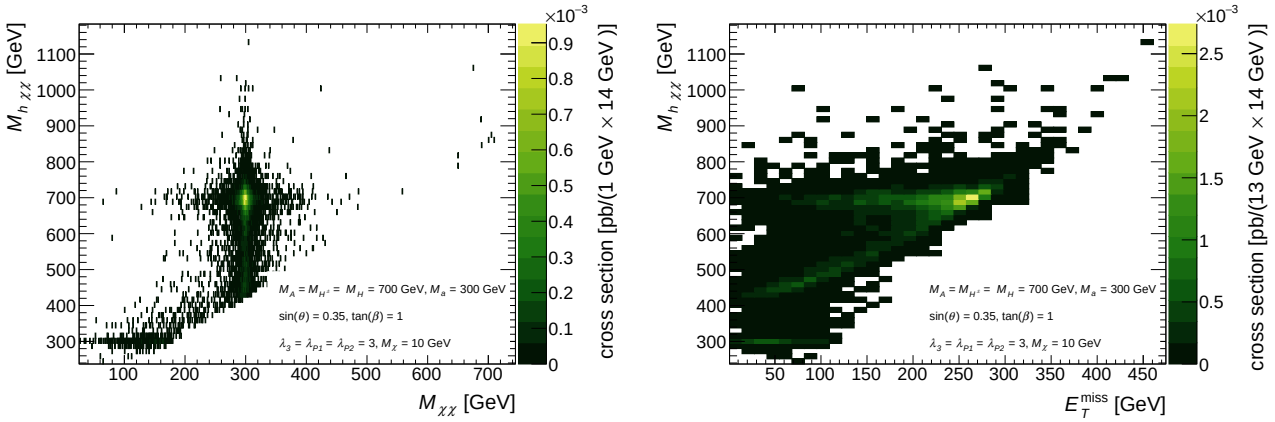

(a) Histogram of $M_{\chi\bar{\chi}}$ and $M_{h\chi\bar{\chi}}$

(b) Histogram of E_T^{miss} and $M_{h\chi\bar{\chi}}$

Figure 6.3: Correlation of kinematic parameters in simulated parton level signal events. $M_{\chi\bar{\chi}}$ and $M_{h\chi\bar{\chi}}$ are mostly uncorrelated and sharply peaked around M_a and M_A, respectively, as shown in (a). E_T^{miss} and $M_{h\chi\bar{\chi}}$ are correlated in a nonlinear and non-unimodal way, as displayed in (b). The shown model has the parameters $M_A = 700\,\text{GeV}$, $M_a = 300\,\text{GeV}$, $M_H = M_{H^\pm} = M_A$, $\sin\theta = 0.35$, and $\tan\beta = 1.0$, $\lambda_{P1} = \lambda_{P2} = \lambda_3 = 3$.

definition. The contributions shown in Figures 4.6(a) and 4.6(e) correspond to the vertical line at constant $M_{\chi\bar{\chi}} = M_a = 300\,\text{GeV}$ extending from $M_{h\chi\bar{\chi}} = M_a + M_h = 425\,\text{GeV}$ to the peak at $M_{h\chi\bar{\chi}} = M_A = 700\,\text{GeV}$.

The correlation of E_T^{miss} and $M_{h\chi\bar{\chi}}$, shown in Figure 6.3(b), demonstrate how the different resonant and non-resonant processes give rise to the E_T^{miss} distribution. The dominant contribution of resonant events at $M_{h\chi\bar{\chi}} = M_A = 700\,\text{GeV}$ show some small variation due to the width of the resonance, i.e. harder E_T^{miss} for events at $M_{h\chi\bar{\chi}}$ a bit above M_A and vice versa. But most of the width of the E_T^{miss} spectrum is due to the transverse projection of the full $\chi\bar{\chi}$ momentum, and thus it is not correlated with $M_{h\chi\bar{\chi}}$. Processes away from the A resonance, such as those shown in Figures 4.6(a) and 4.6(d) give rise to a cluster of events where $M_{h\chi\bar{\chi}}$ and E_T^{miss} are strongly correlated, due to the requirement that $M_{\chi\bar{\chi}} = M_a$. Finally there is the contribution shown in Figure 4.6(e) at $M_{h\chi\bar{\chi}} = M_a$ and soft E_T^{miss}. Overall, Figure 6.3(b) matches what one expects for a model with mostly resonant signal events and thus a E_T^{miss} distribution dominated by a Jacobian peak.

In conclusion, for models with predominantly resonant signal production, M_A shifts the $M_{h\chi\bar{\chi}}$ resonance and thus the Jacobian peak in the E_T^{miss} distribution in accordance with Equation (4.13). This behavior can be used to generate signals with varied kinematics, and which is desirable as a benchmark. Thus M_A is varied in the set of signal models used for the search described in Chapter 7, and other parameters are chosen to enhance the resonant channel.

6.1.2 Non-Resonant Signals

If the dominant signal process is non-resonant, i.e. *not* the process $A \to ha(\to \chi\bar{\chi})$ shown in Figure 4.4 with a and A on their respective mass shells (cf. Section 4.3.3), M_A variations have no effect on the E_T^{miss} distribution. This is shown in Figure 6.4(a). Since A can be strongly off-shell due to its typically large width, the location of the A pole does not affect the signal process, as Figure 6.4(b) demonstrates. Yet M_A does have an effect on the width of A, Γ_A, shown in Figure 6.4(c). This is because it directly affects the trilinear scalar coupling g_{Aah},

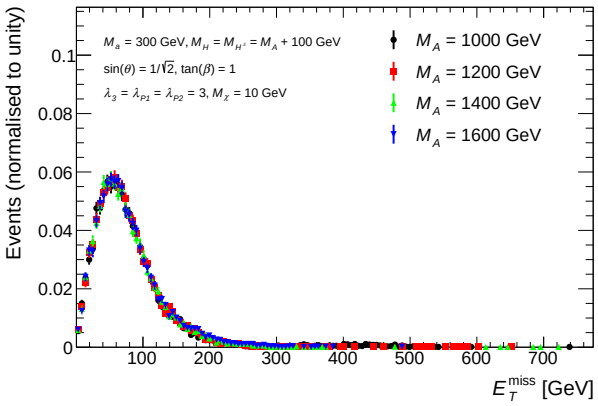

(a) Effect of M_A on E_T^{miss}-shape

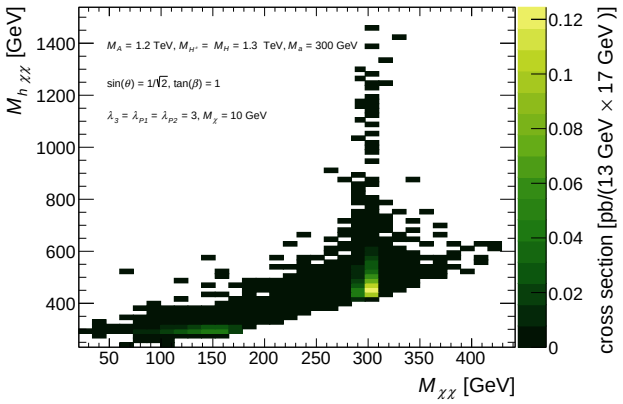

(b) $M_{h\chi\bar{\chi}}$-$M_{\chi\bar{\chi}}$ distribution

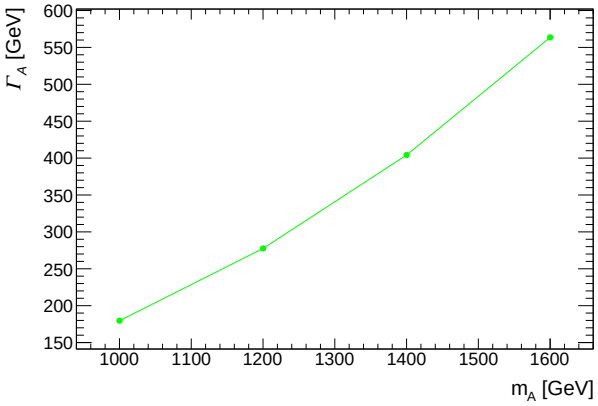

(c) Effect of M_A on Γ_A

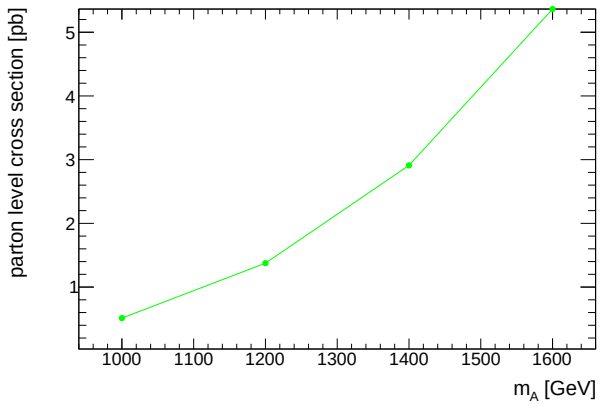

(d) Effect of M_A on the total cross-section

Figure 6.4: Example of models where the signal is mostly one single non-resonant process. Changes in M_A have no effect on the shape of the E_T^{miss} distribution, which is shown in (a). (b) shows how signal events tend to cluster kinematically around the mass scales of the lightest scalar and pseudoscalar, M_h and M_a, irrespective of M_A. Increasing M_A increases the Γ_A, shown in (d), and the cross section, shown in (c). The values of the remaining parameters are $M_a = 300$ GeV, $M_H = M_{H^\pm} = M_A + 100$ GeV, $\sin\theta = 1/\sqrt{2}$, $\tan\beta = 1, \lambda_3 = \lambda_{P1} = \lambda_{P2} = 3$, and $M_\chi = 10$ GeV.

given in Equation (4.6). As a result, M_A variations change the cross-section, as shown in Figure 6.4(d), but not the kinematics, as demonstrated in Figure 6.4(a).

In the general case, both non-resonant production and resonant production $A \to ha(\to \chi\bar{\chi})$ can occur with similar yields in one model. The resulting E_T^{miss} spectra exhibit a superposition of the resonant and non-resonant signals. The soft-E_T^{miss} non-resonant distribution stays soft, independently of M_A. It contributes a larger or smaller fraction of all events, depending on M_A and other parameters. Conversely, the resonant contribution peaks at different E_T^{miss} values, depending on the value of M_A. This superposition of resonant and non-resonant processes is typical for the $h(b\bar{b}) + E_T^{\text{miss}}$ signature as predicted by the 2HDM+a.

The total decay widths Γ_a and Γ_A control how far off-shell the mediators a and A are allowed to be. Thus they change the relative resonant and non-resonant yield. The decay widths, and thus relative on-shell and off-shell amplitudes of the signal process, are affected by many model parameters. M_A itself has a significant effect, as does M_a, which is discussed in Section 6.2. Moreover, the relative amplitudes of on- and off-shell processes are also affected by the scalar masses M_H and $M_{H^\pm}$, as discussed in Section 6.3, the pseudoscalar mixing parameter $\sin\theta$, as discussed in Section 6.4, the ratio of the vacuum expectation values of the two doublets $\tan\beta$, as discussed in Section 6.5, and the free quartic couplings λ_3, λ_{P1}, and λ_{P2}, discussed in Section 6.6.

In conclusion, the non-resonant channel does not exhibit any E_T^{miss} dependence on M_A. This runs counter to the idea of scanning through E_T^{miss} shapes by varying M_A, which is possible with the resonant channel (c.f. Section 6.1.1). Thus the parameter choices in the final design of the parameter scan in Chapter 7 aim to reduce this contribution as much as possible by keeping Γ_A small.

6.1.3 Interference Effects

In any Feynman diagrams contributing to the signal, one can replace A lines with a lines and vice versa, and obtain another valid Feynman diagram. Examples include Figures 4.6(a) and 4.6(b), or Figures 4.4 and 4.6(e). Because the initial and final states of these graphs are identical, they can interfere. A and a are related by a mixing matrix, written in Equation (4.5), which is the matrix of two-dimensional rotations by the mixing angle θ. The off-diagonal entry, $\sin\theta$, is positive above the diagonal and negative below it. Thus the individual amplitudes after exchanging a for A or vice versa incur a relative sign for each vertex $\propto (\sin\theta)^{2n+1}$. This results in destructive interference, reducing the signal cross section. Figure 6.5 demonstrates the effect of the interference on the signal cross section for different mass and mixing angle configurations.

The interference term is negligible when the pseudoscalar masses are sufficiently different. This is because different pseudoscalar masses cause the interfering diagrams to cover mostly disjunct regions of phase space. However, when the pseudoscalars are exactly mass degenerate, there is strong destructive interference, as for the case $M_A = M_a = 200\,\text{GeV}$, shown in Figure 6.5.

The interference is strongest for maximal mixing, i.e. at $\sin\theta = 1/\sqrt{2}$, and weaker for higher or lower $\sin\theta$. This is because $\sin\theta = 1/\sqrt{2}$ represents exactly equal mixing, i.e. a and A can only be distinguished by their masses. For $M_A = M_a$, the amplitudes for the $a - A$ switched diagrams are equal up to a negative sign originating from the off-diagonal entry in the $a - A$ mixing matrix, and the destructive interference is maximal.

The interference effects observed in the simulations are similar to those previously described in Ref. [1], but for the $t\bar{t} + E_T^{\text{miss}}$ and jet $+ E_T^{\text{miss}}$ signatures in the 2HDM+a, including the dependence on $\sin\theta$ and the pseudoscalar masses. However, [1] also describes constructive

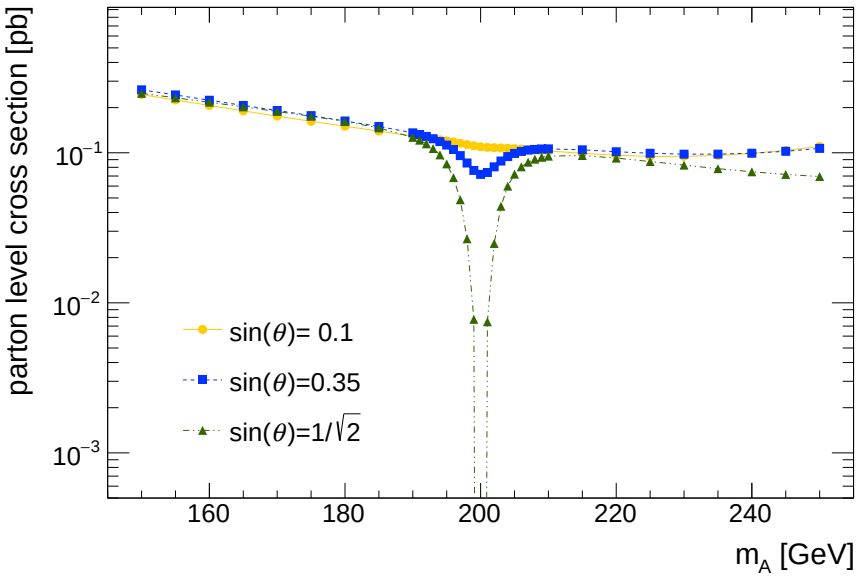

Figure 6.5: Effect of $A - a$ interference on the $h(b\bar{b}) + E_T^{\text{miss}}$ production cross-section for various models with varied M_A, for 3 ensembles of models with $\sin\theta = 0.1, 0.35, 1/\sqrt{2}$. For $\sin\theta = 1/\sqrt{2}$ the cross-section at $M_A = M_a = 200$ is not plotted, since the cross section is less than 10^{-13} pb. The other parameters have the values $M_a = 200\,\text{GeV}, M_H = M_{H^\pm} = M_A + 100\,\text{GeV}, \tan\beta = 1, \lambda_3 = \lambda_{P1} = \lambda_{P2} = 3$, and $M_\chi = 10\,\text{GeV}$.

interference in parts of the parameter space, which does not seem to occur for the $h(b\bar{b}) + E_T^{\text{miss}}$ signature studied here.

6.2 Mass of the Light *CP*-odd Scalar Boson: M_a

6.2.1 Resonant signals

If the signal process is in the resonant s-channel $A \to ha(\to \chi\bar{\chi})$ from Figure 4.4 , with on-shell kinematics such as shown in Figure 6.3, M_a has a large effect on the shape of the E_T^{miss} distribution, as Figure 6.6 demonstrates.

In the resonant case, an on-shell a is produced in association with the Standard Model-like Higgs boson h in the A decay. The total energy available to the products of the A decay, $\sqrt{s}$, is shown as $M_{h\chi\bar{\chi}}$ in Figure 6.7(a). In the resonant case this available energy is fixed by M_A, corresponding to the strong peak around $M_{h\chi\bar{\chi}} = M_A = 700$ GeV. The mass of the Dark Matter pair $M_{\chi\bar{\chi}}$, shown in Figure 6.7(b), has a narrow resonant enhancement at the a pole $M_{\chi\bar{\chi}} = M_a$. The energy used for the a mass does not contribute to the momentum of a relative to h. Thus a higher M_a means that the momentum of a relative to h is reduced. As a result, the Jacobian peak as introduced in Section 4.3.1 is shifted to lower values, in accordance with Equation (4.13). Consequently, higher M_a corresponds to softer E_T^{miss} in the resonant case, as shown in Figure 6.6.

As in the case of M_A described in Section 6.1, this E_T^{miss} variation with M_a is desired for the final set of signal models discussed in Chapter 7, in order to have a set of models with varied E_T^{miss} distributions.

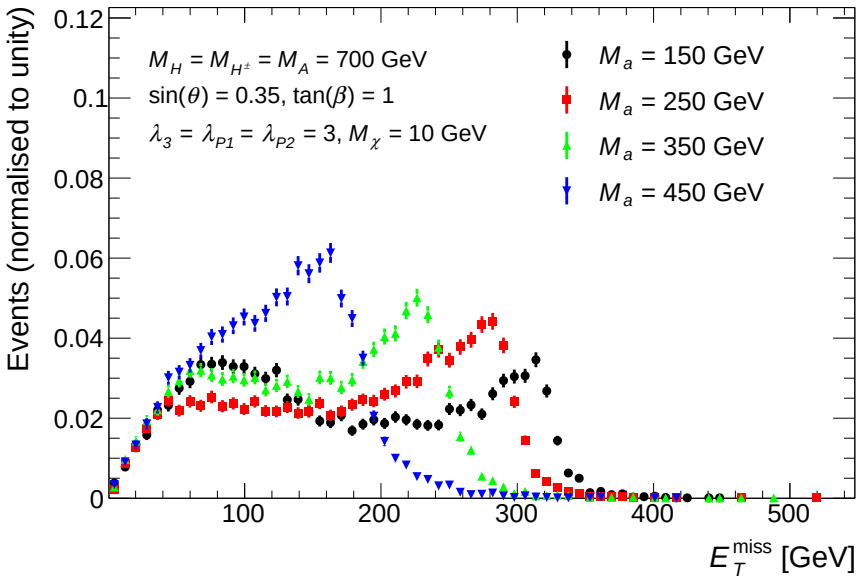

Figure 6.6: Missing transverse momentum distribution in $h \to bb{+}E_T^{\text{miss}}$ signal events at parton level for four representative models with different M_a and fixed $M_A = M_H = M_{H^\pm} = 700$ GeV, $\sin\theta = 0.35, \tan\beta = 1, M_\chi = 10$ GeV, and $\lambda_{P1} = \lambda_{P2} = \lambda_3 = 3$.

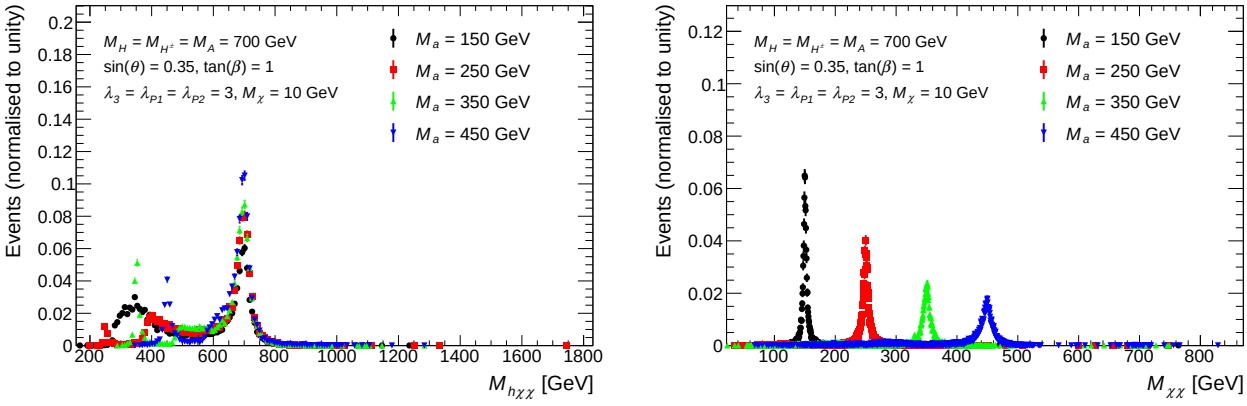

(a) $M_{h\chi\bar{\chi}}$ distributions for varied M_a

(b) $M_{\chi\bar{\chi}}$ distributions for varied M_a

Figure 6.7: Effect of M_a variations on the distributions of $M_{h\chi\bar{\chi}}$, shown in (a), and of $M_{\chi\bar{\chi}}$, displayed in (b) for models with mostly resonant signals. The other parameters values are $M_A = M_H = M_{H^\pm} = 700$ GeV, $\sin\theta = 0.35, \tan\beta = 1, M_\chi = 10$ GeV, and $\lambda_{P1} = \lambda_{P2} = \lambda_3 = 3$

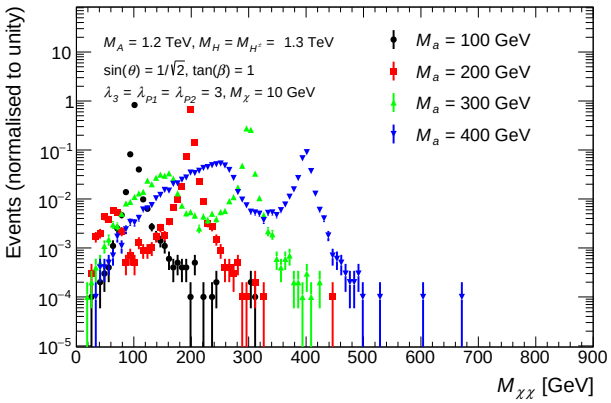

(a) Effect of M_a on $M_{\chi\bar{\chi}}$ distribution

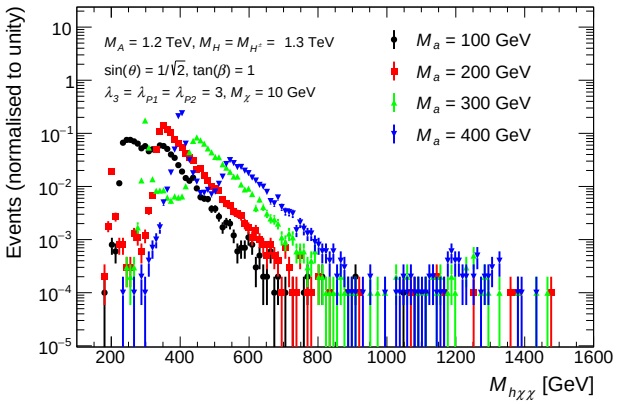

(b) Effect of M_a on $M_{h\chi\bar{\chi}}$ distribution

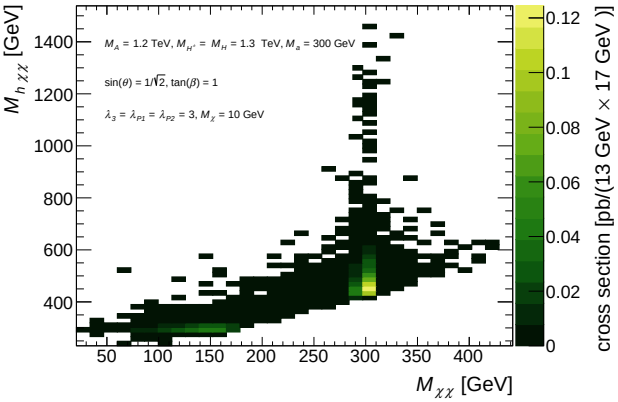

(c) Correlation of $M_{h\chi\bar{\chi}}$ and $M_{\chi\bar{\chi}}$

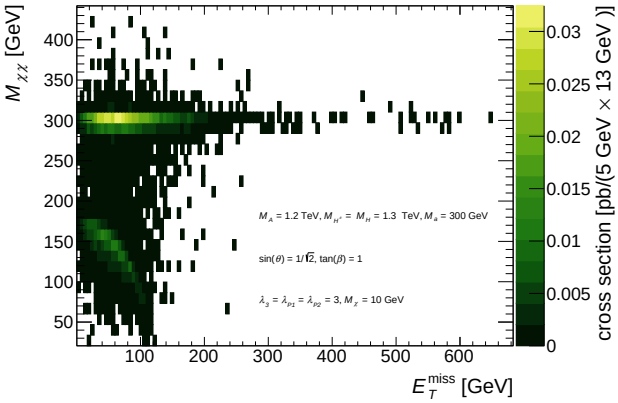

(d) Correlation of E_T^{miss} and $M_{\chi\bar{\chi}}$

Figure 6.8: Effects of M_a variation on non-resonant signals. For non-resonant signals, $M_{\chi\bar{\chi}}$ nevertheless has a peak around M_a, as shown in (a). Changing M_a affects $M_{h\chi\bar{\chi}}$, which is shown in (b), since $M_{h\chi\bar{\chi}}$ is correlated with $M_{\chi\bar{\chi}}$. There is also a residual E_T^{miss}-$M_{\chi\bar{\chi}}$ correlation, shown in (d). The remaining parameters have the values $M_A = 1200\,\text{GeV}, M_H = M_{H^\pm} = 1300\,\text{GeV}, \sin\theta = 1/\sqrt{2}, \tan\beta = 1$, $\lambda_3 = \lambda_{P1} = \lambda_{P2} = 3$, and $M_\chi = 10$ GeV.

6.2.2 Non-resonant signals

For the examples given in Figures 6.6 and 6.7, even though most of the signal is due to the resonant process, there are some non-resonant contributions. These non-resonant contributions can be seen in Figure 6.7(a), where they form the peaks at $M_{h\chi\bar{\chi}} = M_a$ and $M_{h\chi\bar{\chi}} = M_a + M_h$. The peak at $M_{h\chi\bar{\chi}} = M_a$ corresponds to the non-resonant amplitude for $a \to h + A^*(\to \chi\bar{\chi})$ displayed in Figure 4.6(e), whereas the peak at $M_{h\chi\bar{\chi}} = M_a + M_h$ corresponds to the non-resonant amplitude of diagrams such as those shown in Figures 4.6(a) and 4.6(e). These non-resonant processes do not yield strong secondary peaks in Figure 6.7(b) because a is usually on-shell, even in off-shell diagrams, whereas A has a large enough width that decays $A^* \to \chi\bar{\chi}$ have broad $M_{\chi\bar{\chi}}$ distributions.

If the signal process is predominantly non-resonant, M_a still affects the event kinematics, as Figure 6.8 demonstrates. The reason why M_a can still affect the kinematics is that $\Gamma_a \ll \Gamma_A$ for $M_a < M_A$, as shown in Figures 6.9(a) and 6.9(b). Hence a is often on-shell even for many models where there are mostly or only non resonant signal events with off-shell A decays. The exact M_a dependence is not trivial, because there is an interplay of several non-resonant

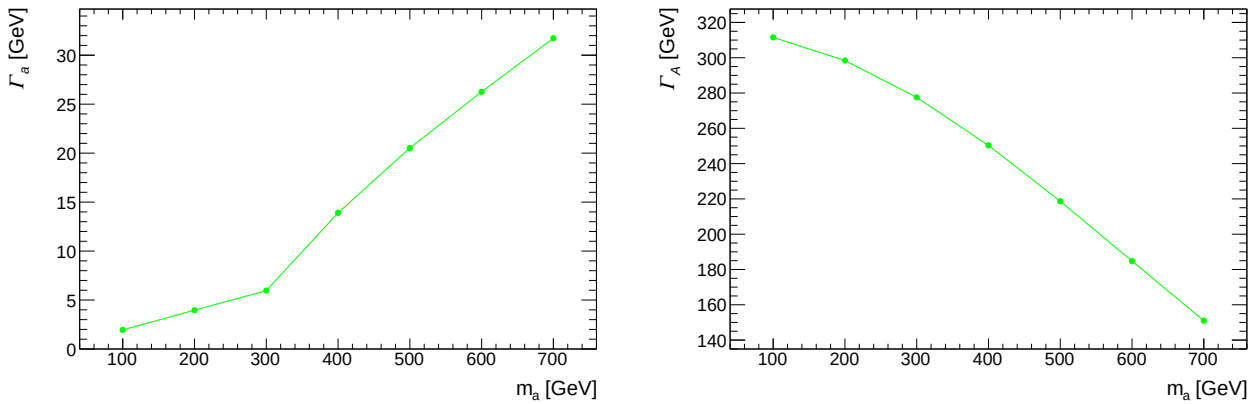

(a) Effect of M_a on Γ_a

(b) Effect of M_a on Γ_A

Figure 6.9: Effect of M_a variations on the width of the light pseudoscalar a, shown in (a), and the width of the heavy pseudoscalar A, shown in (b), for models with mostly non resonant $h(b\bar{b}) + E_T^{\text{miss}}$ production. The remaining parameters have the values $M_A = 1200\,\text{GeV}, M_H = M_{H^\pm} = 1300\,\text{GeV}, \sin\theta = 1/\sqrt{2}, \tan\beta = 1$, $\lambda_3 = \lambda_{P1} = \lambda_{P2} = 3$, and $M_\chi = 10$ GeV.

contributions, as discussed in the following.

There are two kinds of non-resonant processes with an on-shell internal a:

1. **Contributions with internal $a \to \chi\bar{\chi}$ decay:** These consist of $A^* \to ha(\to \chi\bar{\chi})$, as shown in Figure 4.6(d) and the box diagram radiating an on-shell a, which is shown in Figure 4.6(a).

   These contributions give rise to a sharp peak in the $M_{\chi\bar{\chi}}$ distribution, which is displayed in Figure 6.8(a). This is because the $\chi\bar{\chi}$ are the decay products of the on-shell a.

   In the $M_{h\chi\bar{\chi}}$ distribution which is shown in Figure 6.8(b) these contributions yield a broad distribution, rising steeply from 0 at $M_{h\chi\bar{\chi}} \lesssim M_a + M_h$. This steeply rising slope is due to the nonzero Γ_a (which is typically $\gg \Gamma_h \approx \mathcal{O}(10^{-3}\,\text{GeV})$). After reaching its maximum at $M_{h\chi\bar{\chi}} = M_a + M_h$, the distribution then drops exponentially towards higher masses. The handful of events at masses beyond the exponential drop are not part of the dominant non-resonant components, but instead are the few resonant events still present in these models.

   This interpretation of the individual distributions of $M_{h\chi\bar{\chi}}$ and $M_{\chi\bar{\chi}}$ holds up when considering the two-dimensional distribution of events in the $M_{\chi\bar{\chi}} - M_{h\chi\bar{\chi}}$ plane, shown for the example of $M_a = 300\,\text{GeV}$ in Figure 6.8(c). The falling $M_{h\chi\bar{\chi}}$ spectrum only occurs in the $M_{\chi\bar{\chi}} = M_a = 300$ GeV slice, and for other $M_{\chi\bar{\chi}}$ slices above $M_{\chi\bar{\chi}} = M_h + 2M_\chi = 145$ GeV the distribution in $M_{h\chi\bar{\chi}}$ is mostly flat and the cross section is smaller. These flat regions in the $M_{h\chi\bar{\chi}} - M_{\chi\bar{\chi}}$ plane are populated by fully non-resonant events where neither a nor A are on shell, as shown in Figure 4.6(c). Such events are strongly suppressed because both a and A are off-shell.

   The broadness of the $M_{h\chi\bar{\chi}}$ distribution reflects the fact that the overall energy scale of these events is only given by the momentum scales of the incoming partons (i.e. the gluon PDFs) and not fixed by any mass pole. $M_{\chi\bar{\chi}}$ is fixed by the a pole, hence any available energy beyond M_a yields relative momentum between h and the $\chi\bar{\chi}$ system, resulting in a soft, falling E_T^{miss} distribution, as shown in Figure 6.8(d). The increased energy required for higher M_a is never available as E_T^{miss}, since it is by definition bound

up in the $\chi\bar{\chi}$ mass. Thus the changes to the E_T^{miss} distribution due to these contributions with an internal $a \to \chi\bar{\chi}$ decay are small.

2. **Contributions with an on-shell a in the s-channel:** These consist of $a \to hA^*(\to \chi\bar{\chi})$ processes such as shown in Figure 4.6(e).

   This configuration gives rise to a sharp peak around M_a in the $M_{h\chi\bar{\chi}}$ distribution, as demonstrated in Figure 6.8(b). This is because $M_{h\chi\bar{\chi}} = \sqrt{s}$, and a is an s-channel resonance for this contribution. Thus this contribution is kinematically inaccessible for $M_h + 2M_\chi > M_a$, and does not occur. An example is the case of $M_a = 100$ GeV, shown in Figure 6.8(b) as black dots, with are no events below $M_{h\chi\bar{\chi}} = M_h + 2M_\chi = 145$ GeV, and thus no peak at $M_{\chi\bar{\chi}} = M_a = 100$ GeV.

   The $M_{\chi\bar{\chi}}$ distribution associated with this process is very broad, as shown in Figure 6.8(a). It rises slowly from 0 for $M_{\chi\bar{\chi}} < 2M_\chi$ up to $M_{\chi\bar{\chi}} = M_a - M_h$, where it drops sharply because a needs to be off shell in such events, which is suppressed by the small Γ_a. For the example of $M_a = 300$ GeV this behavior is demonstrated in Figure 6.8(c), where the $a \to hA^*(\to \chi\bar{\chi})$ generates the cluster of events around $M_{h\chi\bar{\chi}} = 300$ GeV. The energy available to form relative momentum between the h and the $\chi\bar{\chi}$ system is limited, because $\sqrt{s} = M_{h\chi\bar{\chi}}$ is fixed to M_a. Thus E_T^{miss} and $M_{\chi\bar{\chi}}$ are anti-correlated in this mode, and this anti-correlation is visible in the lower left corner of the two dimensional $E_T^{\text{miss}} - M_{\chi\bar{\chi}}$ distribution shown in Figure 6.8(d).

   Because a is the s-channel mediator for this contribution , and A^* is the mediator decaying to $\chi\bar{\chi}$, increasing M_a can make the E_T^{miss} distribution *harder*.

The first class of non-resonant processes yield soft, falling E_T^{miss} distributions, which are very similar for different M_a. The second class yields E_T^{miss} distributions that can be a bit harder for at higher M_a, e.g comparing the $M_a = 300$ GeV distribution to the $M_a = 400$ GeV one, shown in Figure 6.10. The non-resonant E_T^{miss} distributions for different M_a, shown in Figure 6.10 are overall similar, and especially at soft E_T^{miss}, because the first contribution is the dominant one. The second contribution causes small changes of the E_T^{miss} distribution. One example is the case of $M_a = 100\,\text{GeV}$, where the E_T^{miss} distribution differs from the other examples shown because this second class of signal processes does not contribute. Thus, changes in M_a can still affect the shape of the E_T^{miss} distribution in the non-resonant case.

The overall E_T^{miss} distribution is still mostly soft, however, regardless of the value of M_a. Moreover the effect of M_a on the E_T^{miss} of non-resonant events is small compared to the effect on resonant events. For these two reasons non-resonant events are not wanted when varying M_a in the set of signal models described in Chapter 7. Therefore when scanning M_a, the aim is to keep Γ_A small, and the other parameters are adjusted accordingly.

6.2.2.1 Cross Section

Besides the E_T^{miss} shape, M_a also affects the $h(b\bar{b}) + E_T^{\text{miss}}$ production cross section, as demonstrated in Figure 6.11. The cross section drops with increasing M_a. Several effects contribute to this:

- The width of A, which defines the Breit-Wigner suppression of non-resonant contributions involving off-shell A lines such as those shown in Figure 4.6(d), decreases as M_a is increased. This is demonstrated in Figure 6.9(b). The reason for this width decrease is that increasing M_a reduces the phase space open to resonant A decays such as $A \to aa$ or $A \to ah$, which contribute strongly to the total Γ_A.

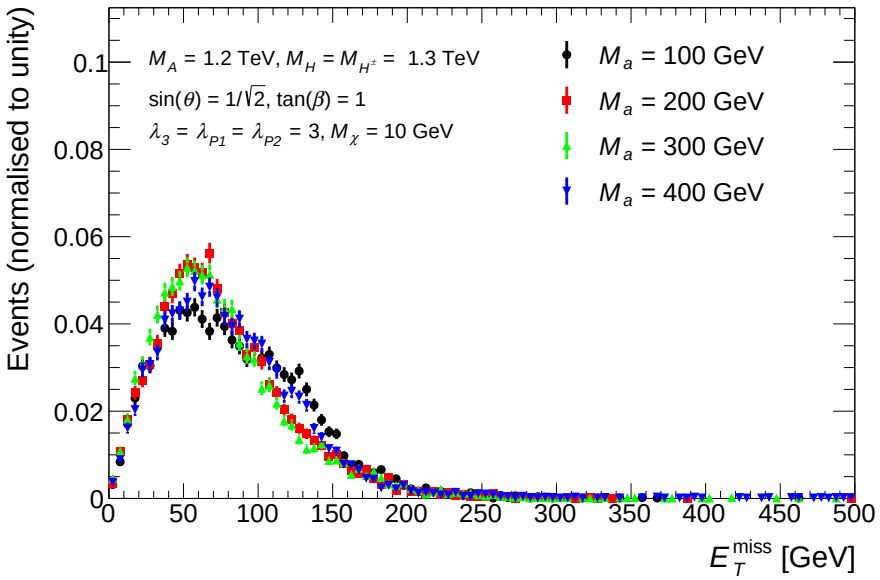

Figure 6.10: Missing transverse momentum distribution in non-resonant $h \to bb + E_T^{\text{miss}}$ signal events at parton level for four representative models with different M_a. The remaining parameters have the values $M_A = 1200\,\text{GeV}, M_H = M_{H^\pm} = 1300\,\text{GeV}, \sin\theta = 1/\sqrt{2}, \tan\beta = 1$, $\lambda_3 = \lambda_{P1} = \lambda_{P2} = 3$, and $M_\chi = 10$ GeV

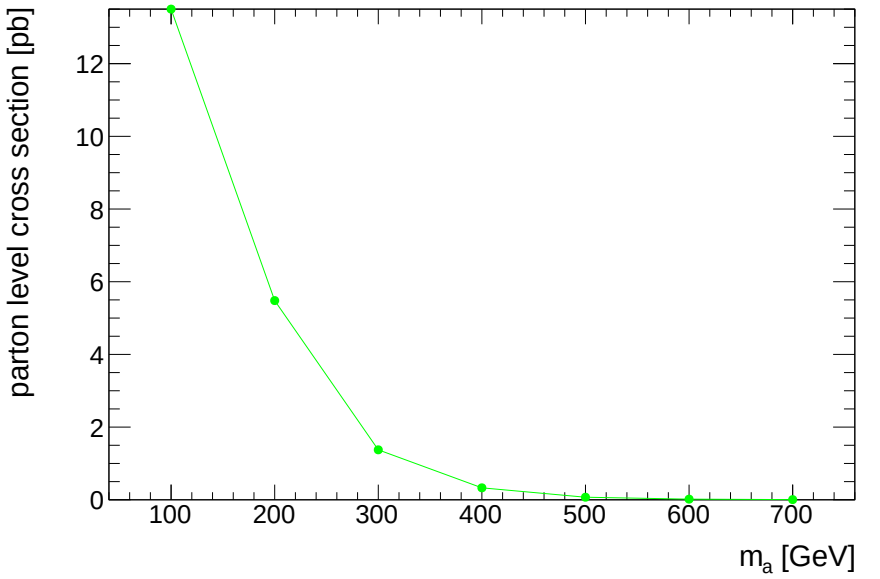

Figure 6.11: $h(b\bar{b}) + E_T^{\text{miss}}$ production cross section scaling with M_a for models with mostly non resonant $h(b\bar{b}) + E_T^{\text{miss}}$ production. The remaining parameters have the values $M_A = 1200\,\text{GeV}, M_H = M_{H^\pm} = 1300\,\text{GeV}, \sin\theta = 1/\sqrt{2}, \tan\beta = 1$, $\lambda_3 = \lambda_{P1} = \lambda_{P2} = 3$, and $M_\chi = 10$ GeV.

- Increasing M_a requires more energy for many non-resonant signal amplitudes involving internal on-shell a lines. This reduces the rate at which such events can occur, since the PDFs of the initial state gluons drop as the gluon momentum fraction increases. There is an increase in Γ_a with increasing M_a, displayed in Figure 6.9(a), but it is not so large that off-shell a become a significant contribution.

- Much of the increase in Γ_a for $M_a \leq 2m_t \approx 350\,\text{GeV}$ is due to $a \to t\bar{t}$ decays, which are the reason for the kink in Γ_a around $M_a = 2m_t \approx 345\,\text{GeV}$. As a consequence of this rise in the partial width to $t\bar{t}$, the $a \to \chi\bar{\chi}$ branching fraction above the $t\bar{t}$ threshold drops from its previous value of ≈ 1. This reduces the $h(b\bar{b}) + E_T^{\text{miss}}$ production cross section, since the probability of the $h\chi\bar{\chi}$ final state given a decay $A \to ah$ is reduced.

6.3 Masses of the Heavy Scalar Bosons: M_H and $M_{H^\pm}$

The heavy neutral and charged scalars H and $H^\pm$ do not appear in any leading order Feynman diagram contributing to the $h(b\bar{b}) + E_T^{\text{miss}}$ signal, some examples of which are shown in Figure 4.6. Nevertheless, their masses M_H and $M_{H^\pm}$ can change the signal cross-section, as demonstrated in Figure 6.12. Furthermore, changing M_H or $M_{H^\pm}$ can change the shape of the E_T^{miss} distribution, which is shown in Figure 6.13.

For brevity, where M_H is mentioned in this and in all following chapters $M_H = M_{H^\pm}$ unless stated otherwise. This choice is made because setting $M_H = M_{H^\pm}$ is a convenient way of avoiding constraints from electroweak precision measurements, as discussed in detail in Sections 4.2.2 and 7.2. It does not qualitatively influence the conclusions of this section.

The cross-section and kinematics depend on M_H because M_H appears in the tree-level trilinear scalar coupling of a, A and h, as written in Equation (4.6). The change in g_{Aah} affects the resonant and non-resonant contributions differently:

- For the *resonant* signal component, with the $A \to ah$ vertex, this directly affects the amplitude, which is proportional to g_{Aah}^2 [1].

- For the *non-resonant* component, the rate and accessible phase-space depend on Γ_A, to which $\Gamma_{A\to ah} \propto g_{Aah}^2$ contributes significantly, but not uniquely. The other summands contributing to Γ_A are at first order independent of g_{Aah} [1]. Thus changes to g_{Aah} cause changes to $\Gamma_{A\to ah}$, which affects Γ_A. Γ_A in turn determines the suppression of the off-resonance signal amplitude relative to the Breit-Wigner peak of the resonance amplitude [121].

Thus the total cross-section depends on M_H as shown in Figure 6.12. This explanation is sufficient for $|M_H - M_A| \lesssim 300\,\text{GeV}$. For very low and very high M_H however, other effects dominate.

When $M_H \ll M_A$, the cross section is much lower than one would expect from just considering g_{Aah}. One can explain this by the low M_H making H production via a top loop much more likely than A production, due to the negative slope of the gluon PDF.

When M_H is very high, the cross section seems to again be lower than one would expect from just the g_{Aah} dependence. However, in this region the width Γ_A becomes very large (e.g. $\Gamma_A \approx 400\,\text{GeV} = M_A/2$ for the $M_H = 1400$ GeV point in Figure 6.12). This makes it likely that the simulation results are no longer a consistent description of the model, because the underlying model description assumes that the widths of the mediators are narrow relative to

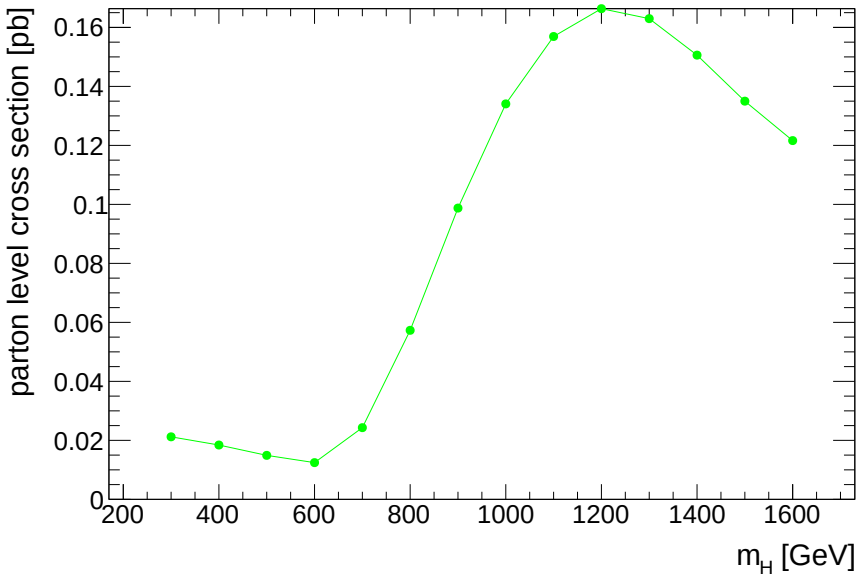

Figure 6.12: Total $h(b\bar{b}) + E_T^{\text{miss}}$ production cross section for different $M_H = M_{H^\pm}$ and fixed $M_a = 300$ GeV, $M_A = 800$ GeV, $\sin\theta = 0.35, \tan\beta = 1, M_\chi = 10$ GeV and $\lambda_{P1} = \lambda_{P2} = \lambda_3 = 3$.

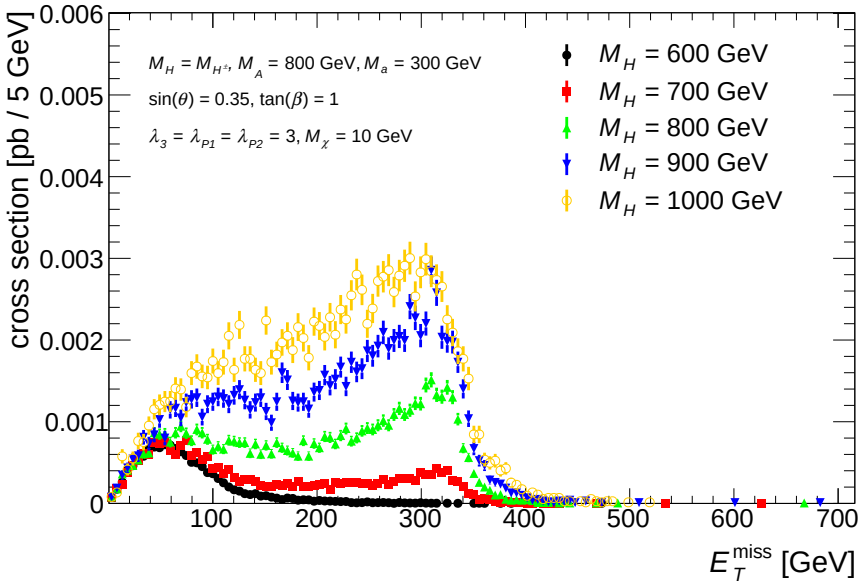

Figure 6.13: The E_T^{miss} distribution of the production cross section of $h \to bb + E_T^{\text{miss}}$ signal events for five representative models with different $M_H = M_{H^\pm}$ and fixed $M_A = 800$ GeV, $M_a = 300$ GeV, $\sin\theta = 0.35, \tan\beta = 1, M_\chi = 10$ GeV and $\lambda_{P1} = \lambda_{P2} = \lambda_3 = 3$.

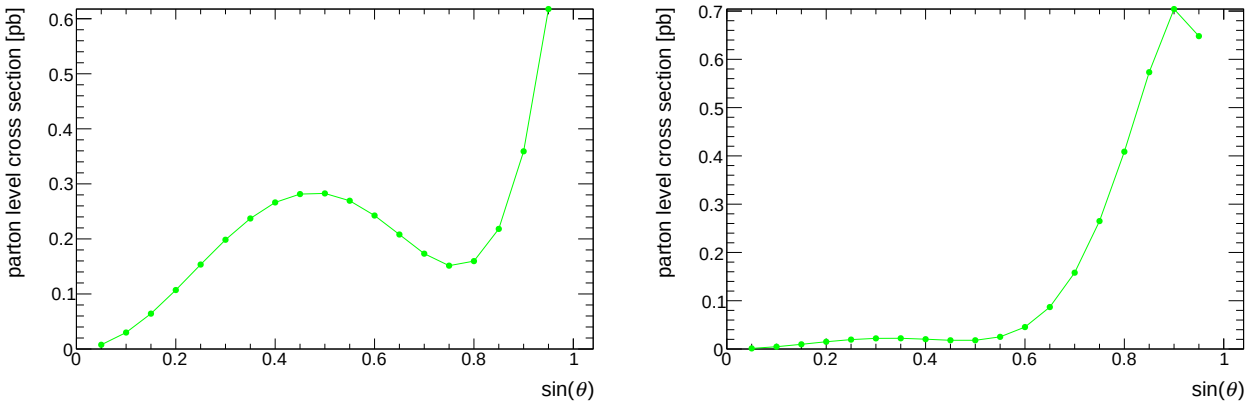

(a) $M_a = 200\,\text{GeV}, M_A = 600\,\text{GeV}$ (b) $M_a = 350\,\text{GeV}, M_A = 1000\,\text{GeV}$

Figure 6.14: Dependence of the $h(b\bar{b}) + E_T^{\text{miss}}$ production cross section on the pseudoscalar mixing angle $\sin\theta$. Models with low pseudoscalar masses, shown in (a), have a different $\sin\theta$ dependence from models with high pseudoscalar masses, shown in (b). The remaining parameters have the values $M_H = M_{H^\pm} = M_A$, $\tan\beta = 1, M_\chi = 10$ GeV, and $\lambda_{P1} = \lambda_{P2} = \lambda_3 = 3$.

the masses of the mediators [1]. This assumption is broken by the simulation results shown in Figure 6.12 for $M_H \gtrsim 1150$, where $\Gamma_A/M_A \gtrsim 0.3$.

The shape of the E_T^{miss} distribution changes non-trivially when changing M_H, as demonstrated in Figure 6.13. This is the result of the M_H dependence of the non-resonant amplitude being different from that of the resonant amplitude due to the different g_{Aah} dependence. However, M_H variations do not change the kinematics of the individual resonant and non-resonant contributions to the signal. Rather, varying M_H changes how likely the resonant process is to contribute to the signal, compared to the non-resonant process. If both contributions had identical kinematics, no changes in the E_T^{miss} shape would be observed.

6.4 Mixing Angle of the CP-odd Scalar Bosons: $\sin\theta$

The mixing of A_0 that is purely 2HDM-like and a_0 that couples purely to Dark Matter into the mass eigenstates a and A is parametrized by the mixing angle θ. Following convention, $\sin\theta$ is discussed here in place of θ itself.

There can only be a $h(b\bar{b}) + E_T^{\text{miss}}$ signal if $\sin\theta \neq 0, 1$, since these values correspond to zero pseudoscalar mixing: $a = a_0, A = A_0$ and $a = A_0, A = a_0$, respectively. When there is no mixing, the only possible portal between the dark sector and the Standard Model and 2HDM+a is given by the quartic scalar couplings λ_{P1} and λ_{P2}, coupling a_0 to Higgs doublets H_1 and H_2, respectively, as Equation (4.4) shows. However, $g_{Aah} = 0$ in those cases irrespective of the values of λ_{P1} or λ_{P2} (cf. Equation (4.6)), and so the contribution depicted in Figure 4.4 vanishes. Furthermore, box diagrams like e.g. shown in Figures 4.6(a) and 4.6(c) also vanish. This is because they cannot arise from quartic scalar interactions, without generating higher final state multiplicities. Thus the $h(b\bar{b})+E_T^{\text{miss}}$ signature can not be generated for $\sin\theta \in \{0, 1\}$.

For other values of $\sin\theta$, the signal cross-section is non-zero, as demonstrated in Figure 6.14. Both the quantitative and qualitative $\sin\theta$-dependence of the cross section are strongly affected by changes in the pseudoscalar masses M_a and M_A, as demonstrated by Figures 6.14(a) and 6.14(b).

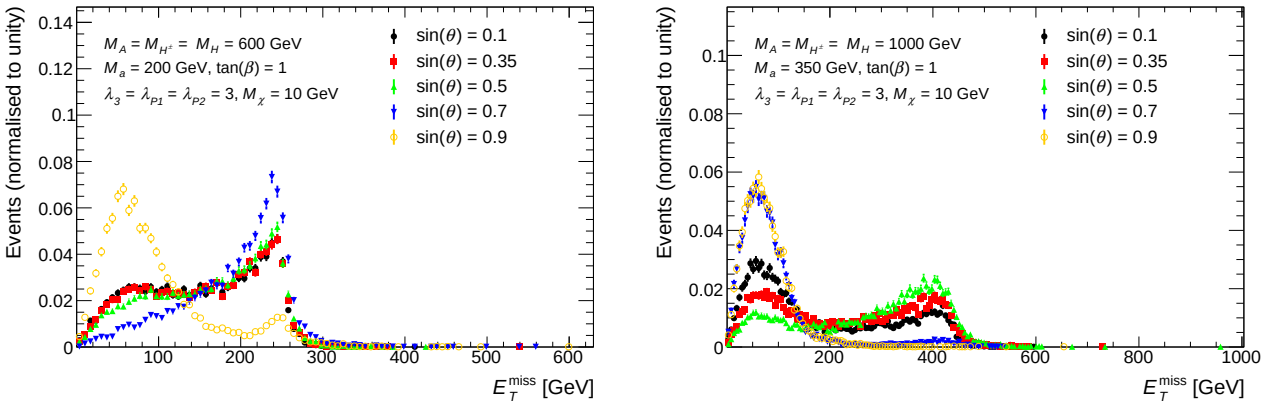

(a) (b)

Figure 6.15: Comparison of E_T^{miss} distributions for different $\sin\theta$ at a low-mass configuration (a) with $M_a = 200$ GeV, $M_A = M_H = M_{H^\pm} = 600$ GeV, and a high-mass configuration (b) with $M_a = 350$ GeV, $M_A = M_H = M_{H^\pm} = 1000$ GeV. The remaining parameters take the values $\tan\beta = 1, M_\chi = 10$ GeV, and $\lambda_{P1} = \lambda_{P2} = \lambda_3 = 3$.

Furthermore, changes in $\sin\theta$ also affect the shape of the E_T^{miss} distribution, as Figure 6.15 shows. The reason for this is that the resonant and non-resonant contributions to the signal amplitude exhibit different $\sin\theta$ dependence. As discussed in Section 4.3, the resonant contribution yields a Jacobian peak the location of which depends sensitively on (M_a, M_A), as discussed in Sections 4.3.1, 6.1.1 and 6.2.1. Conversely the non-resonant contribution yields a broad distribution at soft E_T^{miss} falling as the E_T^{miss} gets harder, as discussed in Sections 4.3.3, 6.1.2 and 6.2.2.

The yields of both the resonant and the non-resonant contribution are affected by $\sin\theta$:

- $\sin\theta$ directly affects the vertices appearing in the diagrams, e.g.:
  - the Aah vertex $g_{Aah} \propto \sin\theta\cos\theta$ (cf. Equation (4.6))
  - vertices where a couples to Dark Matter or A couples to SM fermions: $g_{a-DM}, g_{A-SM} \propto \cos\theta$
  - vertices where A couples to Dark Matter or a couples to SM fermions: $g_{A-DM}, g_{a-SM} \propto \sin\theta$
  - the aah vertex: g_{aah} has summands $\propto \sin^2\theta$ and summands $\propto \cos^2\theta$ (cf. Equation (4.7))

  Thus the diagrams are affected by changes to $\sin\theta$ differently, because the above vertices occuring in a given diagram are different, as shown in Figure 4.6, and only Figure 4.4 is part of the resonant process, whereas the other diagrams give rise to the non-resonant contribution.

- changing $\sin\theta$ induces changes to e.g. g_{Aah} as described above, and thus to Γ_A. This changes the Breit-Wigner suppression of the non-resonant amplitude relative to the peak amplitude on the resonance. Apart from the fact that this effect is caused by the dependence of Γ_A on $\sin\theta$ as opposed to M_H, this is the same mechanism already described in Section 6.3. The differences in the dependence are due to the fact that $\sin\theta$ affects all couplings involving a or A, not just the trilinear scalar couplings.

For very large (e.g. $\sin\theta = 0.9$) and for very small (e.g. $\sin\theta = 0.1$) values of $\sin\theta$, the resonant contributions are weaker than non-resonant ones, as can be seen in Figure 6.15, where at these extreme values of $\sin\theta$ the soft bulk of the distribution is larger than the hard Jacobian peak. A possible explanation is that g_{aah}, as defined in Equation (4.7), is the sum of a contribution $\propto \sin^2\theta$ and another one $\propto \cos^2\theta$. Therefore one of these two terms is always enhanced for low or high $\sin\theta$, and due to the g_{aah} contribution, the non-resonant amplitude is enhanced.

For $g_{Aah} \propto \sin\theta\cos\theta$ the opposite is the case. It is small for $\sin\theta$ or $\cos\theta$ close to 0 or 1, and enhanced for intermediate values. Indeed Figure 6.15 shows that the Jacobian peak is strongest for intermediate values of $\sin\theta$. $g_{Aah} \propto \sin\theta\cos\theta$ suggests that the resonant contribution would be strongest at the maximum of $\sin\theta\cos\theta$, i.e. at $\sin\theta = 1/\sqrt{2} = 0.707107\ldots$. And indeed for the models shown in Figure 6.15(a), the relative resonant contribution is largest for the model with $\sin\theta = 0.7 \approx 1/\sqrt{2}$.

However the model with $\sin\theta = 0.7$ is not the one with the strongest Jacobian peak for the models with higher scalar masses shown in Figure 6.15(b). Instead the relative resonant contribution is strongest for the model with $\sin\theta = 0.5$, and the model with $\sin\theta = 0.7$ is dominated by the non-resonant contribution. Apparently the impact of $\sin\theta$ on the non-resonant contribution, is affected by the different scalar mass configurations of Figure 6.15(a) and Figure 6.15(b).

The reason for this behavior is that the vertices involving a, A or both, are mass dependent, with different vertices having different mass dependencies. For example, the part of the coupling g_{aah} that is $\propto \sin^2\theta$ is also a function of $M_H, M_{H^\pm}$ and M_a, as can be read from Equation (4.7). The part of g_{aah} that is $\propto \cos^2\theta$ does not depend on M_H^2, M_a^2, and $M_{H^\pm}^2$. So the scaling of g_{aah} with $\sin\theta$, and thus the $\sin\theta$-scaling of the relative strength of the non-resonant contribution, is affected by changes of $M_H, M_{H^\pm}$, and M_a.

For most of the models in the scans described in Chapter 7, $\sin\theta$ is fixed to $\sin\theta = 0.35$. This value is chosen so that the signal cross sections and the fractions of resonant events are large for a large number of models in these scans, as discussed in Section 7.2.

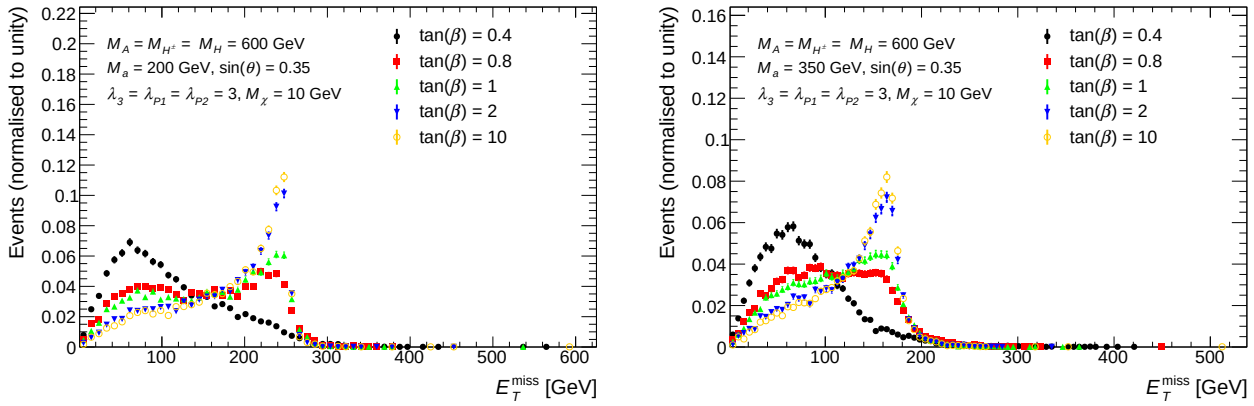

(a) (b)

Figure 6.16: Comparison of E_T^{miss} distributions with varying $\tan\beta$ at a low-mass configuration (a) with $M_a = 200$ GeV and a high-mass configuration (b) with $M_a = 350$ GeV. The remaining parameters take the values $M_A = M_H = M_{H^\pm}600$ GeV, $M_\chi = 10$ GeV, $\sin\theta = 0.35$, and $\lambda_{P1} = \lambda_{P2} = \lambda_3 = 3$. The shown distributions correspond to events produced in gluon fusion only.

6.5 Ratio of Vacuum Expectation Values: $\tan\beta$

The parameter $\tan\beta$ is the ratio of the two vacuum expectation values of the two Higgs doublets. The vacuum expectation values appear in the terms coupling fermions to Higgs bosons. The model used for the simulations described here has Yukawa assignments of type II. This means that the Higgs doublet H_1 couples to down-type quarks and leptons, and H_2 couples to up- type quarks only. This results in the following Yukawa couplings to Standard Model fermions [1]: $y_{\mathcal{U}} = -\sqrt{2}\frac{m_{\mathcal{U}}}{v}\cot\beta$ for any up-type quark $\mathcal{U} = u, c, t$ and $y_{\mathcal{D},\ell} = \sqrt{2}\frac{m_{\mathcal{D},\ell}}{v}\tan\beta$ for any down type quark $\mathcal{D} = d, s, b$ or lepton $\ell = e, \mu, \tau$.

Changes of $\tan\beta$ will in general affect the signal cross-section, since signals originate either from a top loop, or b pair annihilation. Both cases are shown in Figure 6.17. In either case, the coupling to top or bottom quarks, and thus $\tan\beta$, matters.

The change of the E_T^{miss} shape changes when changing $\tan\beta$ is demonstrated in Figure 6.16. The cause of the $\tan\beta$ dependence of the kinematics is that box diagrams, such as shown in Figure 4.6(a), and the triangle graph shown in Figure 4.4 depend on the top Yukawa coupling in different ways. The box diagrams feature two Yukawa-vertices, the triangle diagram only one. The different number of Yukawa vertices means a different power of $\tan\beta$ in the signal amplitude, and thus the relative contribution of the different amplitudes changes with $\tan\beta$. Since only the triangle graph from Figure 4.4 contributes to the events in the Jacobian peak (cf. Section 4.3.1), and all other diagrams yield non-resonant signals, changing $\tan\beta$ changes the relative yield of resonant events with respect to non-resonant events. This results in the changes to the shape of the E_T^{miss} distribution shown in Figure 6.16.

The impact of $\tan\beta$ on the E_T^{miss} distribution does not depend on the masses of the scalars. The relative enhancement of the Jacobian peak with higher $\tan\beta$ for $M_a = 200\,\text{GeV}$, shown in Figure 6.16(a), is the same as the relative enhancement for $M_a = 350\,\text{GeV}$, shown in Figure 6.16(b). The reason is that the $\tan\beta$ dependence of any vertex coupling any (pseudo-)scalar to a Standard Model fermion is identical, irrespective of whether the scalar in question is a, A, H, etc. This is a direct consequence of choosing the Yukawa couplings such that there is only one Higgs doublet coupling to leptons, up-type quarks, and down-type quarks, respecti-

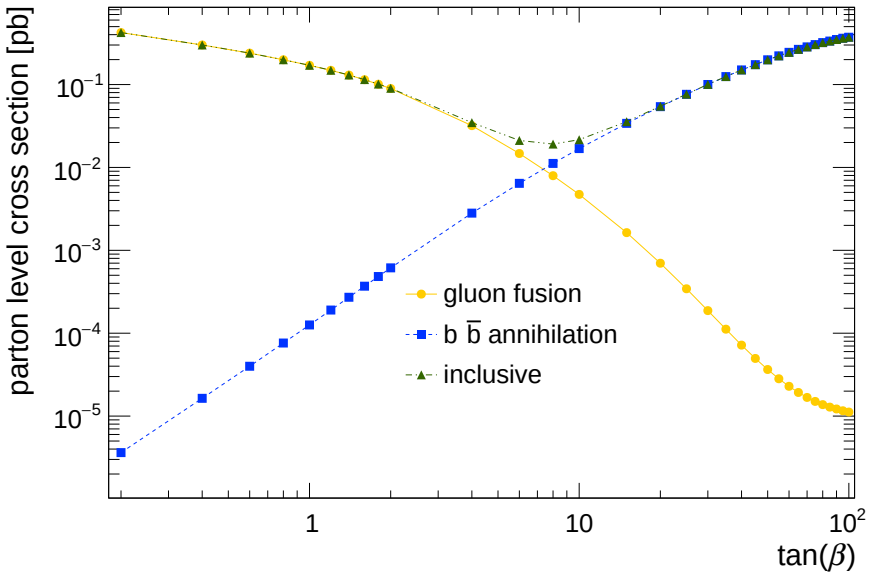

Figure 6.17: Scaling of the cross-section with $\tan\beta$ for only gluon fusion- initiated processes, such as shown in Figure 4.6, and only $b\bar{b}$ annihilation initiated processes, such as shown in Figure 4.7, and the combination. The other parameters have the values $M_a = 200$ GeV, $M_A = M_H = M_{H^\pm}600$ GeV, $M_\chi = 10$ GeV and $\lambda_{P1} = \lambda_{P2} = \lambda_3 = 3$.

vely. This is unlike the behavior of $\sin\theta$ described in Section 6.4 and shown in Figure 6.15, where the relative enhancement is highly mass-dependent, because e.g. the $at\bar{t}$ vertex has a different $\sin\theta$ dependence than the $At\bar{t}$ vertex.

For most of the models in the final parameter scans described in Chapter 7, $\tan\beta$ is fixed as $\tan\beta = 1$. This choice combines an observably large cross-section for gluon fusion induced $h(b\bar{b}) + E_T^{\text{miss}}$ production with a sizeable fraction of resonant signal events.

6.5.1 $h(b\bar{b}) + E_T^{\text{miss}}$ from $b\bar{b}$ Annihilation

For most model parameter points, the dominant signal processes are initiated by two gluons fusing into a top quark loop, as shown in Figure 4.6. The top loop induced processes are dominant because the Yukawa coupling of the Higgs Bosons to top quarks is large (≈ 1).

In principle a coupling to b-quarks exists. However, since the fermion Yukawa couplings are, by construction, proportional to the fermion masses, the Yukawa coupling of b quarks is supressed by a relative factor $m_b/m_t \approx 0.024$ (using quark masses from Ref. [17]) relative to the top quark coupling. Thus, though signal events from initial state $b\bar{b}$ annihilation as shown in Figure 4.7 can occur, the cross-section is usually negligible.

However, as discussed in Section 4.1.1, the model implementation used here has a Yukawa sector of type II. This means that up-type and down-type quarks couple to different respective Higgs doublets. By adjusting the vacuum expectation values of the two Higgs doublets, i.e. by increasing $\tan\beta$, the Higgs doublet that couples to down-types can be tuned to couple much more strongly than the one that couples to up-types. Thus, the smaller Yukawa coupling of b-quarks can be compensated for by a large $\tan\beta$. This results in $b\bar{b} \to h\chi\bar{\chi}$ processes (shown in Figure 4.7) being more likely than the $gg \to h\chi\bar{\chi}$ processes (shown in Figure 4.6) that dominate the production cross section for $\mathcal{O}(\tan\beta) \approx 1$. The quantitative $\tan\beta$ dependencies of the gluon fusion- and $b\bar{b}$-initiated production cross sections are shown in Figure 6.17.

The E_T^{miss} spectrum of the $b\bar{b}$ annihilation induced process is in general different from the

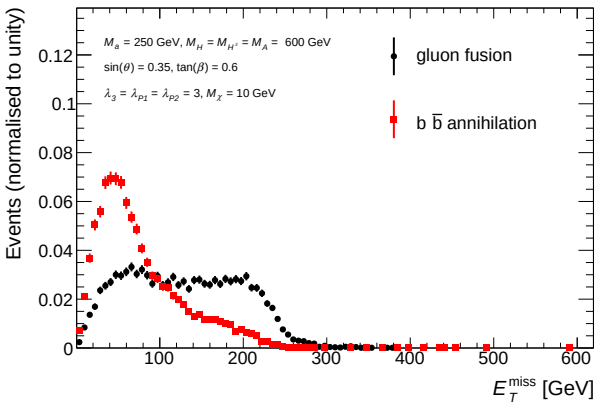

(a) $\tan\beta = 0.6$

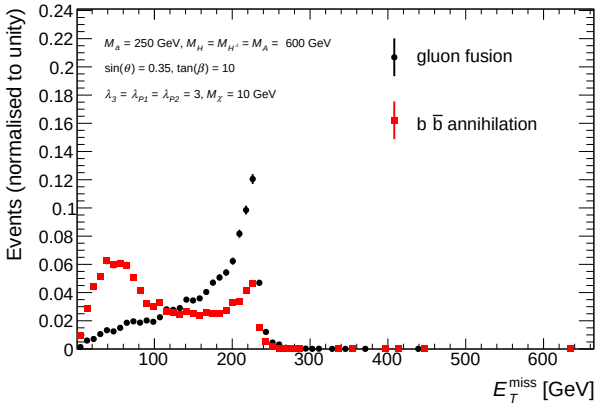

(b) $\tan\beta = 10$

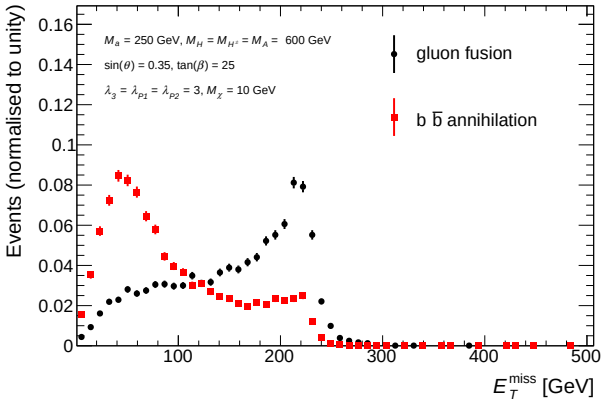

(c) $\tan\beta = 25$

Figure 6.18: Shape comparison of E_T^{miss} distributions for gluon fusion induced processes, as shown in Figure 4.6 and $b\bar{b}$-annihilation induced processes, as shown in Figure 4.7, at three different values of $\tan\beta$((a)- (c)). The remaining parameters take the values $M_a = 200$ GeV, $M_A = M_H = M_{H^\pm}600$ GeV, $M_\chi = 10$ GeV and $\lambda_{P1} = \lambda_{P2} = \lambda_3 = 3$.

gluon fusion induced one, as demonstrated in Figure 6.18 for three different values of $\tan\beta$. The spectrum of the $b\bar{b}$ induced process has a Jacobian peak and a soft-E_T^{miss} non-resonant shoulder at the same E_T^{miss} values as the gluon fusion induced process. However, the relative yields of the two resonant or non-resonant contributions are different between the $b\bar{b}$ and gluon fusion cases, giving rise to the observed shape differences. The event kinematics depend on $\tan\beta$, and the explanation is analogous to the explanation in the case of gluon fusion. A different number of Yukawa vertices in the contributing diagrams leads to a different scaling with $\tan\beta$ of the resonant and non-resonant amplitudes. The $b\bar{b}$ induced signals have neither triangle nor box loops at leading order, since they feature tree-level diagrams. But there are analogous tree level diagrams with either one Figure 4.5 or two Figure 4.7(a) Yukawa vertices.

The relative yield of the non-resonant channels is typically stronger than the resonant channels. This is different from the gluon fusion induced process, where the resonant contribution can be larger than the non-resonant one for many models. One can explain this with the shape of the gluon PDF, which is highest at low proton momentum fraction x, and falls steeply with increasing x. But while the gluon fusion initiated signal uses two gluons directly, and can thus use all the momentum carried by the gluons, the $b\bar{b}$ initiated signal uses b quarks from gluon splitting $g \to b\bar{b}$. Thus the momentum of the initial state b quarks is on average lower than that of initial state gluons. A resonant signal requires that the sum of the initial state parton momenta be at least large enough to produce the heavy pseudoscalar A, i.e. $x_1 x_2 \sqrt{s} \geq M_A$. For a non-resonant signal, depending on Γ_A, either $x_1 x_2 \sqrt{s} \geq M_a + M_h$ or $x_1 x_2 \sqrt{s} \geq M_h + 2M_\chi$ are sufficient. Since the average initial state parton in the $b\bar{b}$ induced production has a lower x_i than in the gluon fusion case, non-resonant signals are more likely.

6.6 The Quartic Trio: λ_3, λ_{P1}, and λ_{P2}

The 2HDM+a Lagrangian contains three coupling parameters λ_3, λ_{P1} and λ_{P2} [1]. λ_3 is a quartic coupling between the two Higgs doublets, contributing with the term $\lambda_3 \left(H_1^\dagger H_1\right)\left(H_2^\dagger H_2\right)$ in Equation (4.1). λ_{P1} and λ_{P2} describe the quartic couplings of the Higgs doublets to the Dark Matter-mediating pseudoscalar a_0 by the term $a_0^2\left(\lambda_{P1} H_1^\dagger H_1 + \lambda_{P2} H_2^\dagger H_2\right)$ in Equation (4.3).

λ_3, λ_{P1} and λ_{P2} are not fixed by the mass spectrum, because they do not take part in diagonalizing the mass terms of the scalars. They are moreover not constrained by known Standard Model decays or coupling strengths, since they only determine couplings between purely Beyond Standard Model field operators. This they only appear in trilinear scalar couplings such as g_{haa} and g_{Aah}. The coupling g_{Aah} is important for the resonant signal process, which always contains the decay $A \to ah$. Considering the exact dependence of g_{Aah} on λ_3, λ_{P1} and λ_{P2} in Equation (4.6):

$$g_{Aah} \supset \frac{2}{vM_A}\left[\left(\lambda_{P1}\cos^2\beta + \lambda_{P2}\sin^2\beta\right)v^2 - \lambda_3 v^2\right]\sin\theta\cos\theta\,, \tag{6.1}$$

one can see that as long as all three parameters are equal $\lambda \equiv \lambda_3 = \lambda_{P1} = \lambda_{P2}$, the terms in Equation (6.1) cancel, and Equation (4.6) becomes:

$$g_{Aah} = \frac{1}{vM_A}\left[M_h^2 - 2M_H^2 - M_A^2 + 4M_{H^\pm}^2 - M_a^2\right]\sin\theta\cos\theta. \tag{6.2}$$

It follows that the resonant contribution to the signal should be independent of λ [110, 122].

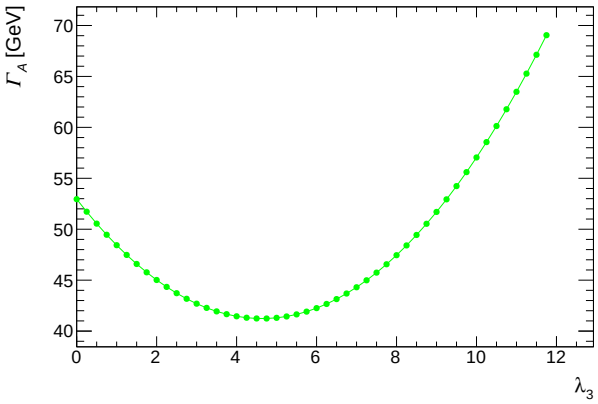

(a) Γ_A dependence on only λ_3

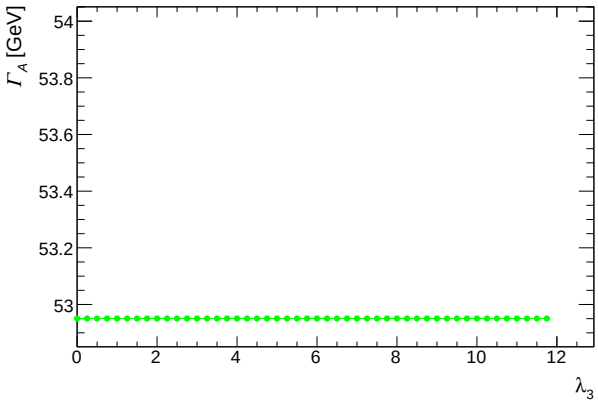

(b) Γ_A dependence on $\lambda_3 = \lambda_{P1} = \lambda_{P2}$

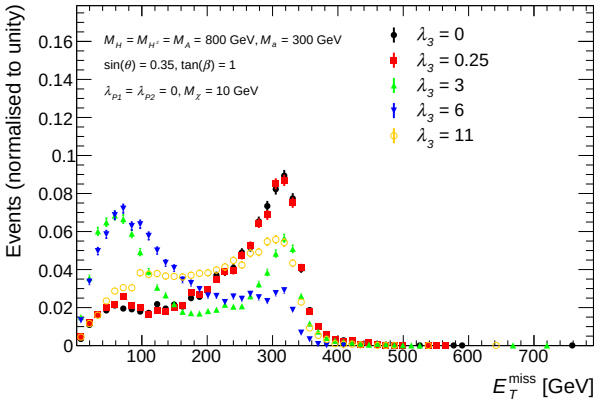

(c) E_T^{miss} dependence on only λ_3

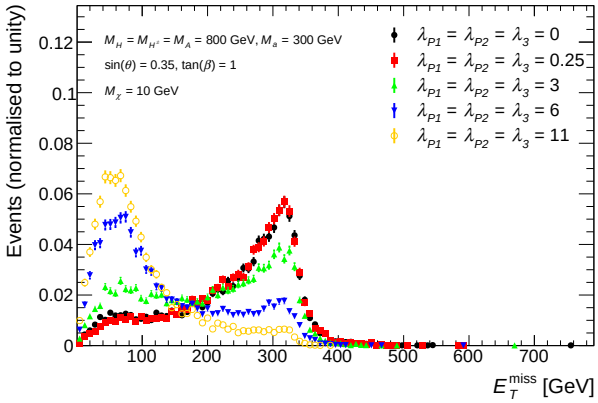

(d) E_T^{miss} dependence on $\lambda_3 = \lambda_{P1} = \lambda_{P2}$

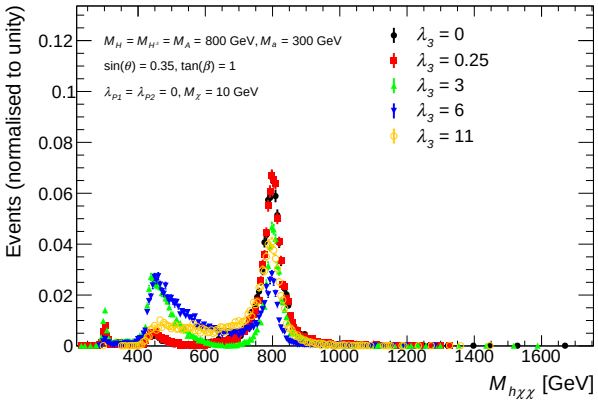

(e) $M_{h\chi\bar{\chi}}$ dependence on only λ_3

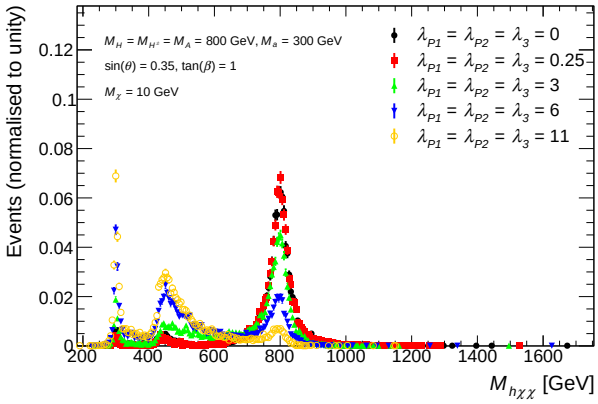

(f) $M_{h\chi\bar{\chi}}$ dependence on $\lambda_3 = \lambda_{P1} = \lambda_{P2}$

Figure 6.19: Impact on the signal process of changing only λ_3, with $\lambda_{P1} = \lambda_{P2} = 0$ (right column, (a), (c), and (e)) or all three λ's simultaneously (left column, (b), (d), and (f)). The top row shows the effect on Γ_A ((a),(b)), the middle row shows the effect on the E_T^{miss} ((c) and (d)), and the last row shows the effect on the invariant mass of the final state system $M_{h\chi\bar{\chi}}$ ((e), (f)). The other parameters have the values $M_a = 300$ GeV, $M_A = M_H = M_{H^\pm} = 800$ GeV, $M_\chi = 10$ GeV, $\tan\beta = 1$, and $\sin\theta = 0.35$.

This is upheld in the simulation as far as the total width of A, Γ_A, is concerned. Figure 6.19(a) shows how Γ_A changes with varying λ_3. This dependence is completely canceled when varying λ instead, as Figure 6.19(b) demonstrates.

Figure 6.19(c) confirms that the E_T^{miss} distribution changes shape when only λ_3 is changed, as expected from its effect on g_{Aah}, which contributes mainly to the resonant process. However, the E_T^{miss} spectra are still affected by changes to λ, as shown in Figure 6.19(d). The dependence differs from the case of varying only λ_3, but it is not canceled.

The remaining dependence on λ is caused by off-shell processes such as $gg \to a \to ha^*(\chi\bar{\chi})$ and $gg \to a* \to ha(\chi\bar{\chi})$, shown in Figure 4.6(f). This can be seen from the dependence of the $M_{h\chi\bar{\chi}}$ distribution on λ_3 and λ, shown in Figures 6.19(e) and 6.19(f) respectively. Changing only λ_3, as displayed in Figure 6.19(e) changes the rate of the resonant process, which peaks at $M_{h\chi\bar{\chi}} = M_A = 800\,\text{GeV}$, relative to the non-resonant processes peaking at $M_a + M_h = 425\,\text{GeV}$ in the case of e.g. $gg \to a* \to ha(\chi\bar{\chi})$ and $M_{h\chi\bar{\chi}} = M_a = 300\,\text{GeV}$ in the case of $gg \to a \to ha^*(\chi\bar{\chi})$. However, the resonant contribution is still large at $\lambda_3 = 11$. This is different when changing the full λ as displayed in Figure 6.19(f), where the resonant peak at $M_{h\chi\bar{\chi}} = M_A = 800\,\text{GeV}$ is continuously diminished as λ is increased. The reason for this is that while the resonant process is not affected by the changes in λ since g_{Aah} as given in Equation (6.2) does not depend on λ, the non-resonant contributions are affected by couplings such as g_{haa}, given in Equation (4.7). For models where $\sin^2\theta \neq \frac{1}{2}$, The coupling g_{haa} has a dependence on λ,

$$g_{haa} \supset \frac{-2}{v} M_h \left[\lambda_3 \sin^2\theta + \left(\lambda_{P1}\cos^2\beta + \lambda_{P2}\sin^2\beta\right)\cos^2\theta\right] . \tag{6.3}$$

Thus, while the resonant contribution remains constant when changing λ in absolute numbers, compared to the non-resonant contributions, which increase due to e.g. the increase of g_{aah}^2, the relative resonant contribution is reduced. This changed relative yield of the resonant and non resonant contributions gives rise to the dependence of the E_T^{miss} distribution on λ that is shown in Figure 6.19(d).

6.7 The Dark Matter Yukawa Coupling: y_χ

The peudoscalars a and A couple to the Dark Matter fermion χ via a Yukawa coupling, with coupling strength y_χ. This coupling strength can change the signal cross-section, as shown in Figure 6.20(b), but the dependence is weak since $a \to \chi\bar{\chi}$ is by far the dominant decay channel of a when $M_a < 2M_t$. For $M_a \geq 2M_t$, $a \to t\bar{t}$ is a second significant decay channel, but the only effect is a reduced $a \to \chi\bar{\chi}$ branching ratio, lowering the signal cross section. The shape of the E_T^{miss} distribution is not affected by y_χ, except for extreme values of y_χ where off-shell processes dominate. The impact of $y_\chi$on the E_T^{miss} distribution is shown in Figure 6.20(a)). Hence, $y_\chi = 1$ is assumed for all other studies presented here.

6.8 The Dark Matter Mass: M_χ

The Dark Matter fermion mass M_χ can affect the E_T^{miss} distribution and the signal cross section, depending on the mass hierarchy of the χ, a, h, A particles. The E_T^{miss} distribution dependence is shown in Figures 6.21 and 6.22, and the cross section dependence is demonstrated in Figures 6.23 and 6.24.

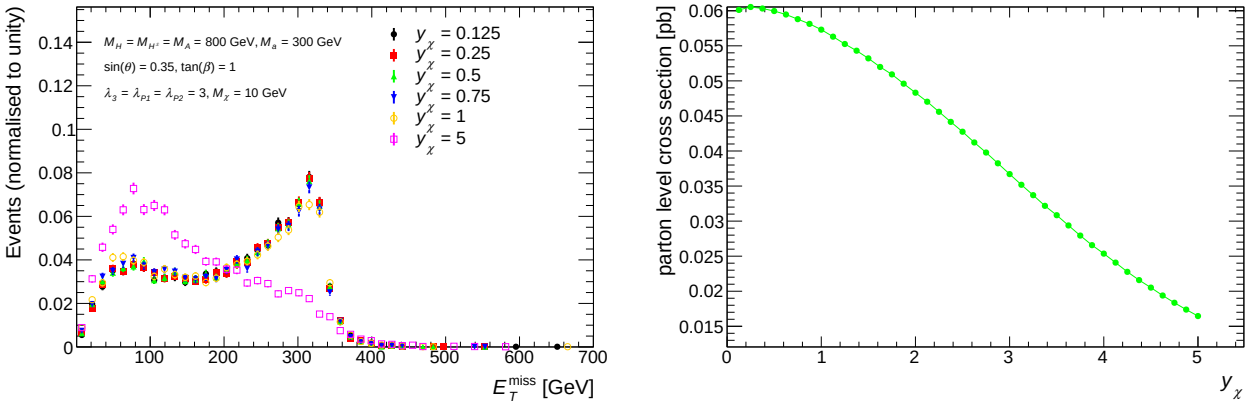

(a) E_T^{miss} spectra for different y_χ

(b) cross section scaling with y_χ

Figure 6.20: Effect of changing y_χ on the signal kinematics (a) and cross section (b). The remaining model parameters are fixed as $M_A = M_H = M_{H^\pm} = 800$ GeV, $M_a = 300$ GeV, $\sin\theta = 0.35, \tan\beta = 1$, and $\lambda_{P1} = \lambda_{P2} = \lambda_3 = 3$.

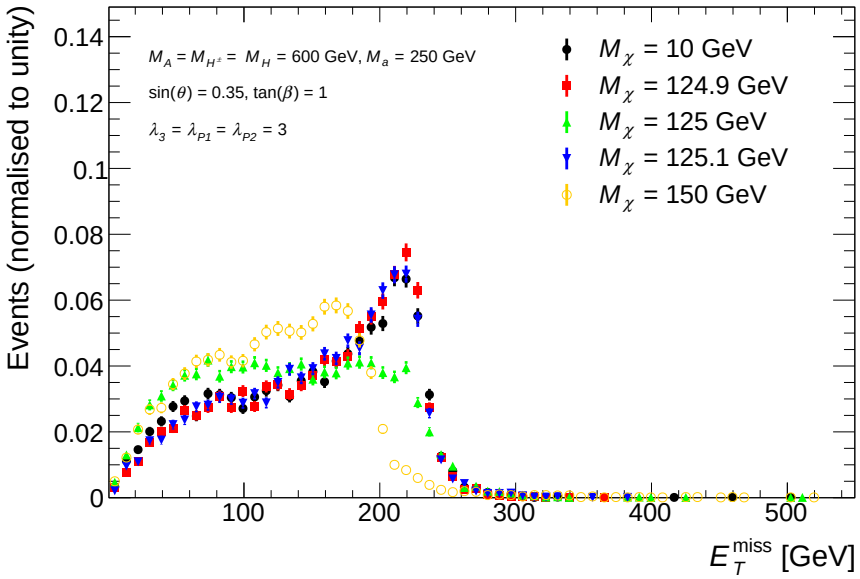

Figure 6.21: Comparison of the E_T^{miss} spectra of 5 representative signal models with different Dark Matter fermion masses M_χ. The remaining model parameters are fixed as $M_A = M_H = M_{H^\pm} = 600$ GeV $M_a = 250$ GeV, $\sin\theta = 0.35, \tan\beta = 1$, and $\lambda_{P1} = \lambda_{P2} = \lambda_3 = 3$. The shape of the E_T^{miss} distribution does not change for $M_\chi < M_a/2$, then changes significantly for $M_\chi >= M_a/2$.

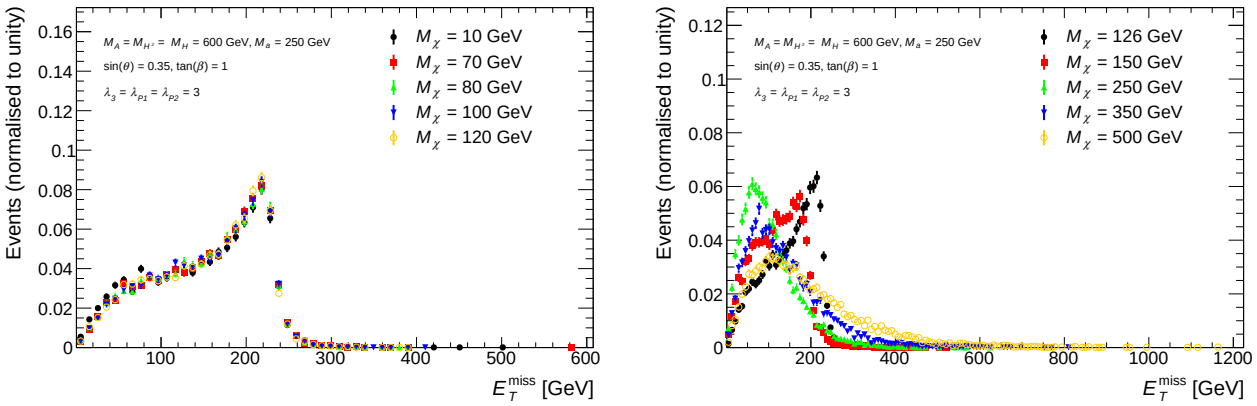

(a) above threshold

(b) below threshold

Figure 6.22: The dependence of the signal E_T^{miss} distribution on the dark matter fermion mass M_χ, above the $a \to \chi\bar{\chi}$ threshold $M_\chi < M_a/2$, shown in (a) , and below the $a \to \chi\bar{\chi}$ threshold $M_\chi > M_a/2$, shown in (b). The remaining model parameters are fixed as $M_A = M_H = M_{H^\pm} =$ 600 GeV $M_a = 250$ GeV, $\sin\theta = 0.35, \tan\beta = 1$, and $\lambda_{P1} = \lambda_{P2} = \lambda_3 = 3$.

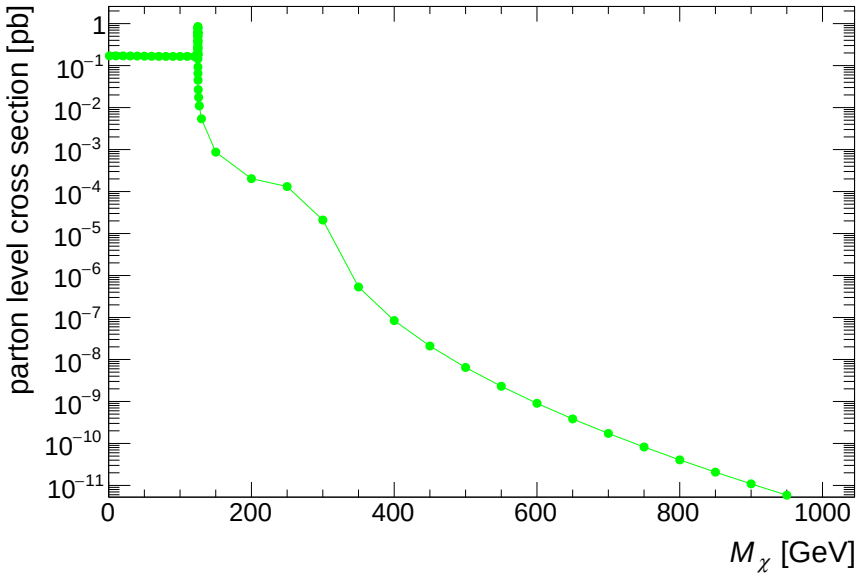

Figure 6.23: Dependence of $h(b\bar{b}) + E_T^{\text{miss}}$ cross section on the Dark Matter fermion mass M_χ. The remaining model parameters are fixed as $M_A = M_H = M_{H^\pm} = 600$ GeV $M_a = 250$ GeV, $\sin\theta = 0.35, \tan\beta = 1$, and $\lambda_{P1} = \lambda_{P2} = \lambda_3 = 3$.

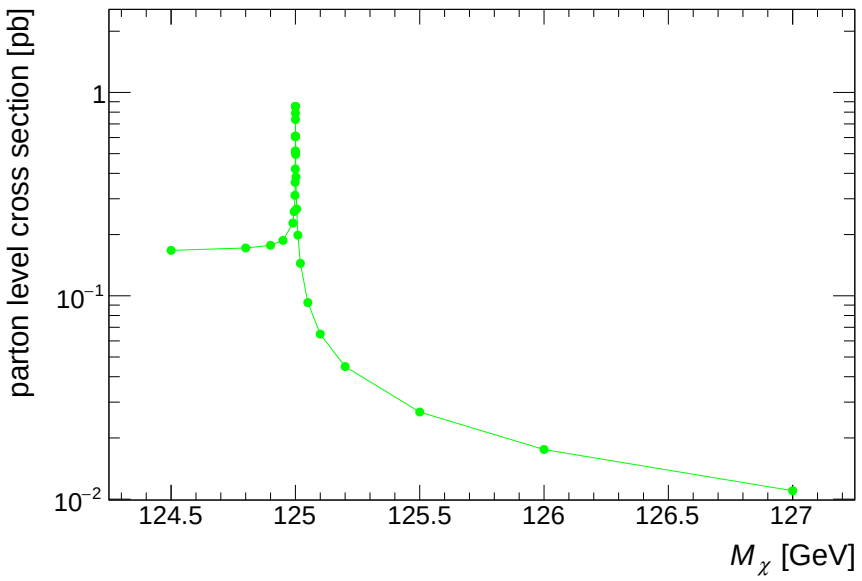

Figure 6.24: Dependence of $h(b\bar{b}) + E_T^{\text{miss}}$ cross section on the Dark Matter fermion mass M_χ near the pair production threshold at $M_\chi = M_a/2$. The remaining model parameters are fixed as $M_A = M_H = M_{H^\pm} = 600$ GeV $M_a = 250$ GeV, $\sin\theta = 0.35, \tan\beta = 1$, and $\lambda_{P1} = \lambda_{P2} = \lambda_3 = 3$.

For very low Dark Matter masses $M_\chi < \frac{1}{2}(M_a - M_h)$ far above the $\chi\bar{\chi}$ pair production threshold, changes of M_χ have no effect on the signal process. The undetectable χ momentum relative to $\bar{\chi}$ is changed, but it is not detected, since both χ and $\bar{\chi}$ leave the detector without interacting with it. The E_T^{miss} spectrum and the total signal cross-section are invariant under changes of M_χ.

For higher Dark Matter masses $\frac{1}{2}(M_a - M_h) < M_\chi < M_a/2$, but still above the production threshold, the situation is very similar. The total cross section is slightly lower, and the very low end of E_T^{miss} spectrum has fewer events. This is due to the non-resonant process $a \to hA^*(\chi\bar{\chi})$ becoming kinematically inaccessible. But since this contribution is small, the differences are negligible. Within this region, both the cross-section and the E_T^{miss} distribution are again invariant, under changes of M_χ, as shown in Figures 6.22(a) and 6.23.

Close to the production threshold at $M_\chi = M_a/2$ the decay $a \to \chi\bar{\chi}$ is enhanced, as demonstrated in Figure 6.24. "Close to" here refers to mass differences $|M_a/2 - M_\chi| \propto \mathcal{O}(10 - 100)$ MeV, far smaller than other typical energy differences in the models studied here, such as e.g. $(M_A - M_A) \propto \mathcal{O}(100\,\text{GeV})$. Both the resonant signal channel corresponding to Figure 4.4, as well as non-resonant signal channels that feature a $a \to \chi\bar{\chi}$ decay, such as Figure 4.6(a), are resonantly enhanced close to the threshold. This leads to a change in the shape of the E_T^{miss} spectrum close to the threshold.

However, in the regime close to the threshold the numerical simulation is likely to be unreliable [123]. This is because the total width of a changes by several orders of magnitude at the threshold. Thus, even a slight virtuality of a can change the width of the corresponding a pole. In other words, the total width of a close to the $a \to \chi\bar{\chi}$ threshold is a function of the momentum carried by the a; Γ_a is a running parameter in this regime. This running of Γ_a is not modeled in the MadGraph 5 matrix element calculation, where Γ_a is assumed to be constant at a given model parameter point [112, 116, 114]. Thus both the total cross section and the phase space properties of the result can not be relied upon to reflect physically

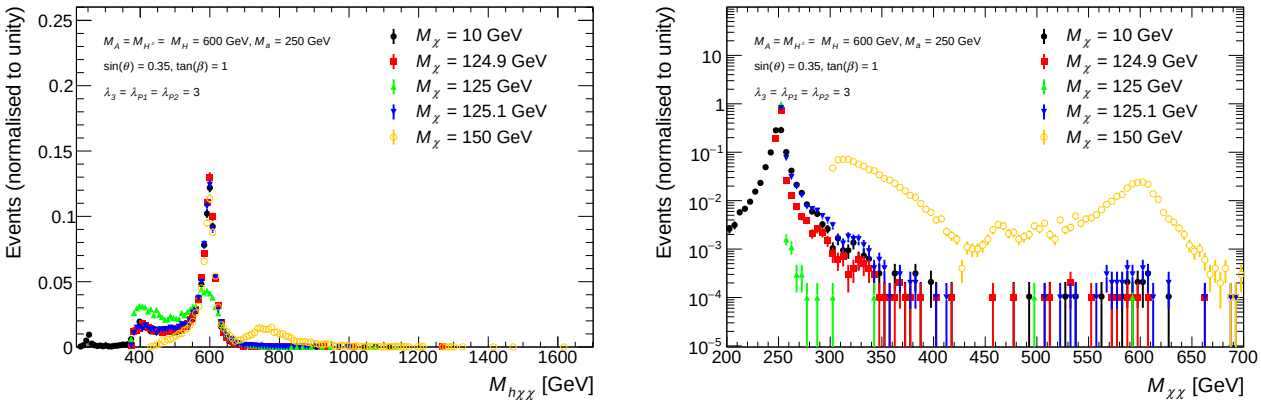

(a) effect of M_χ on $M_{h\chi\bar{\chi}}$

(b) effect of M_χ on $M_{\chi\bar{\chi}}$

Figure 6.25: $M_{h\chi\bar{\chi}}$ (Figure 6.25(a)) and $M_{\chi\bar{\chi}}$ (Figure 6.25(b)) dependence on the Dark Matter fermion mass M_χ. The remaining model parameters are fixed as $M_A = M_H = M_{H^\pm} = 600$ GeV $M_a = 250$ GeV, $\sin\theta = 0.35, \tan\beta = 1$, and $\lambda_{P1} = \lambda_{P2} = \lambda_3 = 3$.

consistent behavior in this regime.

Below threshold, i.e. for $M_\chi > M_a/2$, the signal cross section drops by several orders of magnitude within a few GeV of the production threshold, as demonstrated in Figure 6.23. The reason is that the a decaying to $\chi\bar{\chi}$ is forced to be off-shell, as demonstrated in Figure 6.25(b). As M_χ increases, the accessible invariant mass of the full system is limited from below to $\geq 2M_\chi + M_h$, as shown in Figure 6.25(a)). The kinetic energy available to the final state particles is thus reduced. This continuously distorts the E_T^{miss} spectrum with changing M_χ, as Figure 6.22(b) shows. Furthermore, Figures 6.25(a) and 6.25(b) display a second peak at $M_{h\chi\bar{\chi}} = M_A + M_h = 725\,\text{GeV}, M_{\chi\bar{\chi}} = M_A = 600\,\text{GeV}$, which are the result of an increasing fraction of non-resonant signal events with $A \to \chi\bar{\chi}$. This fraction of events is enhanced near $M_\chi = M_A/2 = 300\,\text{GeV}$, as shown in Figure 6.23. But since the only diagrams that get enhanced are the box diagram shown in Figure 4.6(b) and diagrams with another off-shell s-channel mediator decaying to Ah, this enhancement is not enough to generate an observable signal cross section.

In conclusion, excepting models very close to the $\chi\bar{\chi}$ production threshold, M_χ is either low enough that pair production is allowed, in which case it has no effect on the collider signature. Alternatively M_χ is so large that $a \to \chi\bar{\chi}$ decays are kinematically forbidden, in which case the predicted signal cross section is many orders of magnitudes below the current LHC sensitivity. Thus $M_\chi = 10\,\text{GeV}$ for all other studies in this chapter, and most studies in Chapter 7.

6.9 Summary: The Effects of the Model Parameters on the Signal Kinematics

In this Chapter, the effects of changing 11 out of the 14 parameters of the 2HDM+a on the signal cross-section and E_T^{miss} distribution were studied. The results are briefly summarized in Table 6.1.

The mass of the lightest neutral scalar M_h is not studied, since h is interpreted as the 125 GeV scalar observed at the LHC. The mixing angle α, describing the mixing of the two neutral scalars h and H, also was not studied, instead being fixed such that $\sin(\beta - \alpha) = 0$ in the so-called alignment-decoupling limit. This allows the interpretation of h as an Standard Model-

Table 6.1: Summary of the Results of the Studies of individual 2HDM+a parameters in Chapter 6.

Parameter	Impact on E_T^{miss} distribution ...			Impact on σ?	
	... maximum range:	... height of features:	... none:	yes	no
M_A	✓	✓		✓	
M_a	✓	✓		✓	
$M_H = M_{H^\pm}$		✓		✓	
$\sin\theta$		✓		✓	
$\tan\beta$		✓		✓	
$\lambda_3 = \lambda_{P1} = \lambda_{P2}$		✓		✓	
$y_\chi^\star$			✓	✓	
$M_\chi^\dagger$			✓		✓

*: when $y_\chi \leq 1$, otherwise there is a significant E_T^{miss} shape dependence
†: when $M_\chi < \max(M_a, M_A)$, otherwise cross section and E_T^{miss} shape do change

like Higgs boson, because it fixes the couplings to the W and Z bosons to their Standard Model values. The norm of the vacuum expectation values of the Higgs doublets, $v = \sqrt{(v_1)^2 + (v_2)^2}$ is fixed by measurements of the Fermi Coupling Constant $G_F = v^2/\sqrt{2}$, so it was not studied either.

The masses M_a and M_A of the pseudoscalar mediators directly determine the location of the Jacobian peak in the E_T^{miss} spectrum, and are therefore crucial to the signal acceptance of the search. A further 7 parameters are found to also influence the shape of the E_T^{miss} distribution: M_H, $M_{H^\pm}$, $\sin\theta$, $\tan\beta$, λ_3, λ_{P1}, and λ_{P2}. Although they do not change the location of the E_T^{miss} peak like M_a and M_A, these parameters still affect both the signal acceptance and the signal cross section, and thus the sensitivity of the search to a particular model. Finally, M_χ and y_χ, the mass and Yukawa coupling of the Dark Matter fermion, do not affect the E_T^{miss} distribution significantly, if $M_\chi < M_a/2$ and $y_\chi \leq 1$. While y_χ has some effect on the cross section, M_χ does not.

Chapter 7

Design of the Parameter Scan for Setting Limits on the 2HDM+a

7.1 Introduction

This Chapter describes the design of the benchmark set of 2HDM+a parameters according to the $h(b\bar{b}) + E_T^{\text{miss}}$ sensitivity. This benchmark set of signal models, also called signal grid, is used in Chapter 8 to set limits on the 2HDM+a parameters.

The signal grid is chosen based on the effects of the model parameters on the signal kinematics and the signal cross section described in Chapter 6. These results guide the choice of parameter scans:

- A 2-D scan in the (M_a, M_A) plane is described in in Section 7.4. This scan explores a wide variety of signal kinematics, since M_a and M_A determine the resonant kinematics, as discussed in Sections 6.1 and 6.2.

- A 2-D scan in the $(M_a, \tan\beta)$ plane is described in Section 7.5. It extends the possible comparisons between $h(b\bar{b}) + E_T^{\text{miss}}$ and other searches for Dark Matter, such as collider searches using the $t\bar{t} + E_T^{\text{miss}}$, $b\bar{b} + E_T^{\text{miss}}$ [49], or t + E_T^{miss} [48] signatures. The $\tan\beta$ dependence is furthermore of interest in the larger context of Two-Higgs-Doublet Models irrespective of Dark Matter, since it is a central parameter of this class of model.

- Two auxiliary 1-D scans in $\sin\theta$ at two different M_a, M_A points are described in Section 7.6.1. These scan allow to study the effect of parameters such as $\sin\theta$, which affect the signal kinematics sub-dominantly, as discussed in Section 6.4.

- An auxiliary 1-D scan in M_χ is described in Section 7.6.2. It demonstrates how to interpret the results of the $h(b\bar{b}) + E_T^{\text{miss}}$ search in terms of a thermal relic Dark Matter hypothesis. While M_χ is crucial to a thermal relic interpretation, as discussed in Section 4.2.6, it has no effect on the $h(b\bar{b}) + E_T^{\text{miss}}$ signature for most of the parameter space where the $h(b\bar{b}) + E_T^{\text{miss}}$ search is relevant, as seen in Section 6.8.

7.2 Fixed Parameters

In each of the parameter scans in the above list, all parameters which are not scanned are kept fixed to the values given in Table 7.1. In the following the choice of the values for some of the fixed parameters is discussed.

Table 7.1: Values of fixed parameters in the scans of the 2HDM+a signal grid.

fixed parameter	value
$\sin\theta$	0.35
$\tan\beta$	1
M_H	M_A
$M_{H^\pm}$	M_A
λ_3	3
λ_{P1}	3
λ_{P2}	3
M_χ	10 GeV
y_χ	1

$\sin\theta = 0.35$ Low values of $\sin\theta$ yield a Jacobian peak that is more pronounced relative to the non-resonant bulk of the E_T^{miss} distribution, as discussed in Section 6.4. Variations of the location of the Jacobian peak reflect variations of the signal kinematics. A diverse set of kinematic signal signatures is a desired feature of the signal grid. Thus the Jacobian peak should be pronounced, and $\sin\theta$ small. However, too small $\sin\theta$ reduces the signal cross-section since small $\sin\theta$ means small pseudoscalar mixing, resulting in small couplings of the SM and Dark Matter sectors. The final choice of $\sin\theta = 0.35$ is large enough to give observable signal cross-sections, whilst retaining a pronounced Jacobian peak.

$M_H = M_{H^\pm} = M_A$ Mass degeneracy of H and $H^\pm$ is convenient to comply with electroweak precision constraints, as discussed in Section 4.2.2. Thus $M_H = M_{H^\pm}$, and in the following only the mass difference $\Delta \equiv M_H - M_A = M_{H^\pm} - M_A$ is considered. A larger mass difference[1] Δ yields a larger production cross-section, while $\Delta < 0$ suppresses the signal process, as discusssed in Section 6.3. However, high Δ also reduces the parameter space allowed by vaccum stability, as demonstrated in Section 4.2.4. Therefore, the final choice of $\Delta = 0$, i.e. full mass degeneracy of H, $H^\pm$ and A, compromises between these two constraints.

$\lambda_3 = \lambda_{P1} = \lambda_{P2} = 3$ λ_3 is a curvature parameter of the potential of the two Higgs doublets, and therefore relevant for vacuum stability, as discussed in Section 4.2.4. $\lambda_3 = 3$ is large enough that there is a stable vacuum for much of the parameter space. However, $\lambda_3 = 3$ on its own leads to very large values of g_{Aah} and consequently very large widths of A in parts of the parameter space, as described in Section 6.6. A large width of A leads to many signal events being non-resonant events, which have predominantly soft E_T^{miss}, as Figure 6.19(c) demonstrates. A large fraction of non-resonant signal events is not desirable, because they lack the diversity of signal kinematics of the resonant channel, achieved by varying M_A and M_a. Thus, to avoid large values of g_{Aah}, λ_{P1} and λ_{P2} are set equal to λ_3, such that they cancel in g_{Aah}.

[1] Both the trilinear scalar couplings like g_{Aah} and the vacuum stability constraints are functions of the difference of the *squared* masses of A, H, and $H^\pm$. Fixing Δ means that the change of the couplings and the Higgs vacuum structure across the M_a, M_A plane exhibits a residual dependence on the absolute masses, beyond the Δ dependence. Using the difference of the squared masses in place of Δ would avoid this. However, a linear relation between M_H and M_A is desirable because H and A have analogous kinematics in the $h + E_T^{\text{miss}}$ and $Z + E_T^{\text{miss}}$ channel, respectively [1]. A linear relation between M_H and M_A thus makes comparison of the channels easy.

$M_\chi = 10$ GeV For a collider search such as the one considered here, the Dark Matter mass M_χ has no effect on the production cross section or signal kinematics given that $M_\chi < M_a/2$. Thus the sensitivity of the search is constant as a function of M_χ. For this reason, $M_\chi = 10$ GeV is chosen. $M_a \approx 100$ GeV and below are excluded by $h \to$ inv. searches [1], so a dedicated scan of these low mediator masses is not foreseen. Very low M_χ such as $M_\chi = 10\,\text{GeV}$ does not, in general, yield a Dark Matter relic density compatible with the astrophysical observation [108]. However, it is expected that over the wide range of M_χ values where $M_\chi < M_a/2$ and the collider search result is identical to the $M_\chi = 10$ case, intervals compatible with the observed Dark Matter relic density can be found. The limits of this M_χ insensitivity of the search are explored in the auxiliary scan of M_χ in Section 7.6.2.

7.3 Parton Level Sensitivity and Acceptance Estimates

7.3.1 Sensitivity Estimate Using Limits with Reduced Model Dependence

The outline of the signal grid in the parameter space of the 2HDM+a is given by the list in Section 7.1. To decide on concrete sets of parameter values to include in the grid, an estimate of the signal sensitivity is needed. Too high sensitivity indicates a model that is excluded by existing searches, and so does not need to be included in the grid. Too low sensitivity indicates a model that could not be found by the search at the current sensitivity even if it existed. A search for such a model is meaningless, and thus should not be part of the grid. Therefore, the intermediate parameter space, where a search can contribute information, should be covered by the grid.

The sensitivity of the search for $h(b\bar{b}) + E_T^{\text{miss}}$ described in Ref. [2] to the 2HDM+a is estimated based on the generic cross section limits with reduced model dependence from Ref. [2]. These generic limits with reduced are described in Section 3.5.1. Along with the limits with reduced model dependence, an aggregate estimate of the detector acceptance and efficiency relative to parton level simulations is also provided in Ref. [2]. This allows one to directly use parton level simulations of the 2HDM+a as inputs to the sensitivity estimate. The parton level simulations avoid simulating the parton shower, hadronization, and in particular the detector response. The simulation of the detector response is very costly in terms of CPU-time, so by dropping it, the sensitivity can be estimated much faster. In this way, more iterations on different versions of the signal grid can be performed.

The limits with minimal model dependence are given in [2] in terms of the visible cross-section of $h(b\bar{b})+E_T^{\text{miss}}$ events for four regions of E_T^{miss}: $[150\,\text{GeV}, 200\,\text{GeV})$, $[200\,\text{GeV}, 350\,\text{GeV})$, $[350\,\text{GeV}, 500\,\text{GeV})$, and $E_T^{\text{miss}} > 500\,\text{GeV}$. These limits are reproduced in Table 3.2 and Figure 3.4 to provide context for the studies presented here. To compare these values to the parton level simulation results, an estimate of the detector efficiency as well as the acceptance of the event selections of the analysis is needed. This estimate is provided in Ref. [2] in terms of a single acceptance times efficiency ($\mathcal{A} \times \epsilon$) value per E_T^{miss} bin, reproduced in Table 3.2. The value of $\mathcal{A} \times \epsilon$ corresponds to the probability that an event generated at parton level in a given E_T^{miss} bin is reconstructed in that same E_T^{miss} bin and passes all selections. The limits with minimal model dependence are provided separately for each of the four E_T^{miss} bins used in Ref. [2].

Thus, the simulated events need to be binned into those bins. To obtain the parton level production cross section $\sigma_i^{\text{parton}}(h\chi\bar{\chi})$ in a particular E_T^{miss} region i, a sample of parton level events is generated as described in Section 5.3. The output of the event generation at parton

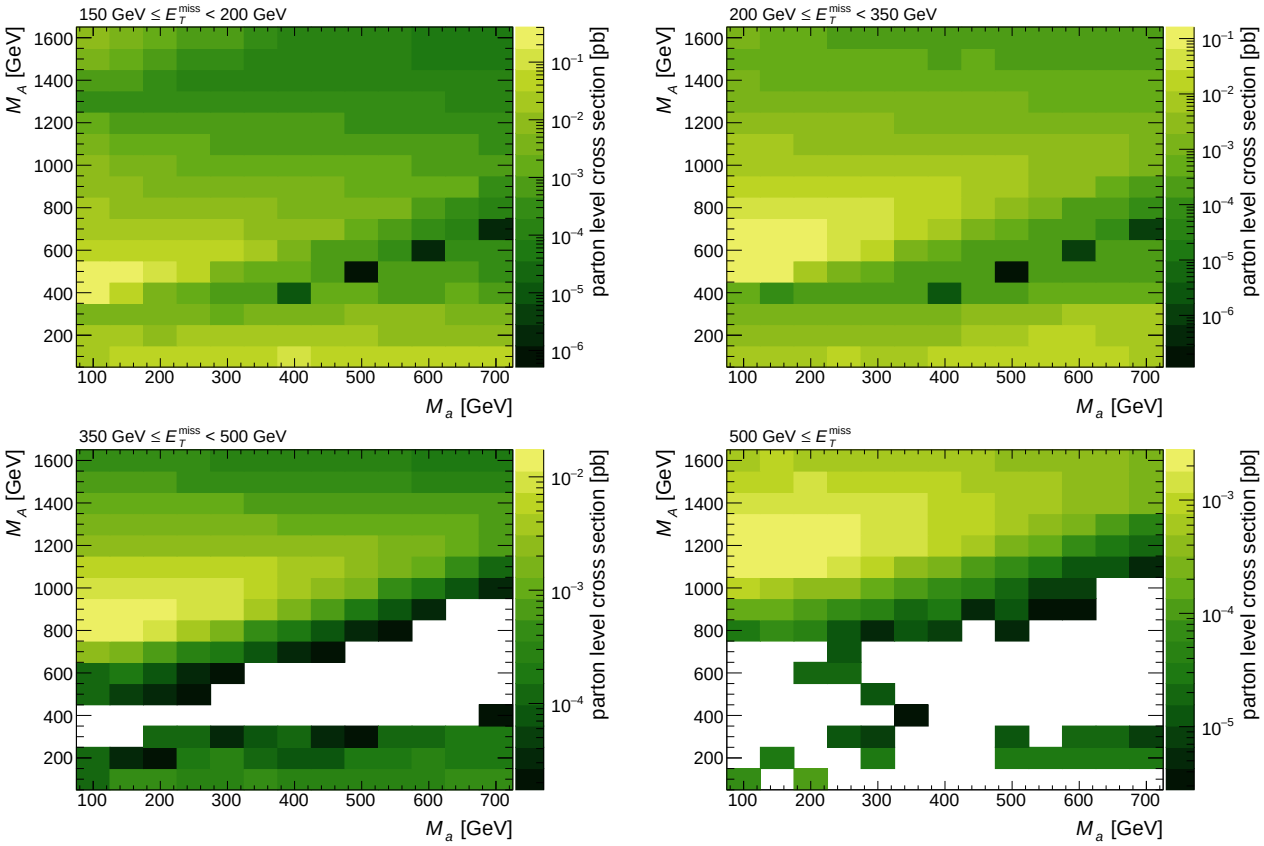

Figure 7.1: The production cross-section of $h + E_T^{\text{miss}}$ signal events at parton level as a function of (M_a, M_A) in each of the four $E_T^{\text{miss}}-$ bins. The remaining parameters have the values $M_H = M_{H^\pm} = M_A, \sin\theta = 0.35, \tan\beta = 1, M_\chi = 10$ GeV and $\lambda_{P1} = \lambda_{P2} = \lambda_3 = 3$. A white model point indicates that no simulated event passed the E_T^{miss} selection.

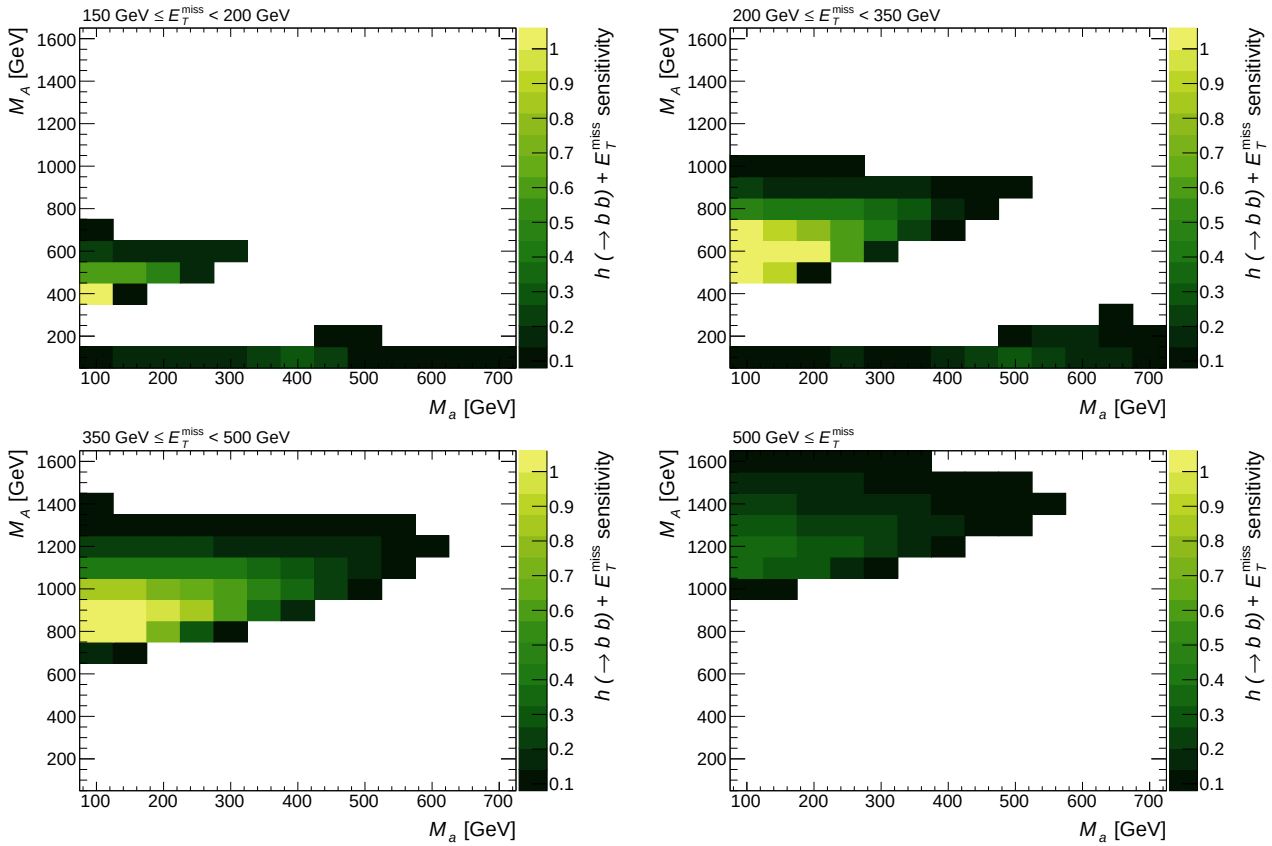

Figure 7.2: Estimated sensitivity to $h(b\bar{b}) + E_T^{\text{miss}}$ events as a function of (M_a, M_A) in each of the four $E_T^{\text{miss}}-$ bins. The sensitivity, defined in Equation (7.2), is based on the limits with reduced model dependence from Ref. [2]. The remaining parameters have the values $M_H = M_{H^\pm} = M_A, \sin\theta = 0.35, \tan\beta = 1, M_\chi = 10$ GeV and $\lambda_{P1} = \lambda_{P2} = \lambda_3 = 3$. Model points colored white indicate that the sensitivity estimate is below 0.1. The color scale is inclusive to high values, i.e. all sensitivities > 1 are displayed in the same color.

level is a file in the LHE format, described in Refs. [124, 125]. The production cross section calculated during the event generation is parsed from the LHE file, as well as the four-momenta of the final state particles. The parton level E_T^{miss} is calculated event by event as the transverse projection of the sum of the momenta of the final state Dark Matter particles in the event. All events in the file are binned into the four E_T^{miss} regions in Table 3.2, and the total cross-section is multiplied by the fraction of events in E_T^{miss} bin i to obtain $\sigma_i^{\text{parton}}(h\chi\bar{\chi})$. Figure 7.1 shows the results of this for the example of the (M_a, M_A) scan.

Then the simulated cross-section in one E_T^{miss} bin i is compared to the limit with minimal model dependence from Ref. [2], yielding a single bin sensitivity estimate, $\sigma_i^{\text{observed}}(h(b\bar{b}) + E_T^{\text{miss}})$, in that E_T^{miss} bin,

$$\mathcal{S}_i = \frac{\sigma_i^{\text{parton}}(h\chi\bar{\chi}) \times \mathcal{BR}_{\text{SM}}(h \to b\bar{b}) \times [\mathcal{A} \times \epsilon]_i}{\sigma_i^{\text{observed}}(h(b\bar{b}) + E_T^{\text{miss}})}, \tag{7.1}$$

where the acceptance times efficiency in E_T^{miss}-bin i from Ref. [2], $[\mathcal{A} \times \epsilon]_i$, translates the parton level result to reconstruction level, to make it comparable to the reconstruction-level limit from Ref. [2], $\sigma_i^{\text{observed}}(h(b\bar{b}) + E_T^{\text{miss}})$. Because the parton level simulation used to calculate $\sigma_i^{\text{parton}}(h\chi\bar{\chi})$ does not include the decay $h \to b\bar{b}$, the branching fraction of this decay predicted

by the Standard Model, $\mathcal{BR}_{\mathrm{SM}}(h \to b\bar{b})$, for $M_h = 125\,\mathrm{GeV}$ is included separately. The value used is $\mathcal{BR}_{\mathrm{SM}}(h \to b\bar{b}) = 0.584$, following Ref. [17]. The resulting sensitivity arising from a single E_T^{miss} region $\mathcal{S}_i$ is shown in Figure 7.2 for the representative example of the (M_a, M_A) scan.

To obtain a single number estimating the sensitivity of a search that uses all four E_T^{miss} bins, the individual contributions are summed[2], resulting in the sensitivity estimate shown in Figure 7.3 for the example of the (M_a, M_A) scan. Thus the sensitvity is estimated as:

$$\begin{aligned} \mathcal{S} &= \sum_{i \in E_T^{\mathrm{miss}}-\mathrm{bins}} \mathcal{S}_i \\ &= \sum_{i \in E_T^{\mathrm{miss}}-\mathrm{bins}} \frac{\sigma_i^{\mathrm{parton}}(h\chi\bar{\chi}) \times \mathcal{BR}_{\mathrm{SM}}(h \to b\bar{b}) \times [\mathcal{A} \times \epsilon]_i}{\sigma_i^{\mathrm{observed}}(h(b\bar{b}) + E_T^{\mathrm{miss}})}. \end{aligned} \tag{7.2}$$

7.3.2 Simplified Acceptance Estimate

After deciding on the concrete parameter points to study, the number of events to simulate at each parameter point will need to be determined. A minimal number of signal events is needed in the input templates to the final signal fit to data, described in Section 3.5. With too few simulated signal events, this fit may not converge stably. So a point-by-point estimate of the size of the sample to be generated is needed, ideally avoiding expensive computations.

The minimum number of signal events needed, drawing on experience from the previous analysis described in [2], is $\mathcal{O}(1000)$ signal events after all selection cuts. To ensure a sufficient number of signal events remain after applying the selection cuts, at least $\mathcal{O}\left(\frac{1000}{[\mathcal{A}\times\epsilon]^{\mathrm{parton}}}\right)$ events need to be originally generated, where $[\mathcal{A} \times \epsilon]^{\mathrm{parton}}$ is the combination of detector acceptance and selection efficiency for some particular model.

$[\mathcal{A} \times \epsilon]^{\mathrm{parton}}$ can be determined by straightforwardly generating events, simulating the detector response, and applying the event selection. However, this straightforward approach is computationally expensive, mainly because of the complexity of the detector simulation. Hence, a faster yet less accurate estimate is chosen. The fast estimate for $[\mathcal{A} \times \epsilon]^{\mathrm{parton}}$ used here is based on the same parton level simulated signal event samples used for the sensitivity estimate described in Section 7.3.1. Similarly to the sensitivity estimate, the events are binned into bins of E_T^{miss}. Unlike for the sensitivity estimate, the bin contents are subsequently weighted by the $\mathcal{A} \times \epsilon$ values from Table 3.2. Finally, the bin contents are divided by the sum of all weights of the events originally generated and then summed, yielding

$$\begin{aligned} [\mathcal{A} \times \epsilon]^{\mathrm{parton}} &= \sum_{i \in E_T^{\mathrm{miss}}-\mathrm{bins}} [\mathcal{A} \times \epsilon]_i^{\mathrm{parton}} \\ &\gtrapprox \sum_{i \in E_T^{\mathrm{miss}}-\mathrm{bins}} \frac{\sum_{\mathrm{j}\in\mathrm{i}} w_j^{\mathrm{parton}} \times [\mathcal{A} \times \epsilon]_i}{\sum_k^{\mathrm{all}} w_k^{\mathrm{parton}}} \end{aligned} \tag{7.3}$$

in analogy to Equation (7.2). Here w_k^{parton} is the weight of parton level event k, and $[\mathcal{A} \times \epsilon]_i$ the acceptance times efficiency in bin i as given in [2]. The"$\gtrapprox$" used in Equation (7.3) indicates that

[2]Typically a model has a E_T^{miss} distribution covering more than one E_T^{miss} bin. This implies that there can be models where the estimated sensitivity in every bin is < 1, yet the sum in Equation (7.2) is > 1. This is desired for the purpose of estimating sensitivity when designing the grid to be used in a dedicated search, since one expects that a dedicated search will take all relevant bins into account. For a rigorous exclusion using only the limits with reduced model dependence the sensitivity in the most sensitive bin is more appropriate.

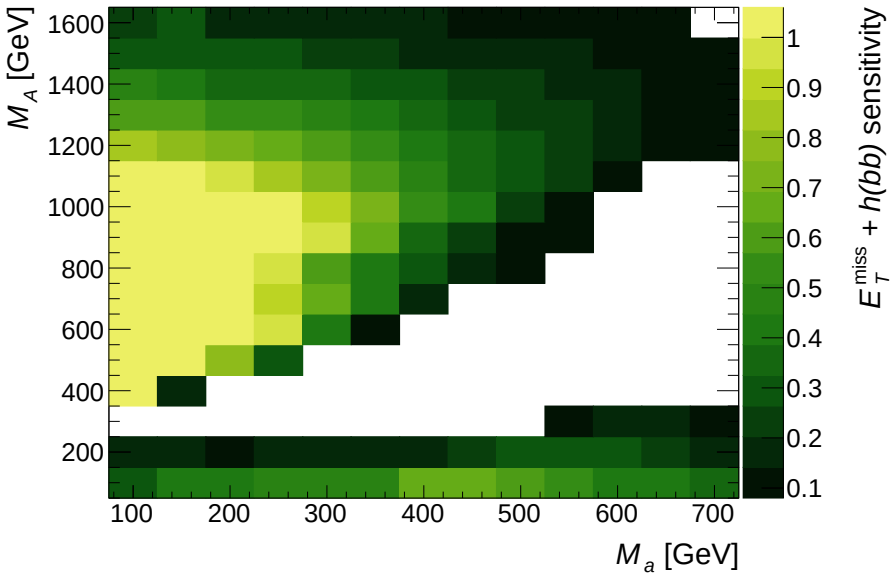

Figure 7.3: Estimated sensitivity to $h(b\bar{b}) + E_T^{\text{miss}}$ events as a function of (M_a, M_A), summed over all four E_T^{miss} bins. The sensitivity, defined in Equation (7.2), is based on the limits with reduced model dependence from Ref. [2]. The remaining parameters have the values $M_H = M_{H^\pm} = M_A, \sin\theta = 0.35, \tan\beta = 1, M_\chi = 10$ GeV and $\lambda_{P1} = \lambda_{P2} = \lambda_3 = 3$. Model points colored white indicate that the sensitivity estimate is below 0.1. The color scale is inclusive to high values, i.e. all sensitivities > 1 are displayed in the same color.

the use of the $\mathcal{A} \times \epsilon$ values from Table 3.2 is a conservative estimate, as these values are not those for the particular model, but rather the lowest values chosen from a range kinematically similar models.

7.4 $M_a - M_A$ Scan

The scan of the $h(b\bar{b}) + E_T^{\text{miss}}$ sensitivity in the sense of Equation (7.2) in the (M_a, M_A) plane is shown in Figure 7.3.

The sensitivity is high for intermediate M_A, which corresponds to large signal cross sections. Moreover the sensitivity is also high for large $M_A - M_a$. This corresponds to resonant signals with large E_T^{miss}, to which the search is most sensitive, as Figure 3.4 demonstrates.

There is a sensitivity drop with increasing $M_A = M_H = M_{H^\pm}$ for $M_A \geq 1$ TeV. This is caused by an increase of Γ_A, which increases the fraction of non-resonant signal events. Many non-resonant signal events have very soft E_T^{miss}, below the lowest accepted E_T^{miss} of 150 GeV. This reduced acceptance causes the loss of sensitivity at extreme M_A.

Near the mass diagonal $M_a = M_A$, the sensitivity is also very low. The reason is that the Jacobian peak is at soft E_T^{miss} for a low mass-splitting $M_A - M_a$, as described by Equation (4.13) and shown in Figures 6.1 and 6.6. Furthermore, the coupling g_{Aah}, given in Equation (4.6), is small when all Higgs bosons are nearly mass degenerate, resulting in a small total cross-section, and lowering the sensitivity even further.

The sensitivity above the mass diagonal ($M_A > M_a$) is larger than the sensitivity below the mass diagonal ($M_A < M_a$) due to two effects:

1. $M_A = M_H = M_{H^\pm}$, i.e. the charged and neutral CP-even scalars have low masses below the diagonal, but high masses above it, introducing an asymmetry. In Figures 6.12

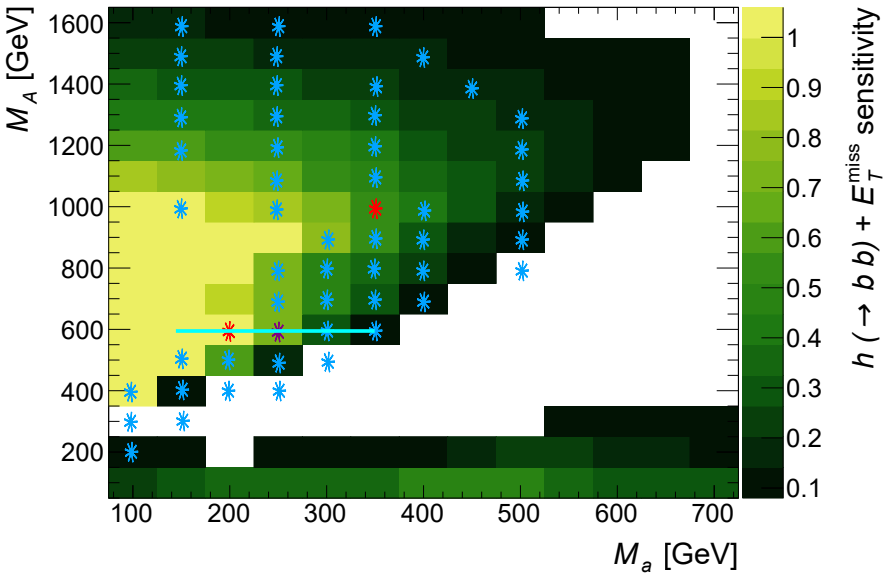

Figure 7.4: The grid of parameter points chosen for the detector level simulation, projected into the (M_a, M_A) plane, overlaid onto the estimated sensitivity in that plane. The red points mark the location of the auxiliary scans of $\sin\theta$, described in Section 7.6.1. The lilac point marks the location of the auxiliary scan of M_χ, discussed in Section 7.6.2. The projection of the scan of M_a and $\tan\beta$, described in Section 7.4 is marked by the turquoise bar.

and 6.13 one can see that values of $M_H = M_{H^\pm}$ below the mass of the higher-mass pseudoscalar give a reduced overall cross-section and a lower fraction of resonant signal events. Both effects reduce sensitivity.

2. $\sin\theta = 0.35 \neq 1/\sqrt{2}$, i.e. the pseudoscalar mixing is asymmetric: A couples comparatively more strongly to SM particles than a, and vice versa for the couplings to the Dark Matter fermion χ. So the coupling situation below the diagonal corresponds to the case of $\sin\theta = \sqrt{1-0.35^2} \approx 0.938$ and $M_A > M_a$. As can be seen in Figure 6.15, this configuration has a larger fraction of soft, nonresonant signal events, and correspondingly lower sensitivity, as also demonstrated in Figures 7.10 and 7.11 below.

The parameter points chosen to be included in the detector level simulation are shown in Figure 7.4. Points are chosen such that they cover the area with estimated sensitivities within $(0.1, ..., 1)$, which is where the edge of the exclusion manifold is expected to fall.

The number of events simulated at detector level in this (M_a, M_A) scan is shown in Table 7.2.

For most of the parameter points simulated at detector level, a simplified version of the fully GEANT4 [120] based simulation of the ATLAS detector, or "full simulation" [81] is used, called "ATLFAST-II" [81]. ATLFAST-II speeds up the simulation of the detector by replacing the GEANT4 simulation of the calorimeter, which is the most time consuming part of the detector simulation for typical hard events, with a faster approximation called FastCaloSim [81]. The FastCaloSim approximation does not simulate the interactions of incoming particles with the calorimeter, but replaces incoming truth particles with calorimeter shower parametrizations, picking a shower parameterization to match the energy and pseudorapidity of the incoming particle and rescaling the shower energy and depth to fit the particle energy [81]. Shower shape and calorimeter cell size effects are approximated by integrating stored shower shape functions over the size of the calorimeter cells [81]. As a result, ATLFAST-II is about 10 times

Table 7.2: Number of events to be generated at each parameter point of the M_a, M_A scan, in units of 1000 events. Samples with $M_A \geq 1.1$ TeV (**bold numbers**) are simulated using the full Geant4 detector simulation [81], the rest are simulated using the fast ATLAS detector simulation ATLFAST-II.

	M_a [GeV]	100	150	200	250	300	350	400	450	500
M_A [GeV]										
1600			**50**		**50**		**35**			
1500			**50**		**35**			**10**		
1400			**25**		**15**		**10**		**10**	
1300			**10**		**10**		**10**			**10**
1200			**10**		**10**		**10**			**10**
1100					**10**		**15**			**10**
1000			10		10		15	10		10
900						10	15	15		15
800					15	10	15	15		25
700					15	15	20	25		
600				20	25	25	50			
500			25	25	50	50				
400		25	100	50	50					
300		50	50							
200		50	50							

faster than the full simulation [81]. Thus most of the samples simulated at detector level in the parameter scans presented here are simulated using ATLFAST-II, to save computing resources.

For models where a significant fraction of signal events in the merged regime, ATLFAST-II can not be used to simulate the detector response. In the merged regime where $E_T^{\text{miss}} > 0.5\,\text{TeV}$, the transverse momentum of the Higgs boson is so large that the $h \to b\bar{b}$ candidate can not be reconstructed as two small-R jets, because the two jets are too close, as discussed in Section 3.3.1.2. In this regime, the Higgs candidate is reconstructed as a single large-R jet [2]. Since the mass of the large-R Higgs candidate depends on the substructure of the large-R jet, which is not modeled correctly by the ATLFAST-II simulation, ATLFAST-II can not be used. Thus, for models with a significant fraction of events in the merged regime, the full simulation is used instead of ATLFAST-II.

To find the models in the signal grid that require the full simulation, the sensitivity estimate in the merged regime $\mathcal{S}_{E_T^{\text{miss}}>0.5\,\text{TeV}}$ as defined in Equation (7.1) is used. The fraction of events in the merged regime is taken to be significant if $\mathcal{S}_{E_T^{\text{miss}}>0.5\,\text{TeV}} > 0.1$, i.e. when it contributes significantly to the estimated sensitivity. These points are those with $M_A \geq 1.1$ TeV, as Figure 7.2 shows.

Thus for models with $M_A < 1.1$ TeV, the signal samples are simulated with ATLFAST-II, and only the 3 E_T^{miss} bins from the resolved regime can be used. Consequently, the sum in Equation (7.3) should only include the 3 E_T^{miss} bins with $E_T^{\text{miss}} \leq 0.5\,\text{TeV}$. This corresponds to the acceptance estimate shown in Figure 7.5(a), which is used to determine the required number of events in the signal samples for models with $M_A < 1.1\,\text{TeV}$.

Conversely, for the models with $M_A \geq 1.1\,\text{TeV}$, the signal samples are simulated with the full simulation and all 4 E_T^{miss} bins can be used in the analysis. Correspondingly the sum in

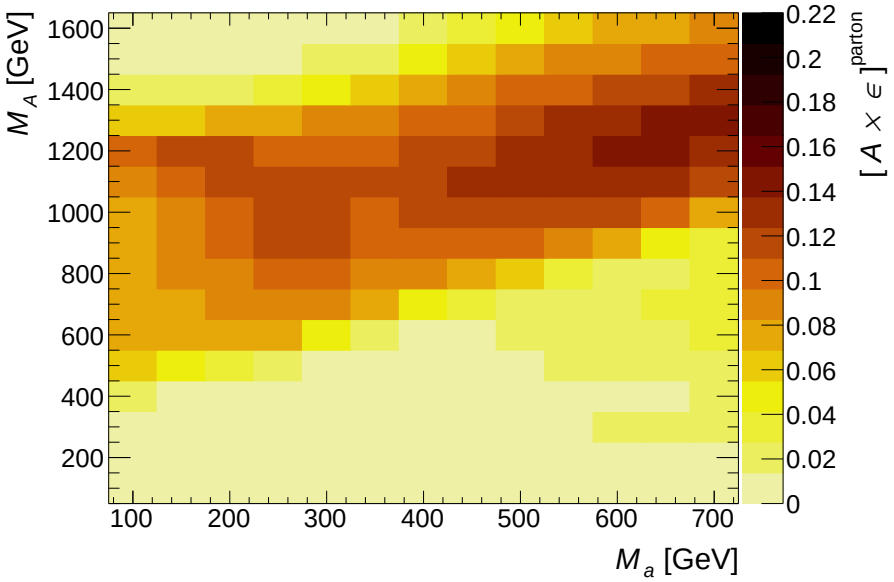

(a) acceptance in the resolved regime only

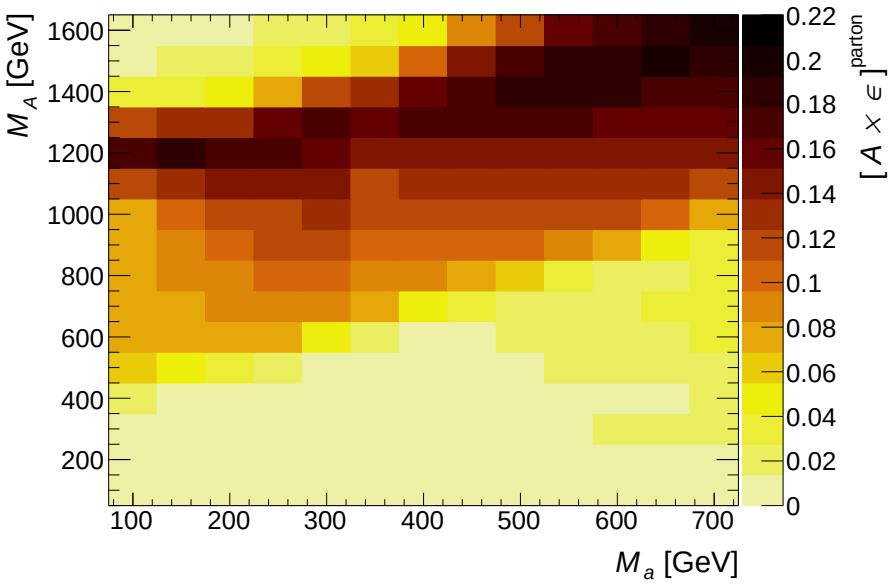

(b) acceptance for full analysis including the merged regime

Figure 7.5: Acceptance × efficiency estimate in the (M_a, M_A) plane, either using only the first three bins corresponding to the resolved regime as shown in (a) or all for 4 bins, including both the resolved and the merged regime as shown in (b). The acceptance is estimated using Equation (7.3). The remaining parameters have the values $M_H = M_{H^\pm} = M_A, \sin\theta = 0.35, \tan\beta = 1, M_\chi = 10$ GeV and $\lambda_{P1} = \lambda_{P2} = \lambda_3 = 3$.

Equation (7.3) should include all 4 E_T^{miss} bins to obtain the relevant acceptance estimate. This acceptance estimate is shown in Figure 7.5(b) and used to determine the required number of events in the signal samples for models with $M_A \geq 1.1\,\text{TeV}$.

7.5 $M_a - \tan\beta$ Scan

The scan in $(M_a, \tan\beta)$ of the sensitivity of the search for $h(b\bar{b}) + E_T^{\text{miss}}$ is shown in Figure 7.6.

At very low $\tan\beta$, the Yukawa coupling to top quarks is large, and most of the signal events come from non-resonant processes, corresponding to amplitudes such as those shown in Figures 4.6(a) to 4.6(c). These non-resonant processes give soft E_T^{miss}, as Figure 6.16 demonstrates. Soft E_T^{miss} lowers the signal acceptance, displayed in Figure 7.7(a), which reduces the sensitivity of the search.

For higher $\tan\beta$ the sensitivity increases. This is due to the reduced top Yukawa coupling. Firstly, the reduced top Yukawa coupling reduces the partial decay width for $A \to t\bar{t}$ decays, yielding a narrower A width and thus a more resonant signal. Secondly, the top Yukawa coupling affects non-resonant contributions like the one in Figure 4.6(a), which have two top Yukawa vertices, comparatively more than the resonant contribution displayed in Figure 4.4, which has only one top Yukawa vertex. Both effects increase the fraction of resonant signal events. Resonant events can have larger E_T^{miss}, and the search is more sensitive to events with larger E_T^{miss}. This leads to the increased sensitivity around $\tan\beta \approx 1.2$ that is visible in Figure 7.6.

However, reducing the top Yukawa coupling also reduces the overall production cross-section. This effect is sub-dominant below $\tan\beta \approx 1.2$, and the sensitivity increases with $\tan\beta$. But above $\tan\beta \approx 1.2$, the sensitivity loss due to reduced cross-section outpaces the sensitivity gain caused by the increased fraction of resonant signal events. Therefore, above $\tan\beta \approx 1.2$, the search gets less sensitive with increasing $\tan\beta$.

At very high $\tan\beta$ (≥ 10), this trend is reversed again, as the $\tan\beta$ enhancement[3] of the coupling to b-quarks relative to top quarks becomes so large that it compensates for the lower b quark Yukawa coupling corresponding to the about 60 times smaller b-quark mass. At this point $b\bar{b}$ initiated processes, such as those shown in Figure 4.7, start to dominate the production cross-section, as Figure 6.17 demonstrates, and drive the increase in sensitivity that is shown in Figure 7.8. This increase in sensitivity with $\tan\beta$ caused by the cross-section increase is partially reduced by a simultaneous decrease in acceptance displayed in Figure 7.7(b), but not enough to cancel it.

Using the same approach and the same decision criteria as in the case of the (M_a, M_A) scan described in Section 7.4, a set of models to simulate at detector level is chosen. These points are displayed in Figure 7.9. Since $M_A = 600$ GeV for all the points in the scan is too low to allow a significant fraction of signal events in the range $E_T^{\text{miss}} \geq 500$ GeV, the number of events to generate is determined using only the acceptance of the resolved regime, shown in Figure 7.7. For most of the scan, gluon fusion is the only relevant production mode, as $\tan\beta$ is small, as demonstrated in Figure 6.17. Therefore, for all points, a gluon fusion initiated sample is generated, and the size of the sample is determined based on the gluon fusion initiated acceptance estimate shown in Figure 7.7(a). However, the $b\bar{b}$ initiated contribution may not be entirely negligible for $\tan\beta = 10$, as its production cross section is of a similar size as the gluon fusion initiated one in this regime. Hence, three $b\bar{b}$ annihilation initiated samples are produced for $\tan\beta = 10$ and $M_a = 150, 200, 250$ GeV respectively, with the necessary number

[3] we are considering a Yukawa sector of type II. See Sections 4.1.2 and 6.5.1 for more details.

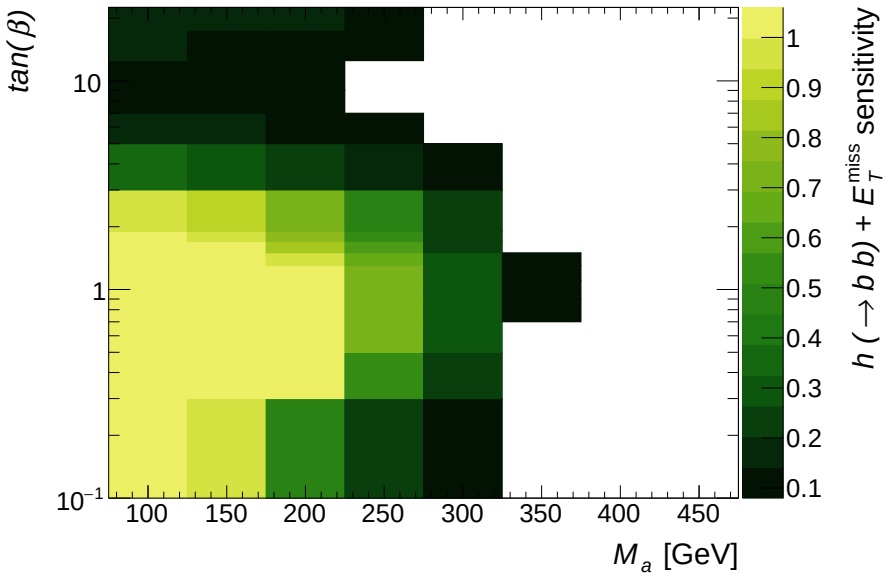

Figure 7.6: Sum over all E_T^{miss}-bins of the estimated signal sensitivity to $h(b\bar{b}) + E_T^{\text{miss}}$ events as a function of $(M_a, \tan\beta)$. The sensitivity, defined in Equation (7.2), is based on the limits with reduced model dependence from Ref. [2]. The remaining parameters have the values $M_H = M_{H^\pm} = M_A = 600$ GeV, $\sin\theta = 0.35, M_\chi = 10$ GeV and $\lambda_{P1} = \lambda_{P2} = \lambda_3 = 3$. Model points colored white indicate that the sensitivity estimate is below 0.1. The color scale is inclusive to high values, i.e. all sensitivities > 1 are displayed in the same color.

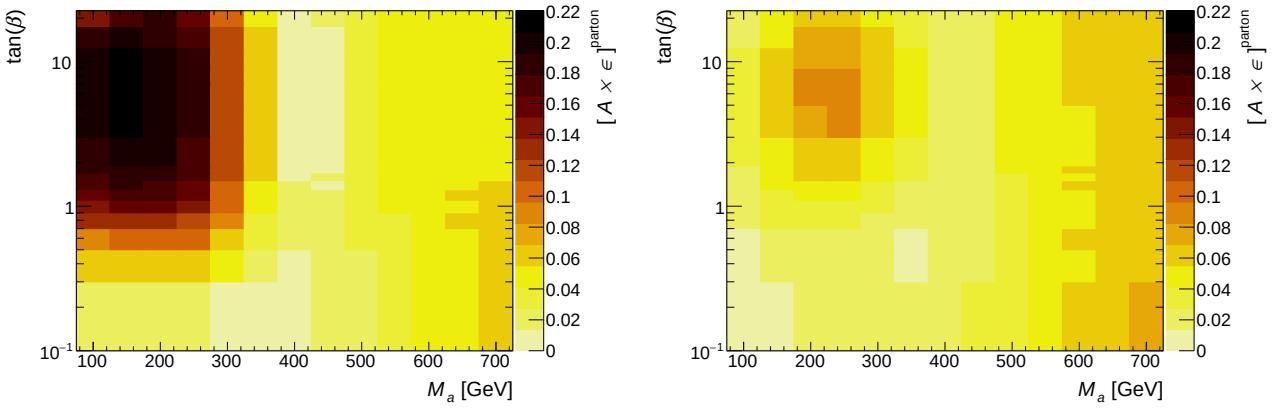

(a) gluon fusion initiated events

(b) $b\bar{b}$ initiated events

Figure 7.7: Signal acceptance $\times$ efficiency estimate in the $M_a, \tan\beta$ plane for the resolved regime. The acceptance of only gluon fusion initiated events is shown in (a), and the acceptance of $b\bar{b}$ -annihilation initiated events is shown in (b). The acceptance $\times$ efficiency estimate is defined in Equation (7.3). The remaining parameters have the values $M_H = M_{H^\pm} = M_A = 600GeV, \sin\theta = 0.35, M_\chi = 10$ GeV and $\lambda_{P1} = \lambda_{P2} = \lambda_3 = 3$.

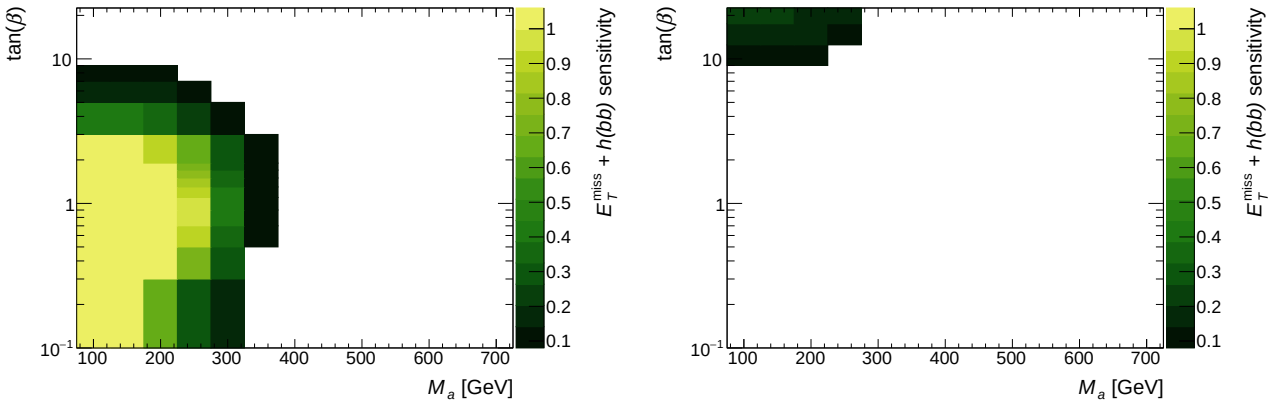

(a) sensitivity to gluon fusion initiated events

(b) sensitivity to $b\bar{b}$ initiated events

Figure 7.8: $h(b\bar{b}) + E_T^{\text{miss}}$ sensitivity comparison of gluon fusion and $b\bar{b}$ initiated production in the $(M_a, \tan\beta)$ plane for the resolved regime. The sensitivity of only gluon fusion induced events is shown in (a), and the sensitivity of $b\bar{b}$ -annihilation initiated events is shown in (b). The sensitivity, defined in Equation (7.2), is based on the limits with reduced model dependence from Ref. [2]. The remaining parameters have the values $M_H = M_{H^\pm} = M_A = 600\,\text{GeV}, \sin\theta = 0.35, M_\chi = 10$ GeV and $\lambda_{P1} = \lambda_{P2} = \lambda_3 = 3$. Model points colored white indicate that the sensitivity estimate is below 0.1. The color scale is inclusive to high values, i.e. all sensitivities > 1 are displayed in the same color.

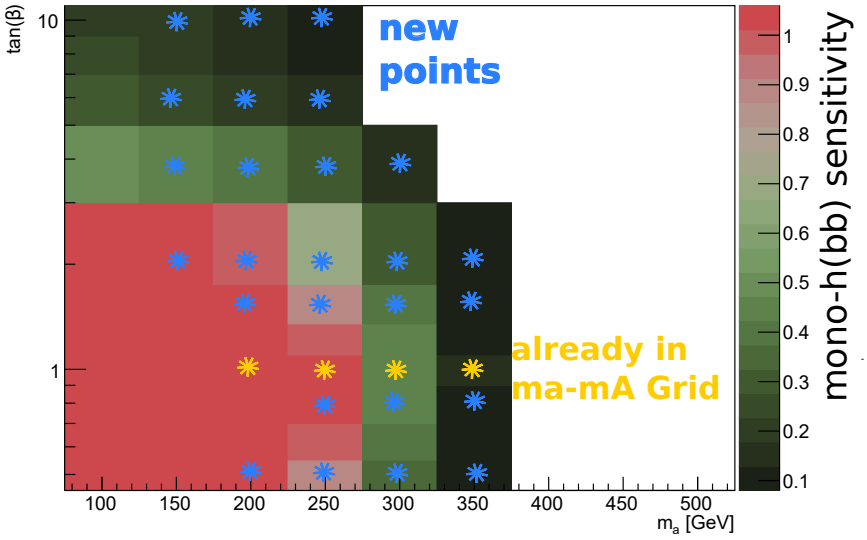

Figure 7.9: The grid of parameter points chosen for the detector level simulation, projected onto the $M_a, \tan\beta$ plane, overlaid with the estimated sensitivity.

Table 7.3: Number of events generated at each parameter point of the $(M_a, \tan\beta)$ scan, in units of 1000 events. The numbers shown in this table correspond to only the gluon fusion initiated samples. In addition to what is shown, three $b\bar{b}$ annihilation initiated samples are also generated, for $\tan\beta = 10$ and $M_a \in \{150\text{ GeV}, 200\text{ GeV}, 250\text{ GeV}\}$, of 10000 events each.

	M_a [GeV]	150	200	250	350	350
$\tan\beta$						
10		10	10	10		
6		10	10	10		
4		10	10	10	20	
2		10	10	15	20	25
1.5			10	15	20	40
0.8				20	25	40
0.5			25	35	40	50

of events estimated based on Figure 7.7(b). The resulting size of the samples in the $(M_a, \tan\beta)$ scan is shown in Table 7.3.

7.6 Auxilliary Scans

7.6.1 $\sin\theta$ Scans

The sensitivity of the search as a function of $\sin\theta$ is shown in Figures 7.10 and 7.11, for two different (M_a, M_A) points. Both points are chosen such that for the nominal value for all other scans of $\sin\theta = 0.35$, they are close to, but not at, sensitivity 1, as can be seen in Figure 7.4.

The sensitivity is 0 at $\sin\theta = 0$ and $\sin\theta = 1$, since those values correspond to the absence of pseudoscalar mixing. As discussed in more detail in Section 6.4, in the absence of mixing, the remaining portal terms do not generate a coupling of the Dark Matter fermions to Standard Model particles that can give rise to signals such as shown in Figures 4.6 and 4.7. Thus the signal cross section vanishes exactly, and the search is not sensitive to $\sin\theta = 0$ and $\sin\theta = 1$.

The sensitivity is in general not monotonous in $\sin\theta$, as Figures 7.10 and 7.11 demonstrate. For intermediate values, $\sin\theta$ influences the couplings of the pseudoscalars a and A to Dark Matter and to standard model fermions [1], as well as the coupling strength of trilinear scalar vertices such as g_{Aah}, given in Equation (4.6). Because these couplings occur differently in the various diagrams shown in Figure 4.6, the amplitudes have different dependencies on $\sin\theta$. This leads to the non-monotonous cross section dependence on $\sin\theta$ demonstrated in Figure 6.14, where the cross section has multiple maxima at different $\sin\theta$ values. These multiple maxima are carried over to the sensitivity curve, as Figure 7.11 demonstrates. Furthermore, changes of $\sin\theta$ change the fraction of resonant signal events, as shown in Figure 6.15. Therefore, the choice of $\sin\theta$ strongly affects the signal acceptance, as Figure 7.12 shows, which further modifies the sensitivity dependence on $\sin\theta$.

The number and location of maxima and turning points in the sensitivity depends on the precise interplay of the couplings. The couplings also depend on most of the other model parameters, including all the masses of all Higgs bosons. This is demonstrated by the markedly different $\sin\theta$ dependence exhibited in the low mass $\sin\theta$ scan in Figure 7.10, compared to the high-mass scan shown in Figure 7.11. The two mass points are chosen specifically to

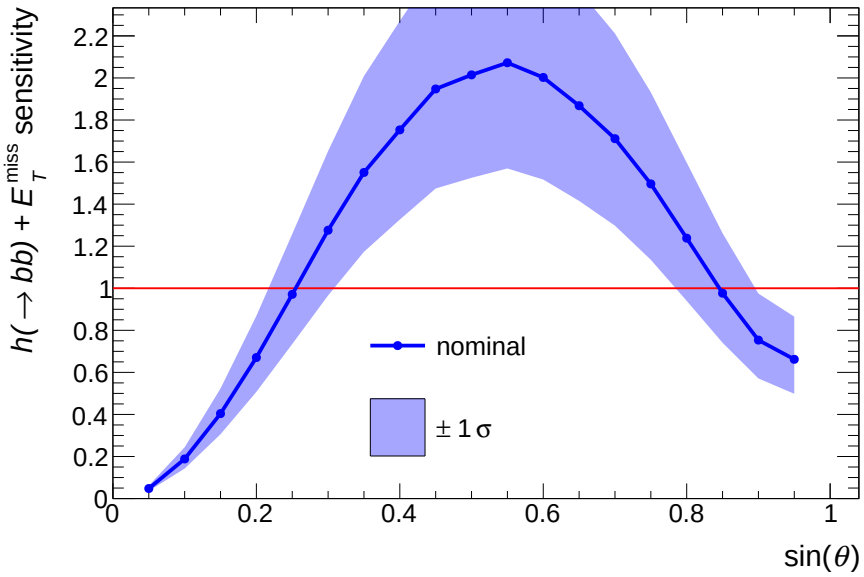

Figure 7.10: Sum over all E_T^{miss}-bins of the estimated signal sensitivity to $h \to bb + E_T^{\text{miss}}$ events as a function of the pseudoscalar mixing parameter $\sin\theta$. The sensitivity, defined in Eq. 7.2, and its uncertainty are based on the limits with reduced model dependence from Ref. [2] and the uncertainties described therein. The remaining parameters have the values $M_a = 200$ GeV, $M_H = M_{H^\pm} = M_A = 600$ GeV, $M_\chi = 10$ GeV, $\tan\beta = 1$, and $\lambda_{P1} = \lambda_{P2} = \lambda_3 = 3$.

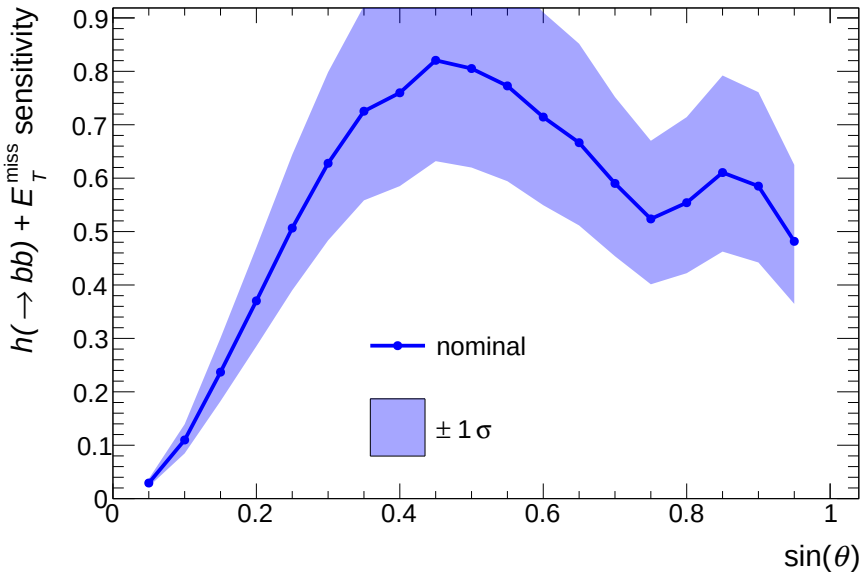

Figure 7.11: Sum over all E_T^{miss}-bins of the estimated signal sensitivity to $h \to bb + E_T^{\text{miss}}$ events as a function of the pseudoscalar mixing parameter $\sin\theta$. The sensitivity, defined in Equation (7.2), and its the uncertainty are based on the limits with reduced model dependence from Ref. [2] and the uncertainties described therein. The remaining parameters have the values $M_a = 350$ GeV, $M_H = M_{H^\pm} = M_A = 1000$ GeV, $M_\chi = 10$ GeV, $\tan\beta = 1$, and $\lambda_{P1} = \lambda_{P2} = \lambda_3 = 3$.

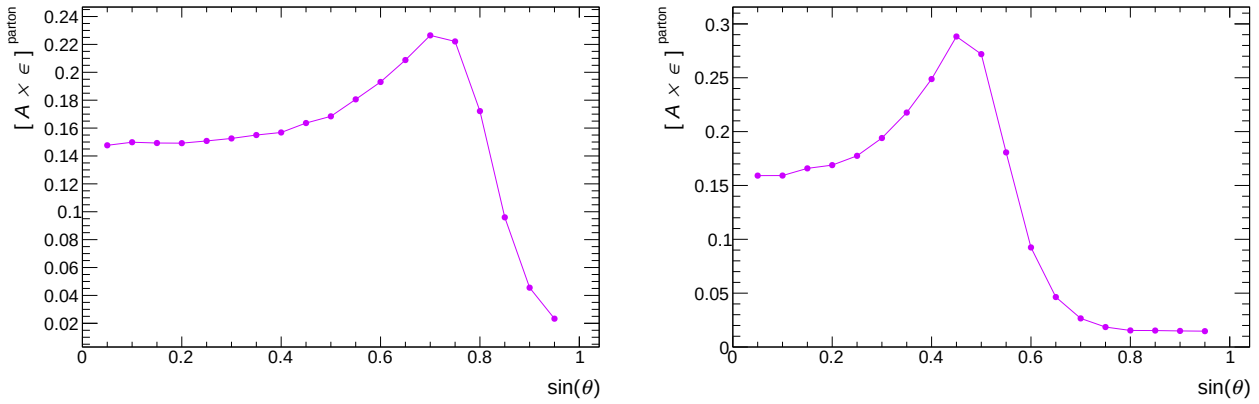

(a) low-mass (b) high-mass

Figure 7.12: Signal acceptance × efficiency estimate as a function of $\sin\theta$ in the low-mass $\sin\theta$ scan with $M_a = 200$ GeV, $M_H = M_{H^\pm} = M_A = 600$ GeV, shown in (a), and in the high-mass $\sin\theta$ scan with $M_a = 350$ GeV, $M_H = M_{H^\pm} = M_A = 1000$ GeV, shown in (b). The acceptance × efficiency estimate is defined in Equation (7.3). The remaining parameters take the values $M_\chi = 10$ GeV, $\tan\beta = 1$, and $\lambda_{P1} = \lambda_{P2} = \lambda_3 = 3$.

Table 7.4: Number of events generated for the low-mass $\sin\theta$ scan.

$\sin\theta$	number of events/1000
0.1	25
0.2	25
0.5	25
0.8	25
0.9	50
0.95	50

demonstrate these differences in dependence due to different M_a and M_A. For the models in the low mass scan at $M_A = 600\,\text{GeV}$, $M_a = 200\,\text{GeV} < 2m_t \approx 345\,\text{GeV}$, $A \to t\bar{t}$ is an allowed decay, but $a \to t\bar{t}$ is kinematically forbidden. Consequently, the width of a scales as $\Gamma_{a\to\chi\bar{\chi}} \propto \cos^2\theta$ [1], but Γ_A has many contributions, including $\Gamma_{A\to t\bar{t}} \propto \cos^2\theta$ and $\Gamma_{A\to\chi\bar{\chi}} \propto \sin^2\theta$ [1]. This is different from the high mass scan at $M_A = 1000\,\text{GeV}$, $M_a = 350\,\text{GeV} > 2m_t \approx 345\,\text{GeV}$, where Γ_a gains an additional contribution from $\Gamma_{a\to t\bar{t}} \propto \sin^2\theta$. Thus, neither the cross section nor the acceptance have the same $\sin\theta$ dependence.

In conclusion, tuning the $\sin\theta$ of a parameter scan to the sensitivity in a single point can lead to sub-optimal sensitivity in other points. This is demonstrated in the two dedicated scans of $\sin\theta$ at two different (M_a, M_A) points. The $\sin\theta$ scans thus provide context for the choice of $\sin\theta = 0.35$ in the other scans, which does lead to sufficient sensitivities for many models in these scans. However, as stated in Section 7.2, the overriding motivation for choosing $\sin\theta = 0.35$ is that with this choice, the signal kinematics can be sensitively changed by varying M_A and M_a, because $\sin\theta = 0.35$ yields a pronounced Jacobian peak. This effect on the relative yield of resonant vs. non-resonant processes, which many model parameters have, is also demonstrated by the scans of $\sin\theta$, as shown in Figures 6.15 and 7.12.

The parameter points included in the scans of $\sin\theta$ simulated at detector level, chosen

Table 7.5: Number of events generated for the high-mass $\sin\theta$ scan.

$\sin\theta$	number of events/1000
0.1	15
0.5	10
0.6	10
0.7	50
0.9	50

based on the sensitivity estimates displayed in Figures 7.10 and 7.11, and the number of simulated events generated for these points, chosen based on the acceptance estimates shown in Figure 7.12, are listed in Tables 7.4 and 7.5.

7.6.2 M_χ Scan

The sensitivity to models with varying M_χ is shown in Figure 7.13. It depends most strongly on the mass hierarchy of a and χ, i.e. the size of M_a compared to the $a \to \chi\bar{\chi}$ threshold at $2M_\chi$.

Above threshold, where $M_\chi < M_a/2$, the sensitivity stays constant. This constant sensitivity results from the invariant signal E_T^{miss} shape and constant signal cross- section in this regime, as shown in Figures 6.22(a) and 6.23, respectively.

At threshold, where $M_\chi = M_a$, the sensitivity is enhanced because the partial width of the decay $a \to \chi\bar{\chi}$ is resonantly enhanced, increasing the signal cross-section. However, the numerical simulation is not expected to predict the correct size of the enhancement, since it does not take into account the momentum dependence of the effective width of the a pole [123], as discussed in Section 6.8.

Below threshold, where $M_\chi > M_a/2$, the sensitivity drops rapidly, because $M_\chi > M_a/2$ requires a virtual $a^\star \to \chi\bar{\chi}$ decay in the signal event. The rate of this virtual a decay is strongly suppressed by the typically narrow width of a. The width of a is reduced even further once $a \to \chi\bar{\chi}$ is kinematically inaccessible, as $\Gamma_{a\to\chi\bar{\chi}}$ is a large contribution to the total width of a for $M_\chi \leq M_a/2$ in general [1]. In fact, $\Gamma_{a\to\chi\bar{\chi}}$ is the only relevant contribution to Γ_a if $M_a < 2m_t$ and $\tan\beta$ is small ($\mathcal{O}(1)$) as it is the case here. There is a slight bump in sensitivity for $M_\chi \approx M_A/2$, when the $A \to \chi\bar{\chi}$ decay hits its threshold, but the absolute sensitivity remains negligible, as it is everywhere below the $a \to \chi\bar{\chi}$ threshold.

The signal acceptance to the M_χ scan is shown in Figure 7.14. It is almost flat above threshold, with residual fluctuations due to the bins with the highest $\mathcal{A} \times \epsilon$ being populated most sparsely. At threshold the acceptance changes rapidly, caused by the E_T^{miss} shape at threshold being significantly different to that just above or below threshold. As discussed above, the MC modelling is expected to fail close to threshold, thus it is unclear to what extent this behavior matches the correct threshold enhancement. Below threshold, continuous changes in the E_T^{miss} spectrum, as shown in Figure 6.22(b), lead to a continuously changing signal acceptance.

The event numbers in the samples simulated at detector level for the M_χ scan, that are chosen based on the acceptance estimates in Figure 7.14, are shown in Table 7.6. The points included in the scan are chosen based on the sensitivity estimate from Figure 7.13, with the aim of demonstrating the behavior of the sensitivity above, at, and below the $a \to \chi\bar{\chi}$ threshold.

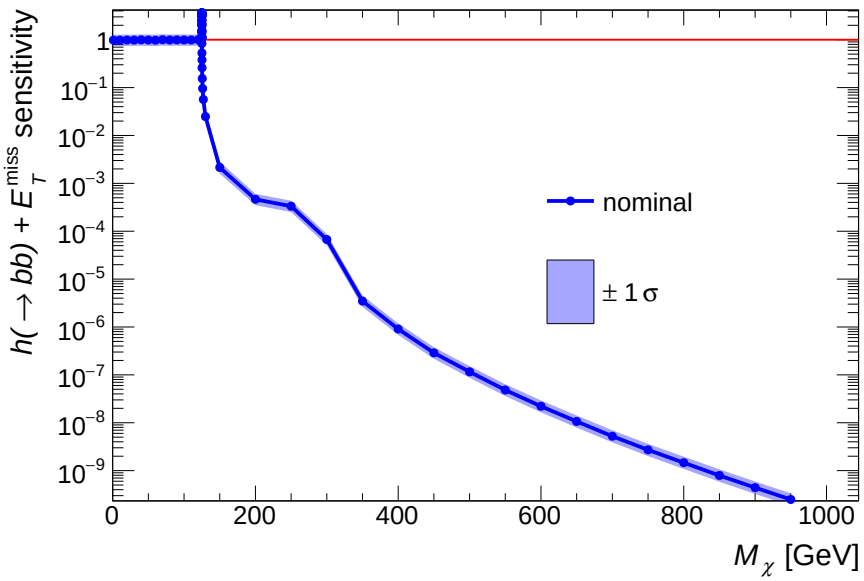

Figure 7.13: Sum over all E_T^{miss}-bins of the estimated signal sensitivity to $h \rightarrow bb + E_T^{\text{miss}}$ events as a function of the Dark Matter mass M_χ. The sensitivity, defined in Eq. 7.2, and its uncertainty are based on the limits with reduced model dependence from Ref. [2] and the uncertainties described therein. The remaining parameters have the values $M_a = 250$ GeV, $M_H = M_{H^\pm} = M_A = 600$ GeV, $\sin\theta = 0.35, \tan\beta = 1$, and $\lambda_{P1} = \lambda_{P2} = \lambda_3 = 3$.

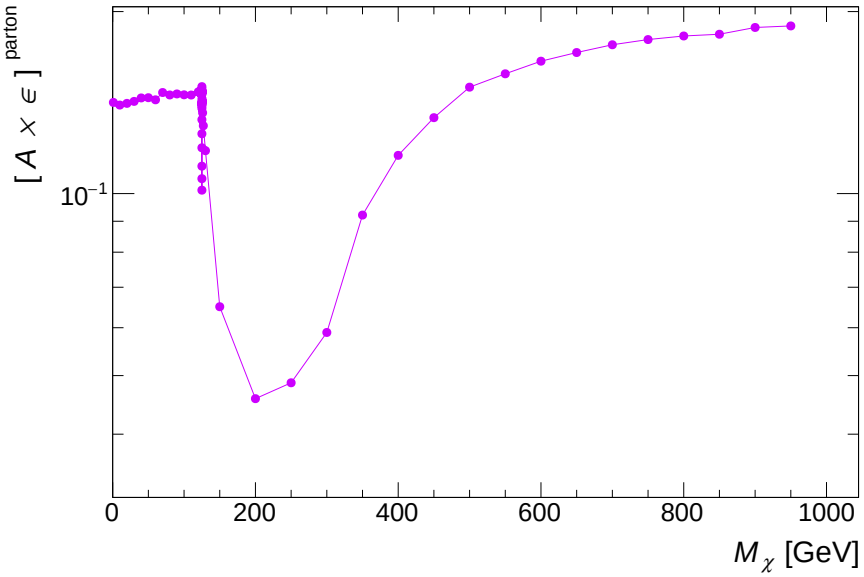

Figure 7.14: Estimated acceptance × efficiency of signal events in the E_T^{miss} bins of the resolved region as a function of the Dark Matter mass M_χ. The acceptance × efficiency estimate is defined in Equation (7.3). The remaining parameters have the values $M_a = 250$ GeV, $M_H = M_{H^\pm} = M_A = 600$ GeV, $\sin\theta = 0.35, \tan\beta = 1$, and $\lambda_{P1} = \lambda_{P2} = \lambda_3 = 3$

Table 7.6: Number of events generated for the M_χ scan.

M_χ[GeV]	number of events/1000
100	25
124.9	25
125	35
125.005	25
125.01	25
125.05	25
125.2	25
126	25
200	50
500	25

As discussed in Section 7.2, this demonstrates to which extent a collider limit set for a low Dark Matter mass can be applied to models with higher Dark Matter mass that reproduce the observed Dark Matter relic density. For the models studied here, the collider limit derived for $M_\chi = 10\,\text{GeV}$ applies to any model where the $a \to \chi\bar{\chi}$ decay is kinematically allowed, i.e. for any $M_\chi < M_a/2$, which typically includes a model where the observed relic density is reproduced [109, 108].

7.7 Summary

In this Chapter, a scan of the parameter space of the 2HDM+a is performed. Based on the parameter studies of Chapter 6, the scan consists of two two-dimensional scans in the M_a, M_A and $M_a, \tan\beta$ planes of the parameter space, as well as one-dimensional scans in M_χ and $\sin\theta$. The scan of the M_a, M_A plane is done to obtain models with a large variety of kinematic signatures. The remaining scans are included to demonstrate specific aspects of how the scanned parameters affect the collider phenomenology and its interpretation.

Based on fast parton level simulations, the sensitivity of the search to the models and the acceptance of the predicted signal in the search are estimated in these scans. Using these sensitivity estimates, a benchmark set of points in the scanned dimensions is chosen. This benchmark set of points is studied in a separate detector-level search , described in Chapter 8. These points are chosen such that the scans cover the region where the exclusion contour of the detector-level search is expected to be. Then the acceptance estimate is used to determine the appropriate number of MC events to generate at the chosen parameter points. The final set of points consists of 105 samples, with 1 490 000 events. Of these 21 samples and 405 000 events use the full detector simulation, the remainder use the faster ATLFAST-II method.

Chapter 8

Limits Obtained with the Full Analysis

This chapter describes the detector level search for the 2HDM+a in the $h(b\bar{b})+E_T^{\text{miss}}$ signature. The detector level search is implemented as an interpretation of the latest $h(b\bar{b})+E_T^{\text{miss}}$ analysis, which is described in Chapter 3, using a set of detector level MC signal samples for the models decided upon in Chapter 7. The implementation of the interpretation is described in Section 8.1. The exclusion intervals resulting from the interpretation are presented and discussed in Section 8.2.

8.1 Description of the Detector Level Interpretation

The detector level 2HDM+a search is an interpretation of the $h(b\bar{b})+E_T^{\text{miss}}$ analysis in Ref. [2]; they use the exact same background estimate, selection cuts, signal and control regions, fit strategy, and input data samples. These are summarize in Chapter 3. The only difference to the existing analysis are the MC samples corresponding to the signal hypothesis. Instead of the Z'-2HDM samples used in Ref. [2], a set of 2HDM+a signal samples is produced according to the specifications derived and described in Chapter 7, using the standard ATLAS simulation tools [81]. These detector level signal samples are the inputs used in the interpretation.

The interpretation is implemented using the RECAST [126] framework. The $h(b\bar{b})+E_T^{\text{miss}}$ search as published in Ref. [2] has previously been integrated into RECAST using the `yadage` python package [127, 126]. This framework uses docker images. Docker is a freely distributed, industry standard tool combining files, file systems, environment variables, dependencies, setup scripts etc. into one object, called a docker image, that can be mounted and run on any system running a docker daemon [128]. Such docker images are used for the RECAST $h(b\bar{b})+E_T^{\text{miss}}$ analysis preservation to store the status of the workspace, the analysis code, and all tools, dependencies, and fixed inputs (e.g. calibration files). The only exception are the input data and the simulated data for signal and background, which are stored on the CERN eos file storage system. The analysis workflow is described as explicit "workflow manifests" in a set of YAML files.

The RECAST implementation of the $h(b\bar{b})+E_T^{\text{miss}}$ analysis assumes that all input signal MC samples are produced using the full GEANT4 simulation [81, 120] of the ATLAS detector. However, as discussed in Section 7.4, most of the signal MC samples used for the 2HDM+a interpretation are simulated using the faster ATLFAST-II [81] method. In ATLFAST-II, interacting particles (e.g. hadrons) entering the calorimeter are simulated by stored shower templates [81], whereby the substructure of the jet is mismodelled. In the resolved regime, with $E_T^{\text{miss}} < 0.5\,\text{TeV}$, no jet substructure observables are used [2], and thus the simulation with ATLFAST-II is sufficient. However, in the merged regime with $E_T^{\text{miss}} \geq 0.5\,\text{TeV}$, the Higgs

candidate mass is reconstructed as the mass of a single large-R jet, using track information to increase the mass resolution [2, 88]. Thus, the mass of the Higgs candidate in the merged regime is affected by the ATLFAST-II mismodelling. To make sure that no events in the merged regime are used in the signal samples simulated with ATLFAST-II, the interpretation with these samples drops all events in the merged regime from the signal MC inputs. This is done by constructing a modified RECAST workflow, that is used for interpretation with ATLFAST-II samples. The interpretation with the fully simulated samples listed in Table 7.2 uses the unmodified workflow instead.

The output of the RECAST framework are upper limits on the signal cross section, corresponding to the results of the fit described in Section 3.5. The upper limits are derived using the CL_s method, which is described in Section 8.1.1. In order to allow straightforward interpretation of the results, limits on the signal strength μ are calculated as:

$$\mu = \frac{\sigma_{\text{fit}}(h(b\bar{b}) + E_T^{\text{miss}})}{\sigma_{\text{2HDM+}a}(pp \to \bar{\chi}\chi h) \times \mathcal{BR}_{\text{SM}}(h \to \bar{b}b)}\,, \tag{8.1}$$

where $\sigma_{\text{fit}}(h(b\bar{b}) + E_T^{\text{miss}})$ is the fitted cross section, $\sigma_{\text{2HDM+}a}(pp \to \bar{\chi}\chi h)$ is the signal cross section predicted by the 2HDM+a, and $\mathcal{BR}_{\text{SM}}(h \to \bar{b}b) = 0.584$ [17] is the branching ratio $h \to b\bar{b}$ predicted by the SM. With μ defined as in Equation (8.1), interpretation of the fit results is straightforward: hypotheses with $\mu < 1$ are excluded because the smallest signal yield consistent with the observation is already smaller than what the 2HDM+a predicts. Conversely, variants with $\mu \geq 1$ are not excluded, since the signal yield predicted by the 2HDM+a and all expected backgrounds does not significantly differ from the observed number of events.

8.1.1 CL_s Exclusion Intervals

The CL_s method [129, 130], or modified frequentist method, is a way of calculating exclusion limits that builds on the classic definition of a frequentist confidence interval [131].

A classical frequentist confidence region is defined by its coverage probability. That is, a confidence region is a parameter region constructed such that if one repeats the measurement often enough, the fraction of times that the constructed regions *cover* the true value will eventually converge to the coverage probability [131]. In a limit setting context, a frequentist upper limit at confidence level CL then corresponds to the upper edge of a confidence interval with a $1 - CL$ coverage probability.

In the CL_s method, the confidence interval definition is modified such that exclusions or discoveries of models to which the search is not sensitive are suppressed [129]. This avoids unintuitive, though strictly consistent features of the classical confidence interval. For example, a search with larger backgrounds can set a stronger frequentist limit than one with smaller backgrounds, if both observe no events [131, 129].

To achieve this, the CL_s method introduces the two so called "confidence levels" CL_{s+b} and CL_b. By convention, the confidence levels are defined in terms of a test statistic Q that is monotonously increasing for more signal-like observations and monotonously decreasing for more background like observations. Typically, Q is a ratio of likelihoods such as $\frac{\mathcal{L}(s+b)}{\mathcal{L}(s_{\text{best fit}}+b)}$ [130, 93]. This choice makes Q the optimally powerful test statistic given the likelihoods, as shown by Neyman and Pearson in Ref. [132]. With such a Q, $CL_{s+b}(Q) = P(Q \leq Q_{\text{obs.}}|s+b)$ is the signal + background confidence level, meaning the probability that Q is at least as signal-unlike (or background-like) as the observed $Q_{\text{obs.}}$, assuming that there is signal on top of the background [129]. Similarly, $CL_b(Q) = 1 - P(Q \leq Q_{\text{obs.}}|b)$ is the probability that Q is

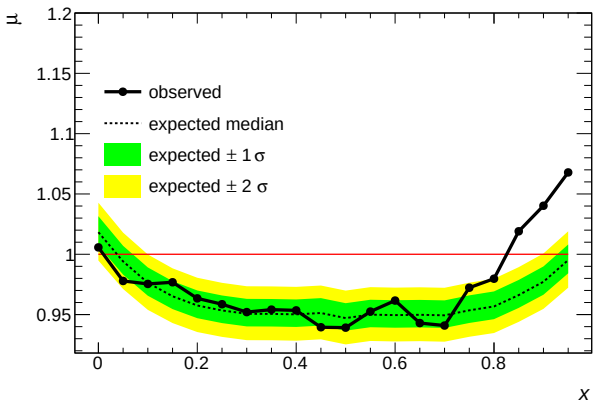

Figure 8.1: Generic example of a CL_s limit plot, illustrating the observed and expected upper limits on the observable μ as a function of the model parameter x.

as least as background-unlike as the observed $Q_{\text{obs.}}$, assuming that there is only background [129].

With the above definitions, a CL_s exclusion interval at CL confidence level is then an interval I where [129]:

$$CL_s(Q) = \frac{CL_{s+b}(Q)}{CL_b(Q)} \leq 1 - CL \quad \forall Q \in I \quad . \tag{8.2}$$

Such an interval can be constructed in analogous ways to the confidence intervals from before, but using CL_s in the place of the acceptance probability.

In Equation (8.2) the classical confidence is renormalised by the background confidence level CL_b Hence, when $CL_b \approx 1$, i.e. a result is very unlike the background expectation, the CL_s limit is similar to the frequentist coverage interval [129]. However, when $CL_b < 1$, i.e. for results that are likely even under the background-only hypothesis, the limit is weaker [129]. This is desired, since the search is not sensitive to this signal hypothesis. However, the resulting limit is weakened in regions of low sensitivity compared to the classical coverage interval. Since the coverage probability is larger than its confidence level CL [129], the CL_s limit is not a frequentist confidence interval of confidence level CL. Instead, a CL_s limit only ensures that the probability of the excluded region containing the true value is $\lesssim 1 - CL$, without making complementary claims about the unexcluded region [130].

The observations and predictions used in the limit setting procedure are rarely known without any systematic uncertainty [129]. Since an exclusion is intrinsically a statistical statement about some distribution, no uncertainties on the limit are calculated [129]. Instead, both in Ref. [2] and here, the statistical uncertainties are incorporated into the limits by adding parameters describing the systematically uncertain effects into the likelihood. Since estimates of these additional s.c. nuisance parameters are not the aim of a search, the likelihood is then profiled. This means that the nuisance parameters are replaced by their maximum likelihood estimate conditional on the parameter(s) of interest [92, 93]. Here, as in Ref. [2], the parameter of interest is the signal yield $\sigma_{fit}(h(b\bar{b}) + E_T^{\text{miss}})$, which we afterwards transform into a signal strength μ for easier interpretation, using Equation (8.1).

Generally, the profiled likelihood is more broadly distributed than the likelihood constructed considering only statistical fluctuations of signal and background. Thus, incorporating the systematic uncertainties yields larger acceptance intervals, and correspondingly weaker limits [129].

In the technical implementation used to set the CL_s limits on the $h(b\bar{b}) + E_T^{\text{miss}}$ signal yield given in Ref. [2] and here, the limits are *not* calculated by repeating the analysis for a large number of different signal cross sections to find the interval I of Equation (8.2). Instead, the edge of the interval, i.e. the upper limit, is inferred analytically by assuming that the best fit signal yield is a representative member of the underlying ensemble of hypothetical signal yields, i.e. using the so called asymptotic approximation for Asimov representation [92, 93].

A generic example of a typical plot illustrating a CL_s exclusion limit is shown in Figure 8.1. Besides the observed limits, constructed as described above, the expected limit is also indicated. The expected limit is obtained by replacing the real data used to calculate the observed limit by simulated data describing the total expected backgrounds. Since the background expectation is affected by systematic uncertainties, there is a distribution of expected limits, with associated probabilities given by the profile likelihood. This distribution of expected limits is illustrated in Figure 8.1 by its median and its uncertainty bands corresponding to 1 and 2 standard deviations from the median.

The distribution of expected limits indicates the sensitivity of the search [130]. That is, the search is only sensitive when the the expected upper limit on μ is smaller than 1. This is useful when interpreting the observed limits. An observed limit $\mu > 1$ for some signal model can indicate

- either that the signal model can not be excluded because the data deviate significantly from the background expectation, which could be evidence of new physics, or an underestimate of some background or uncertainty [130] ;
- or, more commonly, that the search is not sensitive to that signal model, and thus cannot exclude it, as was demanded in the construction of CL_s above.

These two cases can be distinguished by comparing the observed limit to the distribution of the expected limits based on the background-only hypothesis.

8.2 Results

8.2.1 2D Scans of M_a, M_A and $M_a, \tan\beta$

The expected and observed 95% C.L. CL_s limits on the signal strength μ are shown in Figure 8.2 for the (M_a, M_A) scan, and in Figure 8.3 for the scan in $(M_a, \tan\beta)$. The limits on the signal strength μ shown in Figures 8.2 and 8.3 are necessarily discrete, corresponding to the discrete set of simulated signal samples used to set the limits. In order to obtain continuous exclusion contours, the discrete points in Figures 8.2 and 8.3 are interpolated, and the points where the interpolation crosses $\mu = 1$ are connected to form contours in the (M_a, M_A) and $(M_a, \tan\beta)$ planes, respectively. The technical details of the interpolation are described in Appendix D. The resulting interpolated exclusion contours are shown in Figures 8.4 and 8.5.

Figure 8.4 shows that models with light pseudoscalar masses up to $M_a = 350\,\text{GeV}$ or heavy pseudoscalar masses between $M_A \geq 400\,\text{GeV}$ and $M_A \leq 1.3\,\text{TeV}$ can be excluded, depending on the respective other pseudoscalar mass. Figure 8.5 demonstrates that models with $M_a \leq 250\,\text{GeV}$ and $\tan\beta \leq 2.5$ are excluded.

By comparing the expected signal strength at reconstruction level to the sensitivity estimated at parton level the quality of the parton level sensitivity estimate defined in Equation (7.2) can be evaluated. The sensitivity estimates at parton-level using the generic limits from Ref. [2] shown in Figures 7.3 and 7.6 are very close to the respective expected limits in Figures 8.2(b)

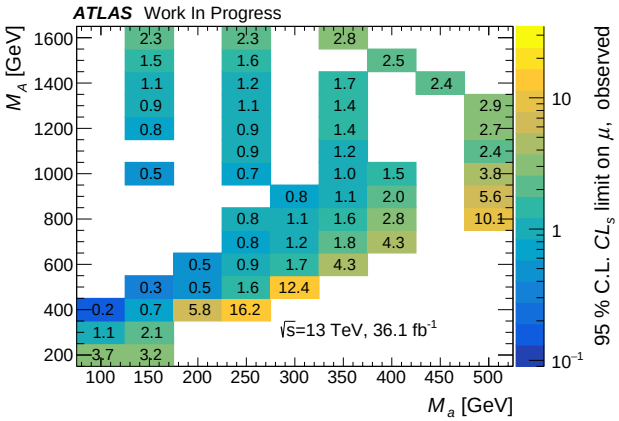

(a) observed limits

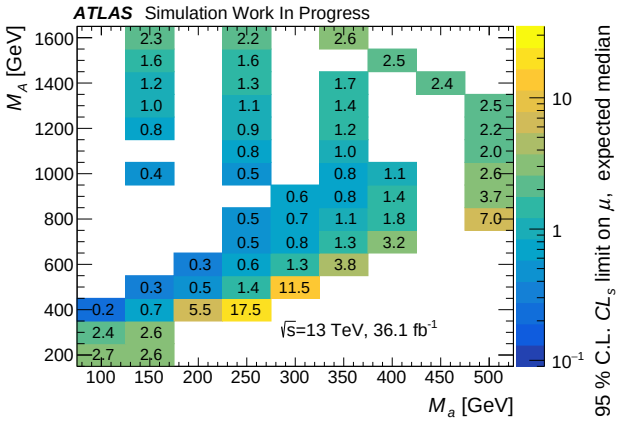

(b) median expected limits

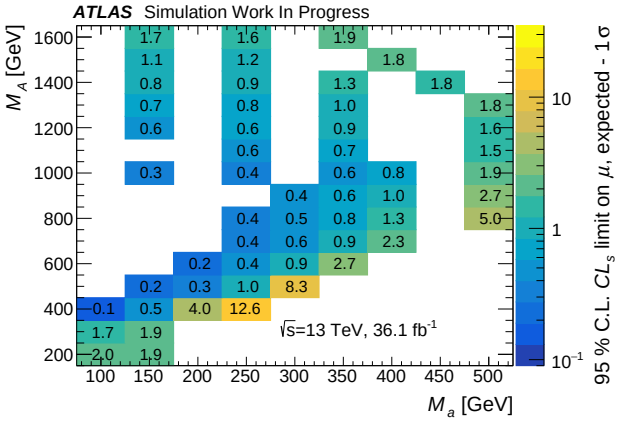

(c) -1σ variation of expected limits

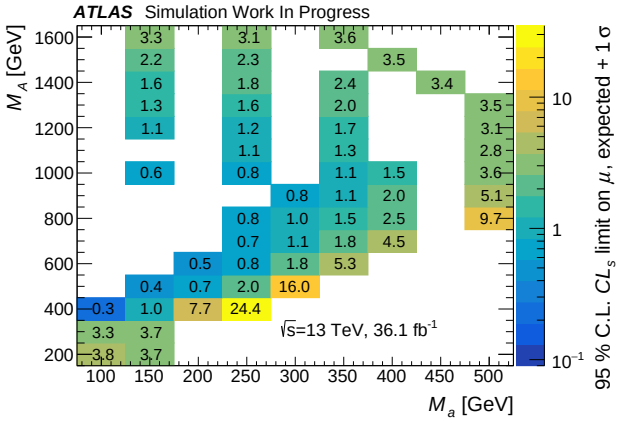

(d) $+1\sigma$ variation of expected limits

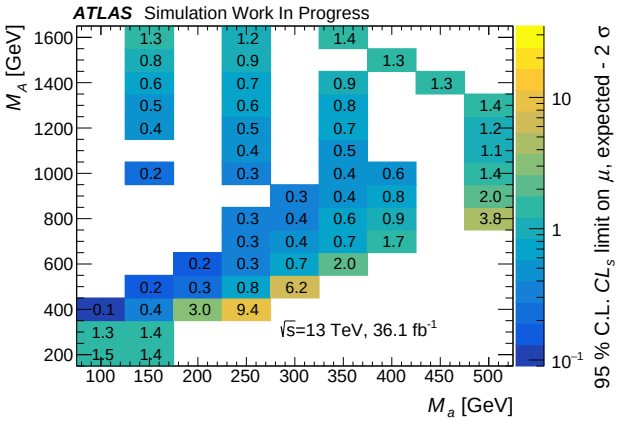

(e) -2σ variation of expected limits

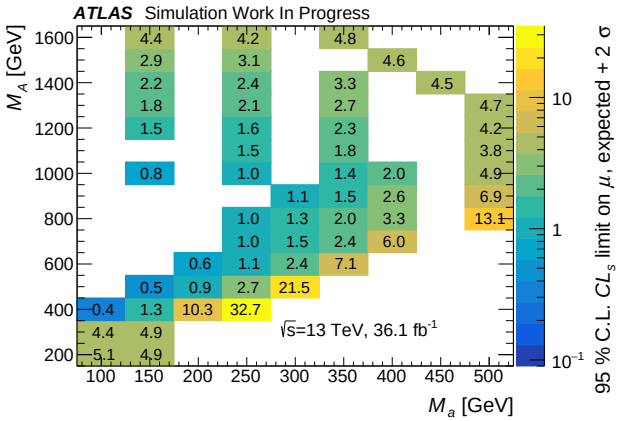

(f) $+2\sigma$ variation of expected limits

Figure 8.2: CL_s upper limits at 95% confidence level on the 2HDM+a $h(b\bar{b}) + E_T^{\text{miss}}$ signal strength, as defined in Equation (8.1), as a function of (M_a, M_A). The remaining parameters have the values $M_H = M_{H^\pm} = M_A$, $\sin\theta = 0.35$, $\tan\beta = 1, M_\chi = 10$ GeV, and $\lambda_{P1} = \lambda_{P2} = \lambda_3 = 3$.

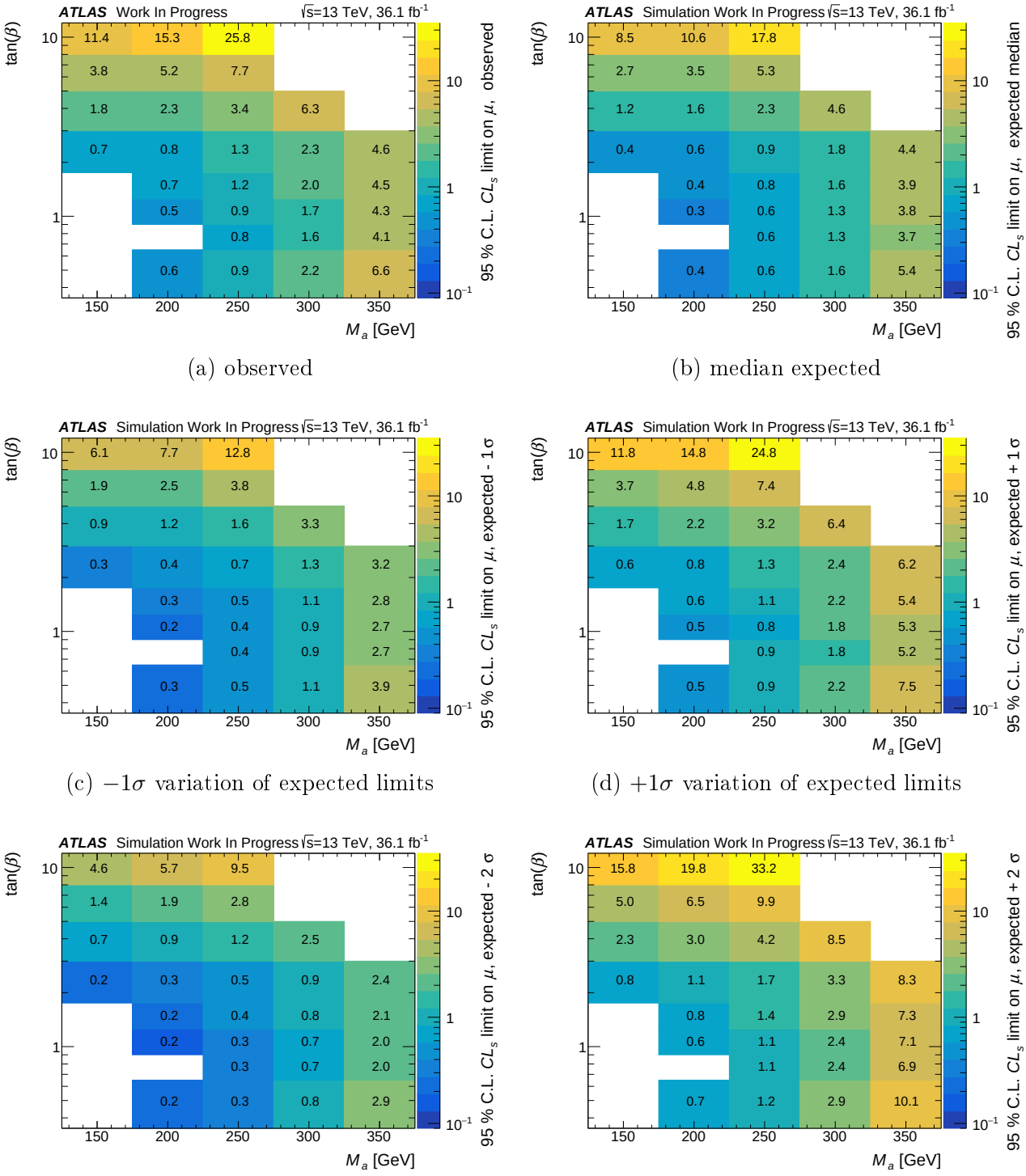

(a) observed

(b) median expected

(c) -1σ variation of expected limits

(d) $+1\sigma$ variation of expected limits

(e) -2σ variation of expected limits

(f) $+2\sigma$ variation of expected limits

Figure 8.3: CL_s upper limits at 95% confidence level on the 2HDM+a $h(b\bar{b}) + E_T^{\text{miss}}$ signal strength, as defined in Equation (8.1), as a function of $(M_a, \tan\beta)$. The remaining parameters have the values $M_H = M_{H^\pm} = M_A = 600\,\text{GeV}$, $\sin\theta = 0.35$, $M_\chi = 10$ GeV, and $\lambda_{P1} = \lambda_{P2} = \lambda_3 = 3$.

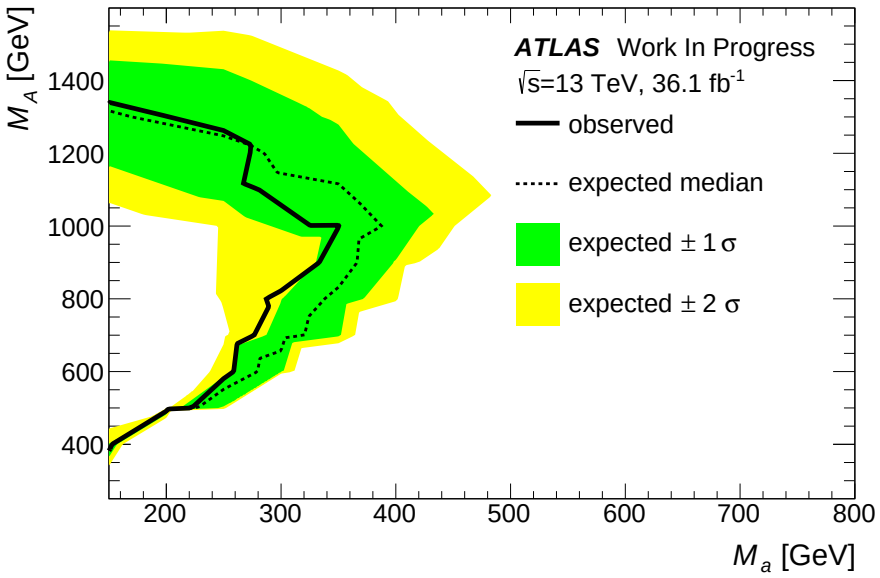

Figure 8.4: Interpolated CL_s limit contours at 95% confidence level in the (M_a, M_A) plane. The other parameters have the values $M_H = M_A = M_{H^\pm}, \tan\beta = 1, \sin\theta = 0.35, \lambda_3 = \lambda_{P1} = \lambda_{P2} = 3$, and $M_\chi = 10\,\text{GeV}$.

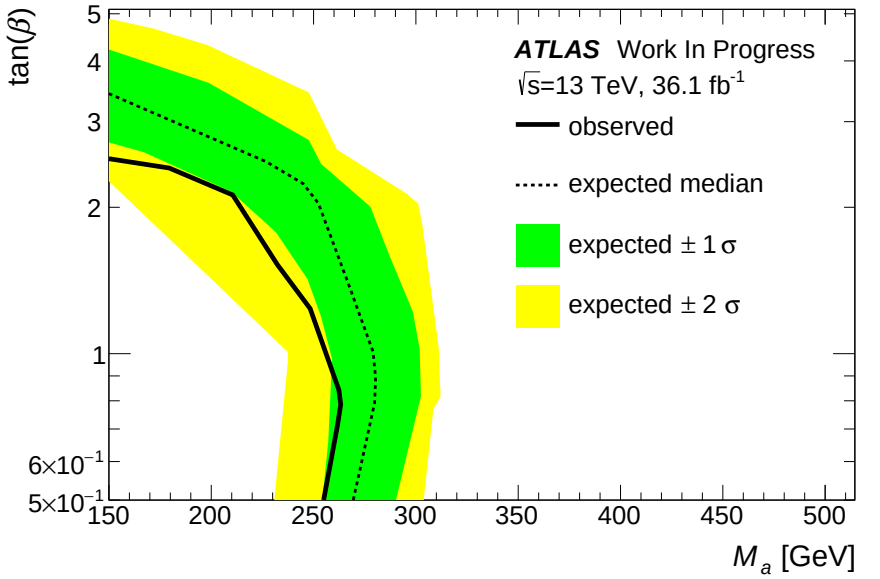

Figure 8.5: Interpolated CL_s limit contours at 95% confidence level in the $(M_a, \tan\beta)$ plane. The other parameters have the values $M_H = M_A = M_{H^\pm} = 600\,\text{GeV}, \sin\theta = 0.35, \lambda_3 = \lambda_{P1} = \lambda_{P2} = 3$, and $M_\chi = 10\,\text{GeV}$.

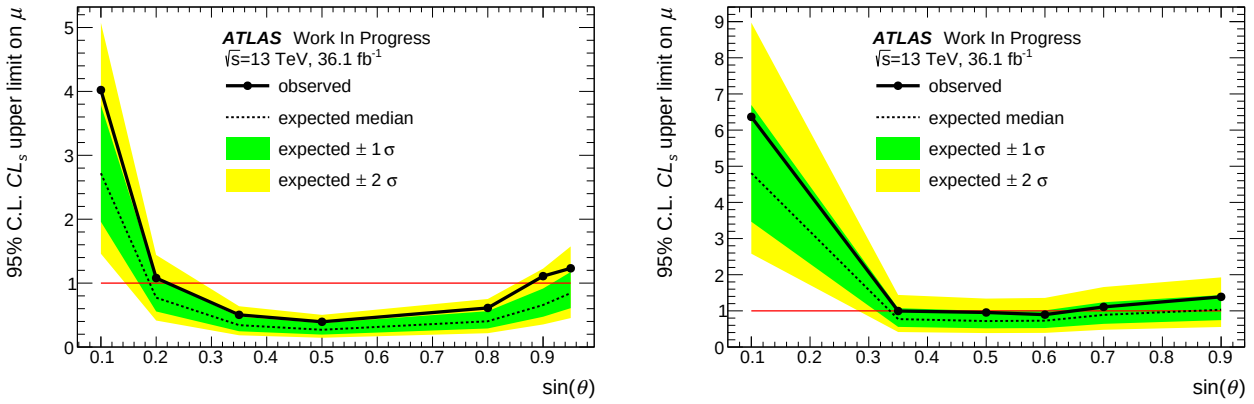

(a) $M_a = 200\,\text{GeV}, M_A = 600\,\text{GeV}$ (b) $M_a = 350\,\text{GeV}, M_A = 1000\,\text{GeV}$

Figure 8.6: CL_s upper limits at 95% confidence level on the 2HDM+a $h(b\bar{b}) + E_T^{\text{miss}}$ signal strength, as defined in Equation (8.1), as a function of $\sin\theta$. The limits on models with low pseudoscalar masses are shown in (a). The limits on models with high pseudoscalar masses are shown in (b). The remaining parameters have the values $M_H = M_{H^\pm} = M_A$, $\tan\beta = 1, M_\chi = 10$ GeV, and $\lambda_{P1} = \lambda_{P2} = \lambda_3 = 3$.

and 8.3(b). There is however some bias of the parton-level estimates towards reduced sensitivity. In other words, the parton level sensitivity estimate is slightly conservative but otherwise valid. The fact that the parton level estimate is somewhat conservative is expected, since it is constructed using the limits with reduced model dependence from [2], discussed in Section 3.5.1, which are constructed as the weakest limit out of a fiducial selection.

Comparing the limits on the M_a, M_A parameters of the 2HDM+a shown in Figure 8.4 to those on the $m_A, m_{Z'}$ parameters of the Z'-2HDM shown in Figure 3.3 one can see qualitatively similar behavior: when $M_A \gg M_a$ in the 2HDM+a ($m_{Z'} \gg m_A$ in the $Z'-$2HDM), the uncertainties are large, and the observed limit is somewhat stronger than the median expectation. Closer to the M_a, M_A ($m_A, m_{Z'}$) mass diagonal, the uncertainties are small, and the observed limit is a bit weaker than the median expectation. This behavior reflects two facts

- both interpretations use the same analysis and dataset, only the signal fit template is different;
- the kinematics of the resonant $Z' \to Ah$ decay of the $Z'-$2HDM are similar to those of the resonant $A \to ah$ decay of the 2HDM+a.

However, the excluded mass ranges differ, which is a result of the different cross section dependence on the masses, and the additional non-resonant decay channels present only in the 2HDM+a.

8.2.2 Auxiliary 1D Scans

8.2.2.1 $\sin\theta$ Scans

The observed CL_s upper limits at 95% confidence level (C.L.) on the 2HDM+a $h(b\bar{b}) + E_T^{\text{miss}}$ signal strength μ as a function of the mixing parameter $\sin\theta$ are shown in Figure 8.6. Based on results of the low mass $\sin\theta$ scan in Figure 8.6(a),$\sin\theta \in (0.22, 87)$ can be excluded at 95% confidence level. Based on the high mass $\sin\theta$ scan in Figure 8.6(b) no meaningful exclusion

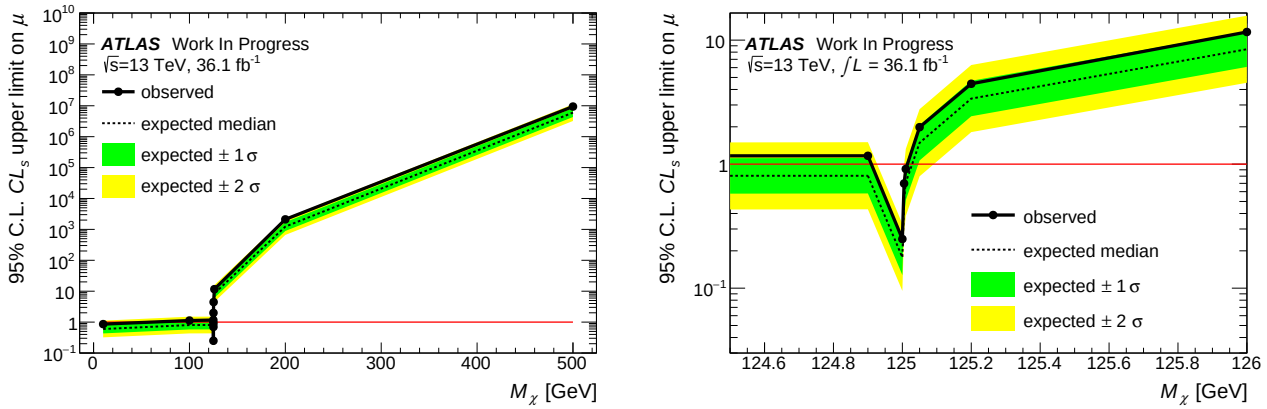

(a) full M_χ scan

(b) close to $a \to \bar{\chi}\chi$ threshold

Figure 8.7: CL_s upper limits at 95% confidence level on the 2HDM+a $h(b\bar{b}) + E_T^{\text{miss}}$ signal strength, as defined in Equation (8.1), as a function of M_χ. The full range of M_χ is shown in (a). To allow one to distinguish the behavior close to threshold, only the mass range close to the threshold at $M_\chi = M_a/2$ is plotted in (b). The remaining parameters have the values $M_H = M_{H^\pm} = M_A = 600\,\text{GeV}, M_a = 250\,\text{GeV}$, $\tan\beta = 1, \sin\theta = 0.35$, and $\lambda_{P1} = \lambda_{P2} = \lambda_3 = 3$.

interval in $\sin\theta$ exists, since systematic effects are to strong to allow to distinguish between $\mu > 1$ and $\mu < 1$

For the $\sin\theta$ scan at low pseudoscalar masses $M_a = 200\,\text{GeV}$ and $M_A = 600\,\text{GeV}$, shown in Figures 7.10 and 8.6(a) respectively, the parton level estimate is less sensitive than the full search. However, it correctly estimates lower sensitivity for extreme values of $\sin\theta$ and good sensitivity for intermediate values. For the $\sin\theta$ scan at high pseudoscalar masses $M_a = 350\,\text{GeV}$ and $M_A = 1000\,\text{GeV}$, the comparison gives a similar result. The parton level estimate predicts the search to be slightly less than sensitive, while the reconstruction level analysis indicates some sensitivity, which however is not significant.

8.2.2.2 M_χ Scan

The observed and expected CL_s upper limits at 95% confidence level (C.L.) on the 2HDM+a $h(b\bar{b}) + E_T^{\text{miss}}$ signal strength μ as a function of the Dark Matter mass M_χ are shown in Figure 8.7. Comparing the expected limit to the parton level sensitivity estimate in Figure 7.13, the parton level sensitivity estimate seems to match the detector level result very well. This is somewhat surprising since an overall bias towards weaker parton level estimates is expected. The expectation that there is no significant effect of the DM mass on the $h(b\bar{b}) + E_T^{\text{miss}}$ signal above the $a \to \bar{\chi}\chi$ threshold is confirmed at detector level, as can be seen by comparing the points $M_\chi = 10\,\text{GeV}, M_\chi = 100\,\text{GeV}$, and $M_\chi = 124.9\,\text{GeV}$ in Figure 8.7(a). At the threshold, the search is more sensitive, and below it, it has no sensitivity, as is demonstrated in Figure 8.7(b). This too is as expected based on the parton level results in Figure 7.13.

Similarly ignoring points where the search is not sensitive, based on Figure 8.7(b), $M_\chi \in (125\,\text{GeV}, 125.05\,\text{GeV})$ appear to be excluded. However, the large predicted cross section in this parameter region are the result of a threshold enhancement, which is not well modeled as the width Γ_a becomes dependent on the centre of mass energy $\sqrt{s}$, since the width Γ_a is assumed to be constant w.r.t. $\sqrt{s}$ in the numerical calculations [123, 121, 112, 114, 115]. Thus the exact value of the threshold enhancement is likely wrong, as discussed in Section 6.8, and

the limits close to the threshold region cannot be interpreted consistently in the 2HDM+a.

Chapter 9

Conclusion and Outlook

In the preceding Chapters of this Thesis, several studies and their corresponding results are discussed. This Chapter will attempt to draw the most essential conclusions from this work, and then provide a tentative outlook on potential avenues of future.

The stated aim of this Thesis is to define a sensible parameter benchmark for studies of the 2HDM+a, tuned to the sensitivity of the ATLAS $h(b\bar{b}) + E_T^{\text{miss}}$ search. The first step towards this aim consists of a parton-truth-level study of the $h(b\bar{b}) + E_T^{\text{miss}}$ final state properties in the 2HDM+a, and their dependence on the model parameters, detailed in Chapter 6. The key findings of this study are:

- The resonant signal kinematics are determined by the masses of the pseudoscalar mediators, as expected.
- Depending on the choice of model parameters, the non-resonant signal yield can exceed the resonant yield overwhelmingly. This was not expected, but can be understood as being the result of the complex, and potentially large new physics couplings the 2HDM+a introduces.
- Most of the parameters the 2HDM+a introduces can affect the ratio of non-resonant vs. resonant signal events.

Continuing on the path towards a 2HDM+a benchmark, the next step is the estimate of the $h(b\bar{b}) + E_T^{\text{miss}}$ sensitivity to the 2HDM+a prediction, as described in Chapter 7. This allows selecting a varied range of models to which the $h(b\bar{b}) + E_T^{\text{miss}}$ signature is sensitive. To this end, generic cross section limits with reduced model dependence are used. As expected, this approach proves useful by allowing quick sensitivity estimates of many different benchmark variations.

The 2HDM+a benchmark thus obtained is used to simulate detector level samples of $h(b\bar{b}) + E_T^{\text{miss}}$ events. These samples are then used to analyze and interpret the dataset of the ATLAS $h(b\bar{b}) + E_T^{\text{miss}}$ search, as discussed in Chapter 8. This results in

- the first limits set on the 2HDM+a parameter space using the $h(b\bar{b}) + E_T^{\text{miss}}$ signature; and
- a reference to compare the sensitivity estimates based on the generic cross section limits with reduced model dependence to. The result of this comparison is that the estimates work well; the expected bias towards weaker limits is smaller than the effects of the systematic uncertainties.

Of course, this Thesis is not in any way an exhaustive treatment of the subject. Thus, it ends with some possible avenues of research that could extend, complement, or improve the work presented in it. Specifically, these improvements aim to find or implement better ways of:

- dealing with the large number of parameters of the 2HDM+a,
- tuning a benchmark to a large set of signatures, instead of just one signature,
- reducing the bias and improving the accuracy of the sensitivity estimate using generic cross section limits with reduced model dependence, without sacrificing the speed advantage,
- improving the sensitivity of the $h(b\bar{b}) + E_T^{\text{miss}}$ search

Reweighting

The 2HDM+a has a very large number of free parameters, most of which have some effect on the properties of the signal, as demonstrated in Chapters 6 and 7. Thus covering the entire physically consistent region of the 14-dimensional parameter space with dedicated samples of simulated events requires prohibitive amounts of computing resources or time. This makes it challenging to exhaustively explore the entire potential phenomenology of this class of models. One possible solution to this problem could be a reweighting scheme.

In one example of a reweighting approach [133], used in the ATLAS search for $h(\gamma\gamma)+E_T^{\text{miss}}$ [134], a few large samples covering a maximal phase space volume are generated and simulated to detector level. These samples are then used to simulate other parts of the model parameter space by differentially updating the weights of individual events or individual bins. The weights are chosen to map the truth level distributions of the relevant observables in the simulated samples to the truth level distributions of the target model. Using the same weights on the detector level sample will transform the detector level expectation to that of the target model. Thus large and high-dimensional parameter spaces can be covered comparatively quickly.

A different reweighting approach equips each generated event with a vector of weights, each entry corresponding to a different signal model [111]. Thus many models can be simulated simultaneously, but the detector simulation is shared between the models. Since the computing bottleneck is the detector simulation, this approach is approximately as CPU-intensive as simulating a single model. Thus it is much faster than one dedicated detector simulation per model would be.

Phenomenological Parameter Choices

The number of free parameters of the 2HDM+a is large, and many of them affect the signal kinematics in some way, as seen in Chapter 6. However, these effects on the final state kinematics occur in (combiantions of) only two classes:

- shifts of the location of the maximum of the Jacobian shoulder, i.e. M_a, M_A,
- changes of the ratio of the yields of resonant and non-resonant events, e.g. $M_A, M_H, \sin\theta$, etc.

This observation suggests that when considering primarily the observable phenomena, the fourteen parameter dimensions of the 2HDM+a reduce to two meaningful ones: one associated

with $E_T^{\text{miss},max}$ from Equation (4.13), and another one associated (primarily) with Γ_A. In principle there is a third dimension associated with cross section scaling, but this does not require additional Monte Carlo events to be generated, so we can ignore it. An exhaustive parameter scan in two dimensions, as opposed to fourteen, is eminently more feasible. For example, this Thesis includes two such scans. Thus, it would be beneficial if one could identify some "orthogonal basis" of parameter combinations corresponding to a clean decorrelation of the two effects listed above. If the method of obtaining such a parameter set can be used on any generic (simplified) model, it would furthermore vastly increase the future utility of the search. It is however not obvious that finding this parametrization is easier than implementing any of the other approaches to dealing with the large parameter dimensions of the model outlined in this Chapter.

More Generic Simplified Models

Another way to reduce the many dimensions of the parameter space might be to consider a less specific class of models that includes the 2HDM+a as a limiting case. Such a model can e.g. be constructed as a hybrid of explicit mediator exchange interactions and contact interaction terms [135]. The number of parameters may then be reduced by combining several of them into one parameter characterizing the strength of the contact interaction. However, when the explicit mediator part contains a SM-gauge invariant pseudoscalar, one needs at least a Two-Higgs Doublet model, or something even more complex, to construct that pseudoscalar. Thus one starts off already with a large number of model parameters, and the complexity reduction unfortunately is limited.

Tuning a Benchmark to Many Signatures Simultaneously

The key feature of the 2HDM+a is the large diversity of LHC signatures it predicts. The benchmark constructed in this Thesis is constructed considering just the $h(b\bar{b}) + E_T^{\text{miss}}$ signature. It can of course be compared to and aligned with similar benchmarks tuned to other signatures. But such an approach might produce sub-optimal results. For example, a parameter region simultaneously relevant to all signatures may not be optimal for any individual signature. Thus such a parameter region might be ignored when combining and aligning several signature-specific benchmarks. To mitigate this risk, it may be interesting to build parameter benchmarks using a combined sensitivity estimate, or combined likelihood, to design and evaluate benchmarks. A combined sensitivity estimate could be constructed using generic cross section limits with reduced model dependence, similar to the estimate described in Section 7.3.1, if they are available for all relevant models. Alternatively a more advanced combined likelihood or significance could be constructed, e.g. using Rivet [136] routines in a way similar to the approach taken in Ref. [137]. Such a combined likelihood, sensitivity, or significance, could then be used instead of, or in parallel to, sensitivity studies focused on individual channels.

Improved Limits with Reduced Model Dependence and Sensitivity Estimate

The sensitivity estimate based on the generic limits with minimal model dependence was found to be a good approximation of the real sensitivity. It would be interesting to quantify this statement, and the observed conservative bias of the generic limits. Based on such a result, one could evaluate different methods of comparing parton level differential cross sections to the generic cross section limits. In this Thesis, the most naive approach of a sum of the ratios

of limits and cross sections is used, i.e. the definition in Equation (7.2). However, it may well be that e.g. using the expected number of events, or their ratios, or likelihood (-ratio), or significance, may yield better estimates. Many approaches can be imagined that should not slow down the estimate significantly. Finally, a quantitative comparison of a generic-limit-based sensitivity estimate and the actual sensitivity can be used to evaluate different approaches to constructing generic limits.

Improve $h(b\bar{b}) + E_T^{\text{miss}}$ Sensitivity by Improving the Jet Mass Reconstruction

The mass of the Higgs candidate is the discriminant used in the combined signal and background fit of the search for $h(b\bar{b}) + E_T^{\text{miss}}$. Hence the Higgs candidate mass resolution and response are crucial to the $h(b\bar{b}) + E_T^{\text{miss}}$ sensitivity. In the resolved regime this mass depends on the angular distance, rapidity and energy of the two small-R jets. In the merged regime this mass is the mass of the large-R jet, reconstructed as a combined mass, described in Section 3.3.1.2. To go beyond the current mass resolution, more intricate combinations of the calorimeter and tracking information can be considered. One such approach is to construct the large-R jet from even smaller-R (i.e. $R = 0.2$) subjets and tracks, match the tracks to the subjets, and rescale the momenta of the tracks using the momentum of the subjet to which they are associated [138]. From these tracks and subjets the large-R jet can then be constructed, and its mass calculated. The resulting mass observable is called the Track Assisted Reclustered (TAR) or Small-R jet Assisted Track (SAT) jet mass, depending on the details of the large-R jet construction from its constituents [138]. The TAR and SAT algorithms are expected to provide improved jet mass response and resolution compared to the combined mass used so far [138]. Implementing and using these algorithms to better reconstruct the mass of the large-radius jet is thus expected to improve the $h(b\bar{b}) + E_T^{\text{miss}}$ sensitivity.

Acknowledgements

I thank my Supervisor, Oleg Brandt, for his encouragement, a steady supply of interesting challenges and valuable opportunities, and his thoughtful and poignant advice and feedback. I am very grateful to my second reader Tilman Plehn for agreeing to read my Thesis, which is far too long to impose upon anyone, especially those inclined towards regular food, sufficient sleep, good health, or finite working hours. If you have come this far, I congratulate your stamina. I am deeply thankful towards Thomas Malte Spieker, Sebastian Mario Weber, and Pavel Starovoitov for the stable operation and continued improvement of the KIP computing farm, as well as the support they continue to provide to its users with characteristically great quality and low latency. I am further exceedingly grateful towards Martin Bauer of the Heidelberg Institute for Theoretical Physics, whose patient answers to my itinerant questions on the 2HDM+a, the workings of MC generators, and phenomenology in general were as on the point as they were fast to arrive, and who never failed to point out relevant and interesting literature. I am very thankful to all the members of the ATLAS and HEP-Detectors groups at KIP, who make a great group, and were very friendly to welcome me as readily as they did. They are all wonderful colleagues, but Sebastian, Thomas, Merve, Stanislav, Hannah, Manuel, Philipp, Claire, Martin, Hanno, and Sascha deserve a special mention, for without their helpful, critical, and constructive reading of earlier drafts of this Thesis, it would have been far worse than it is. I thank Lukas Alexander Heinrich of New York University and Patrick Rieck of the Max Planck Institute for Particle Physics in Munich who gave me access to their hard-earned RECAST/`yadage` preservation of the ATLAS $h(b\bar{b}) + E_T^{\text{miss}}$ analysis, and who helped me immensely with understanding and running it. Without the flexible framework and powerful cluster developed and established by Lukas, I could not have finished this work by now. I also thank the members of the LHC Dark Matter Working Group, who with fruitful, stimulating discussions and email exchanges provided a fertile environment to grow, test, compare and weed out ideas. I owe a debt of gratitude to Sebastian Stapelberg of the Institute for Theoretical Astrophysics in Heidelberg, for many interesting discussions. The insight of his answers on all that is Astrophysics or Cosmology is only matched by the depth of his questions on everything particle physics. Lastly, but certainly not leastly, I thank my family, my friends, and especially Tania, whose unwavering, amazing support, and (particularly in the final few months) abiding patience, enabled me to in the first place do this work and write this Thesis. Ni mitz tlazohtla Tania no moyolotzin.

Appendix A

2HDM Tree Level Vacuum Stability Conditions in the Alignment Limit

This chapter gives the detailed steps that allow translating the general 2HDM tree level vacuum stability conditions given in terms of quartic couplings in Inequality (4.10) into the same conditions expressed as a function of physically meaningful masses, mixing angles, v, and λ_3, in Equation (4.11).

The starting point is Inequality (4.10), as given in [99]:

$$\lambda_1 > 0, \quad \lambda_2 > 0, \quad \lambda_3 > -\sqrt{\lambda_1 \lambda_2}, \quad \lambda_3 + \lambda_4 - |\lambda_5| > -\sqrt{\lambda_1 \lambda_2} \quad . \tag{A.1}$$

Furthermore, we assume the alignment limit, that is, $\sin(\beta - \alpha) = 1$, and $M_H = M_{H^\pm}$. These two choices allow couplings of h similar to the SM Higgs, and avoid constraints from electroweak precision measurements, as detailed in Sections 4.1.1 and 4.2.2, respectively.

Next we express all the λ_i in terms of masses and mixing angles. For this we apply the following relations, which are true in the alignment limit [139],

$$\begin{aligned}
v^2\lambda_1 &= M_h^2 - \frac{\tan\beta\mu_3^2 - M_H^2 \sin\beta\cos\beta}{\cos^2\beta}\,, \\
v^2\lambda_2 &= M_h^2 - \frac{\mu_3^2 - M_H^2 \sin\beta\cos\beta}{\tan\beta\sin^2\beta}\,, \\
v^2\lambda_3 &= M_h^2 - \frac{\mu_3^2 - M_H^2 \sin\beta\cos\beta}{\sin\beta\cos\beta}\,, \\
v^2\lambda_4 &= M_{A_0}^2 + \frac{\mu_3^2 - M_H^2 \sin\beta\cos\beta}{\sin\beta\cos\beta}\,, \\
v^2\lambda_5 &= M_H^2 - M_{A_0}^2 + \frac{\mu_3^2 - M_H^2 \sin\beta\cos\beta}{\sin\beta\cos\beta}\,,
\end{aligned} \tag{A.2}$$

where $M_H = M_{H^\pm}$ is already used to simplify the expressions. Writing

$$X \equiv \frac{\mu_3^2 - M_H^2 \sin\beta\cos\beta}{v^2} \tag{A.3}$$

we can identify X in A.2 and obtain:

$$\lambda_1 = \frac{M_h^2}{v^2} - \frac{\tan\beta}{\cos^2\beta} X \,, \tag{A.4}$$

$$\lambda_2 = \frac{M_h^2}{v^2} - \frac{1}{\tan\beta \sin^2\beta} X \,, \tag{A.5}$$

$$\lambda_3 = \frac{M_h^2}{v^2} - \frac{1}{\sin\beta\cos\beta} X \,, \tag{A.6}$$

$$\lambda_4 = \frac{M_{A_0}^2}{v^2} + \frac{1}{\sin\beta\cos\beta} X \,, \tag{A.7}$$

$$\lambda_5 = \frac{M_H^2 - M_{A_0}^2}{v^2} + \frac{1}{\sin\beta\cos\beta} X \,. \tag{A.8}$$

Using Equation (A.6) as $X = \sin\beta\cos\beta\left(\frac{M_h^2}{v^2} - \lambda_3\right)$ we can trade X for λ_3

$$\lambda_1 = \frac{M_h^2}{v^2}(1 - \tan^2\beta) + \tan^2\beta\lambda_3 \,, \tag{A.9}$$

$$\lambda_2 = \frac{M_h^2}{v^2}(1 - \cot^2\beta) + \cot^2\beta\lambda_3 \,, \tag{A.10}$$

$$\lambda_4 = \frac{M_{A_0}^2 - M_H^2 + M_h^2}{v^2} - \lambda_3 \,, \tag{A.11}$$

$$\lambda_5 = \frac{M_H^2 - M_{A_0}^2 + M_h^2}{v^2} - \lambda_3 \,, \tag{A.12}$$

which is convenient because λ_3 is an exposed parameter in the numerical implementation. At this point, let us consider the first two conditions of Inequality (A.1)

$$\lambda_1 \geq 0 \,, \tag{A.13}$$

$$\lambda_2 \geq 0 \,, \tag{A.14}$$

which, when using Equations (A.9) and (A.10), yield

$$\frac{1}{\tan^2\beta} > 1 - R \,, \tag{A.15}$$

$$\tan^2\beta > 1 - R \,, \tag{A.16}$$

with $R \equiv \frac{\lambda_3 v^2}{M_h^2}$. Note that this requires $R > 0$, i.e. $\lambda_3 > 0$. We now choose to further restrict ourselves to $R \geq 1$, i.e. $\lambda_3 \geq \frac{M_h^2}{v^2} \approx 0.2581$, since this ensures that Inequalities (A.15) and (A.16) are fulfilled for any $\tan\beta$. This choice is not required by Inequalities (A.13) and (A.14), but for $R < 1$ Inequalities (A.13) and (A.14) yield conditions on $\tan\beta$, which we want to avoid if at all possible, since we scan $\tan\beta$ in Chapter 7. Turning our attention to the third condition in Inequality (A.1)

$$\lambda_3 > -\sqrt{\lambda_1\lambda_2} \,, \tag{A.17}$$

we first notice that since we already have $\lambda_1, \lambda_2 \geq 0$ from the previous conditions, and have seen that with our choices of $M_{H^\pm} = M_H$ and $\sin(\beta - \alpha)$ these can only simultaneously be true

with $\lambda_3 > 0$. Thus Inequality (A.17) is already fulfilled at this point. It will however be useful to insert Equations (A.9) and (A.10), such that we get:

$$1 > -Y \equiv -\sqrt{\left(\frac{1-\tan^2\beta}{R} + \tan^2\beta\right)\left(\frac{1-\tan^{-2}\beta}{R} + \tan^{-2}\beta\right)}\,, \tag{A.18}$$

If in Inequality (A.18) we consider only the argument of the square root

$$\left(\frac{1-\tan^2\beta}{R} + \tan^2\beta\right)\left(\frac{1-\tan^{-2}\beta}{R} + \tan^{-2}\beta\right) \tag{A.19}$$

$$=1 + \left(\frac{1}{R} - \frac{1}{R^2}\right)\left(\tan^2\beta + \tan^{-2}\beta - 2\right), \tag{A.20}$$

we see that the right factor is never negative as $\tan^2\beta + \tan^{-2}\beta \geq 2$ since $\tan^2\beta \geq 0$ by definition, and neither is the left factor given our previous choice of $R \geq 1$. Thus $Y \geq 1$ always, which we will use in the following.

At last, inserting as before into the final condition

$$\lambda_3 + \lambda_4 - |\lambda_5| > -\sqrt{\lambda_1\lambda_2}, \tag{A.21}$$

we get

$$\frac{M_{A_0}^2 - M_H^2 + M_h^2}{\lambda_3 v^2} - \left|\frac{M_H^2 - M_{A_0}^2 + M_h^2}{\lambda_3 v^2} - 1\right| > -Y\,, \tag{A.22}$$

where we can use the previous result that $Y > 1$ for $R > 1$ irrespective of the value of $\tan\beta$. With it we have

$$1 + \frac{M_{A_0}^2 - M_H^2 + M_h^2}{\lambda_3 v^2} - \left|\frac{M_H^2 - M_{A_0}^2 + M_h^2}{\lambda_3 v^2} - 1\right| > 0 \tag{A.23}$$

which is

$$R^{-1} - Q - \left|R^{-1} + Q\right| > 0 \tag{A.24}$$

where $Q \equiv \frac{M_H^2 - M_{A_0}^2}{\lambda_3 v^2} - 1$. Inequality (A.24) is solved by $R^{-1} > 0, Q < 0$, the first of which is always true with our choice of $R > 1$, and the second of which yields

$$\lambda_3 v^2 > M_H^2 - M_{A_0}^2\,. \tag{A.25}$$

Together with the assumptions of $\sin(\beta-\alpha) = 1, M_H = M_{H^\pm}$, and $\lambda_3 \geq \frac{M_h^2}{v^2}$ that we have put in, this is the set of conditions stated in Equation (4.11).

Appendix B

Constraints on M_A, M_a, and $\tan\beta$ from Scalar Widths

The total decay width of the mediating (pseudo-) scalars can be used to identify the regions of the parameter space of the 2HDM+a where the numerical matrix element calculation can be relied upon. There are two such constraints that the widths can be indicative of:

- the model implementation assumes that the mediator widths are narrow relative to the mediator masses [1], thus models with high width are outside of the range of models the numerical implementation was constructed to study;
- excessive coupling strengths can lead to large mediator widths. The couplings should not be arbitrarily large, since perturbation theory requires small coupling parameter to control the convergence of the resummation series. If the coupling parameters are too large, the assumption (made in both the LO matrix element calculation of MadGraph 5 , and the analytical formulas presented in citeBauer:2017ota) that the first (two first, etc.) elements of that series are approximations of the full matrix element.

Hence, to ensure that these issues are avoided, the widths of the mediating scalars are studied during the construction of the 2HDM+a benchmarks designed in Chapter 7. An exemplary

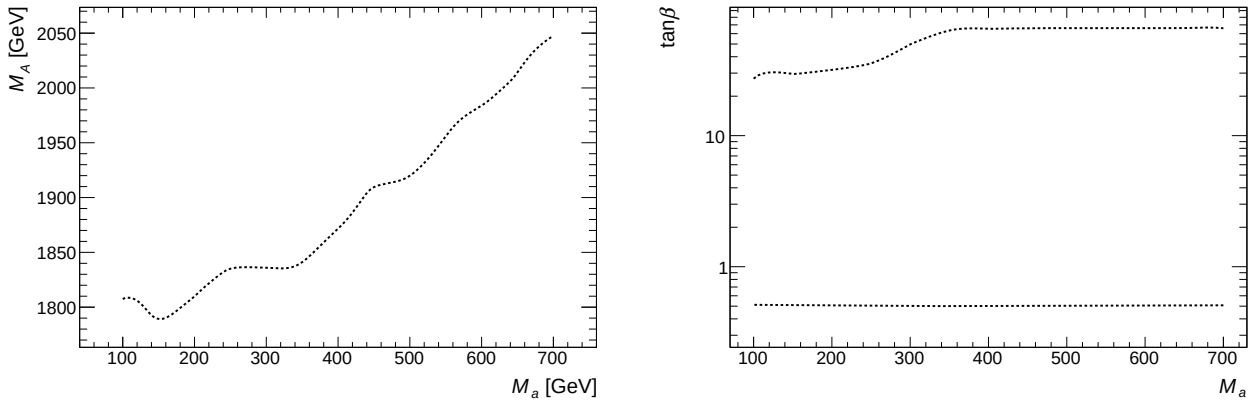

(a) (b)

Figure B.1: Contours of $\max(\{\Gamma_S/M_S |\, S = a, A, h, H, H^\pm\}) = 0.2$. In (a), the maximum relative width is larger than 0.2 in the upper left, and lower than 0.2 on the other side of the line. In (b) the maximum relative width is larger than 0.2 both for very high and very low $\tan\beta$, and lower in between.

result of these studies for the M_a, M_A is shown Figure B.1(a), the corresponding example for the $M_a, \tan\beta$ scan in Figure B.1(b). The underlying widths were calculated using the MadGraph 5 width calculator [112, 116].

Appendix C

Estimate of $h(\gamma\gamma) + E_T^{\text{miss}}$ Sensitivity using Generic Cross Section Limits

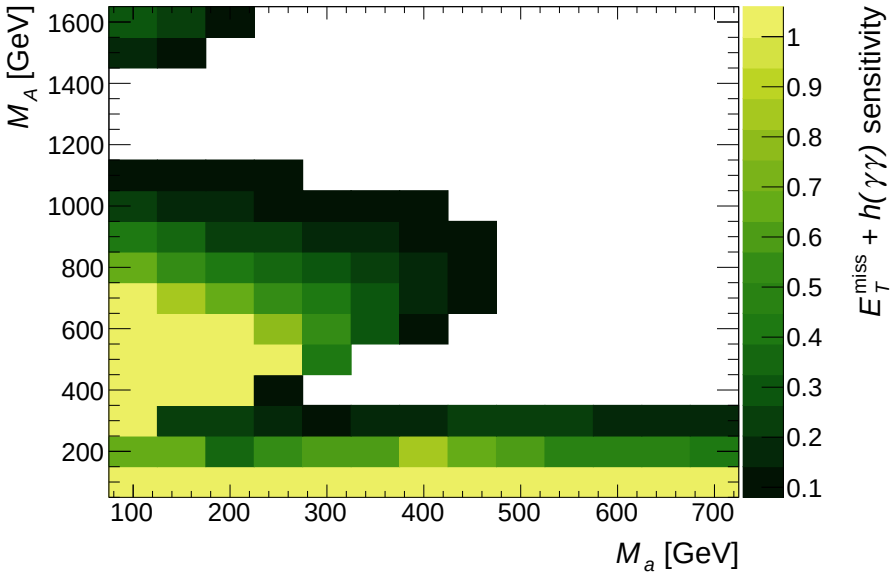

Figure C.1: Estimated sensitivity to $h(\gamma\gamma) + E_T^{\text{miss}}$ events as a function of (M_a, M_A). The sensitivity, defined in analogy to Equation (7.2), is based on the limit with reduced model dependence from Ref. [134]. The remaining parameters have the values $M_H = M_{H^\pm} = M_A, \sin\theta = 0.35, \tan\beta = 1, M_\chi = 10$ GeV and $\lambda_{P1} = \lambda_{P2} = \lambda_3 = 3$. Model points colored white indicate that the sensitivity estimate is below 0.1. The color scale is inclusive to high values, i.e. all sensitivities > 1 are displayed in the same color.

The sensitivity estimate constructed in Section 7.3.1 for the $h(b\bar{b}) + E_T^{\text{miss}}$ signature is straightforward to extend to other signatures. The only requirement is that meaningful generic cross section limits with reduced model dependence are available, as well as an estimate of $\mathcal{A} \times \epsilon$ in the sense of Table 3.2. In this section, one example of this is provided in the form of estimates of the ATLAS $h(\gamma\gamma) + E_T^{\text{miss}}$ [134] sensitivity to the 2HDM+a. The estimates use the single-bin cross section limit of 0.19 fb on $h(\gamma\gamma) + E_T^{\text{miss}}$ production with $E_T^{\text{miss}} > 90\,\text{GeV}$ provided by Ref. [134], It moreover assumes $\mathcal{A} \times \epsilon = 50\%$ in that bin, which is at the low end of the range quoted in Ref. [134] for the kinematically similar Z'-2HDM. The SM branching ratio for a 125 GeV Higgs boson of $\mathcal{BR}_{\text{SM}}(h \to \gamma\gamma) = 2.27 \times 10^{-3}$ is used, following Ref. [17].

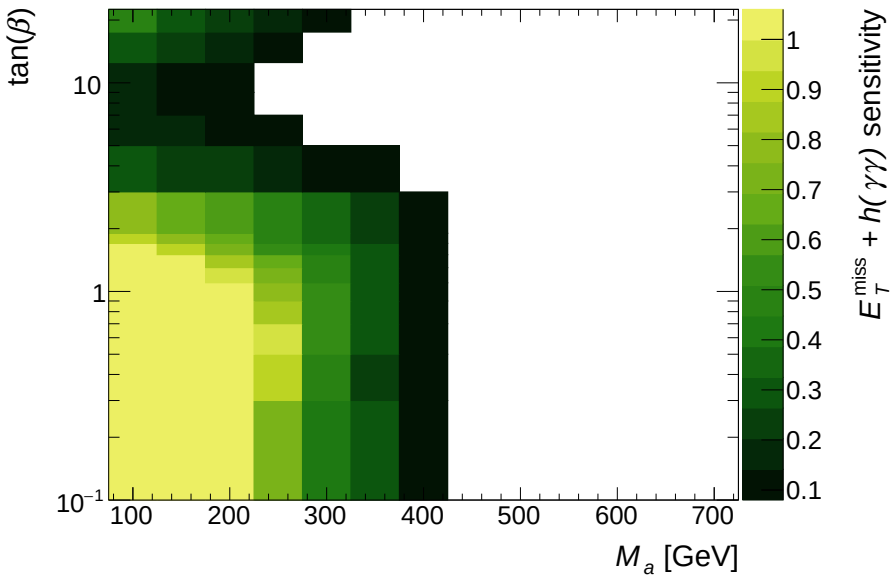

Figure C.2: Estimated sensitivity to $h(\gamma\gamma) + E_T^{\text{miss}}$ events as a function of $(M_a, \tan\beta)$. The sensitivity, defined in analogy to Equation (7.2), is based on the limit with reduced model dependence from Ref. [134]. The remaining parameters have the values $M_H = M_{H^\pm} = M_A = 600\,\text{GeV}, \sin\theta = 0.35, M_\chi = 10$ GeV and $\lambda_{P1} = \lambda_{P2} = \lambda_3 = 3$. Model points colored white indicate that the sensitivity estimate is below 0.1. The color scale is inclusive to high values, i.e. all sensitivities > 1 are displayed in the same color.

Using the same parton level samples as used for the $h(b\bar{b}) + E_T^{\text{miss}}$ estimates, the resulting sensitivity estimates are shown in Figures C.1 and C.2. The lower minimum E_T^{miss} cut makes $h(\gamma\gamma) + E_T^{\text{miss}}$ more sensitive to models with small a, A mass differences, but for most of the remaining parameter space, $h(b\bar{b}) + E_T^{\text{miss}}$ is more sensitive.

Appendix D

2D Interpolation for Exclusion Limit Contours

To obtain more rapidly understood plots, the fitted upper signal strength limits of the 2D parameter scans, shown in Figures 8.2 and 8.3, are converted into continuous limit contours in the respective parameter plane, as shown in Figures 8.4 and 8.5. In this Chapter, the technical details of how this is done are illustrated.

The two-dimensional contour interpolation proceeds in two steps:

1. Upsampling the low-granularity grid of simulated signal points into a highly-granular interpolated grid. This highly granular grid can be thought to approximate the "surface" of idealized arbitrarily granular upper limits on the signal strength.

2. Finding the intersection of this idealized limit surface with the plane where the signal strength is 1. This intersection corresponds to the drawn contour.

The parameter points where the limits on the signal strength have been fitted are sparse. To construct the continuous limit contour, the sparse base points are interpolated by a function describing the signal strength as a function of the two scanned model parameters, i.e. (M_a, M_A) or $(M_a, \tan\beta)$. This is a purely cosmetic operation, since unlike the fitted points on the signal grid, the value of the interpolating function has no statistical meaning. As the shape of the extracted contour depends sensitively on the interpolation method, the interpolation step is described in some more detail below.

The interpolation function is a piecewise linear bivariate interpolation, implemented using the `scipy` python module's `scipy.interpolate.griddata` function [140]. For the linear interpolation this function uses the QuickHull [141] algorithm library to triangulate the convex hull of the grid of fitted points into a mesh of triangles with one vertex at each fitted parameter point. For a given point target P_t inside the convex hull, the three grid points $G_{1,2,3}$ forming the triangle that the point lies inside are determined. The interpolated limit is then calculated by linearly interpolating between the signal strength limits $\mu_i = \mu(G_i)$ [142]

$$\mu_\mathrm{t}^{\mathrm{interp.}} = \lambda_\mathrm{t}^1\mu_1 + \lambda_\mathrm{t}^2\mu_2 + \lambda_\mathrm{t}^3\mu_3\,,$$

where the λ_t^i are the barycentric coordinates of the target point P_t.

Barycentric coordinates are the masses which, when placed at the three vertices of the triangle, would have have a center of mass located at the point they parametrize [143], i.e. P_t. They are normalized such that $\mu_i^{\mathrm{interp.}} = \mu_i$.

Having defined an interpolation function for the grid points at every point in the convex hull of the grid, it isin principle possible to use some root-finding algorithm to determine the

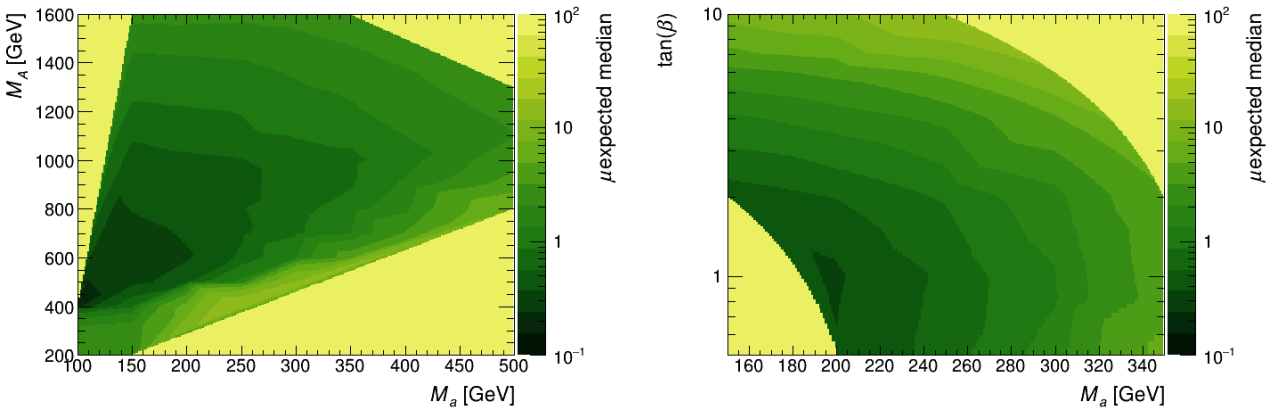

(a) (b)

Figure D.1: The result of the piecewise bilinear interpolation of the signal strength limits in the two two- dimensional parameter scans of Chapter 8. Outsides the convex hull of the grid points an arbitrary fixed value is shown. The hull looks concave in (b) due to the logarithmic $\tan\beta$ scale of the plot, despite being convex on a linear scale, where the interpolation is performed.

intersection with $\mu = 1$ to the desired accuracy. This approach can however be expensive and unstable, depending on the implementation of the root finding algorithm. In practice it is easier to simply define a dense grid of target points, and evaluate the interpolation function at each point of that grid. Due to the interpolation in one triangle being independent from that in another, this approach is simple to parallelize (if that is necessary). The resulting upsampled grids for the two two-dimensional parameter scans are shown in Figure D.1.

Bibliography

[1] Martin Bauer, Ulrich Haisch, and Felix Kahlhoefer. "Simplified dark matter models with two Higgs doublets: I. Pseudoscalar mediators". In: *JHEP* 05 (2017), p. 138. DOI: 10.1007/JHEP05(2017)138. arXiv: 1701.07427 [hep-ph].

[2] Morad Aaboud et al. "Search for Dark Matter Produced in Association with a Higgs Boson Decaying to $b\bar{b}$ using 36 fb^{-1} of pp collisions at $\sqrt{s} = 13$ TeV with the ATLAS Detector". In: *Phys. Rev. Lett.* 119.18 (2017), p. 181804. DOI: 10.1103/PhysRevLett.119.181804. arXiv: 1707.01302 [hep-ex].

[3] Gianfranco Bertone, Dan Hooper, and Joseph Silk. "Particle dark matter: Evidence, candidates and constraints". In: *Phys. Rept.* 405 (2005), pp. 279–390. DOI: 10.1016/j.physrep.2004.08.031. arXiv: hep-ph/0404175 [hep-ph].

[4] Marco Taoso, Gianfranco Bertone, and Antonio Masiero. "Dark Matter Candidates: A Ten-Point Test". In: *JCAP* 0803 (2008), p. 022. DOI: 10.1088/1475-7516/2008/03/022. arXiv: 0711.4996 [astro-ph].

[5] Lars Bergström. "Nonbaryonic dark matter: Observational evidence and detection methods". In: *Rept. Prog. Phys.* 63 (2000), p. 793. DOI: 10.1088/0034-4885/63/5/2r3. arXiv: hep-ph/0002126 [hep-ph].

[6] M. Kamionkowski. "WIMP and axion dark matter". In: *High-energy physics and cosmology. Proceedings, Summer School, Trieste, Italy, June 2-July 4, 1997*. 1997, pp. 394–411. arXiv: hep-ph/9710467 [hep-ph].

[7] Felix Kahlhoefer. "Review of LHC Dark Matter Searches". In: *Int. J. Mod. Phys.* A32.13 (2017), p. 1730006. DOI: 10.1142/S0217751X1730006X. arXiv: 1702.02430 [hep-ph].

[8] Douglas Clowe et al. "A direct empirical proof of the existence of dark matter". In: *Astrophys. J.* 648 (2006), pp. L109–L113. DOI: 10.1086/508162. arXiv: astro-ph/0608407 [astro-ph].

[9] Teresa Marrodán Undagoitia and Ludwig Rauch. "Dark matter direct-detection experiments". In: *J. Phys.* G43.1 (2016), p. 013001. DOI: 10.1088/0954-3899/43/1/013001. arXiv: 1509.08767 [physics.ins-det].

[10] Gianfranco Bertone and David Merritt. "Dark matter dynamics and indirect detection". In: *Mod. Phys. Lett.* A20 (2005), p. 1021. DOI: 10.1142/S0217732305017391. arXiv: astro-ph/0504422 [astro-ph].

[11] O. Buchmueller, Matthew J. Dolan, and Christopher McCabe. "Beyond Effective Field Theory for Dark Matter Searches at the LHC". In: *JHEP* 01 (2014), p. 025. DOI: 10.1007/JHEP01(2014)025. arXiv: 1308.6799 [hep-ph].

[12] Mark Thomson. *Modern particle physics*. New York: Cambridge University Press, 2013. ISBN: 9781107034266. URL: http://www-spires.fnal.gov/spires/find/books/www?cl=QC793.2.T46::2013.

[13] J. D. Vergados. *The Standard Model and Beyond*. Singapore: World Scientific, 2017. ISBN: 9789813228559. DOI: 10.1142/10669.

[14] Fermilab Particle Data Group PBS NOVA. *Standard Model Particle Content*. 2008. URL: https://en.wikipedia.org/wiki/File:Standard_Model_of_Elementary_Particles.svg.

[15] Eric Drexler. *Elementary Particle Interactions in the Standard Model*. 2014. URL: https://en.wikipedia.org/wiki/File:Elementary_particle_interactions_in_the_Standard_Model.png.

[16] Michael E. Peskin and Daniel V. Schroeder. *An Introduction to quantum field theory*. Reading, USA: Addison-Wesley, 1995. ISBN: 9780201503975, 0201503972. URL: http://www.slac.stanford.edu/~mpeskin/QFT.html.

[17] C. Patrignani et al. "Review of Particle Physics". In: *Chin. Phys.* C40.10 (2016), p. 100001. DOI: 10.1088/1674-1137/40/10/100001.

[18] John Ellis. "Higgs Physics". In: arXiv:1312.5672. KCL-PH-TH-2013-49. LCTS-2013-36. CERN-PH-TH-2013-315 (Dec. 2013), 117–168. 52 p. URL: https://cds.cern.ch/record/1638469.

[19] Georges Aad et al. "Combined Measurement of the Higgs Boson Mass in pp Collisions at $\sqrt{s} = 7$ and 8 TeV with the ATLAS and CMS Experiments". In: *Phys. Rev. Lett.* 114 (2015), p. 191803. DOI: 10.1103/PhysRevLett.114.191803. arXiv: 1503.07589 [hep-ex].

[20] D. M. Webber et al. "Measurement of the Positive Muon Lifetime and Determination of the Fermi Constant to Part-per-Million Precision". In: *Phys. Rev. Lett.* 106 (2011). [Phys. Rev. Lett.106,079901(2011)], p. 041803. DOI: 10.1103/PhysRevLett.106.041803,10.1103/PhysRevLett.106.079901. arXiv: 1010.0991 [hep-ex].

[21] Georges Aad et al. "Measurements of the Higgs boson production and decay rates and constraints on its couplings from a combined ATLAS and CMS analysis of the LHC pp collision data at $\sqrt{s} = 7$ and 8 TeV". In: *JHEP* 08 (2016), p. 045. DOI: 10.1007/JHEP08(2016)045. arXiv: 1606.02266 [hep-ex].

[22] K. G. Begeman, A. H. Broeils, and R. H. Sanders. "Extended rotation curves of spiral galaxies: dark haloes and modified dynamics". In: *Monthly Notices of the Royal Astronomical Society* 249.3 (1991), pp. 523–537. DOI: 10.1093/mnras/249.3.523. eprint: /oup/backfile/content_public/journal/mnras/249/3/10.1093_mnras_249.3.523/2/mnras249-0523.pdf.

[23] Peter Schneider. *Extragalactic Astronomy and Cosmology*. 2nd ed. Springer-Verlag Berlin-Heidelberg, 2015. ISBN: 978-3-642-54083-7. DOI: 10.1007/978-3-642-54083-7. URL: https://link.springer.com/book/10.1007%2F978-3-642-54083-7.

[24] A. C. Fabian and S. W. Allen. "X-rays from clusters of galaxies". In: *Proceedings, 21st Texas Symposium on Relativistic Astrophysics (Texas in Tuscany): Florence, Italy, December 9-13, 2002*. 2003, pp. 197–208. DOI: 10.1142/9789812704009_0018. arXiv: astro-ph/0304020 [astro-ph].

[25] R. A. Sunyaev and Ya. B. Zeldovich. "Small scale fluctuations of relic radiation". In: *Astrophys. Space Sci.* 7 (1970), pp. 3–19.

[26] Maxim Markevitch. "Chandra observation of the most interesting cluster in the universe". In: (2005). [ESA Spec. Publ.604,723(2006)]. arXiv: astro-ph/0511345 [astro-ph].

[27] Planck Collaboration et al. "Planck 2013 results. I. Overview of products and scientific results". In: *A&A* 571 (2014), A1. DOI: 10.1051/0004-6361/201321529. URL: https://doi.org/10.1051/0004-6361/201321529.

[28] ESA and the Planck collaboration. *Planck CMB*. Released under CC BY-SA 3.0 IGO: https://creativecommons.org/licenses/by-sa/3.0/igo/. 2013. URL: https://www.esa.int/spaceinimages/Images/2013/03/Planck_CMB.

[29] P. A. R. Ade et al. "Planck 2015 results. XIII. Cosmological parameters". In: *Astron. Astrophys.* 594 (2016), A13. DOI: 10.1051/0004-6361/201525830. arXiv: 1502.01589 [astro-ph.CO].

[30] Wayne Hu, Naoshi Sugiyama, and Joseph Silk. "The Physics of microwave background anisotropies". In: *Nature* 386 (1997), pp. 37–43. DOI: 10.1038/386037a0. arXiv: astro-ph/9604166 [astro-ph].

[31] Wayne Hu and Scott Dodelson. "Cosmic microwave background anisotropies". In: *Ann. Rev. Astron. Astrophys.* 40 (2002), pp. 171–216. DOI: 10.1146/annurev.astro.40.060401.093926. arXiv: astro-ph/0110414 [astro-ph].

[32] Tisserand, P. et al. "Limits on the Macho content of the Galactic Halo from the EROS-2 Survey of the Magellanic Clouds". In: *A&A* 469.2 (2007), pp. 387–404. DOI: 10.1051/0004-6361:20066017. URL: https://doi.org/10.1051/0004-6361:20066017.

[33] Judd D. Bowman et al. "An absorption profile centred at 78 megahertz in the sky-averaged spectrum". In: *Nature* 555.7694 (2018), pp. 67–70. DOI: 10.1038/nature25792.

[34] Hiroyuki Tashiro, Kenji Kadota, and Joseph Silk. "Effects of dark matter-baryon scattering on redshifted 21 cm signals". In: *Phys. Rev.* D90.8 (2014), p. 083522. DOI: 10.1103/PhysRevD.90.083522. arXiv: 1408.2571 [astro-ph.CO].

[35] R. Barkana. "Possible interaction between baryons and dark-matter particles revealed by the first stars". In: *Nature* 555 (2018). DOI: 10.1038/nature25791.

[36] M. Ackermann et al. "The Fermi Galactic Center GeV Excess and Implications for Dark Matter". In: *Astrophys. J.* 840.1 (2017), p. 43. DOI: 10.3847/1538-4357/aa6cab. arXiv: 1704.03910 [astro-ph.HE].

[37] Samuel K. Lee, Mariangela Lisanti, and Benjamin R. Safdi. "Distinguishing Dark Matter from Unresolved Point Sources in the Inner Galaxy with Photon Statistics". In: *JCAP* 1505.05 (2015), p. 056. DOI: 10.1088/1475-7516/2015/05/056. arXiv: 1412.6099 [astro-ph.CO].

[38] Kevork N. Abazajian. "The Consistency of Fermi-LAT Observations of the Galactic Center with a Millisecond Pulsar Population in the Central Stellar Cluster". In: *JCAP* 1103 (2011), p. 010. DOI: 10.1088/1475-7516/2011/03/010. arXiv: 1011.4275 [astro-ph.HE].

[39] L. Accardo et al. "High Statistics Measurement of the Positron Fraction in Primary Cosmic Rays of 0.5–500 GeV with the Alpha Magnetic Spectrometer on the International Space Station". In: *Phys. Rev. Lett.* 113 (2014), p. 121101. DOI: 10.1103/PhysRevLett.113.121101.

[40] Nikolas Zimmermann. "Dark Matter signal from $e^+/e^-/\bar{p}$ with the AMS-02 Detector on the International Space Station". In: *PoS* EPS-HEP2017 (2017), p. 090. DOI: 10.22323/1.314.0090.

[41] Joachim Kopp. "Constraints on dark matter annihilation from AMS-02 results". In: *Phys. Rev.* D88 (2013), p. 076013. DOI: 10.1103/PhysRevD.88.076013. arXiv: 1304.1184 [hep-ph].

[42] M. Di Mauro et al. "Interpretation of AMS-02 electrons and positrons data". In: *JCAP* 1404 (2014), p. 006. DOI: 10.1088/1475-7516/2014/04/006. arXiv: 1402.0321 [astro-ph.HE].

[43] M. Kruskal, S. P. Ahlen, and G. Tarlé. "Secondary Production as the Origin of the Cosmic-ray Positron Excess". In: *Astrophys. J.* 818.1 (2016), p. 70. DOI: 10.3847/0004-637X/818/1/70. arXiv: 1410.7239 [astro-ph.HE].

[44] Rouven Essig et al. "Constraining Light Dark Matter with Low-Energy e^+e^- Colliders". In: *JHEP* 11 (2013), p. 167. DOI: 10.1007/JHEP11(2013)167. arXiv: 1309.5084 [hep-ph].

[45] Morad Aaboud et al. "Search for dark matter and other new phenomena in events with an energetic jet and large missing transverse momentum using the ATLAS detector". In: *JHEP* 01 (2018), p. 126. DOI: 10.1007/JHEP01(2018)126. arXiv: 1711.03301 [hep-ex].

[46] Morad Aaboud et al. "Search for dark matter at $\sqrt{s} = 13$ TeV in final states containing an energetic photon and large missing transverse momentum with the ATLAS detector". In: *Eur. Phys. J.* C77.6 (2017), p. 393. DOI: 10.1140/epjc/s10052-017-4965-8. arXiv: 1704.03848 [hep-ex].

[47] M. Aaboud et al. "Search for an invisibly decaying Higgs boson or dark matter candidates produced in association with a Z boson in pp collisions at $\sqrt{s} = 13$ TeV with the ATLAS detector". In: *Phys. Lett.* B776 (2018), pp. 318–337. DOI: 10.1016/j.physletb.2017.11.049. arXiv: 1708.09624 [hep-ex].

[48] Georges Aad et al. "Search for invisible particles produced in association with single-top-quarks in proton-proton collisions at $\sqrt{s} = 8$ TeV with the ATLAS detector". In: *Eur. Phys. J.* C75.2 (2015), p. 79. DOI: 10.1140/epjc/s10052-014-3233-4. arXiv: 1410.5404 [hep-ex].

[49] Georges Aad et al. "Search for dark matter in events with heavy quarks and missing transverse momentum in pp collisions with the ATLAS detector". In: *Eur. Phys. J.* C75.2 (2015), p. 92. DOI: 10.1140/epjc/s10052-015-3306-z. arXiv: 1410.4031 [hep-ex].

[50] Morad Aaboud et al. "Search for new phenomena in dijet events using 37 fb^{-1} of pp collision data collected at $\sqrt{s}$ =13 TeV with the ATLAS detector". In: *Phys. Rev.* D96.5 (2017), p. 052004. DOI: 10.1103/PhysRevD.96.052004. arXiv: 1703.09127 [hep-ex].

[51] Georges Aad et al. "Search for new phenomena in the dijet mass distribution using $p-p$ collision data at $\sqrt{s} = 8$ TeV with the ATLAS detector". In: *Phys. Rev.* D91.5 (2015), p. 052007. DOI: 10.1103/PhysRevD.91.052007. arXiv: 1407.1376 [hep-ex].

[52] The ATLAS collaboration. "Search for new light resonances decaying to jet pairs and produced in association with a photon or a jet in proton-proton collisions at $\sqrt{s} =$ 13 TeV with the ATLAS detector". In: (2016). URL: https://cdsweb.cern.ch/record/2206221.

[53] Morad Aaboud et al. "Search for low-mass dijet resonances using trigger-level jets with the ATLAS detector in pp collisions at $\sqrt{s} = 13$ TeV". In: (2018). arXiv: 1804.03496 [hep-ex].

[54] G. Angloher et al. "Results on light dark matter particles with a low-threshold CRESST-II detector". In: *Eur. Phys. J.* C76.1 (2016), p. 25. DOI: 10.1140/epjc/s10052-016-3877-3. arXiv: 1509.01515 [astro-ph.CO].

[55] E. Aprile et al. "First Dark Matter Search Results from the XENON1T Experiment". In: *Phys. Rev. Lett.* 119.18 (2017), p. 181301. DOI: 10.1103/PhysRevLett.119.181301. arXiv: 1705.06655 [astro-ph.CO].

[56] Andi Tan et al. "Dark Matter Results from First 98.7 Days of Data from the PandaX-II Experiment". In: *Phys. Rev. Lett.* 117.12 (2016), p. 121303. DOI: 10.1103/PhysRevLett.117.121303. arXiv: 1607.07400 [hep-ex].

[57] D. S. Akerib et al. "Results from a search for dark matter in the complete LUX exposure". In: *Phys. Rev. Lett.* 118.2 (2017), p. 021303. DOI: 10.1103/PhysRevLett.118.021303. arXiv: 1608.07648 [astro-ph.CO].

[58] D. S. Akerib et al. "Results on the Spin-Dependent Scattering of Weakly Interacting Massive Particles on Nucleons from the Run 3 Data of the LUX Experiment". In: *Phys. Rev. Lett.* 116.16 (2016), p. 161302. DOI: 10.1103/PhysRevLett.116.161302. arXiv: 1602.03489 [hep-ex].

[59] Andreas Albert et al. *Recommendations of the LHC Dark Matter Working Group: Comparing LHC searches for heavy mediators of dark matter production in visible and invisible decay channels*. 2017. arXiv: 1703.05703 [hep-ex].

[60] The ATLAS Collaboration. *Summary plots from the ATLAS Exotic physics group*. July 2017. URL: https://atlas.web.cern.ch/Atlas/GROUPS/PHYSICS/CombinedSummaryPlots/EXOTICS/.

[61] Lyndon Evans and Philip Bryant. "LHC Machine". In: *JINST* 3 (2008), S08001. DOI: 10.1088/1748-0221/3/08/S08001.

[62] Xabier Cid Vidal and Ramon Cid Mandano. *Taking a closer look at the LHC*. 2018. URL: https://www.lhc-closer.es/taking_a_closer_look_at_lhc.

[63] G. Aad et al. "The ATLAS Experiment at the CERN Large Hadron Collider". In: *JINST* 3 (2008), S08003. DOI: 10.1088/1748-0221/3/08/S08003.

[64] Felix Müller. "Jet Production Measurements at the ATLAS Experiment". PhD thesis. Heidelberg University, 2013. URL: https://www.kip.uni-heidelberg.de/Veroeffentlichungen/details.php?id=2966.

[65] K. Aamodt et al. "The ALICE experiment at the CERN LHC". In: *JINST* 3 (2008), S08002. DOI: 10.1088/1748-0221/3/08/S08002.

[66] S. Chatrchyan et al. "The CMS Experiment at the CERN LHC". In: *JINST* 3 (2008), S08004. DOI: 10.1088/1748-0221/3/08/S08004.

[67] A. Augusto Alves Jr. et al. "The LHCb Detector at the LHC". In: *JINST* 3 (2008), S08005. DOI: 10.1088/1748-0221/3/08/S08005.

[68] J. Pequeano CERN PhotoLab. *Computer generated image of the whole ATLAS detector*. 2008. URL: https://cds.cern.ch/record/1095924.

[69] G. Aad et al. "The ATLAS Inner Detector commissioning and calibration". In: *Eur. Phys. J.* C70 (2010), pp. 787–821. DOI: 10.1140/epjc/s10052-010-1366-7. arXiv: 1004.5293 [physics.ins-det].

[70] J. Pequeano and CERN PhotoLab. *Computer generated image of the ATLAS calorimeter*. 2018. URL: https://cds.cern.ch/record/1095927.

[71] T. Barillari. "The ATLAS liquid argon hadronic end-cap calorimeter: Construction and selected beam test results". In: *Nucl. Phys. Proc. Suppl.* 150 (2006). [,102(2004)], pp. 102–105. DOI: 10.1016/j.nuclphysbps.2004.10.087. arXiv: physics/0407026 [physics.ins-det].

[72] M. Aharrouche et al. "Energy linearity and resolution of the ATLAS electromagnetic barrel calorimeter in an electron test-beam". In: *Nucl. Instrum. Meth.* A568 (2006), pp. 601–623. DOI: 10.1016/j.nima.2006.07.053. arXiv: physics/0608012 [physics].

[73] T. Davidek. "ATLAS tile calorimeter performance for single particles in beam tests". In: *J. Phys. Conf. Ser.* 160 (2009), p. 012057. DOI: 10.1088/1742-6596/160/1/012057.

[74] B. Dowler et al. "Performance of the ATLAS hadronic end-cap calorimeter in beam tests". In: *Nucl. Instrum. Meth.* A482 (2002), pp. 94–124. DOI: 10.1016/S0168-9002(01)01338-9.

[75] J. P. Archambault et al. "Energy calibration of the ATLAS liquid argon forward calorimeter". In: *JINST* 3 (2008), P02002. DOI: 10.1088/1748-0221/3/02/P02002.

[76] Georges Aad et al. "Muon reconstruction performance of the ATLAS detector in proton–proton collision data at $\sqrt{s}$ =13 TeV". In: *Eur. Phys. J.* C76.5 (2016), p. 292. DOI: 10.1140/epjc/s10052-016-4120-y. arXiv: 1603.05598 [hep-ex].

[77] V. Cindro et al. "The ATLAS beam conditions monitor". In: *JINST* 3 (2008), P02004. DOI: 10.1088/1748-0221/3/02/P02004.

[78] S. van der Meer. *Calibration of the Effective Beam Height in the ISR*. Tech. rep. CERN, 1968.

[79] H Burkhardt and P Grafström. *Absolute Luminosity from Machine Parameters*. Tech. rep. LHC-PROJECT-Report-1019. CERN-LHC-PROJECT-Report-1019. CERN, 2007. URL: https://cds.cern.ch/record/1056691.

[80] A. K. Barlow et al. "Instrumentation and beam diagnostics in the ISR". In: *Proceedings of the 8th International Conference on High- Energy Accelerators*. Ed. by M. Hildred Blewett. CERN. Jan. 1971, pp 426-30. URL: https://www.researchgate.net/publication/41585617_Instrumentation_and_beam_diagnostics_in_the_ISR.

[81] G. Aad et al. "The ATLAS Simulation Infrastructure". In: *Eur. Phys. J.* C70 (2010), pp. 823–874. DOI: 10.1140/epjc/s10052-010-1429-9. arXiv: 1005.4568 [physics.ins-det].

[82] Asher Berlin, Tongyan Lin, and Lian-Tao Wang. "Mono-Higgs Detection of Dark Matter at the LHC". In: *JHEP* 06 (2014), p. 078. DOI: 10.1007/JHEP06(2014)078. arXiv: 1402.7074 [hep-ph].

[83] Matteo Cacciari, Gavin P. Salam, and Gregory Soyez. "The Anti-k(t) jet clustering algorithm". In: *JHEP* 04 (2008), p. 063. DOI: 10.1088/1126-6708/2008/04/063. arXiv: 0802.1189 [hep-ph].

[84] The ATLAS collaboration. *In-situ measurements of the ATLAS large-radius jet response in 13 TeV pp collisions*. Tech. rep. CERN, 2017. URL: https://cds.cern.ch/record/2275655.

[85] David Krohn, Jesse Thaler, and Lian-Tao Wang. "Jet Trimming". In: *JHEP* 02 (2010), p. 084. DOI: 10.1007/JHEP02(2010)084. arXiv: 0912.1342 [hep-ph].

[86] The ATLAS collaboration. *Optimisation of the ATLAS b-tagging performance for the 2016 LHC Run*. Tech. rep. ATL-PHYS-PUB-2016-012. Geneva: CERN, June 2016. URL: https://cds.cern.ch/record/2160731.

[87] Morad Aaboud et al. "Electron efficiency measurements with the ATLAS detector using 2012 LHC proton–proton collision data". In: *Eur. Phys. J.* C77.3 (2017), p. 195. DOI: 10.1140/epjc/s10052-017-4756-2. arXiv: 1612.01456 [hep-ex].

[88] The ATLAS collaboration. *Jet mass reconstruction with the ATLAS Detector in early Run 2 data*. Tech. rep. ATLAS-CONF-2016-035. Geneva: CERN, July 2016. URL: http://cds.cern.ch/record/2200211.

[89] Morad Aaboud et al. "Performance of the ATLAS Trigger System in 2015". In: *Eur. Phys. J.* C77.5 (2017), p. 317. DOI: 10.1140/epjc/s10052-017-4852-3. arXiv: 1611.09661 [hep-ex].

[90] Georges Aad et al. "Reconstruction of hadronic decay products of tau leptons with the ATLAS experiment". In: *Eur. Phys. J.* C76.5 (2016), p. 295. DOI: 10.1140/epjc/s10052-016-4110-0. arXiv: 1512.05955 [hep-ex].

[91] Daniel Isaac Narrias Villar. "Search for Dark Matter produced in association with a Higgs boson decaying to $b\bar{b}$ using 36 fb^{-1} of pp collisions at $\sqrt{s} = 13$ TeV with the ATLAS Detector". Presented 06 Feb 2018. PhD thesis. Ruprecht-Karls-Universität Heidelberg, Nov. 2017. URL: https://cds.cern.ch/record/2302160.

[92] Georges Aad et al. "Search for the $b\bar{b}$ decay of the Standard Model Higgs boson in associated $(W/Z)H$ production with the ATLAS detector". In: *JHEP* 01 (2015), p. 069. DOI: 10.1007/JHEP01(2015)069. arXiv: 1409.6212 [hep-ex].

[93] Glen Cowan et al. "Asymptotic formulae for likelihood-based tests of new physics". In: *Eur. Phys. J.* C71 (2011). [Erratum: Eur. Phys. J.C73,2501(2013)], p. 1554. DOI: 10.1140/epjc/s10052-011-1554-0, 10.1140/epjc/s10052-013-2501-z. arXiv: 1007.1727 [physics.data-an].

[94] Seyda Ipek, David McKeen, and Ann E. Nelson. "A Renormalizable Model for the Galactic Center Gamma Ray Excess from Dark Matter Annihilation". In: *Phys. Rev.* D90.5 (2014), p. 055021. DOI: 10.1103/PhysRevD.90.055021. arXiv: 1404.3716 [hep-ph].

[95] Jose Miguel No. "Looking through the pseudoscalar portal into dark matter: Novel mono-Higgs and mono-Z signatures at the LHC". In: *Phys. Rev.* D93.3 (2016), p. 031701. DOI: 10.1103/PhysRevD.93.031701. arXiv: 1509.01110 [hep-ph].

[96] Dorival Goncalves, Pedro A. N. Machado, and Jose Miguel No. "Simplified Models for Dark Matter Face their Consistent Completions". In: *Phys. Rev.* D95.5 (2017), p. 055027. DOI: 10.1103/PhysRevD.95.055027. arXiv: 1611.04593 [hep-ph].

[97] Felix Kahlhoefer et al. "Implications of unitarity and gauge invariance for simplified dark matter models". In: *JHEP* 02 (2016), p. 016. DOI: 10.1007/JHEP02(2016)016. arXiv: 1510.02110 [hep-ph].

[98] G. C. Branco et al. "Theory and phenomenology of two-Higgs-doublet models". In: *Phys. Rept.* 516 (2012), pp. 1–102. DOI: 10.1016/j.physrep.2012.02.002. arXiv: 1106.0034 [hep-ph].

[99] John F. Gunion and Howard E. Haber. "The CP conserving two Higgs doublet model: The Approach to the decoupling limit". In: *Phys. Rev.* D67 (2003), p. 075019. DOI: 10.1103/PhysRevD.67.075019. arXiv: hep-ph/0207010 [hep-ph].

[100] Alex Pomarol and Roberto Vega. "Constraints on CP violation in the Higgs sector from the rho parameter". In: *Nucl. Phys.* B413 (1994), pp. 3–15. DOI: 10.1016/0550-3213(94)90611-4. arXiv: hep-ph/9305272 [hep-ph].

[101] Georges Aad et al. "Constraints on new phenomena via Higgs boson couplings and invisible decays with the ATLAS detector". In: *JHEP* 11 (2015), p. 206. DOI: 10.1007/JHEP11(2015)206. arXiv: 1509.00672 [hep-ex].

[102] Gautam Bhattacharyya et al. "Scalar sector properties of two-Higgs-doublet models with a global U(1) symmetry". In: *JHEP* 10 (2013), p. 081. DOI: 10.1007/JHEP10(2013)081. arXiv: 1308.4297 [hep-ph].

[103] Andreas Crivellin, Ahmet Kokulu, and Christoph Greub. "Flavor-phenomenology of two-Higgs-doublet models with generic Yukawa structure". In: *Phys. Rev.* D87.9 (2013), p. 094031. DOI: 10.1103/PhysRevD.87.094031. arXiv: 1303.5877 [hep-ph].

[104] Julian A. King et al. "Stringent null constraint on cosmological evolution of the proton-to-electron mass ratio". In: *Phys. Rev. Lett.* 101 (2008), p. 251304. DOI: 10.1103/PhysRevLett.101.251304. arXiv: 0807.4366 [astro-ph].

[105] S. Alekhin, A. Djouadi, and S. Moch. "The top quark and Higgs boson masses and the stability of the electroweak vacuum". In: *Phys. Lett.* B716 (2012), pp. 214–219. DOI: 10.1016/j.physletb.2012.08.024. arXiv: 1207.0980 [hep-ph].

[106] Florian Staub. "Reopen parameter regions in Two-Higgs Doublet Models". In: *Phys. Lett.* B776 (2018), pp. 407–411. DOI: 10.1016/j.physletb.2017.11.065. arXiv: 1705.03677 [hep-ph].

[107] Robert J. Scherrer and Michael S. Turner. "On the Relic, Cosmic Abundance of Stable Weakly Interacting Massive Particles". In: *Phys. Rev.* D33 (1986). [Erratum: Phys. Rev.D34,3263(1986)], p. 1585. DOI: 10.1103/PhysRevD.33.1585,10.1103/PhysRevD.34.3263.

[108] Valerio Ippolito. *2HDM+a: Relic density or: does this DM model solve the DM problem?* Aug. 2017. URL: https://indico.cern.ch/event/658607/contributions/2685736/attachments/1505647/2346133/20170808_relic2hdm.pdf.

[109] The LHC Dark Matter Working Group. "LHC Dark Matter Working Group Recommendations for the Two Higgs Doublet with a Pseudoscalar Mediator". In preparation.

[110] Martin Bauer. private communication. 2017.

[111] Olivier Mattelaer. "On the maximal use of Monte Carlo samples: re-weighting events at NLO accuracy". In: *Eur. Phys. J.* C76.12 (2016), p. 674. DOI: 10.1140/epjc/s10052-016-4533-7. arXiv: 1607.00763 [hep-ph].

[112] J. Alwall et al. "The automated computation of tree-level and next-to-leading order differential cross sections, and their matching to parton shower simulations". In: *JHEP* 07 (2014), p. 079. DOI: 10.1007/JHEP07(2014)079. arXiv: 1405.0301 [hep-ph].

[113] Giovanni Ossola, Costas G. Papadopoulos, and Roberto Pittau. "Reducing full one-loop amplitudes to scalar integrals at the integrand level". In: *Nucl. Phys.* B763 (2007), pp. 147–169. DOI: 10.1016/j.nuclphysb.2006.11.012. arXiv: hep-ph/0609007 [hep-ph].

[114] Valentin Hirschi et al. "Automation of one-loop QCD corrections". In: *JHEP* 05 (2011), p. 044. DOI: 10.1007/JHEP05(2011)044. arXiv: 1103.0621 [hep-ph].

[115] Pierpaolo Mastrolia, Edoardo Mirabella, and Tiziano Peraro. "Integrand reduction of one-loop scattering amplitudes through Laurent series expansion". In: *JHEP* 06 (2012). [Erratum: JHEP11,128(2012)], p. 095. DOI: 10.1007/JHEP11(2012)128, 10.1007/JHEP06(2012)095. arXiv: 1203.0291 [hep-ph].

[116] Johan Alwall et al. "Computing decay rates for new physics theories with FeynRules and MadGraph 5_aMCNLO". In: *Comput. Phys. Commun.* 197 (2015), pp. 312–323. DOI: 10.1016/j.cpc.2015.08.031. arXiv: 1402.1178 [hep-ph].

[117] Celine Degrande et al. "UFO - The Universal FeynRules Output". In: *Comput. Phys. Commun.* 183 (2012), pp. 1201–1214. DOI: 10.1016/j.cpc.2012.01.022. arXiv: 1108.2040 [hep-ph].

[118] Richard D. Ball et al. "Parton distributions for the LHC Run II". In: *JHEP* 04 (2015), p. 040. DOI: 10.1007/JHEP04(2015)040. arXiv: 1410.8849 [hep-ph].

[119] Torbjörn Sjöstrand et al. "An Introduction to PYTHIA 8.2". In: *Comput. Phys. Commun.* 191 (2015), pp. 159–177. DOI: 10.1016/j.cpc.2015.01.024. arXiv: 1410.3012 [hep-ph].

[120] S. Agostinelli et al. "GEANT4: A Simulation toolkit". In: *Nucl. Instrum. Meth.* A506 (2003), pp. 250–303. DOI: 10.1016/S0168-9002(03)01368-8.

[121] Arno R. Bohm and Yoshihiro Sato. "Relativistic resonances: Their masses, widths, lifetimes, superposition, and causal evolution". In: *Phys. Rev.* D71 (2005), p. 085018. DOI: 10.1103/PhysRevD.71.085018. arXiv: hep-ph/0412106 [hep-ph].

[122] Jose Miguel No. *2HDM Pseudoscalar + DM Benchmarks*. June 2017. URL: https://indico.cern.ch/event/646857/contributions/2634493/attachments/1479924/2294462/DMLHC_No_June.pdf.

[123] Felix Kahlhoefer and Ulrich Haisch. private communication. 2018.

[124] E. Boos et al. "Generic user process interface for event generators". In: *Physics at TeV colliders. Proceedings, Euro Summer School, Les Houches, France, May 21-June 1, 2001*. 2001. arXiv: hep-ph/0109068 [hep-ph]. URL: http://lss.fnal.gov/archive/preprint/fermilab-conf-01-496-t.shtml.

[125] Johan Alwall et al. "A Standard format for Les Houches event files". In: *Comput. Phys. Commun.* 176 (2007), pp. 300–304. DOI: 10.1016/j.cpc.2006.11.010. arXiv: hep-ph/0609017 [hep-ph].

[126] Kyle Cranmer and Itay Yavin. "RECAST: Extending the Impact of Existing Analyses". In: *JHEP* 04 (2011), p. 038. DOI: 10.1007/JHEP04(2011)038. arXiv: 1010.2506 [hep-ex].

[127] Kyle Cranmer and Lukas Heinrich. "Yadage and Packtivity - analysis preservation using parametrized workflows". In: *J. Phys. Conf. Ser.* 898.10 (2017), p. 102019. DOI: 10.1088/1742-6596/898/10/102019. arXiv: 1706.01878 [physics.data-an].

[128] Docker Inc. *Docker Documentation*. Feb. 2018. URL: https://docs.docker.com/.

[129] Alexander L. Read. "Modified frequentist analysis of search results (The CL(s) method)". In: *Workshop on confidence limits, CERN, Geneva, Switzerland, 17-18 Jan 2000: Proceedings*. 2000, pp. 81–101. URL: http://weblib.cern.ch/abstract?CERN-OPEN-2000-205.

[130] Alexander L. Read. "Presentation of search results: The CL(s) technique". In: *J. Phys.* G28 (2002). [,11(2002)], pp. 2693–2704. DOI: 10.1088/0954-3899/28/10/313.

[131] Gary J. Feldman and Robert D. Cousins. "A Unified approach to the classical statistical analysis of small signals". In: *Phys. Rev.* D57 (1998), pp. 3873–3889. DOI: 10.1103/PhysRevD.57.3873. arXiv: physics/9711021 [physics.data-an].

[132] J. Neyman and E. S. Pearson. "IX. On the problem of the most efficient tests of statistical hypotheses". In: *Philosophical Transactions of the Royal Society of London A: Mathematical, Physical and Engineering Sciences* 231.694-706 (1933), pp. 289–337. ISSN: 0264-3952. DOI: 10.1098/rsta.1933.0009. eprint: http://rsta.royalsocietypublishing.org/content/231/694-706/289.full.pdf.

[133] James S. Gainer et al. "Exploring Theory Space with Monte Carlo Reweighting". In: *JHEP* 10 (2014), p. 078. DOI: 10.1007/JHEP10(2014)078. arXiv: 1404.7129 [hep-ph].

[134] Morad Aaboud et al. "Search for dark matter in association with a Higgs boson decaying to two photons at $\sqrt{s} = 13$ TeV with the ATLAS detector". In: *Phys. Rev.* D96.11 (2017), p. 112004. DOI: 10.1103/PhysRevD.96.112004. arXiv: 1706.03948 [hep-ex].

[135] Martin Bauer, Martin Klassen, and Valentin Tenorth. *Universal Properties of Pseudoscalar Mediators*. 2017. arXiv: 1712.06597 [hep-ph].

[136] Andy Buckley et al. "Rivet user manual". In: *Comput. Phys. Commun.* 184 (2013), pp. 2803–2819. DOI: 10.1016/j.cpc.2013.05.021. arXiv: 1003.0694 [hep-ph].

[137] Jonathan M. Butterworth et al. "Constraining new physics with collider measurements of Standard Model signatures". In: *JHEP* 03 (2017), p. 078. DOI: 10.1007/JHEP03(2017)078. arXiv: 1606.05296 [hep-ph].

[138] Jason Veatch, Oleg Brandt, and Gabriel Palacino. *Using track-assisted techniques to calculate large-R jet substructure observables*. Tech. rep. ATL-COM-PHYS-2018-398. Geneva: CERN, Apr. 2018. URL: https://cds.cern.ch/record/2313282.

[139] Felix Kling, Jose Miguel No, and Shufang Su. "Anatomy of Exotic Higgs Decays in 2HDM". In: *JHEP* 09 (2016), p. 093. DOI: 10.1007/JHEP09(2016)093. arXiv: 1604.01406 [hep-ph].

[140] The Scipy Community. *scipy.interpolate.griddata*. SciPy Reference Guide. May 2014. URL: https://docs.scipy.org/doc/scipy-0.14.0/reference/generated/scipy.interpolate.griddata.html.

[141] Huhdanpaa H.T., Dobkin D.P., and Barber C.P. "The Quickhull algorithm for convex hulls". In: *ACM Trans. on Mathematical Software* 22.4 (Dec. 1996), pp. 469–483. URL: http://www.qhull.org.

[142] *Barycentric coordinate system*. Mar. 2018. URL: https://en.wikipedia.org/wiki/Barycentric_coordinate_system.

[143] Eric W. Weisstein. *Barycentric Coordinates*. MathWorld–A Wolfram Web Resource. Feb. 2018. URL: https://mathworld.wolfram.com/BarycentricCoordinates.html.

List of Figures

List of Tables

Erklärung:

Ich versichere, dass ich diese Arbeit selbstständig verfasst habe und keine anderen als die angegebenen Quellen und Hilfsmittel benutzt habe.

Heidelberg, den 30. April 2018 .....